Dynamic Grid Adaptation Applied to Large Eddy Simulation Turbulence Modelling

Govert de With

A thesis submitted in partial fulfilment of
the requirements of the University of Hertfordshire
for the degree of Doctor of Philosophy

The programme of research was carried out in the
Department of Aerospace, Mechanical and Civil Engineering,
Faculty of Engineering and Information Sciences,
University of Hertfordshire

November 2001

Ter nagedachtenis aan mijn Moeder

Hoe kan ik mijn dankbaarheid tonen aan haar die ik zoveel schuldig ben.
Hoe kan ik mijn gevoel van verlies uiten van zij die zo belangrijk voor mij was.
Ik kan slechts mijn waardering tonen voor wat ze heeft gedaan,
de jeugd die ze mij heeft gegeven en de steun die ze had voor al mijn handelen.

Dat je zo vroeg van ons bent heengegaan was niet wat je verdiende.
Het was veel te vroeg en het kwam veel te snel,
wat is achtergebleven is de pijn van hen die van je hielden.

In memory to my Mother

How can I express my gratitude to someone I owe so much.
How can I express the loss of someone so special to me.
I can only show my appreciation for what she has done,
the childhood she gave me and the support she had for all my actions.

To lose your live when you did was not what you deserved.
It was too soon and it came too early,
what remains is the pain of those who loved you.

Acknowledgement

This thesis presents the results of my work performed at the University of Hertfordshire for a period of three years. I would like to express my gratitude to Professor A. E. Holdø for the trust he had in me and for the freedom I got to do this research project. His guidance and stimulations were indispensable for the completion of this thesis. Also thanks to my supervisor Dr. S. Nasser for his contribution to the project.

The key factor in this work was the use of the CFD code REACFLOW developed by the Joint Research Centre in Ispra (I). I would like to express my gratitude to Dr. T. A. Huld for the excellent software development and the patience in testing the CFD software.

I would like to extend my gratitude to all my colleagues at the CFD research group of the Hertfordshire University for the pleasant working environment, the stimulating discussions and their friendship. Throughout the three years of my PhD I had a very good feedback from my fellow PhD students Adun Janyalertadun and Konstantinos Pikos. In the fruithful discussions we studied the numerous aspects of fluid dynamics. Furthermore, I would like to thank John Davies for his willingness and enthusiasm to discuss my research project as well for the support he gave during the preparation of this thesis. Also special thanks are due to the research fellow Raj Calay for creating the best environment for research and discussion.

Abstract

At present a large number of fluid dynamics applications are found in aerospace, civil and automotive engineering, as well as medical related fields. In many applications the flow field is turbulent and the computational modelling of such flows remains a difficult task. To resolve all turbulent flow phenomena for flow problems where turbulence is of key interest is a priori not feasible in a Computational Fluid Dynamics (CFD) investigation with a conventional mesh. The use of a Dynamic Grid Adaptation (DGA) algorithm in a turbulent unsteady flow field is an appealing technique which can reduce the computational costs of a CFD investigation. A refinement of the numerical domain with a DGA algorithm requires reliable criteria for mesh refinement which reflect the complex flow processes. At present not much work has been done to obtain reliable refinement criteria for turbulent unsteady flow.

The purpose of the work presented in this thesis is to use both a DGA algorithm and Large Eddy Simulation (LES) turbulence model for predicting turbulent unsteady flow. The criteria for mesh refinement used in this work are derived from the equation for turbulent viscosity in the LES turbulence model. By using a modification to the turbulent viscosity as a refinement variable there is a link between both DGA algorithm and turbulence model. The smaller scale turbulence is modelled via the LES turbulence model, while the larger scales are resolved.

In comparison with the simulations using a conventional mesh, substantial reduction in mesh size has been obtained with the use of a DGA algorithm. The reduction in mesh size is obtained without a decay in the quality of the prediction. It is shown that the use of a DGA algorithm in the context of turbulence modelling is a suitable tool which can be used as a next step in an attempattempt to resolve turbulence more realistically.

Notation

Symbol	**Unit**	**Description**
A_{tr}		Element surface
A^{+}	$[-]$	Constant
C_D	$[-]$	Drag coefficient
$\overline{C}_D$	$[-]$	Integrated drag coefficient
$\widetilde{C}_D$	$[-]$	Fluctuating drag coefficient
C_L	$[-]$	Lift coefficient
$\overline{C}_L$	$[-]$	Integrated lift coefficient
$\widetilde{C}_L$	$[-]$	Fluctuating lift coefficient
C_p	$[-]$	Pressure coefficient
$\overline{C}_p$	$[-]$	Integrated pressure coefficient
C_m	$[-]$	Adaptation variable for mesh
C_s	$[-]$	Smagorinsky constant
C_{str}	$[-]$	Adaptation variable for strain
D	$[m]$	Cylinder diameter
D_{damp}	$[-]$	Damping variable
e	$[Nm]$	Energy
e_i		Estimated error
F_D	$[N]$	Drag force
F_L	$[N]$	Lift force
f	$[Hz]$	Frequency
g	$[\frac{m}{s^2}]$	Gravity
k	$[\frac{W}{mK}]$	Thermal conductivity
L	$[m]$	Integral scale
L_r	$[m]$	Recirculation length
l_s	$[m]$	Length scale
n	$[-]$	Instantaneous number of time step
N	$[-]$	Number of neighbour elements
p	$[\frac{N}{m^2}]$	Pressure
$\overline{p}$	$[\frac{N}{m^2}]$	Integrated pressure
q_i		Refinement variable
$\widehat{q}_i$		Interpolated refinement variable

R	$[-]$	Correlation coefficient
Re	$[-]$	Reynolds number
Re_{LES}	$[-]$	Reynolds number based on LES length scale
r	$[-]$	Flux limiter variable
S		Bounding surface of discretisation element
$\lvert\overline{S}\rvert$	$[\frac{1}{s}]$	Magnitude of strain
S_{ij}	$[\frac{1}{s}]$	Strain tensor
S_t	$[-]$	Strouhal number
s		Primitive variable
T	$[K]$	Temperature
t	$[s]$	Time
u	$[\frac{m}{s}]$	Streamwise velocity component
u^*	$[\frac{m}{s}]$	Streamwise intermediate velocity component
u_i	$[\frac{m}{s}]$	u,v,w for i=1,2,3 respectively
u_i^*	$[\frac{m}{s}]$	u^*,v^*,w^* for i=1,2,3 respectively
$\overline{u}$	$[\frac{m}{s}]$	Integrated velocity
$\overline{u}_{cl}$	$[\frac{m}{s}]$	Integrated centreline velocity
$\widehat{u}_i$	$[\frac{m}{s}]$	Interpolated velocity
u'	$[\frac{m}{s}]$	Streamwise fluc. velocity component
u_τ	$[\frac{m}{s}]$	Shear friction velocity
u_∞	$[\frac{m}{s}]$	Main streamwise velocity
v	$[\frac{m}{s}]$	Lateral velocity component
v'	$[\frac{m}{s}]$	Lateral fluc. velocity component
x	$[m]$	Space in streamwise direction
x_i	$[m]$	x,y,z for i=1,2,3 respectively
y	$[m]$	Space in lateral direction
y^+	$[-]$	Distance in wall shear units
Δ	$[m]$	Subgrid length scale
Δ_x	$[m]$	Subgrid length scale in streamwise direction
Δ_y	$[m]$	Subgrid length scale in lateral direction
Θ_s	$[^\circ]$	Separation angle
Ω	$[m^3]$	Discretisation element
α	$[-]$	Kolmogorov coefficient
δ	$[-]$	Kronecker delta
ε	$[\frac{m^2}{s^3}]$	Dissipation rate of turbulent kinetic energy
η	$[m]$	Kolmogorov scale
μ	$[\frac{Ns}{m^2}]$	Dynamic viscosity
μ_t	$[\frac{Ns}{m^2}]$	Turbulent viscosity
τ_{ij}	$[\frac{N}{m^2}]$	Reynolds stress tensor
τ_w	$[\frac{N}{m^2}]$	Wall shear stress
ν	$[\frac{m^2}{s}]$	Kinematic viscosity
ρ	$[\frac{kg}{m^3}]$	Density

Contents

Chapter 1

Introduction

1.1 Motivation

It was the Italian Leonardo da Vinci (1452-1519) who first emphasized the direct study of fluid mechanics in its many aspects. Leonardo's hydraulic observations extended to the detailed characteristics of jets, waves, and eddies, not to mention the flight of birds and comparable facets of essentially every other field of knowledge. Since that time he has been considered to be one of the first pioneers in the field of fluid mechanics. Further contribution to the field of fluid mechanics was made three centuries later with the mathematical work of Navier, Poisson, Saint-Venant and Stokes who described the fundamental motions of fluid. Their mathematical equations were an extension of Newton's 2^{nd} law applied to fluids and are still known as the governing equations. Experimental and mathematical work on turbulent flow has been done by Helmholtz, Kelvin, Rayleigh and Reynolds who investigated the issue of instability of a fluid flow. In an experimental investigation Reynolds [51] discovered that the stability of a flow is governed by a dimensionless number which is nowadays widely known as the Reynolds number. In the hundred years that followed Reynolds's seminal investigation of fluid instabilities there developed a substantial body of literature on the subject of fluid instability and non-uniqueness of a flow field. This included not only work in the mathematical field but also a large body of work in the engineering, physics, astrophysics, oceanographic and meteorological disciplines. People like Lin [33], Chandrasekhar [10], Joseph [28], Drazin & Reid [14], Gorman & Swinney [21] have contributed much to the various aspects of the theory of fluid stability.

At present, a large number of scientific applications are found in aerospace, civil and automotive engineering, as well as medically-related fields. In many industrial applications the flow field is turbulent. The lack of understanding of turbulence still remains a key problem. The notion of turbulence is generally accepted and its meaning is associated with a chaotic or restless character of the fluid. However, an analytical, mathematical description of turbulence is still not apparent and as a consequence mathematical algorithms have shown to be non-universal in predicting turbulent flow motions.

It is the increase of computer power in the last decade which has allowed researchers to use numerical methods as a new means of investigating turbulent flow. The science of replacing the governing equations of fluid flow with discretised equations and to solve these equations at discrete points in time and space is called Computational Fluid Dynamics (CFD). To apply the CFD techniques to a specific flow problem a so-called mesh is required. The mesh is a numerical representation of the geometry, containing the boundaries of the flow domain as well a finite number of discrete points, called nodes, at which the discretised equations are solved. The use of CFD has been a big step forward in making flow predictions useful in the design of industrial products where turbulence is of major interest. Nevertheless, even with the affordable computers available nowadays, numerical flow predictions are time-consuming and the flow prediction strongly relies on the configuration of the numerical algorithm as well the mesh resolution. A high mesh resolution, i.e. using relatively large number of nodes, throughout the numerical domain should improve the flow prediction but leads to an excessive demand for computational power. Conversely a low mesh resolution will reduce the computational costs but the flow prediction will be dominated by all sorts of numerical errors. In many flows where turbulence is of key interest the calculation time is mainly determined by the number of nodes utilised in the mesh. A well-designed mesh is necessary to minimize calculation time and to improve the accuracy of the flow prediction. In such a mesh a high resolution will be used in the region where complex flow phenomena are expected while a lower resolution should be maintained in the regions where the flow is expected to remain laminar.

For flow problems where turbulence is of key interest the mesh resolution required to resolve all flow phenomena is a priori not feasible. To combat the lack in resolving flow detail, turbulence models are applied additional to the discretised governing equations. The difficulty in modelling turbulence lies mainly in the complex velocity patterns associated with it. As a consequence, a wide range of deterministic concepts for modelling turbulence have been developed during the last decades. Such models are commonly distinguished by the adopted averaging method, space or time averaging respectively. The need for such deterministic models is apparent in flows which are dominated by convection where a high Reynolds number exists. For flows dominated by diffusion no complex velocity field is apparent and consequently all flow features can be predicted without a turbulence model; simulations of this type are commonly called Direct Numerical Simulation (DNS).

In a turbulent unsteady flow field, which requires the use of a turbulence model, a good mesh design is important to resolve most of the flow phenomena. However, the criteria for good mesh design at one instant can cause conflict subsequently. Regions which are characterised by a high turbulent intensity at some point during the simulation require a high mesh resolution. However, as the simulation progresses these regions can lose their significance and consequently the nodes allocated in these regions become redundant. An appealing approach for reducing computational costs in such situations is the use of a Dynamic Grid Adaptation (DGA) algorithm whereby the flow field is monitored throughout the simulation. Based on some predefined criteria for mesh refinement the mesh is continuously improved while the simulation is progressing.

The use of a DGA algorithm in a turbulent unsteady flow field is attractive in reducing the computational costs of a CFD investigation. However, important work has to be done to determine reliable criteria for mesh refinement which reflect the complex flow processes. It is hoped that a well-posed mesh refinement method will be a step forward in a more solver and mesh independent CFD process which enables the CFD user to obtain reliable flow predictions without a priori knowledge of the flow field.

1.2 Aims

In this work numerical simulations of a turbulent unsteady flow using an incompressible CFD solver together with both a DGA algorithm and a turbulence model are carried out. The purpose of the work is to use these means to predict turbulent unsteady flow. The specific aims of this work are as follows:

- To establish a method for modelling turbulent unsteady flow where the large turbulent eddies are captured by a DGA algorithm and resolved by the mesh itself while smaller turbulent eddies are modelled with a LES turbulence model.
- To determine a proper DGA refinement variable for an unsteady turbulent flow field.
- To investigate the mesh requirements for turbulent unsteady flow and the sensitivity towards mesh resolution and flow solver.
- To gain a further insight into flows where turbulence is a key flow feature.

In this work the CFD code REACFLOW has been used. This code has adopted the projection method in the solution procedure and uses a triangular mesh.

The turbulence modelling is accomplished by means of Large Eddy Simulation (LES) rather than turbulence models based on Reynolds Averaged Navier-Stokes (RANS) equations because the inherent averaging is inadequate for unsteady flows and the method does not utilise the potential of finer grids to enhance the resolution of turbulent quantities. Similar in spirit to DNS, LES is based on simulating the turbulent fluctuations that can be resolved by the mesh as an integral part of the flow solution. Only turbulent fluctuations with a length scale smaller than the mesh spacing are modelled. Instead of an averaging procedure as in RANS, a Sub Grid Scale (SGS) model is introduced to account for the turbulent motion too small to be captured by the mesh resolution. In addition to the possibilities for more accurate simulation of turbulent flows, LES also offers the advantage of producing more information about the flow field as no averaging procedure is applied to large scale turbulent structures.

The triangular mesh as used in the REACFLOW code puts extra complexity on the determination of the length of the SGS scales. For this reason the definition of length scale in the LES turbulence model has to be considered. A substantial part of this work will focus on the determination of a suitable length scale for a triangular mesh.

The determination of an appropriate refinement variable to approximate the need for additional mesh refinement heavily relies on the physical problem investigated. Widely-used refinement variables in this respect are the density, pressure and velocity gradients. However, the discretisation error describing the deviation from the analytical solution of the set of differential equations is not directly accessible. Therefore the refinement variable is a compromise of the quality of the error indication and the computational complexity of the refinement variable.

The refinement variable used in this work is derived from the equation for turbulent viscosity in the LES turbulence model. By using a modification to the turbulent viscosity as a refinement variable there is a link between both DGA algorithm and turbulence model. The smaller scale turbulence is modelled via the LES turbulence model, while the larger scales are resolved in an explicit way by increasing the mesh resolution.

To validate the proposed method a turbulent unsteady flow has to be selected. A type of flow which is considered to be a challenging test case for CFD is the vortex shedding behind a circular cylinder in the sub-critical flow regime. The flow separates from the cylinder in the laminar mode and a transition takes place to turbulent flow conditions in the shear layers. The phenomenon of transition which is apparent in this kind of flow is subtle and requires a suitable turbulence model as well as a reasonably complex mesh. Results obtained from the numerical simulations are validated by comparing the data of an experimental study carried out by Cantwell & Coles [9] of the flow in a near wake behind a circular cylinder at a Reynolds number of $1.4 \cdot 10^5$.

1.3 Outline of the thesis

Figure 1.1 presents a schematic outline of the thesis. The central part of this thesis is formed by section 2.4 and chapter 3. Section 2.4 describes the objectives of this work and the novelty which lies in the proposed work. In chapter 3 an overview is given of the CFD code REACFLOW and the code development which has been done as part of this work. An overview of the relevant literature is given in chapter 2. The literature review covers three areas which are: numerical methods for solving the governing equations, turbulence and turbulence modelling and DGA methods for unsteady CFD flows. In chapter 4 the results of the CFD simulations are presented. The first section presents the result obtained from simulations with a conventional mesh and gives a validation of the length scale definition for the

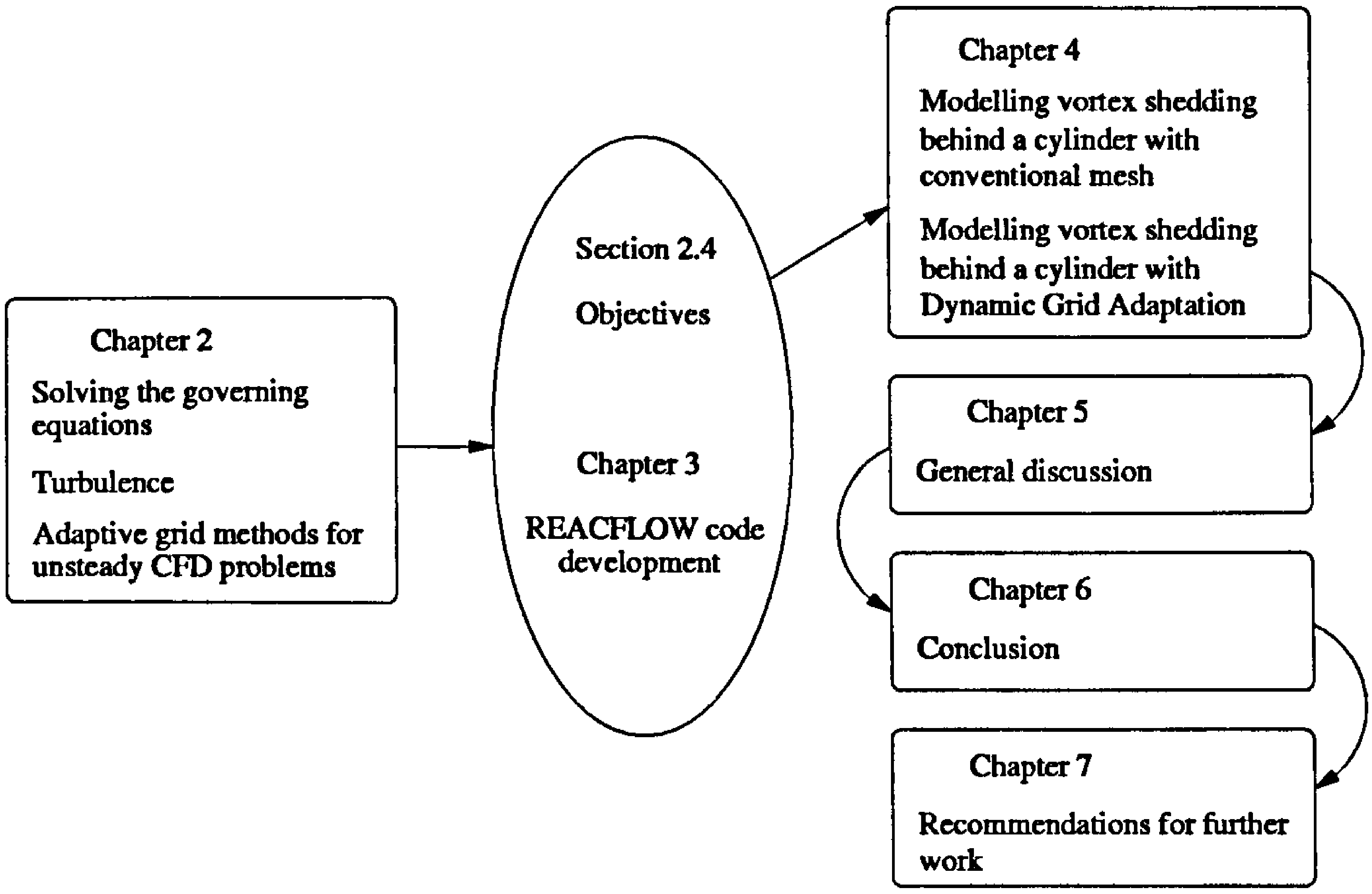

Figure 1.1: Structure of the proposed method for modelling unsteady turbulent flow and validation of the method.

LES turbulence model best suited for a triangular mesh. In the second section the results for simulations with DGA algorithm are presented and compared with experimental data from Cantwell & Coles [9]. The results chapter is followed by a general discussion presented in chapter 5. It is here that the author gives his opinions and explanations for the wide variety of flow phenomena discovered in this work. Strengths and weaknesses of the flow prediction are explained generating new questions for further research. Previously published work is used to discover trends in the flow field and to expose the mechanisms by which vortex shedding takes place. Some questions will remain unanswered and limitations in the data available do restrict the author to validate every aspect of the analysis. However, it is the purpose of this work to bring new light to the phenomenon of vortex shedding even if this gives rise to new questions. In chapter 6 the conclusions of this work are highlighted. Finally suggestions for obtaining improved results and recommendations for further research are presented in chapter 7.

Chapter 2

Background and literature review

The prediction of an unsteady turbulent flow field is despite intensive research still considered to be a difficult task. The limited success of modelling a turbulent flow field reflects the lack of understanding of turbulence as a physical phenomenon. Investigating turbulence mechanisms by means of a numerical study requires the discretised version of the governing equations to be resolved. Despite significant growth in computer power, computational requirements for predicting flows where turbulence is a key interest can not be fulfilled at present. As a consequence, a wide range of concepts for modelling turbulence have been presented in recent decades. It has already been mentioned that an appealing approach for reducing computational costs in a numerical study is the use of DGA, whereby the mesh adapts to flow field. The present work has focused on the governing equations, turbulence modelling and DGA. In this chapter a review will be given of the work done in these areas.

2.1 Solving the governing equations

The basic equations of fluid dynamics are the continuity, momentum and energy equations. They are the mathematical statements of three fundamental physical principles upon which all fluid dynamics is based.

2.1.1 Governing equations

Conservation of mass

The mathematical notation for conservation of mass is shown in equation 2.1.

$$\frac{\partial \rho}{\partial t} + \frac{\partial (\rho u_i)}{\partial x_i} = 0 \qquad (2.1)$$

Conservation of momentum

Conservation of momentum is obtained for a general linear viscous fluid by substituting the stress relations into Newton's 2^{nd} law. It states that the net force on the fluid element is the product of its mass and the acceleration of the element.

This equation is known as the Navier-Stokes equation. Equation 2.2 expresses this:

$$\frac{\partial(\rho u_i)}{\partial t} + \frac{\partial(\rho u_i u_j)}{\partial x_i} = -\frac{\partial p}{\partial x_i} + \mu\frac{\partial^2 u_i}{\partial x_j \partial x_j} + \rho g_i \tag{2.2}$$

The left hand side of equation 2.2 contains the convection terms including the non-linear advection terms, while the right hand side contains the pressure, viscous and gravitational terms. A flow problem which is dominated by the advective terms is called turbulent, while a laminar type of flow is dominated by the viscous terms. A measure for the ratio between advective and viscous terms is given by the Reynolds number. The Reynolds number describes the ratio of the inertial forces to the viscous forces and is given by the following formula:

$$Re = \frac{\rho u D}{\mu} \tag{2.3}$$

where ρ is the fluid density, μ is the dynamic viscosity of the fluid, u is the uniform upstream velocity and D is the characteristic length.

Conservation of energy

The 1^{st} law of thermodynamics when applied to a moving fluid element states that; the rate of change of energy inside a fluid element is equal to the net flux of heat into the element plus the rate of work done on the element. The energy equation is written as used in the REACFLOW code.

$$\frac{\partial(\rho e_i)}{\partial t} + \frac{\partial(\rho u_j e_i)}{\partial x_i} = k\frac{\partial^2 T}{\partial x_j x_j} \tag{2.4}$$

2.1.2 Important consideration of numerical methods

For the solution of realistic problems, one is forced to consider approximate solution methods. Computational fluid dynamics (CFD) is the science of replacing the governing equations of fluid flow with discretised equations and solving these equations at discrete points in time and space. The three principal numerical methods are the Finite Difference Method (FDM), the Finite Element Method (FEM) and the Finite Volume Method (FVM), were FVM is the method used in this work. The FVM approach is as an integral technique applied to the conservative forms of the governing equations and can be considered as a hybrid, lying between classical FDM and FEM. From a finite element perspective the FVM approach can be considered as a special case of the method of weighted residuals, in which the weighting function is chosen to be unity over a control volume and zero everywhere else.

An example of a FVM notation is shown in equation 2.5. The first integral represent the integration over a volume and the terms within the surface integral represent the mass flow through the bounding surface of the volume in a direction perpendicular to the surface.

$$\int_{\Omega} \frac{\partial \rho}{\partial t} \partial \Omega + \oint_{S} (\rho \vec{v}) \bullet \vec{dS} = 0 \tag{2.5}$$

The integration method over a volume guarantees that the basic quantities of mass, momentum and energy will remain conserved in the discrete representation of the equations. In addition, the integral approach provides a more intuitive association between the physical processes occurring across the bounding surfaces of a volume and the governing equations.

In order to solve the discretised equations using any of the above numerical methods, it is necessary to consider a number of numerical aspects.

- Time integration
- Pressure coupling
- Discrete field representation
- Upwinding schemes

Time integration Many fluid flow problems have a time dependent or transient behaviour. It is therefore necessary to generate FVM formulations as functions of time. The solution algorithm for a transient flow analysis can be categorised as being either explicit or implicit. In the explicit formulation, the dependent variable at the new step is obtained from known values at the previous time step. This is a direct solution on the control volumes. In the implicit formulation, the dependent variable at the new step is most often calculated from both values at the previous time step and unknown quantities at the new time step via an iterative process.

The explicit solver is simple and fast. However, as the unknown value of the flow variable can be calculated from a single equation, it is only conditionally stable. The integration may become unstable when the time step is too large for the flow field leading to oscillations in the numerical method which gradually grow as the solution proceeds. The requirements for stability are described in terms of maximum values for the Fourier constant and Courant Friedrichs Levy (CFL) constant. The Fourier constant is a stability indicator for the diffusion terms, while the CFL number is an indicator for the convection terms. The implicit method, however, is much more stable as its stability is not governed by the size of time steps, but it requires more computational time compared to the explicit solution due to the fact that a set of simultaneous equations has to be solved to find the unknown values of the flow variable.

Pressure coupling One of the terms to be modelled within the momentum equation is the pressure derivative. For the momentum equation, once integrated, this

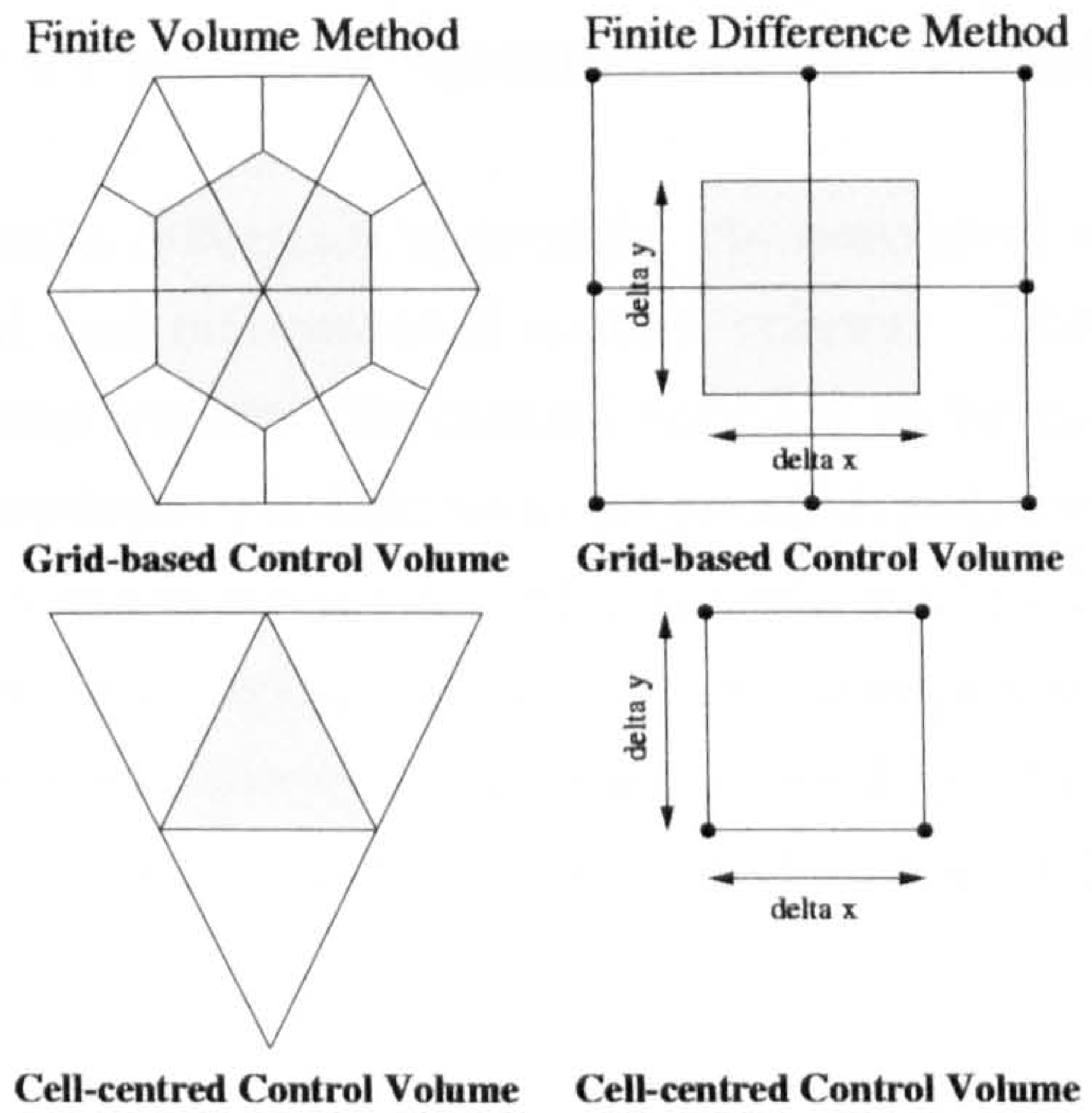

Figure 2.1: Subdivision of Domain.

takes the form of:

$$-\left([p\Omega]_{x+} - [p\Omega]_{x-}\right) \tag{2.6}$$

The terms within the square brackets represent values on the faces of the control volume perpendicular to the x-axis and Ω represents the area of the cell face. The discretisation of these terms causes a particular problem related to the generation of physically unrealistic pressure oscillations, colloquially known as chequer boarding. Consider the situation where all dependent variables are stored at the cell centred node and the pressure at a cell face is obtained using linear interpolation. Then on a uniform cartesian grid the above equation becomes:

$$-\left[\frac{1}{2}\left(p_{i+1,j} + p_{i,j}\right)\Omega - \frac{1}{2}\left(p_{i,j} + p_{i-1,j}\right)\Omega\right] \tag{2.7}$$

Clearly the contribution from the pressure stored at the actual node will cancel out and therefore the pressure can take on any value without affecting the velocity at the same node. Pressure decoupling of this sort results in an unrealistic pressure field typically showing a series of wiggles in a chequer board style, hence the colloquial name. The most common method for overcoming the problem in low speed flows is the concept of staggering the storage locations of the velocity components from the pressure.

Discrete field representation In a FVM procedure the numerical domain is subdivided into a number of control volumes. The integral forms of the transport equations are then applied to each control volume. The two principal methods for defining the boundaries of the control volumes and the locations of the nodes within are grid-based and cell-centered control volumes, as shown in figure 2.1. The cell-centered control volumes are usually referred to as elements and in a numerical domain used for CFD purposes both grid-based control volumes and elements are used to stagger the locations of the velocity component from the pressure. Due to the integral forms of the governing equations, control volumes have no restrictions on size and shape.

In the classical finite difference approach, the numerical domain is also subdivided into grid-based and cell-centered control volumes. The differential forms of the governing equations require the control volumes to be defined in terms of ∂x, ∂y and ∂z. These requirements lead to substantial drawbacks for complex geometries and very often necessitate the use of a transformation technique which maps the numerical domain to a logical domain. As a consequence, the grid used in the FDM is structured while in the FVM an unstructured grid is utilised that can deal with complex geometries comparatively easily and this is preferable for most CFD problems.

Upwinding schemes The governing equations as presented in section 2.1 require a numerical scheme which models the propagation of the flow field in a physically correct manner. This includes the physical properties of fluid and also the propagation of flow information. It is natural that a numerical scheme for solving the equations is consistent with the velocity and direction with which information propagates throughout the flow field. It is this problem which has controlled the development of upwinding schemes in modern CFD. Upwinding schemes (or simply upwinding) are designed to numerically simulate more properly the direction of the propagation of information in a flow field along streamlines. As a result, if upwinding is carried out in a proper fashion, the calculation of sharp velocity gradients with no spurious, calculation-induced oscillations is possible.

In the case of a first order numerical scheme the use of upwinding will show a monotonic variation (no-oscillations) in the flow prediction. The direct application of a second order numerical scheme leads the advection terms to be calculated more accurately. However, the use of an upwinding scheme is not sufficient to maintain monotonic variation in regions where steep gradients exist and consequently a solution can become unstable. Such instability is inevitable in flow regions where convection is strong compared to diffusion. This instability appears in the solution variable and the numerical solution suffers from oscillatory errors. To remedy non-physical oscillations, a local gradient limiter is required. The concept of non-linear limiters is introduced by Boris & Book [6] and Van Leer [30] and later generalized via the important concept of Total Variation Diminishing (TVD) schemes introduced by Harten [23], whereby the variation of the numerical solution is controlled in a non-linear way, such as to forbid the appearance of any new extremum. The gradient limiter is aimed to hold the TVD criteria with respect to time. A scheme is said to be TVD with respect to time if the total variation for the new time step is smaller than that for the previous one, where the total variation of a discretised function a on a mesh is defined as $TV(a) = \sum_{j=-\infty}^{\infty} |a_{j+1} - a_j|$, where the subscripts j stands for the nodal location. The local gradient limitation necessarily implies that second order spatial accuracy is lost in the vicinity of a steep gradient. The relative importance of this effect depends also on the choice made for the limiting function. The most widely known flux limiters are the minmod limiter, the Osher-Chakravarthy limiter and the superbee limiter. The minmod limiter is the most diffusive one, but possibly yields the more robust numerical solutions, whereas the superbee limiter yields sharper profiles near discontinuities, but is more weak.

2.2 Turbulence

The modelling of turbulence still remains a hugely difficult task and numerical methods as discussed in the previous section have shown to be too time-consuming and inefficient to capture all the complex, associated flow motions. As a consequence a wide range of deterministic concepts for modelling turbulence have been evolved over the last fifty years. Turbulence models are aimed at accounting for the effect of turbulent flow motions on the flow field and are commonly distinguished by the adopted averaging method, which is either space or time averaging. Most models are based on the eddy viscosity concept, where an additional viscosity μ_t varies in time and space to account for the turbulent activity in the flow field. The necessity of such deterministic models is apparent in flows which are dominated by convection where a high Reynolds number is maintained. For flows dominated by diffusion no complex velocity field is apparent and consequently all flow features can be predicted without a turbulence model.

Physics of turbulence

It is difficult to agree on a definition of turbulence. Certainly, it is the broad spectrum of vortices that is one of the characteristics of turbulence and the motions observed can be treated as a series of vortices with different geometric scales. The kinetic energy in the vortices is transported from the larger to the smaller with the mean flow providing energy to the large vortices which is dissipated in the smaller. Vortices are generally anisotropic, i.e. intensity varies in each direction. Some flows can be idealised as isotropic, but usually only very small vortices can be modelled with some accuracy.

Turbulence originates from instabilities in the flow field which are associated with the convective terms of the Navier-Stokes equations. The phenomenon of turbulence is commonly associated with high Reynolds numbers and it is widely accepted that turbulence is 3-dimensional [25], even when the mean flow is predominantly 1- or 2-dimensional.

Another characteristic of turbulence is diffusivity; a rapid mixing of momentum, heat and mass is typical for turbulent flows. This can be seen in so-called coherent structures in the turbulent flow. Coherent structures can be observed because of their strong cohesion and their distinct geometrical properties which characterise regions of high dissipation or large vorticity. At present there is no universally agreed upon definition for the term coherent structure. The coherent structures are an important factor governing the macrocharacteristics of turbulent flows, like mass

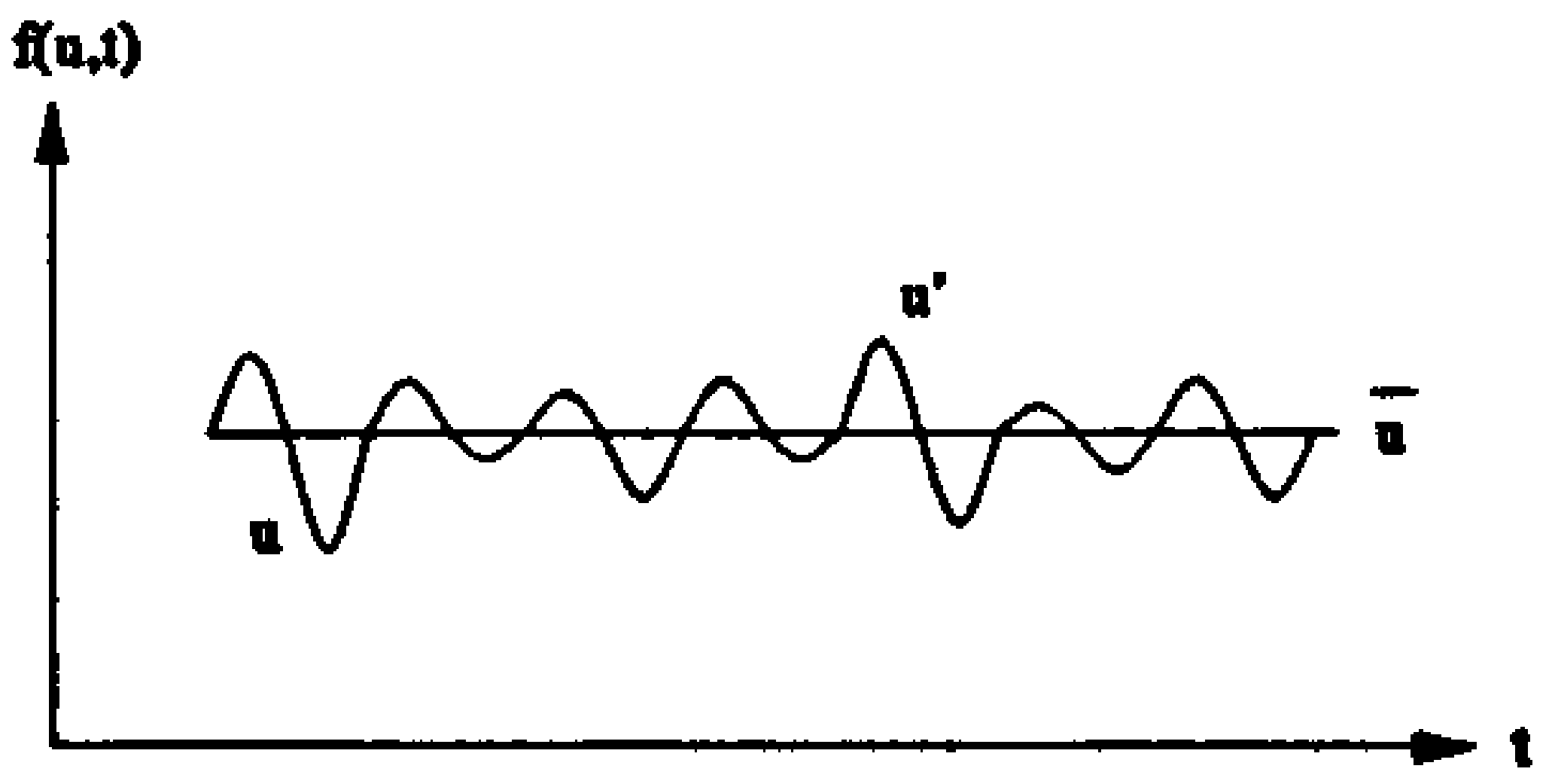

Figure 2.2: Velocity fluctuations, u consists of an average component $\bar{u}$ and a fluctuation component u'.

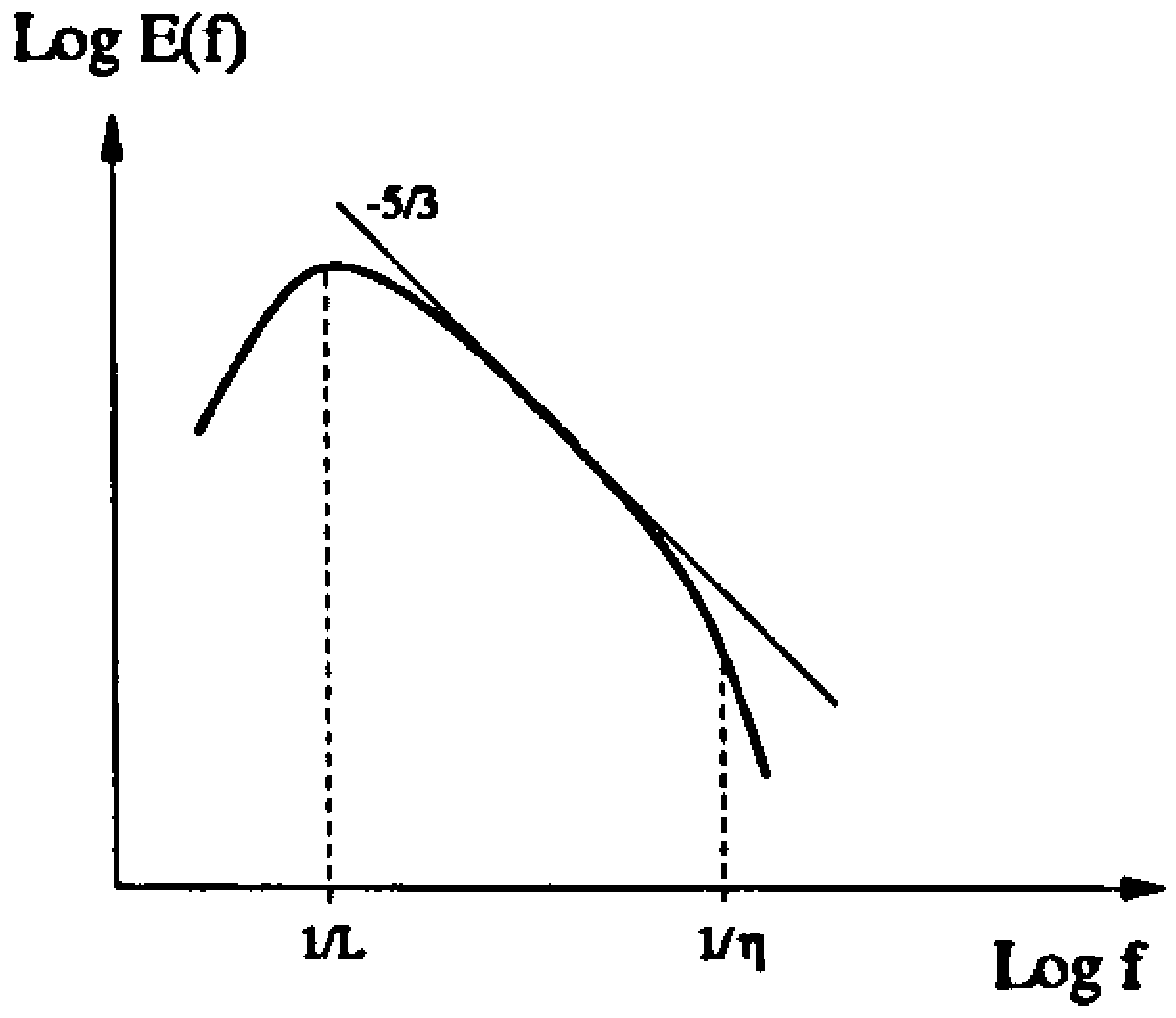

Figure 2.3: Energy spectrum for homogeneous turbulence.

and heat transfer and mixing properties [18].

2.2.1 Turbulence spectrum

A main characteristic of turbulence is the broad spectrum of vortices in the flow. Vortices are sometimes called eddies and large eddies are associated with a low frequency while small eddies are associated with a high frequency. Large eddies are initiated by the mean flow and therefore the large scale size is related to the characteristic dimension of the mean flow and the largest one is most often called the integral scale. The smallest scales of turbulence are the Kolmogorov scales η, or 'inner' scales. These scales are related to the dissipation of turbulent energy, as shown in equation 2.8:

$$\eta \equiv \left(\frac{\nu^3}{\varepsilon}\right)^{\frac{1}{4}} \tag{2.8}$$

$$\varepsilon \approx \frac{U^3}{L} \tag{2.9}$$

Assuming the local production of turbulent energy is equal to the local turbulence dissipation rate [29], it can be stated that the Reynolds number is the ratio between the integral-scale L and Kolmogorov scale η.

Every vortex scale can be linked to an amount of energy, which means the flow energy is distributed along the different scales, for the vortex range established by the Reynolds number. Figure 2.3 shows an energy spectrum of a typical turbulent flow. The function $E\left(f\right)$ generally exhibits one or more low-wave number peaks associated with the integral scales L of the problem. An inertial subrange, associated with the energy cascade from larger to smaller eddies, where $E(f)$ follows more or less closely the theoretical $f^{-\frac{5}{3}}$ trend, and a cutoff in correspondence with the Kolmogorov scale η of dissipative eddies, above which $E(f)$ falls steeply down to negligible values.To observe the energy of the smaller scales of turbulence, all velocity motions have to be resolved but this requires a fine grid with a resolution associated to the Kolmogorov scale. It is what the DNS is aiming to do. Unfortunately, most predictions average the small motions of turbulence so that the small scales cannot be observed in the mean flow any more. The process of averaging is a consequence of the finite number of nodes and the finite time step. Consequently no energy is represented by the small scales and it is for this reason that turbulence models have been developed in order to impose the effect of turbulence on the mean flow.

Closure Problem

The complexity of modelling turbulence is formally stated in the number of unknown parameters to the number of equations. This disparity in number between unknowns and equations is known as the closure problem which can be illustrated by the equations 2.10 to 2.12, which show the conservation equations for Newtonian fluids for turbulent flow. $\overline{u}_i$ is the mean flow velocity and u'_i is the unresolved fluctuating component.

$$\frac{\partial \overline{u}_i}{\partial x_i} = 0 \tag{2.10}$$

$$\frac{\partial u'_i}{\partial x_i} = 0 \tag{2.11}$$

$$\frac{\partial \overline{u}_i}{\partial t} + \overline{u}_j \frac{\partial \overline{u}_i}{\partial x_j} = \frac{1}{\rho}\frac{\partial}{\partial x_j}\left(-\overline{p}\delta_{ij} + 2\mu S_{ij} - \rho\overline{u'_i u'_j}\right) \tag{2.12}$$

$$S_{ij} \equiv \frac{1}{2}\left(\frac{\partial \overline{u}_i}{\partial x_j} + \frac{\partial \overline{u}_j}{\partial x_i}\right) \tag{2.13}$$

Equation 2.12 is the Reynolds equation of motion which on the right-hand side contains the total mean stress tensor for turbulent flow. The contribution of turbulent motion to the mean stress tensor is called the Reynolds stress. Every direction contains three Reynolds stresses, which means a total of nine Reynolds stresses exist, as shown in matrix 2.14:

$$\tau_{ij} = -\rho \begin{bmatrix} \overline{u'_1 u'_1} & \overline{u'_1 u'_2} & \overline{u'_1 u'_3} \\ \overline{u'_2 u'_1} & \overline{u'_2 u'_2} & \overline{u'_2 u'_3} \\ \overline{u'_3 u'_1} & \overline{u'_3 u'_2} & \overline{u'_3 u'_3} \end{bmatrix} \tag{2.14}$$

Based on $\overline{u'_i u'_j} = \overline{u'_j u'_i}$ there are six independent components of the Reynolds stress tensor. Together with the unknown mean pressure $\overline{p}$ and the three mean velocity components $\overline{u}$, a total of ten unknowns exist with four equation for a three dimensional flow. The fundamental problem of classical turbulence modelling is to relate the six Reynolds stresses to the mean flow quantities, $\overline{u}$ and $\overline{p}$, in some physical plausible manner.

Correlation

Correlation gives information about velocity fluctuations at different points or times. Correlation coefficients indicate the scale and structure of turbulent motion and play an important role in both theoretical and experimental studies of turbulence. For two-velocity components the correlation coefficient is defined as shown in 2.15:

$$\overline{u_i' u_j'} \tag{2.15}$$

and the corresponding correlation coefficient is:

$$R = \frac{\overline{u_i' u_j'}}{\sqrt{\overline{u_i'^2}}\sqrt{\overline{u_j'^2}}} \tag{2.16}$$

2.2.2 Direct Numerical Simulation

The ideal and potentially most accurate approach to turbulence simulation is to solve the Navier-Stokes equations without averaging or approximation. Therefore, all length and time scales which exist simultaneously in the flow field have to be resolved by the numerical mesh for a realistic simulation. If successful in doing so, the procedure is called a Direct Numerical Simulation (DNS). It is important to recognize that the considered domain must be at least that of the largest turbulent eddy; from a practical point of view this means that the linear dimension of the domain must be at least a few times the integral scale L. On the other hand, for a simulation to capture all of the dissipation, which occurs on the small scales where viscosity is active, the grid must be no larger than the viscously-determined Kolmogorov scale, η. For homogeneous turbulence, the simplest type of turbulence, there is no reason to use anything other than a uniform grid. In this case, the number of grid points in each direction must be at least $\frac{L}{\eta}$; it is easily shown by Tennekes & Lumley [57] that this ratio is proportional to $Re^{\frac{3}{4}}$. Since this number of points must be employed in each of the three coordinate directions, and the time step is related to the grid size, the cost of a simulation scales as Re^3. This means that DNS can be carried out only at moderate Reynolds numbers. For homogeneous turbulent flows, the Reynolds number of interest must be based on the turbulent velocity and the length scales. As these scales are typically an order of magnitude smaller then the corresponding macroscopic scale, the ability to compute flows with turbulent Reynolds numbers allows DNS to reach only the low end of the range of Reynolds numbers of engineering interest.

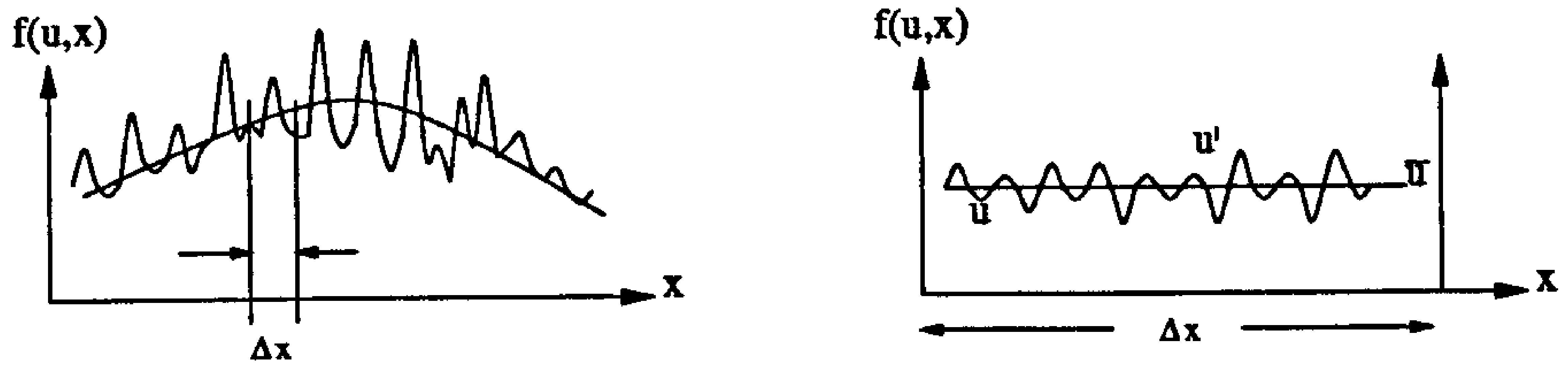

Figure 2.4: Sketch of Large Scale field.

2.2.3 Large Eddy Simulation

The space averaging method is commonly known as LES. The term space averaging refers to the implicit averaging which takes place as a consequence of the applied numerical method to the Navier-Stokes equation in which the small scale velocity motions are unresolved or averaged due to a finite number of nodes. The LES method separates the low frequency motions from the high frequent motions. To take into account the high frequency motion of turbulence (small scales) in a numerical simulation the LES method then estimates the effect of the small scales while the larger scales are modelled by the mesh itself.

Recent research by Breuer [8], Ma et al. [39], Vallès [63] and Tutar & Holdø [60] has indicated that for the flow investigated in this thesis a space averaging turbulence model like LES is preferable.

Filtering

Real turbulent flow contains a very complex flow pattern in time and space. High frequency motions can be observed in the flow by taking a set of data characterising the flow at an instant. Numerical simulation of the flow will only predict the global behaviour due to limited number of nodes, as shown in figure 2.4. As a consequence, there will be a filtering of the flow field. Using this concept the velocity u can be separated into two components, $\overline{u}$ and u'. $\overline{u}$ is the grid scale or filtered velocity and u' is the subgrid value, which is unresolved. The LES modelling of the smaller scales is different from the time averaging method where none of the scales are calculated directly and where the turbulence model is applied on the whole range of scales.

The mesh containing a finite number of nodes acts like a frequency filter. The velocity can be filtered by using a convolution operator. The derived general space-average is:

$$\overline{f}(x) \equiv \int_{-\infty}^{\infty} G\left(x - x'\right) f\left(x'\right) dx' \tag{2.17}$$

The function $G\left(x - x'\right)$ is a weighting function which ascribes a weighting factor to every value of x', in which the total weighting of the interval is 1. The weighted function is sometimes called the filter function and the two most commonly employed filter functions are the 'top-hat' or 'box-car' filter and the Gaussian filter [1].

Filtered Navier-Stokes equation To obtain the space-averaged equations, all the terms are simply filtered or averaged. The filtered continuity and Navier-Stokes equations can be written as:

$$\frac{\partial \overline{u}_i}{\partial x_i} = 0 \tag{2.18}$$

$$\frac{\partial \overline{u}_i}{\partial t} + \frac{\partial\left(\overline{u_i u_j}\right)}{\partial x_j} = -\frac{1}{\rho}\frac{\partial \overline{p}}{\partial x_i} + \nu\frac{\partial^2 \overline{u}_i}{\partial x_j \partial x_i} \tag{2.19}$$

The over bar means a space-filtered, or averaged quantity. Mathematically each term has been filtered by applying the rules of addition, differentiation to the convolution operator. The difficulty comes from the nonlinear term $\overline{u_i u_j}$. This term is a product of the filtered and subgrid velocity, as shown in equations 2.20 and 2.21:

$$\overline{u_i u_j} = \overline{\left(\overline{u}_i + u'_i\right) \cdot \left(\overline{u}_j + u'_j\right)} \tag{2.20}$$

$$\overline{u_i u_j} = \overline{\overline{u}_i \overline{u}_j} + \overline{\overline{u}_i u'_j} + \overline{u'_i \overline{u}_j} + \overline{u'_i u'_j} \tag{2.21}$$

The first term on the right hand side in equation 2.21 contains the filtered velocity component and therefore this term can be resolved mathematically. The last three terms contain subgrid velocities, and therefore have to be modelled. It has to be mentioned that within space averaging the average fluctuation is non-zero ($\overline{u'} \neq 0$) and filtering a second time does not reproduce the original filtered field ($\overline{\overline{u}} \neq \overline{u}$). Consequently none of the terms in equation 2.21 can be neglected.

It is theoretically possible to resolve the first term of equation 2.21; this requires the use of a Taylor series expansion in which this term will be resolved partly, as shown in equation 2.22 with Δ to be the smallest resolved scale:

$$\overline{\overline{u}_i \overline{u}_j} = \overline{u}_i \overline{u}_j + \frac{\Delta^2}{24}\Delta^2 \overline{u}_i \overline{u}_j \tag{2.22}$$

$$\tau_{ij} = \left(\overline{\overline{u}_i \overline{u}_j} - \overline{u}_i \overline{u}_j\right) + \left(\overline{\overline{u}_i u'_j} + \overline{\overline{u}_j u'_i}\right) + \overline{u'_i u'_j} \tag{2.23}$$

- The first term on the right hand side of equation 2.23 can be computed explicitly from the filtered vector field; $\overline{u}$, represents the interaction between two resolved scale eddies to produce small scale turbulence. It has been called the Leonard stress and, sometimes, the outscatter term.

- The second term represents the interaction between the resolved scale eddies and the unresolved small scale eddies. This term is also called the cross stress, and represents the transfer of energy in either direction. On average the main transfer of energy is from large scales to small scales. If energy is transfered to the resolved scales, it is called backscatter.

- The third term represents the interaction between two small scale eddies to produce a large scale eddy. It produces energy transfer from the small to the large scales, and is also called the backscatter term.

The net energy transfer from the large scales to the small scales appears as an energy loss from the large scales. For this reason the subgrid model should be dissipative, although some energy flows in both directions. It has been estimated that the gross energy transfer to the small scale is 1.5 times the net energy transfer [18]. This means that about one third of the energy transferred to the small scales is returned to the large scales. Ideally, subgrid models should represent the effect of these energy transfers on the large scale motion.

In LES turbulence modelling the calculation of SGS is far from exact and the uncertainty in the modelling defeats any attempt at precision. For this reason the different terms are not modelled separately; instead the entire SGS Reynolds stress is modeled as a single unit. The SGS Reynolds stress is a local average of the small scale field and SGS models should therefore be based on the local velocity field.

Smagorinsky model

The first LES model is that proposed by Smagorinsky [54], since then a wide range of models have been proposed of which the most well known is the Dynamic model proposed by Germano et al. [19]. In addition many models used in RANS calculations are modified and adapted as an SGS model [18]. However, these more complex models including the Dynamic model, are less robust and more sensitive to the mesh being used [18]. These features can be a significant drawback in a numerical domain where the mesh is continuously changing. Therefore, the Smagorinsky LES model has been selected for this work. The model, proposed by Smagorinsky [54], is by far the most commonly used LES model and and is widely used for flow behind a bluff body [54] [8] [39] [63] [60].

At high Reynolds numbers, the dissipation in a turbulent flow takes place at very small scales while energy is introduced at the largest scales. Between these is a regime in which there is neither significant production nor dissipation of turbulent energy. In this inertial subrange, only inviscid mechanisms are active and energy is transferred from large to small scales. Since it is the non-linear (advective) term in the Navier-Stokes equations that is responsible for the energy transfer, the rate of transfer to the small scales may be estimated as the magnitude of the contribution of this term to the kinetic energy equation, which is $\frac{1}{2}\frac{\partial(u_i u_i u_j)}{\partial x_j}$. As the large energetic scales supply the largest contribution to this term, the magnitude scales as:

$$\varepsilon \approx \frac{U^3}{L} \tag{2.24}$$

where U is a velocity scale for the energetic eddies and L is the integral scale of the turbulence. The next assumption is that the largest subgrid scales are far removed from the viscous scales. A repeat of the above argument then shows that:

$$\varepsilon \approx \frac{u^3}{\Delta} \tag{2.25}$$

where u is a velocity typical of the subgrid scale field and Δ is the size of the largest subgrid eddies, the length scale associated with the filter. In a large eddy simulation, the large scales lose energy by transferring it to the subgrid scales. From the point of view of the large scale eddies, this appears to be dissipation i.e.: it is energy lost never to be recovered. A model of the eddy viscosity type represents this energy transfer as effective viscous dissipation. Since the model mostly effects the smallest resolved scales (size Δ), the magnitude of the effective dissipation may be estimated as:

$$\varepsilon \approx \nu_t \frac{u^2}{\Delta^2} \tag{2.26}$$

Equation 2.27 shows that the eddy viscosity must take the form:

$$\nu_t \propto u\Delta \tag{2.27}$$

which could have been derived via dimensional arguments. u can be found by using equations 2.24 and 2.25 and substituting into equation 2.27 to obtain:

$$\nu_t \approx U\Delta^{\frac{4}{3}} L^{-\frac{1}{3}} \tag{2.28}$$

Finally, estimating U as:

$$U \approx L\sqrt{(\overline{S}_{ij}\overline{S}_{ij})} = L\left|\overline{S}\right| \tag{2.29}$$

and inserting a model parameter to produce equality gives:

$$\nu_t = C_S^2 \Delta^{\frac{4}{3}} L^{\frac{2}{3}} \left|\overline{S}\right| \tag{2.30}$$

The presence of the integral scale L in the formulation of eddy viscosity makes the model difficult to use. Computing the integral scale, especially in inhomogeneous flows, could require a great deal of effort. For this reason the substitution:

$$\Delta^{\frac{4}{3}} L^{\frac{2}{3}} \rightarrow \Delta^2 \tag{2.31}$$

is often used, leading to the usual form of the Smagorinsky model:

$$\mu_t = \rho (C_s \Delta)^2 \left|\overline{S}\right| \tag{2.32}$$

$$l_s = C_s \Delta \tag{2.33}$$

The spatial filter that is inherent in the LES equation smears out the fluctuations that are considerable smaller than the effective length scale l_s. A physical interpretation is that the subgrid scales are damped out by the eddy viscosity, which depends on l_s and which is usually several orders of magnitude larger than the Kolmogorov scale η to be modelled. In other words, one might presume that the effective length scale l_s in the LES equation acts like the Kolmogorov scale η in the

Navier-Stokes turbulence. In full analogy to the Kolmogorov scale η the effective length scale l_s can be considered as a dissipation length in the LES model. However, in the LES 'fluid' l_s is a property of the specific LES 'fluid' and the turbulent viscosity is derived from the effective length scale l_s, while the Newtonian fluid kinematic viscosity is the fluid property and the Kolmogorov scale η is derived from the viscosity property.

The definition of the effective length scale l_s relies on two variables; these are the Smagorinsky constant C_s and the subgrid length scale Δ. The subgrid length scale Δ indicates the smallest scales being resolved in the mesh, while C_s determines the amplitude of the energy spectrum. Equation 2.34 describes the energy spectrum for homogeneous turbulent flow in which the Kolmogorov constant α is in the order of 1.5. Muschinski [46] derived an $\alpha - C_s$ relationship and proved that for a dissipation spectrum similar to Lilly's [31] cut-off model, C_s is supposed to be of the order of 0.17 to hold the energy spectrum for homogeneous turbulent flow.

$$E(f) = \alpha \varepsilon^{\frac{2}{3}} f^{-\frac{5}{3}} \tag{2.34}$$

Ferziger [18] suggested that C_s is more a parameter than a constant and concluded that most of these derivations are truly valid only for isotropic turbulence. The substitution used to produce the standard version of the Smagorinsky model may mean that the parameter, C_s, is not a true constant but rather a function of $\frac{\Delta}{L}$ which is in turn a function of Reynolds numbers. This means the parameter C_s should be a function of Reynolds number [18].

Flows affected by walls require a reduction of C_s, as a result of decreasing vorticity. A known damping function is the Van Driest damping function used to reduce the near-wall eddy viscosity. The Van Driest function describes the distance to the wall in terms of wall-shear units. In this work a alternative version to the Van Driest damping function has been used [12], as shown in equation 2.37. The shear velocity u_τ is related to the wall shear stress τ_w via $\sqrt{\frac{\tau_w}{\rho}}$. A^+ is a constant usually taken to be approximately 26 [15].

$$D_{\text{damp}} = 1 - e^{-\left(\frac{y^+}{A^+}\right)^2} \tag{2.35}$$

$$l_s = C_s \Delta D_{\text{damp}} \tag{2.36}$$

$$y^+ = \frac{y u_\tau}{\nu} \tag{2.37}$$

An alternative to the Van Driest function is to relate the viscosity to the subgrid-scale Reynolds number. Models like this are suggested by McMillan & Ferziger [44] and by Yakhot & Orszag [70]. However, as turbulence in the near-wall region is of anisotropic nature, turbulence scales in the streamwise direction can be ten times the spanwise direction, which requires another definition of subgrid length scale. Suggestions for a subgrid length scale in the vicinity of the wall are made by Ferziger [18] who suggested $\Delta = \sqrt{\Delta_x^2 + \Delta_y^2 + \Delta_z^2}$.

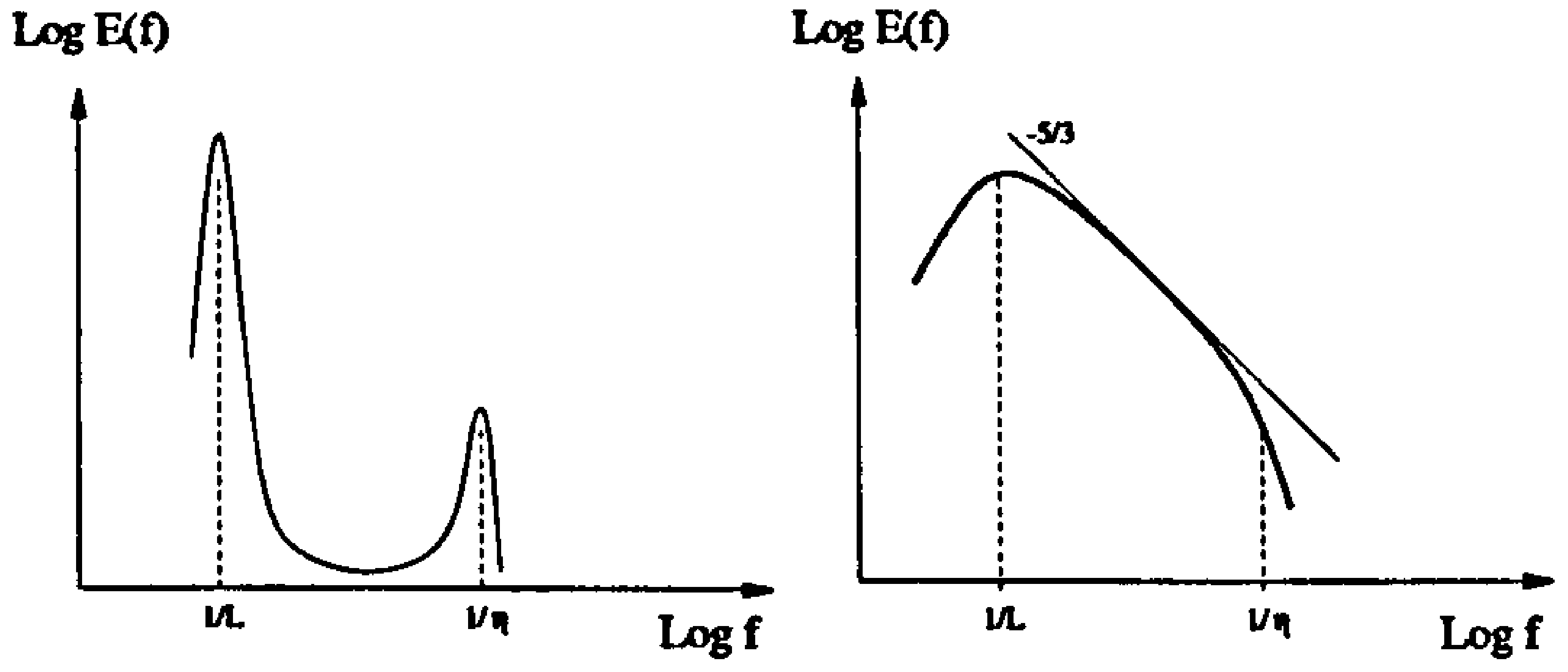

(a) laminar (b) turbulent

Figure 2.5: Energy spectra for a fluid in the laminar and turbulent mode respectively. The transition from laminar to turbulent flow conditions is associated with a transition from the laminar energy spectrum to the turbulent energy spectrum.

2.2.4 Transition from laminar to turbulent flow conditions

It is shown that the system of equations for incompressible fluid motions are nonlinear. The equations can be linearised and solved for equilibrium conditions; however, when non-equilibrium conditions prevail a unique solution does not exist anymore.

For fluid flows at sufficiently low Reynolds numbers a single stable solution exists that is either stationary or periodic. Such system is called to be in the laminar mode and will tend towards independence of the initial conditions. With increasing Reynolds number a critical value is reached beyond which the solution becomes unstable and new type of motions appear. A further increase of the Reynolds number will lead to irregular and chaotic flow motions both in time and space. Nevertheless, in principle the system is still deterministic and governed by the same equations as in the laminar mode. It is a consequence of the systems non-linearity that the governing equations can have a solution so complex as not to look like the result of a deterministic process.

The onset of turbulence in a fluid at sufficiently high Reynolds number is normally preceded by the appearance of instabilities, the precise nature of which will depend on the geometry involved. The growth of these instabilities cause mass, momentum and energy transfers throughout the fluid and eventually leads to a spectrum of flow motions which is regarded as turbulence.

The modelling of transition from laminar to turbulent flow conditions has been subject to numerical investigation [50]. In a transitional flow field the energy spectrum varies in time and space as shown in figure 2.5. As a consequence, the flow features to be modelled are unknown and model assumption as used in LES models do not hold. Significant work on the transition separation zone behind a bluff body has been done by Persillon & Braza [50] who concluded that the modelling of transition should not rely on a turbulence model, but instead has to be done by the mesh itself on which the Navier-Stokes equation are applied. Therefore the modelling of transition in a physically correct manner can only be successful if sufficient mesh resolution is used.

2.3 Adaptive grid methods for unsteady CFD problems

The search for solutions free from numerical error has been one of the main goals of CFD research. An indisputable way to reduce the numerical error is by reducing the size of the discretisation elements. However, an excessive increase in mesh resolution would lead to insurmountable demand for computational power. As a consequence, a mesh sensitivity analysis is very usual and mostly required with conventional mesh to find a compromise between numerical error and computational requirements. This requires the user to estimate beforehand the regions of interest. In order to overcome demanding mesh requirements and still obtain results of good quality the present work investigates the suitability of a DGA algorithm.

Frequently meshes are generated where due to mesh construction methods the resolution is high in regions where gradients are not significant. Consequently, such meshes have a large number of redundant cells. Conversely, due to time variations in the computed flow field, there will be regions where the mesh resolution is insufficient. A well-developed and robust DGA algorithm can lead to a reduction in both numerical error and computational power and this appealing feature has enforced the CFD society to develop a whole range of algorithms for DGA of different applicability and complexity.

The DGA algorithms are intended to refine the mesh based on the interim flow field prediction. Additionally, refinement can be geometry based [72]. The latter is typically used for steady state CFD problems as well for refinement implementation in automatic mesh generators. Nevertheless, this thesis deals only with solution-based mesh refinement where the physical problem under investigation is of an unsteady, turbulent nature. Significant contribution to the development and understanding of DGA algorithms has been made by Zienkiewicz & Zhu [73]. His work is devoted to the development of numerical methods in general and DGA algorithms in particular. A conjunction of DGA algorithms in combination with turbulence modelling was first suggested by McGuirk & Rodi [42]. More recent it is the work of Lohner [35], who investigated adaptive methods for transient problems, and Habashi et al. [22], who linked the use of stabilisation artifices with DGA.

2.3.1 Refinement strategies

In recent years a whole series of strategies have been developed. A small number of these strategies are preprocessing-based and focus on geometry-based mesh refinement but the majority focuses on solution-based mesh refinement. Three approaches can be distinguished;

R-refinement In this approach a basically fixed number of grid points is used but the point positions are moved in such a way so that the grid points concentrate in critical spatial areas [13].

H-refinement In this approach a variable number of grid points is used. Points are added to, or removed from, the grid according to the local requirements without changing the positions of the other grid points. As a result, the grid is locally refined or coarsened [35].

P-refinement In this approach essentially a fixed grid is used but adaptive solution is obtained by locally varying the order of spatial discretisation. Methods which do accomplish the addition of higher order shape functions are either the conventional polynomials [4], spectral element functions [41] or hierarchical shape-functions [73]. P-refining methods are increasingly used in finite-element methods, often together with h-refining methods [35].

Existing grid strategies typically either belong to one of the above strategies, or represent their combinations. In addition, a further distinction is made in the p and h-refinement methods with the introduction of static and dynamic refinement methods. In static methods new grid points (or local higher order methods) may be inserted but will remain for the rest of the simulation. In dynamic grid refinement, the refinement may be removed at a later time when the region is no longer of special interest.

R-refinement plays an important and growing role in CFD especially where the fluid interacts with moving walls (as in piston engines or in structure yielding to an overpressure). However, as a substitute for other refining methods they have certain weaknesses. The most important of these is that it may often be impossible to avoid an excessive depletion of the grid around the features of interest [67]. In addition, procedures for redistributing the grid points can produce distorted control volumes [47].

P-refining seem to have great potential but are also of considerable mathematical complexity. They are essentially restricted to finite-element methods, though a limited version could be envisaged also for finite volume methods [27]. Possible reasons for the lack of success with p-refinement are the limited accuracy that is achievable due to monotonicity enforcement close to discontinuities and the lack of accurate turbulence models, as well the much higher coding complexity of p-refinement or h/p-refinement as compared to straightforward h-refinement.

By far the most successful mesh enrichment strategy has been the h-refinement [35] and two reasons can be given for this success:

- Conservation is maintained naturally with h-refinement.
- No interpolations other than the ones naturally given by the element shape functions are required. Therefore, no numerical diffusion is introduced by the adaptive refinement procedure. This is in contrast to adaptive re-meshing,

where the grids before and after a mesh change may not have the same points in common. The required interpolations of the unknowns will result in an increased amount of numerical diffusion [34] [36] [37] .

2.3.2 Indication of error

In flow simulations the regions of interest will naturally be regions where there is variation in one or more important properties. While regions of constant properties may be interesting from an engineers' point of view, no additional accuracy is gained by using more grid points. The key issue of grid refinement is to modify the grid and focus on the regions where interesting physics take place.

The information about the regions where the grid should be refined or coarsened should be provided ideally by an error estimator. Error estimation of fluid flow calculations is not an easy task. The Navier-Stokes equations, together with the transport equations for turbulence modelling quantities, are a coupled, nonlinear system, and errors present in any one of these fields in general will effect the solutions of all others in a nonlinear manner difficult to describe accurately. The discretisation error describes the deviation from the analytical solution of the set of differential equations, but is not directly accessible. A fully adaptive grid strategy should control the errors of the numerical solutions and guarantee that they remain below the magnitudes assumed as acceptable. In practice, controlling the global errors is a difficult matter and adaptive grid strategies often control local errors only and are an approximation to the numerical error.

Some authors, e.g. McGuirk et al. [43], have used the difference between upwind and central difference expressions for the convection term to identify the regions in the flow calculation with large numerical diffusion produced by first order upwind differencing on a given grid. This technique is limited to convection-dominated problems, and only when convection is modelled by the first-order upwind differencing scheme [47].

Refining the grids in regions with large gradients is one possibility, but this must be treated with caution. A gradient may be large but constant across a series of elements. In this case there will be no gain in solution accuracy by further refining in this region. Furthermore, some problems, like free jets, have gradients that are nearly infinite close to the orifice, while further downstream the gradients are of lower order. In this case different refinement conditions are probably necessary within the computational domain.

There are a number of adaptive methods in CFD which are designed to be used in combination with FDM, FVM and FEM. A list of the most popular error indicators presently used is given by Lohner [35]:

- Jump in indicator variables
- Interpolation method
- Comparison of derivatives

- Energy of spatial modes

Jump in indicator variables

The simplest error indicator is obtained by evaluating the jump (i.e. the undivided difference) of some indicator variable like the turbulent viscosity, pressure or temperature within an element or along an edge. This error indicator implicitly makes the assumption:

$$e_j = c_1 \Delta \left| \frac{\partial u_i}{\partial x_j} \right| \tag{2.38}$$

i.e. first-order accuracy for the underlying scheme. Error indicators of this form have been used in industrial applications with success [35], even if the underlying numerical discretisation was of higher than first order.

Interpolation method

Making the assumption that the solution is smooth, one may approximate the error in the elements by a derivative one order higher than the element shape function. For 1-dimensional systems this would result in the error indicator at the element level of the form

$$e_i = c_1 \Delta^p \left| \frac{\partial^p u_i}{\partial x_j^p} \right| \tag{2.39}$$

where the p^{th} derivative is obtained by some recovery procedure. The total error in the computational domain is then given by:

$$e_\Omega = c_2 \left[\int \Delta^p \left(\frac{\partial^p u_i}{\partial x_j^p} \right) d\Omega \right] \tag{2.40}$$

This error indicator gives superior results for smooth regions. On the other hand, at discontinuities the local value of e_i will stay the same no matter how fine the mesh is made.

Comparison of derivatives

Again making the assumption that the solution is smooth, one may compare significant derivatives using schemes of different order. The assumption would allow a good estimate of the error in the higher derivatives. Moreover, the method can give an indication of whether it is more efficient to use h-refinement, or to increase the order of accuracy (p-refinement).

Energy of spatial modes

For higher-order methods, such as spectral methods, a way to measure errors and convergence is to separate the energy contents associated with the different shape functions. The decrease of energy contained in the higher-order shape functions gives a reliable measure of convergence [41]. At the same time, this way of measuring errors provides an immediate strategy when to perform h-refinement (slow decrease of energy content with increasing shape function polynomial) or p-refinement (rapid decrease of energy content with increasing shape function polynomial).

2.3.3 Error magnitudes and refinement variables

It is very surprising that there exists a vast literature devoted to the development of adaptive methods and adaptive grid strategies but almost nothing has been done to develop refinement variables for numerical solutions [16] [35] [47] [22]. However, the success of adaptive grid strategies depends to a very large extent on the reliable error estimation and on the adequate determination of acceptable error bounds with which the estimated errors are compared.

Flow features used for refinement variables

An important choice in a refinement procedure is the choice of refinement variable that is to be monitored. Obviously there is no single choice suitable for all problems. However, investigations have been done over recent years to find suitable refinement variables for flow problems where turbulent flow features are of primary interest.

Lin & Leschziner [32] and Muzaferija & Gosman [47] suggested that for jets where strong shearing flows exist, it is the variation in the streamwise velocity component which was observed to respond sensitively to both turbulence modelling and numerical resolution. The relatively uniform core of the jet was not refined so much while refinement took place in the mixing layers of the jets where strong velocity variation was present.

Suggestions for refinement variables for the backward facing step problem are given by Wang [65] and De Zeeuw & Powell [71]. In a comprehensive study which was conducted by De Zeeuw & Powell [71], they found a criterion based on compressibility and rotationality most suitable. Wang [65] suggested the use of the local cell Reynolds number as a refinement variable in the vicinity of the wall instead of the divergence and curl.

Despite the variety of refinement variables suitable for flow problems where turbulent flow features are of primary interest, it is the use of velocity gradients which they all have in common. Centreline velocity variation, rotationality and local cell Reynolds number are all obtained from the local velocity gradients. The reason for using the velocity gradient is twofold. In a flow field driven by convection, it is the complex flow pattern which are characterised by the velocity gradient in space. From a numerical perspective it is the local cell Reynolds number, and indirectly the velocity gradient, which is a measure for the discretisation error of the convection terms. This idea is supported by Habashi et al. [22] who stated that the need for CFD stabilisation artifices, such as upwinding or artificial viscosity, are drastically reduced, if not altogether eliminated with a well-posed error estimator.

A flow parameter which incorporates all the velocity gradients is the turbulent viscosity, which is used in conventional eddy viscosity models to indicate for turbulent activity. Although the turbulent viscosity is an inaccurate parameter for predicting the turbulent activity in transitional regions it has an interesting potential. As discussed in section 2.2.4, it is known that transitional flow can only be solved in a physically correct manner by the mesh itself. Nevertheless, turbulent viscosity can remain a suitable refinement variable for transitional flows.

In transitional flow there is a transition from laminar to turbulent flow conditions where the laminar flow is characterised by a low level of turbulent activity. Despite the laminar flow conditions there is a potential for turbulent flow behaviour as the Reynolds number indicates. This means that due to the increased inertia forces in comparison with viscous forces, the laminar region has got the potential to become fully turbulent. It is the velocity gradient in the shear layer that can indicate for the potential of turbulent activity and it is the turbulent viscosity which is a measure for the potential of turbulent activity. Although the turbulence models do not model the flow in a physically correct manner, turbulent viscosity, or a modification to it, can be a suitable refinement variable.

2.4 Objectives

In the present work a DGA algorithm in combination with a turbulence model is used for predicting unsteady turbulent flows. The turbulence model chosen for this investigation is the standard LES model as proposed by Smagorinsky [54]. Recent work of Breuer [8], Ma et al. [39] , Vallès [63] and Tutar & Holdø [60] suggested that the LES method gives improved results compared to those of RANS-based models. In the LES turbulence model, turbulent viscosity is proportional to the cell size of the element and therefore an increase in mesh resolution will lead to a reduction in local turbulent viscosity. In case of a very fine mesh the contribution of the LES turbulence model vanishes and the flow is practically calculated without the turbulence model. In a numerical domain where the mesh is not known beforehand such parameterisation of the small scales is an important preference to other types of turbulence models.

There have been many developments related to adaptive methods and adaptive grid strategies [16] [35] [47] [22]. However, there is comparatively little work reported on grid refinement with turbulent, unsteady flows. The present work is focussed on the determination of a reliable refinement variable. A suitable variable for unsteady turbulent flows dominated by convection is the turbulent viscosity. In a LES turbulence model, turbulent viscosity accounts for the small turbulence taking place in the subgrid scales. In the context of a DGA algorithm turbulent viscosity is a measure indicating regions with a potentially high rate of turbulence. The refinement variable proposed in this thesis is a modification of the turbulent viscosity as prescribed in the LES model notation. The choice of a modified turbulent viscosity as a refinement variable in combination with the LES turbulence model implies a sophisticated interaction between the methods of both models. The lower range of unresolved scales is modelled with the LES turbulence model, while for larger scales, where the turbulence model potentially suffers a lack of accuracy, mesh refinement will take place and vortices are resolved by the mesh itself.

The implementation of the LES turbulence model and the DGA algorithm in the REACFLOW code leads to the following thesis objectives:

- To obtain a suitable definition for the LES subgrid length scale in a triangular unstructured mesh. The subgrid length scale will be validated by a comparison with experimental data from Cantwell & Coles [9] on the flow behind a circular cylinder in a sub-critical flow regime at a Reynolds number of $1.4 \cdot 10^5$.
- To propose a DGA refinement variable which is a modification to the LES equation for turbulent viscosity. Validation of the simulation results obtained with DGA will be done with the same experimental data as used above.
- To implement the Van Driest boundary function for reducing the turbulent viscosity in the vicinity of the wall.
- To analyse the numerical data from simulations using DGA and conventional mesh to gain a further insight into turbulent flow and the numerical requirements for modelling unsteady flow.

Chapter 3

REACFLOW code development

The REACFLOW code [55] is designed to treat chemical reacting flows and the numerical approach adopted is an extension of the projection method, proposed by Chorin [11] and Teman [56]. A full description of the code and the implementation of the discretised governing equations is given in section 3.1. In the two additional sections the turbulence model with Van Driest damping function is presented, as well as the DGA algorithm used in this work.

3.1 Time and space discretisation

For the simulations carried out in this thesis the CFD code REACFLOW [55] has been utilised. REACFLOW calculates the solution to the multicomponent, variable-density incompressible Navier-Stokes equations. The spatial discretisation of the equations is based on an unstructured triangular mesh. The primitive variables are all discretised in a cell-centered fashion, with one value for each variable in each triangular element. The variables are assumed to have a given functional dependency inside each element.

The pressure p is discretised in a grid-based or vertex-centred fashion, where each pressure value is defined on a *control volume*, delimited by the medians in all the triangles surrounding the given vertex. This choice of discretisation has been made to suppress the "checkerboard" instability [3].

For incompressible flows the velocity must satisfy the divergence-free criterion: $\partial u_i/\partial x_i = 0$. This introduces an extra constraint which replaces the traditional equation of state. It also makes the sound speed infinite, so a degree of implicitness must be employed in the time stepping.

The numerical method used is similar to the predictor-corrector method of Chorin [11]. The solutions to the equations for mass, mass fractions and internal energy are all advanced in an explicit fashion.

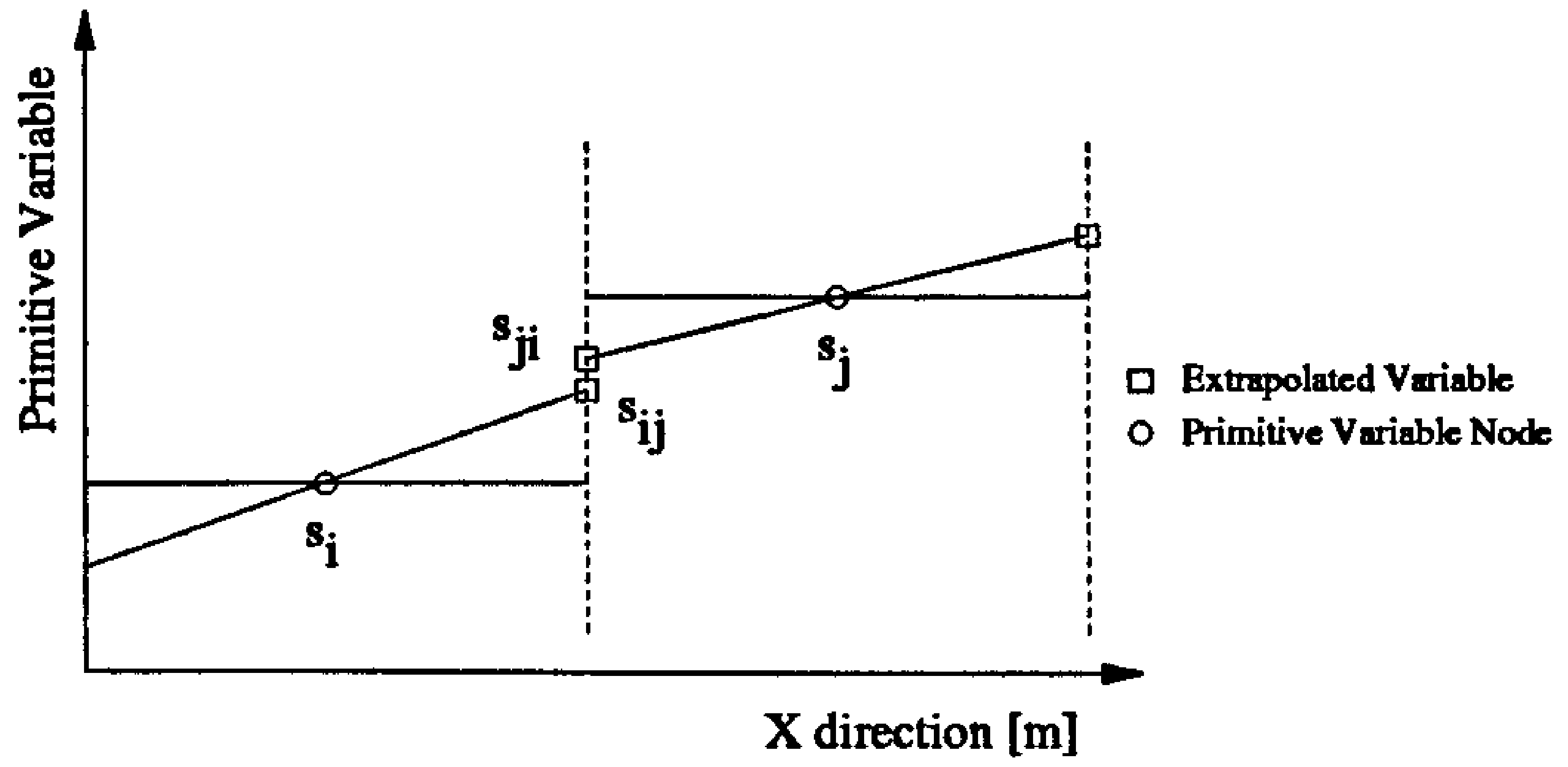

Figure 3.1: Spatial second order flux evaluation.

For the velocity, an intermediate state, u_i^* is found by advancing all the terms except the pressure gradient term explicitly. A Poisson equation is then found for the pressure by taking the divergence of the velocity equation:

$$\frac{\partial u_i^{n+1}}{\partial x_i} = \frac{\partial u_i^*}{\partial x_i} - \frac{\Delta t}{\rho^{n+1}} \frac{\partial}{\partial x_i} \left(\frac{\partial p^{n+1}}{\partial x_i} \right) \tag{3.1}$$

The final velocity must be divergence-free, so the term on the left-hand side of equation 3.1 vanishes.

The solver uses a numerical discretisation method based on the FVM method, where the unknowns are the integrals of the primitive variables over each element. The contributions from the advective terms may then be calculated as an integral over the element boundary of the fluxes, denoted as $\bar{s}_j \equiv \int_{\Omega_j} s(x_i) d\Omega / |\Omega_j|$. For a given element Ω and a given field s this gives:

$$\int_\Omega u_i^n \frac{\partial s^n}{\partial x_i} d\Omega \simeq u_i^n \int_\Omega \frac{\partial s^n}{\partial x_i} d\Omega = u_i^n \int_{\partial\Omega} n_i s^n dS \tag{3.2}$$

where Green's theorem is used to obtain the surface integral in the last equality.

The finite-volume formulation gives values for the integral over the elements of the primitive variables. In order to calculate the surface integrals of equation 3.2 a function $\tilde{s}_j(x_i)$ for s must be found in Ω_j such that $\int_{\Omega_j} \tilde{s}_j d\Omega = |\Omega_j| \overline{s_j}$.

If $\tilde{s}_j(x_i)$ is assumed constant (equal to $\bar{s}_j$), the resulting numerical scheme will be first order accurate in space. The extension to second order accuracy in space can be achieved by means of a higher-order representation of the primitive variables within the control volumes. The extension to second order accuracy in time can be achieved by means of a Lax-Wendroff-like treatment of the convection operator, similar to the Taylor-Galerkin approach to the unsteady Navier-Stokes equations.

3.1.1 Second order in space

If an estimation of the gradient of all primitive variables is available, the cell constant representation of the primitive variables can be replaced by a linear representation around the same cell-averaged value, thus allowing for better estimates of the primitive variables at the cell boundaries, where the advective contributions are to be computed. The procedure is illustrated in figure 3.1, where a cut on the line joining the centre of gravity of two triangles is showed. The second order fluxes are obtained using the extrapolated primitive variables on the boundary s_{ij} and s_{ji}, rather than the cell-averaged primitive variables s_i and s_j.

Choosing a linear dependency in space for $\widetilde{s}_j$ nearly 2^{nd} order accuracy in space can be obtained. To find the associated constant gradient the gradient of s in the control volumes is determined. This can be found using Green's theorem over the control volume boundary, using the (assumed constant) values of s inside each element touching the control volume. The gradient in the element may then be found by the following rule:

$$|w|_e = \begin{cases} r \min_{CV|e} |s|_{CV|e}, & \text{if} \quad r \min_{CV|e} |s|_{CV|e} < \min^*_{CV|e} |s|_{CV|e} \\ \min^*_{CV|e} |s|_{CV|e}, & \text{if} \quad r \min_{CV|e} |s|_{CV|e} > \min^*_{CV|e} |s|_{CV|e} \end{cases} \tag{3.3}$$

where $\min_{CV|e}$ is the minimum over the control volumes touching element e, and $\min^*$ is the minimum of all the values but the minimum (i.e. the second-smallest value). If $r = 1$ the minimum of the gradients in the control volumes is always chosen. This corresponds to the *minmod* limiter [26]. In order to preserve the TVD property it must be demanded that $r \leq 2$, with $r = 2$ corresponding to the *Superbee* limiter [26]. The minmod limiter is the most diffusive one, but possibly yields the more robust numerical solutions, whereas the superbee limiter yields sharper profiles near discontinuities. To minimize the numerical diffusion in order not to mask the effects of turbulent viscosity Roe's superbee limiter was selected.

3.1.2 Second order in time

A method to compute a second-order approximation in space of the convective term has been outlined. However, to ensure that the numerical scheme be second-order accurate, second order accuracy in time has to achieved. That can be made by means of a Lax-Wendroff-like formulation, accommodated to the present finite volume discretisation scheme. The main simplification with respect to a 'true' Lax-Wendroff treatment consists of taking into consideration only the convective terms, thus neglecting the pressure term ($\nabla p/\rho$) as well as the source term. Having in mind these assumptions, the conservation of a vector quantity s reads:

$$\frac{\partial s_i}{\partial t} + \nabla \cdot [u s_i] = 0 \tag{3.4}$$

The solenoidal condition for u provides:

$$\nabla \cdot [u s_i] = (u \cdot \nabla)\, s_i \tag{3.5}$$

If u does not depend on W (mass and energy equations), and assuming that the partial derivative of the velocity with respect to time is (locally) small, it gives:

$$\frac{\partial^2 s_i}{\partial t^2} = \nabla \cdot [u (u \cdot \nabla) s_i] \tag{3.6}$$

When considering the momentum equations ($s = u$), the preceding assumption seems no longer adequate. In this case:

$$\frac{\partial^2 u_i}{\partial t^2} = \nabla \cdot [u ((u \cdot \nabla) u_i)] + \nabla \cdot [((u \cdot \nabla) \cdot u) u_i] \tag{3.7}$$

Using the Taylor expansion in time for variable s:

$$s^{n+1} = s^n + \frac{\partial s^n}{\partial t} \Delta t + \frac{1}{2} \frac{\partial^2 s^n}{\partial t^2} (\Delta t)^2 + O\left((\Delta t)^3\right) \tag{3.8}$$

it can be verified that a time quasi-second order approximation for the convective terms of the Navier-Stokes equations is given by:

$$\begin{gathered}
\frac{\rho_\gamma^{n+1} - \rho_\gamma^n}{\Delta t} + [u \cdot \nabla \rho_\gamma]^n = \frac{\Delta t}{2} \nabla \cdot [u (u \cdot \nabla) \rho_\gamma]^n \\
\frac{u^{n+1} - u^n}{\Delta t} + [(u \cdot \nabla) u]^n + \left[\frac{\nabla p}{\rho}\right]^{n+1} = \\
\left[\frac{\nabla \cdot \tau + \rho g}{\rho}\right]^n + \frac{\Delta t}{2} \nabla \cdot [u ((u \cdot \nabla) \cdot u)] + \frac{\Delta t}{2} \nabla \cdot [((u \cdot \nabla) \cdot u) u] \\
\frac{e^{n+1} - e^n}{\Delta t} + [u \cdot \nabla e]^n = - \left[\frac{\nabla (k \nabla t)}{\rho}\right]^n + \frac{\Delta t}{2} \nabla \cdot [u (u \cdot \nabla) e]^n
\end{gathered} \tag{3.9}$$

Having written the Lax-Wendroff terms in conservative form, and since they depend on the gradients of the primitive variables, they are calculated and integrated together with the diffusive fluxes. The way in which this task can be done is illustrated in the next section. However, it is important to underline that the above second-order terms are not to be viewed as corrective numerical viscosity, but rather as the improved time-differencing terms expressed in a spatial basis.

3.2 Turbulence modelling

3.2.1 Large Eddy Simulation turbulence model

The LES turbulence model, implemented in the REACFLOW code, is belonging to the eddy viscosity turbulence models and calculates a turbulent viscosity on a local base from the local flow properties. The turbulent viscosity, which is added to the dynamic viscosity, is described by means of the rate of strain, subgrid scale length and the Smagorinsky Constant C_s, as shown in equation 2.32. In the REACFLOW implementation the turbulent viscosity is calculated element wise, this means that the variables necessary for the turbulent viscosity are element related. Consequently the velocity gradients over the element, needed for calculating the rate of strain, are derived from the higher-order representation of the primitive variables over the control volume.

A proper choice for the C_s value is difficult as the constant C_s depends on the resolution and the flow, however previous work in this field has shown that good results can be obtained with a C_s value in the range of 0.1 to 0.2, therefore the C_s value is chosen to be 0.15 [18].

The turbulent viscosity is calculated at the end of the second substep after the Poisson solver, this will ensure that the divergence free condition $(\partial u_i/\partial x_i = 0)$ after the first substep will hold. The contribution of the turbulent viscosity to the diffusive fluxes will be calculated in the next time step, in which turbulent viscosity is added to the dynamic viscosity, conform $\tau = (\mu + \mu_t)\left(\frac{\partial u_i}{\partial x_j} + \frac{\partial u_j}{\partial x_i}\right)$.

Subgrid length scale definition in triangular mesh

With Δ to be the subgrid length scale, the resultant energy dissipation of the large scales is consistent with the Kolmogorov energy spectrum [46] whereby the Kolmogorov constant α is dependent on the Smagorinsky constant C_s. The mathematical relation between Smagorinsky constant C_s and Kolmogorov constant α is given by Muschinski [46] and shows that for a filter as proposed by Lilly the C_s constant has to be in the order of 0.17 to maintain a Kolmogorov constant α of 1.5. Nevertheless the Smagorinsky constant C_s only holds if the resolved and unresolved scales are distinguished properly by the subgrid length scale Δ.

A widely used definition for 2-D rectangular mesh is $\Delta = \sqrt{\Delta_x\Delta_y}$, nevertheless in several studies it was found that $\Delta = 2\sqrt{\Delta_x\Delta_y}$ leads to more accurate results than $\Delta = \sqrt{\Delta_x\Delta_y}$ [64] and in some cases even $\frac{\Delta}{\sqrt{\Delta_x\Delta_y}} > 2$ seems necessary [38]. In the work of Vreman et al. [64] the filter width Δ in LES was set equal to $2\sqrt{\Delta_x\Delta_y}$, indicating that a minimum of two elements is taken to represent the smallest eddies resolved in the flow field. Obtaining a good definition for the subgrid length scale is the main objective of this section, i.e. what is the minimum grid being necessary for resolving a turbulent scale. In using a triangular unstructured mesh the smallest possible scale to be modelled employs three grid point, it is questionable or this is sufficient and therefore two definitions for the subgrid length scale are proposed. The first definition for the subgrid length scale is based on the surface area of the element and reads:

$$\Delta = \sqrt{\frac{\Delta_x\Delta_y}{2}} = \sqrt{A_{tr}} \tag{3.10}$$

In the second definition for subgrid length scale a conventional definition is utilised which reads:

$$\Delta = \sqrt{\Delta_x\Delta_y} = \sqrt{2A_{tr}} \tag{3.11}$$

This definition suggests that two elements are required for resolving a turbulent scale. Compared to $\Delta = \sqrt{A_{tr}}$, LES results obtained with $\Delta = \sqrt{2A_{tr}}$ are less sensitive to discretisation errors. A larger $\frac{\Delta}{\sqrt{A_{tr}}}$ ratio leads to smaller discretisation errors, but on the other hand the $\frac{\Delta}{\sqrt{A_{tr}}}$ ratio is required to be as small as possible in order to retain a maximum amount of information in the resolved scales.

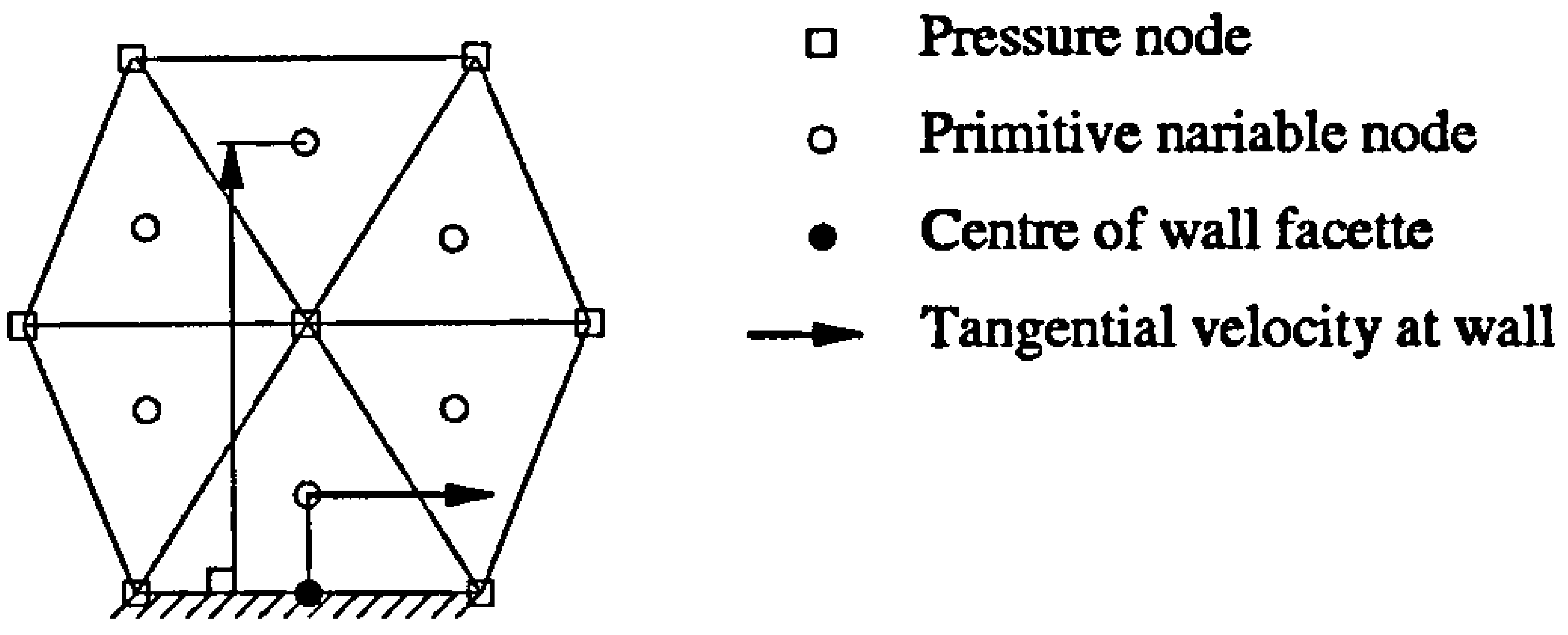

Figure 3.2: Wall Shear Friction.

3.2.2 Van Driest damping function

Due to a reduction of turbulent intensity in the vicinity of the wall the length scale l_s has to be reduced, as discussed in chapter 2.2.3. The damping function has an alternative form to the standard Van Driest damping function as shown in equation 3.12. This was suggested by Ciafalo [12] who indicated that the use of the standard Van Driest wall function for separated flows, i.e. a flow passing a circular cylinder, is questionable. The region on which the Van Driest damping function has to be applied has to be described in terms of wall-shear units y^+. However due to the limited mesh resolution in the vicinity of the wall there is a lack in accuracy of the y^+ value, therefore the region on which the Van Driest damping function is applied is described in terms of the geometrical distance to the wall. Based on the work of Tutar [59], a region of 10% of the cylinder diameter is chosen.

For the calculation of the damping factor D_{damp}, the wall-shear units to the wall have to be known, as shown in equations 3.13. The y^+ value can be calculated from the distance of the element to the wall, the viscosity of flow and the wall shear friction u_τ. The wall shear friction has to be calculated from the velocity gradient in the nearest element to the wall. This element lies adjacent to a wall facette, which is the nearest wall facette to the element for which damping function has to be calculated, as shown in figure 3.2.

$$D_{\text{damp}} = 1 - e^{\left(\frac{y^+}{A^+}\right)^2} \tag{3.12}$$

$$y^+ = \frac{y u_\tau}{\nu} \tag{3.13}$$

Here A^+ is a constant, which in accordance with literature, is assumed to be 26 [15], y^+ is the distance of the element to the wall in terms of wall-shear units, i.e. $y^+ = \frac{y u_\tau}{\nu}$. The shear friction velocity u_τ is calculated from the velocity gradient at the wall, i.e. $u_\tau = \sqrt{\nu \frac{du}{dy}}$. Thus, by taking the wall effects into account, a damped value for the length scale is calculated in the wall region via $l_s = C_s \Delta D_{\text{damp}}$.

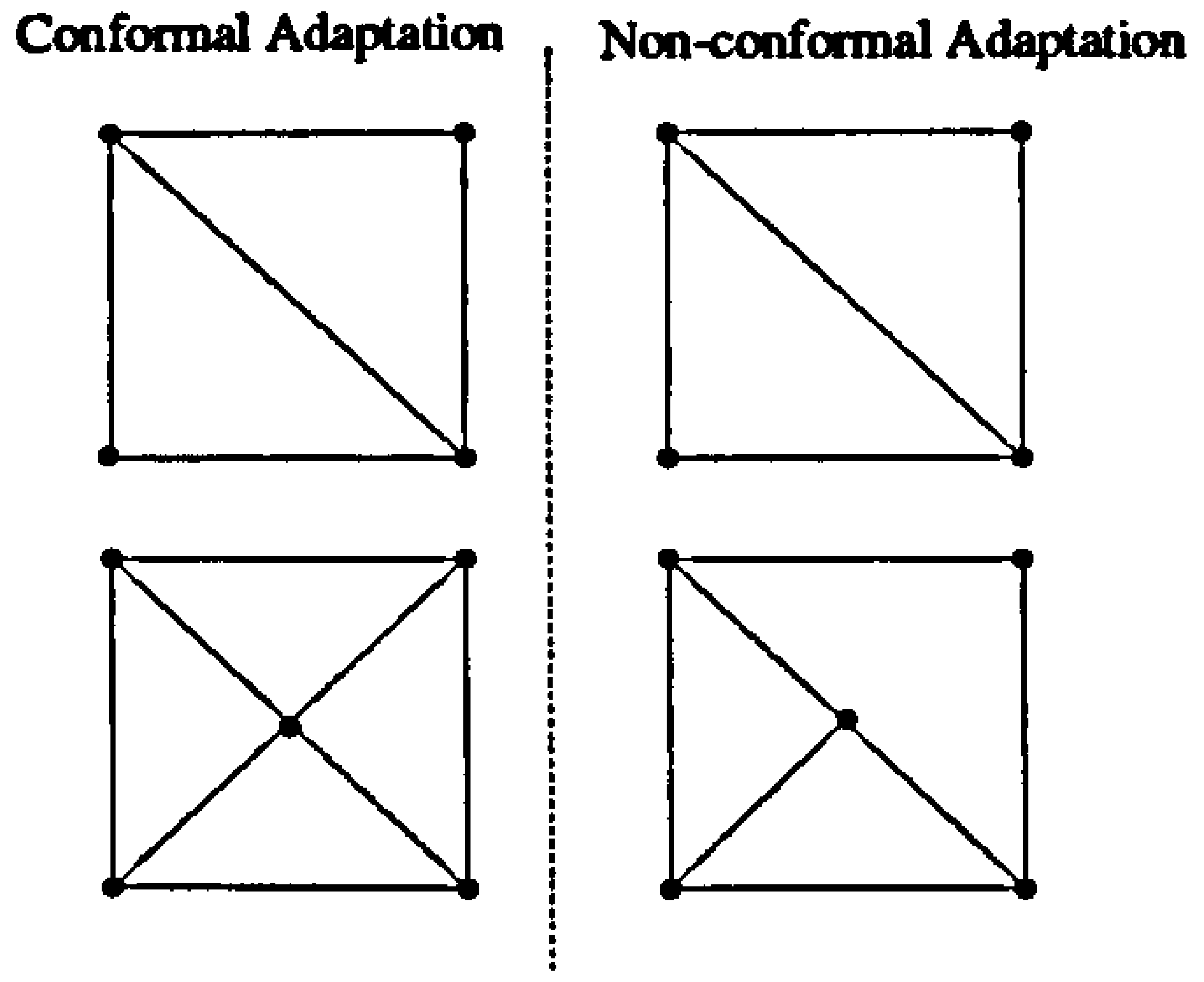

Figure 3.3: Conformal and Non-conformal Grid Adaptation.

3.3 Dynamic Grid Adaptation in REACFLOW

3.3.1 Refinement strategy in REACFLOW code

The refinement strategy adopted in the REACFLOW code is the so called h-refinement strategy. Furthermore, new grid points are always inserted at the mid-point between two existing grid points. The new point thus bisect the existing edge between the two grid points. The elements touching that edge will be divided. The criteria for refinement and coarsening are based on the evaluation of an refinement variable. The variation of this refinement variable in a given control volume may be evaluated in different ways:

- As the absolute value of the gradient projected onto the directions of the neighbouring grid points.
- By an arithmetic-mean estimate of the interpolation error

The thresholds for refinement and coarsing are defined as a percentage of a user defined range of values.

Conformal and non-conformal grid adaptation

The refinement method is based on a conformal insertion of new grid points. When a new grid point is inserted into the grid neighbouring elements and/or control volumes may also be changed. If the change in the elements is such that all elements will remain the same type, the refinement is called conformal. Such an refinement is shown in the left-hand-side of figure 3.3 for a two-dimensional triangle based grid. When the new grid point is inserted the two neighbouring triangles are both divided so that the new triangles all have the new grid point as a vertex. In this way, all triangular elements will continue to have exactly three neighbouring points. In the non-conformal refinement shown on the right hand side of figure 3.3, only one of the neighbouring elements is divided. In the other element the new grid point appears as a 'hanging node' somewhere along the side of the element.

Among the two alternatives, it is not entirely clear what is the most advantageous [27]. The non-conformal methods seem to be able to concentrate the new grid points better in the area where they are needed. On the other hand it will introduce some extra complexity into the code. Huld & Wilkening [27] mentioned that in a node-based system, where the number of neighbours to a given volume is already variable, it is an important simplification that at least the number of neighbours to each element will be known beforehand.

Refinement algorithm

There are several steps to the refinement process. To produce a complete refinement scan for the grid the following steps are necessary:

1. Find possible candidates for refinement by finding single or pairs of control volumes that satisfy the refinement criterion.
2. Elements touching the candidate control volumes are marked for refinement.
3. Look through the elements and process those marked for refinement. To avoid constructing elements with very small solid angles, an element is always divided by bisecting the longest edge of that element. However, this will give rise to a potential problem, especially in 3D. Since a given edge touches more than one element the other element(s) may be bisected along a short edge. Therefore the algorithm thus look through the other elements sharing that edge. If one of these elements has an even longer edge that one will be processed instead. This will mean that the actual point inserted may be somewhat removed from where it was originally intended. On the other hand it enables the code to 'look ahead' a bit and start inserting new nodes in front of a moving disturbance.
4. Repeat the search for the longest edge starting from the originally defined edge and bisect the edge found, until the process arrives at the originally defined edge. In this way the refinement will be performed in the entire region from the edge found in the first step back to the edge where the refinement process was started.
5. Update the other geometrical features, such as the segments of the surfaces of the control volumes, the boundary facettes, etc.
6. Compute the state in the new control volumes. At present the element-based variables in the new elements are simply the ones in the original element.

Coarsening algorithm

The basic criteria for when to remove grid points are the same as for refinement, except that the variation must of course be lower than a coarsening value and the flow variables in the new, bigger, element are found by averaging between the two original elements. In addition, it must have remained under this threshold for a user-defined number of steps. To avoid excessive coarsing it is required that the refinement process is reversible. This means that the grid must be returned to its original state once the refinement in a certain region is no longer needed. Once it has been established that the grid point can be removed safely, the original elements must be restored and the other geometrical features updated.

Threshold ratio The threshold ratio is the ratio between the threshold value for mesh coarsening and mesh refinement, as defined in equation 3.14. A decrease of the threshold ratio means that the error indicated by the DGA algorithm has to become smaller before a previously added node will be removed from the mesh.

$$threshold ratio = \frac{coarsening\, threshold}{refinement\, threshold} * 100\% \tag{3.14}$$

3.3.2 Error indication in REACFLOW

Jump in property variable

The simplest error indicator is obtained by evaluating the jump of some indicator variable like the turbulent viscosity, pressure or temperature within an element or along an edge. This error indicator implicitly makes the assumption

$$e_j = c_1 \Delta \left| \frac{\partial u_i}{\partial x_j} \right| \tag{3.15}$$

i.e. first order accuracy for the underlying scheme. If the absolute value in jump exceeds a threshold value, a new grid point should be inserted between the two points. Error indicators of this form have been used in industrial applications with success [35], even if the underlying numerical discretisation was of higher than first order.

Interpolation method

A simple implementation of this type is the estimation of the local interpolation error Huld & Wilkening [27]. An error estimation of this kind thus assume the solution to be smooth. For a given variable of interest, u, and define an interpolated value for a grid point x_i. This value $\widehat{u}_i$ can be defined in various ways. The simplest is an arithmetical mean over the neighbour grid points:

$$\widehat{u}_i \equiv \frac{1}{N} \sum_{j=1}^{N} u_j \tag{3.16}$$

where u_j are the values of the variable at the j'th of the N neighbours of the grid point x_i. If the absolute difference between the actual value u_i and the interpolated value $\widehat{u}_i$ is greater than some predefined value e_i:

$$e_i \equiv |u_i - \widehat{u}_i| \tag{3.17}$$

a new grid point should be inserted in the vicinity.

3.3.3 Refinement variables in transitional flow

The determination of an appropriate refinement variable to approximate the discretisation error heavily relies on the physical problem investigated. Widely used refinement variables in this respect are the density, pressure and velocity gradients, as well the turbulent viscosity. However the discretisation error describing the deviation from the analytical solution of the set of differential equations is not directly accessible. Therefore the refinement variable is a compromise of the quality of the error indication and the computational complexity of the refinement variable. As discussed in section 2.4 a modification to the turbulent viscosity will be used as a refinement variable.

Modification to turbulent viscosity for refinement variable

The refinement variable, as shown in equation 3.19, is derived from equation 3.18 for turbulent viscosity in the LES turbulence model. By varying the importance or weight of either the cell size Δ or the strain rate $|\overline{S}|$ another refinement behaviour can be established. The weight for the cell size and the strain rate is controlled by the two variables C_m and C_{str} respectively. The variables C_m and C_{str} have to be defined at the start of the simulation, and are constant throughout the numerical domain. A higher weight of the mesh cell size will lead to a more solution independent mesh refinement, while an increase in weight of the strain rate will lead to a mesh refinement in the regions where high velocity gradients do occur.

$$\mu_t = \rho \left(C_s \Delta\right)^2 |\overline{S}| \tag{3.18}$$

$$q_i = \rho C_s^2 \Delta^{2C_m} |\overline{S}|^{C_{str}} \tag{3.19}$$

The DGA variables C_m and C_{str} can be considered as an engineering tool to keep control over the refinement behaviour of the DGA algorithm. However, a modification to the DGA variables C_m and C_{str} also implies a change in the physical properties being monitored throughout the simulation. The parameterisation of the subgrid scales differ from the criteria for mesh refinement when using DGA variables C_m and C_{str} which do not hold values of 1. From a physical perspective this indicates that the mesh refinement is focusing on other features of the turbulent flow field. With values of 1 for both C_m and C_{str} the refinement variable q_i holds the dimensions for dynamic viscosity $\left(\frac{Ns}{m^2}\right)$. With the DGA variables C_m and C_{str} to be 1 and 2 respectively the refinement variable is the dynamic viscosity per unity of

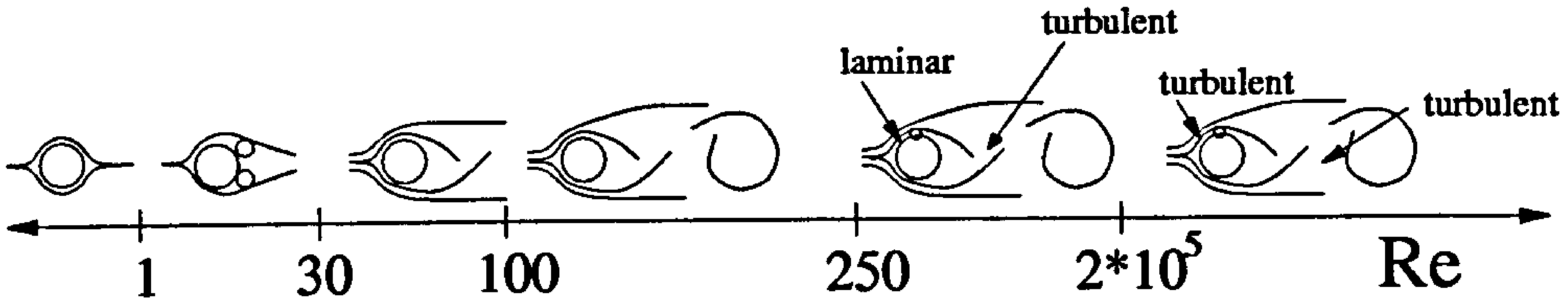

Figure 3.4: Development of wake behind cylinder in terms of Reynolds number

time or dynamic pressure $(\frac{N}{m^2})$. The simulations using DGA variables C_m and C_{str} to be 1 and 1.5 respectively can be considered as an hybrid between both methods, with the dimensions for refinement to be $\left(\frac{N\sqrt{s}}{m^2}\right)$.

3.3.4 Preliminary Dynamic Grid Adaptation investigation

An initial numerical investigation on the modelling of the free jet at low Reynolds numbers has been carried out by De With [69]. The simulations used the DGA algorithm, together with the refinement variable as proposed in this work. The interpolation method for error indication showed to be superior to the jump in variable method. The former method has generated a consistent mesh throughout the numerical domain, while with the latter mesh refinement was sharper and less consistent. Reason for the improved results with the interpolation method is the fact that a total of 4 elements are involved in the calculation of the numerical error, while with the jump in variable method only 2 elements are utilised.

An effective mesh coarsening for flow at low Reynolds numbers has been obtained with a threshold ratio of 50%. Inhere the nodes become redundant when the error is half the error required for mesh refinement. A further increase in bound ratio leads to an unnecessary mesh refinement in the flow field.

3.4 Test case: vortex shedding behind a cylinder

The flow around a circular cylinder is a typical example of bluff body flows. When a fluid flows around a circular cylinder, the flow separates, vortices are shed and a periodic wake is formed. The frequency of the vortex shedding (f) depends upon the cylinder diameter (D), velocity (u_∞) and Reynolds number. Then the non-dimensional vortex shedding frequency or so called the Strouhal frequency (S_t) can be defined as follows:

$$S_t = \frac{fD}{u_\infty} \tag{3.20}$$

The general relationship between Strouhal number and Reynolds number was well documented by Williamson [68]. For a wide range of Reynolds numbers ($1 \cdot 10^2 \leq Re \leq 1 \cdot 10^5$), $S_t \cong 0.2$ for a circular cylinder but absolute values of the Strouhal number would also depend upon cylinder diameter and cylinder length, the blockage ratio of the cylinder, the end conditions, the roughness of the cylinder and the free-stream turbulence level. When a vortex is shed from the cylinder, the local pressure distri-

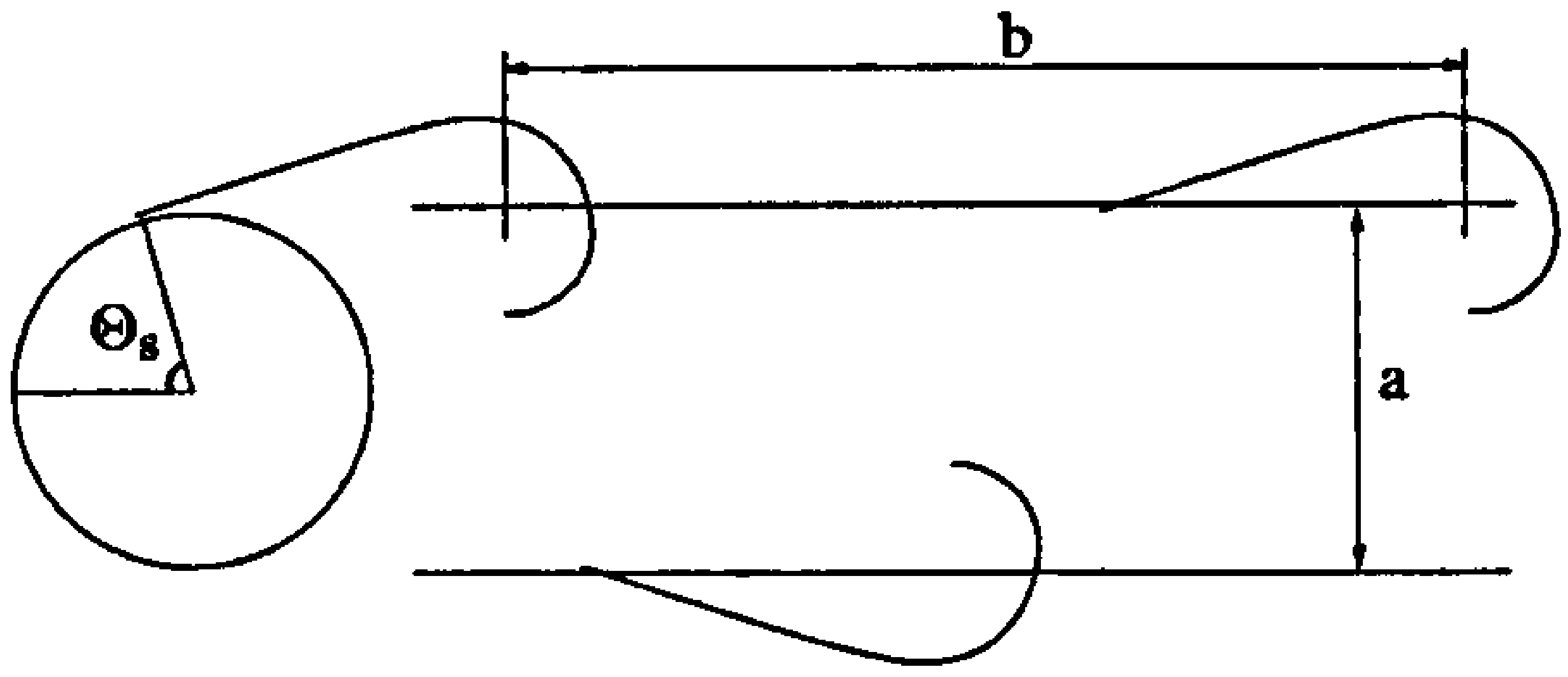

Figure 3.5: Vortex street behind a circular cylinder.

bution behind the cylinder immediately responds and it experiences time varying forces. If the cylinder is no longer fixed, but is flexibly mounted, then a non-linear interaction can arise between the vortex shedding and time varying cylinder deflections due to this force. The non-linear interaction can cause the cylinder to vibrate in either the in-line or cross-flow directions. Under certain conditions the cylinder is forced to oscillate at a frequency close to, or coincident with, its natural frequency. The modelling of the interaction between solid cylinder and flow structures remains beyond the scope of this work, instead this work will only focus on the vortex shedding behind a stable cylinder.

Despite the generalised flow behaviour of flow around a circular cylinder described above, a number of regimes can be identified dependent on their Reynolds number covering the whole Reynolds range from 0 to ∞, as shown in figure 3.4. For a Reynolds number in the order of 0.5 the inertia forces are negligible, and the streamlines come together behind the cylinder. If the Reynolds number is in the range of $2-30$ the boundary layer separates symmetrically from the two sides of the cylinder. Two vortices are formed which rotate in opposite directions and the eddies remain unchanged in their position. With increase of the Reynolds number the vortices elongate but the arrangement is unstable and at Reynolds numbers $40-70$ a periodic oscillation of the wake is observed. Then, at a certain limiting value at a Reynolds number in the order of 100, the eddies break off from each side of the cylinder alternately and are washed downstream. The limiting value of the Reynolds number depends on the turbulence of the oncoming flow, the cylinder roughness and on the nearness of other surfaces. For the next flow regime $250 < Re < 2 \cdot 10^5$ or sub-critical regime the flow inside the wake is considered to be turbulent, however transition from laminar to turbulent flow conditions takes place after the point of separation. In the super-critical regime with Reynolds number above $2 \cdot 10^5$ the flow around the cylinder is turbulent including the boundary layer. A turbulent boundary layer can resist a stronger adverse pressure gradient in contrast to the laminar boundary layer. As a consequence there is an increase in separation angle and a decrease in drag forces when going from the sub-critical flow regime into the super-critical regime.

3.4.1 Boundary layer separation and vortex formation

Within only a thin region adjacent to the cylinder boundary, which is referred as the boundary layer, are the viscous effects important. The velocity of the fluid at the cylinder surface relative to the cylinder is zero, and increases towards the main stream. The shear stress in this zone is very high owing to the extremely high velocity gradients. If the boundary layer is considered along a cylinder surface, several regions may be distinguished in the downstream direction. From the stagnation point on, the boundary layer thickness increases in the downstream direction. The flow in the boundary layer is first laminar, but from a certain point, flow becomes unstable, and transition to turbulent flow may occur if disturbances are present. The location of the transition point depends on the Reynolds number, on the curvature of the surface, on the cylinder surface roughness and on the degree of turbulence in the free stream outside the boundary layer. In a sub-critical flow regime separation takes place after the flow separates from the body, while in the super-critical flow regime separation from the cylinder occurs in the turbulent mode. As there is an adverse-positive pressure gradient in the flow direction, there is a possibility of separation of the boundary layer from the cylinder surface and a change into a third region which is called the vortex shedding. Although a definition of boundary layer separation for all kind of flows has not been well established, its separation can be defined as the point where the normal gradient of the tangential velocity vanishes so that the wall shear stress is zero. This definition implies a breakaway of the streamline at the separation point. The requirement for determination of a separation point remains a major topic in the analysis of flow around a circular body for many steady and unsteady flows. Although separation points are fixed for sharp-edged bluff bodies, there is no fixed separation point for a circular or curved geometry.

Boundary layer separation and vortex shedding behaviour of a bluff body can result in additional time varying forces on the body. The forces acting on the cylinder are due to friction forces and pressure variations at the boundary. It is known that for Reynolds numbers in the sub-critical flow regime ($1.4 \cdot 10^5$) friction forces and the drag associated to it is only a fraction of the total varying force [40], therefore, friction forces will not be considered in this work. The forces in the streamwise and lateral direction are called drag forces (F_D) and lift forces (F_L) respectively. Commonly the drag and lift forces are expressed in a non-dimensional manner relative to density ρ and velocity u_∞ and integrated in time. The drag coefficient C_D and lift coefficient C_L is calculated as the sum of the pressure forces acting on the cylinder relative to the density and inlet velocity as described in equation 3.21.

$$C_D = \frac{2F_D}{\rho u_\infty^2}, C_L = \frac{2F_L}{\rho u_\infty^2} \tag{3.21}$$

For the purpose of quantifying the fluctuating motions in the drag and lift coefficient, the Root Mean Square (r.m.s.) fluctuating lift and drag coefficients $\widetilde{C}_L$ and $\widetilde{C}_D$ are calculated from the integrated pressures over the entire surface.

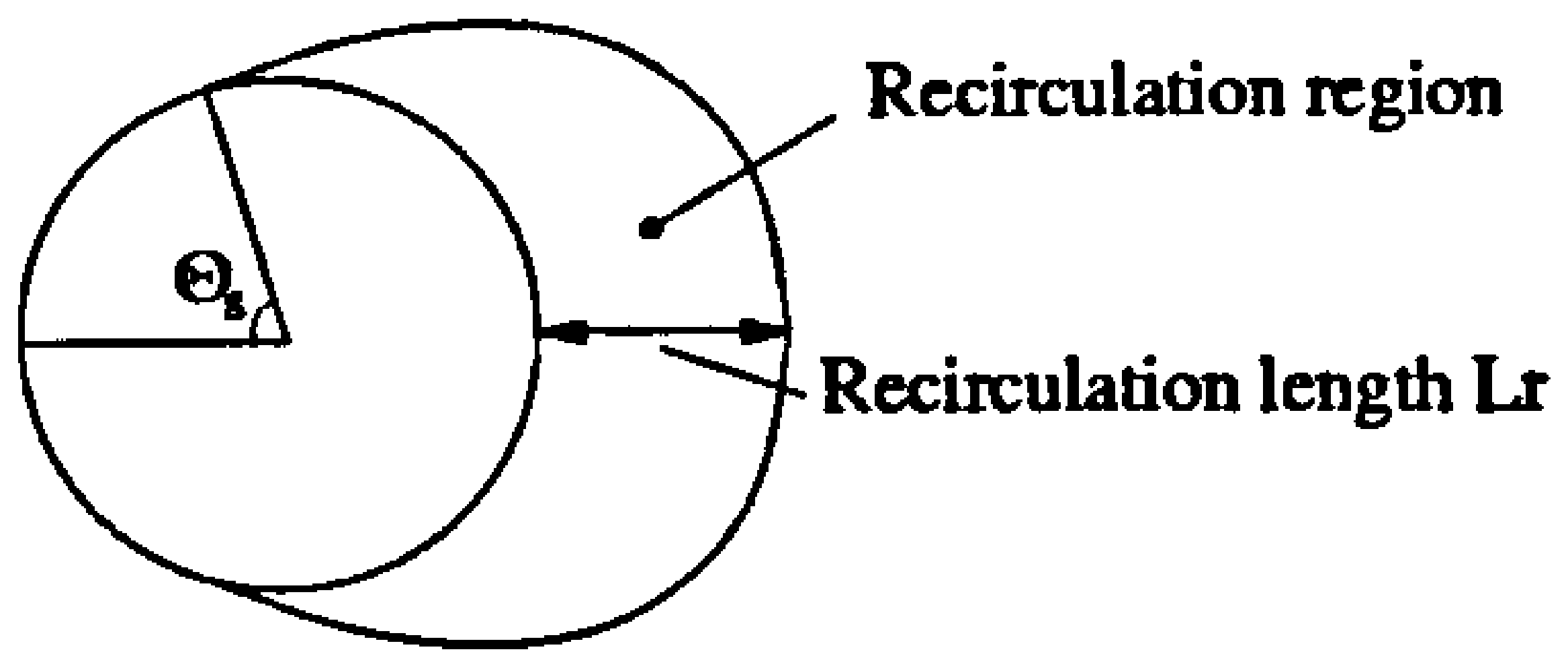

Figure 3.6: Recirculation region behind the cylinder indicated by a reverse flow with a positive velocity component $\overline{u}$ in the upstream flow direction.

The time varying forces are of significant importance in many industrial applications and consequently, the flow around a circular cylinder, has received a great deal of attention in terms of the nature of the vortex shedding mechanism. There have been many studies to understand the interaction of this mechanism with body structure and behaviour of the flow around the bluff body. In the fifteenth century Leonardo da Vinci sketched a row of vortices in the wake of a bluff body in a stream. Quantitative work began with the experiments of Strouhal in the 1870's and he showed the correlation of S_t with Re. In 1908 Benard related the periodicity (f) to the formation of vortex street. In 1911 van Karman showed that in order for a vortex street to remain stable the ratio of vortex width (a) to longitudinal spacing (b) must be equal to 0.28 as shown in figure 3.5.

Von Karman's work, which was based on the idealised vortex street motivated other works related to the vortex shedding mechanism both theoretical and experimental. Since his works, there have been many investigations to understand the mechanics of the formation of wakes. Gerrard [20] gives an extremely useful physical description of the mechanics of the vortex-formation region for a stationary circular cylinder. He indicates that a key factor in the formation of a vortex street wake is the mutual interaction between the two separating shear layers. It is postulated by Gerrard [20] that a vortex continues to grow, fed by circulation from its connected shear layer, until it is strong enough to draw the opposing shear layer across the near wake. The approach of oppositely signed vorticity, in sufficient concentration cuts off further supply of circulation to the growing vortex, which is shed and moves off downstream.

Sarpkaya [53] suggested a more complex process for the shedding of vortices. With the symmetric growth of vortices, the shear layers begin to develop instabilities and is drawn across the wake due to reduced base pressure brought about by the vortex growth. This breaks up the sheet, reducing the supply of vorticity to the growing vortex, bringing it to a minimum, causing the vortex to be shed. The opposite vortex entrains the remaining oppositely signed vorticity. When the circulation for that vortex reaches a minimum, the corresponding shear layer is again drawn across the wake and the vortex is shed, whereupon the process repeats itself.

3.4.2 Periodic flow motions and turbulent shear stress

The existence of periodic waves, as well chaotic motions associated to turbulence in the flow field require data to be integrated in time in order to obtain flow features associated to steady state solution. The time over which data has to be integrated and the need for distinguishing periodic waves from the chaotic motions in the flow field has led to separation of the flow components. The flow in the near wake can be viewed formally as a combination of a global mean component $\bar{s}$, a periodic component $\tilde{s}$, and a chaotic component s', where s is any variable. By definition the total variable s is the sum

$$s = \bar{s} + \tilde{s} + s' \tag{3.22}$$

The mean component is calculated by an averaging process, as shown in equation 3.23,

$$N\bar{s} = \Sigma_{n=1}^{N} s_n \tag{3.23}$$

while the periodic motions are distinguished with an Fast Fourier Transform (FFT). The remaining component s' is associated with turbulence and can be used to calculate the Reynolds stresses $\overline{u_i'u_j'}$.

It is known that at lower Reynolds numbers the total Reynolds stress in the near wake is predominantly due to the time-dependent nature of the von Karman vortex street. At higher Reynolds numbers a dominant frequency corresponding to a large-scale vortex shedding phenomenon can still be observed. However, since transition occurs along the separated shear layers, the instability of the separating shear layers and the near-wake turbulence contribute significantly to the total Reynolds stress. Balachandar et al. [5] concluded that at high Reynolds numbers the Reynolds stress arising from the periodic motion may not be very important. On the other hand the incoherent component plays an increasingly important role at higher Reynolds numbers. One of the important roles of the Reynolds stresses is to balance the force acting on the separation zone as discussed by Balachandar et al. [5]. Here it is the shear stress $\overline{u'v'}$ associated with turbulence which balances the recirculation region in the cross-stream direction, while the normal stresses are concerned with the balance of force at the end of the recirculation region. In here the shear stress plays a major role in the existence and the stability of the recirculation region, consequently leading to an important role in the further flow development.

Chapter 4

Vortex shedding behind a circular cross section bluff body

The modelling of unsteady turbulent flow with the use of the LES turbulence model and a DGA algorithm is the main purpose of this work. To investigate the phenomenon of turbulence together with all complexity associated to it, as e.g. unsteadiness of the flow field, transition and anisotropy of the turbulence, a physical problem like the flow around the circular bluff body in sub-critical flow regime at a Reynolds number of $1.4 \cdot 10^5$ has been selected. Several studies have been reported for this type of flow [9] [60] and it is gradually accepted that it is a difficult test case for CFD modelling [8]. Numerical investigations undertaken by Tutar et al. [61], Travin et al. [58] and Breuer [8] have predicted the flow field in the sub-critical regime with varying success and with strong dependence on the utilised flow solver, turbulence model and mesh resolution. The numerical hazards in predicting this type of flow do reflect the physical complexity of the flow field and make the vortex shedding behind the circular cylinder a suitable flow problem to validate the configuration of both turbulence model and DGA algorithm.

In this work two series of simulations are carried out with the REACFLOW CFD code, simulations are 2-dimensional and use the transient multicomponent variable density incompressible flow solver. The first series undertaken is aimed to obtain a suitable length scale definition for the LES turbulence model. A proper configuration of the LES turbulence model, including the length scale, is not only dependent on the physics being under investigation but also on the mesh resolution and flow solver. For this reason the performance of the LES turbulence model is investigated for a conventional mesh containing $1.8 \cdot 10^4$, $3.3 \cdot 10^4$ and $6.1 \cdot 10^4$ nodes respectively, with a maximum mesh resolution as shown in table 4.1. The purpose of the second series of simulations presented in section 4.2 is to identify suitable criteria for mesh refinement, DGA variables and mesh resolution.

The computational domain and boundary conditions used for the simulations are shown in figure 4.1. At the inlet boundary a uniform velocity profile is imposed,

	Micro scale $[m]$
Cantwell and Coles (1983)	$\eta = 1.38 \cdot 10^{-4}$
$1.8 \cdot 10^4$	$1.06 \cdot 10^{-2}$
$3.3 \cdot 10^4$	$6.50 \cdot 10^{-3}$
$6.1 \cdot 10^4$	$3.73 \cdot 10^{-3}$

Table 4.1: Micro scale based on maximum mesh resolution for a circular cylinder at $Re = 1.4 \cdot 10^5$.

while on the outlet boundary pressure is imposed and velocity is set free. No-slip boundary conditions are applied on the cylinder wall with all velocity components set to zero. On both horizontal boundaries the velocity in the y direction is set to $v = 0$ so that no flow can be drained off or entrained via these boundaries. These conditions mimic the confinement in the experimental setup due to the limited size of the wind tunnel. To ensure conservation of mass in the numerical domain an acceleration in the downstream flow field aside the wake has to take place. The acceleration can be estimated based on the ratio between cylinder diameter and domain width and is expected to be in the order of 4%. To ensure no mesh refinement will take place along the horizontal boundaries, the x-component of the velocity is set equal to the velocity imposed at the inlet in order not to generate any velocity gradient along these boundaries.

For each simulation two animations are available, the first animation shows the general flow field, while the second one shows a detailed picture of the separation region near the cylinder wall. In the text animations are referred to as written in table 4.2.

The work presented here is compared with experimental data from Cantwell & Coles [9]. Although the comparison of simulation results and experimental data is crucial to validate the models presented in this thesis, a critical remark has to be added here. It is well known that the flow around a cylinder not only depends on the Reynolds number but also on a variety of other factors. The most important ones are the ratio between cylinder diameter and cylinder length, the blockage ratio of the cylinder, the end conditions, the roughness of the cylinder and the free-stream turbulence level. This typically leads to highly scattered experimental data as the data of Cantwell & Coles [9] for the drag coefficient and the Strouhal number clearly demonstrate. Therefore one should keep in mind that differences between the experimental conditions and the simulation results will be apparent. The most relevant ones in this investigation are the restricted spanwise extension of the integration domain and the zero turbulence level at the inflow, which is not feasible in wind or water tunnel experiments.

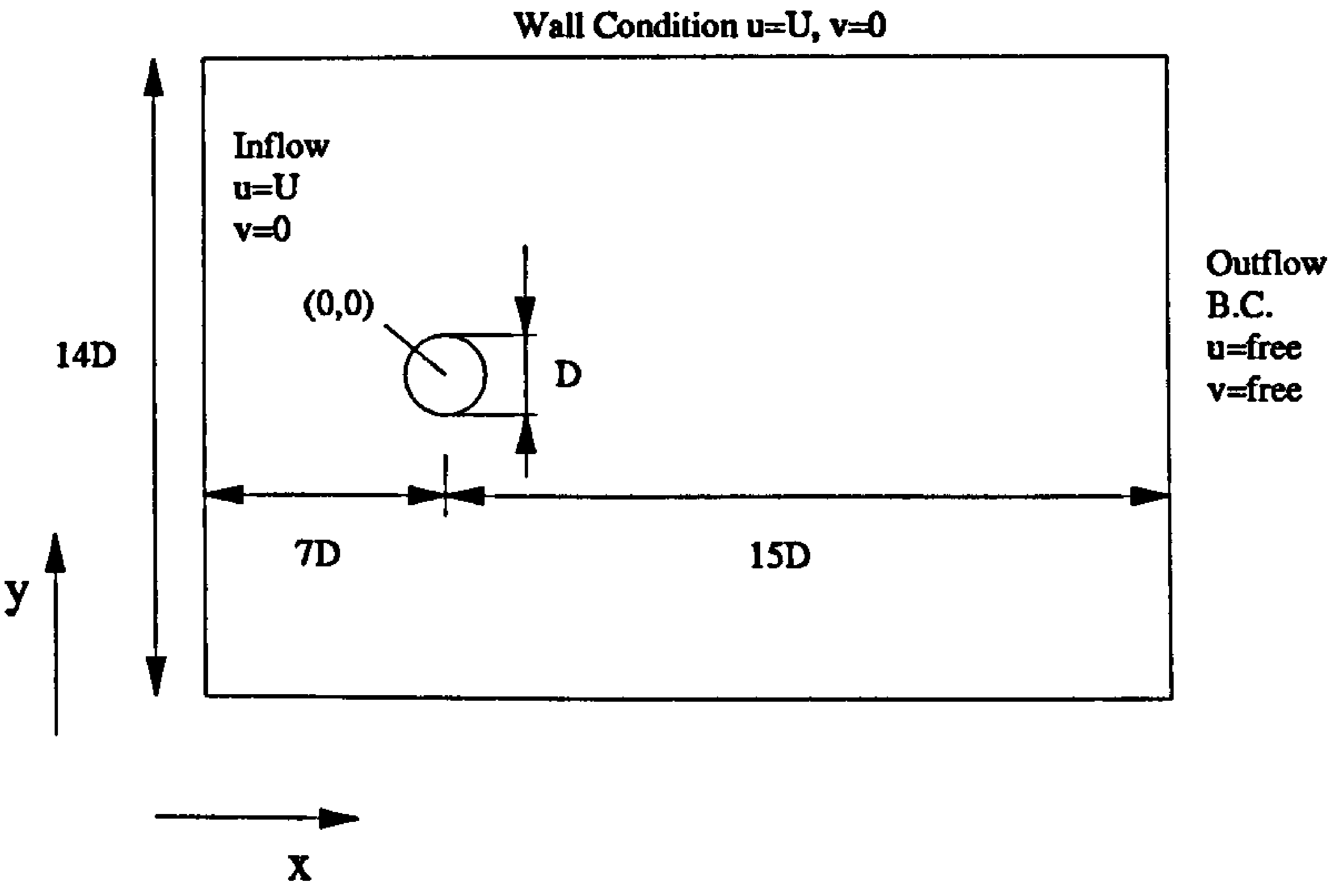

Figure 4.1: Dimensions of simulation model in ratio of cylinder diameter.

	Reference name / Animation name
$\Delta = \sqrt{A_{tr}}$	
$1.8 \cdot 10^4$	$\sqrt{A_{tr}} - 1.8 \cdot 10^4 - 1.avi$
	E:\NO-DGA\ls=A-nodes=18e3_PIC01.avi
	$\sqrt{A_{tr}} - 1.8 \cdot 10^4 - 2.avi$
	E:\NO-DGA\ls=A-nodes=18e3_PIC02.avi
$3.3 \cdot 10^4$	$\sqrt{A_{tr}} - 3.3 \cdot 10^4 - 1.avi$
	E:\NO-DGA\ls=A-nodes=33e3_PIC01.avi
	$\sqrt{A_{tr}} - 3.3 \cdot 10^4 - 2.avi$
	E:\NO-DGA\ls=A-nodes=33e3_PIC02.avi
$6.1 \cdot 10^4$	$\sqrt{A_{tr}} - 6.1 \cdot 10^4 - 1.avi$
	E:\NO-DGA\ls=A-nodes=61e3_PIC01.avi
	$\sqrt{A_{tr}} - 6.1 \cdot 10^4 - 2.avi$
	E:\NO-DGA\ls=A-nodes=61e3_PIC02.avi
$\Delta = \sqrt{2A_{tr}}$	
$1.8 \cdot 10^4$	$\sqrt{2A_{tr}} - 1.8 \cdot 10^4 - 1.avi$
	E:\NO-DGA\ls=2A-nodes=18e3_PIC01.avi
	$\sqrt{2A_{tr}} - 1.8 \cdot 10^4 - 2.avi$
	E:\NO-DGA\ls=2A-nodes=18e3_PIC02.avi
$3.3 \cdot 10^4$	$\sqrt{2A_{tr}} - 3.3 \cdot 10^4 - 1.avi$
	E:\NO-DGA\ls=2A-nodes=33e3_PIC01.avi
	$\sqrt{2A_{tr}} - 3.3 \cdot 10^4 - 2.avi$
	E:\NO-DGA\ls=2A-nodes=33e3_PIC02.avi
$6.1 \cdot 10^4$	$\sqrt{2A_{tr}} - 6.1 \cdot 10^4 - 1.avi$
	E:\NO-DGA\ls=2A-nodes=61e3_PIC01.avi
	$\sqrt{2A_{tr}} - 6.1 \cdot 10^4 - 2.avi$
	E:\NO-DGA\ls=2A-nodes=61e3_PIC02.avi

Table 4.2: The animation file name and the reference name used in the thesis for the animations obtained from simulations with conventional mesh. The first animation indicated by a 1 gives a view of the general flow field, while the animation indicated by a 2 gives a detailed view of the flow in the vicinity of the wall near the point of separation.

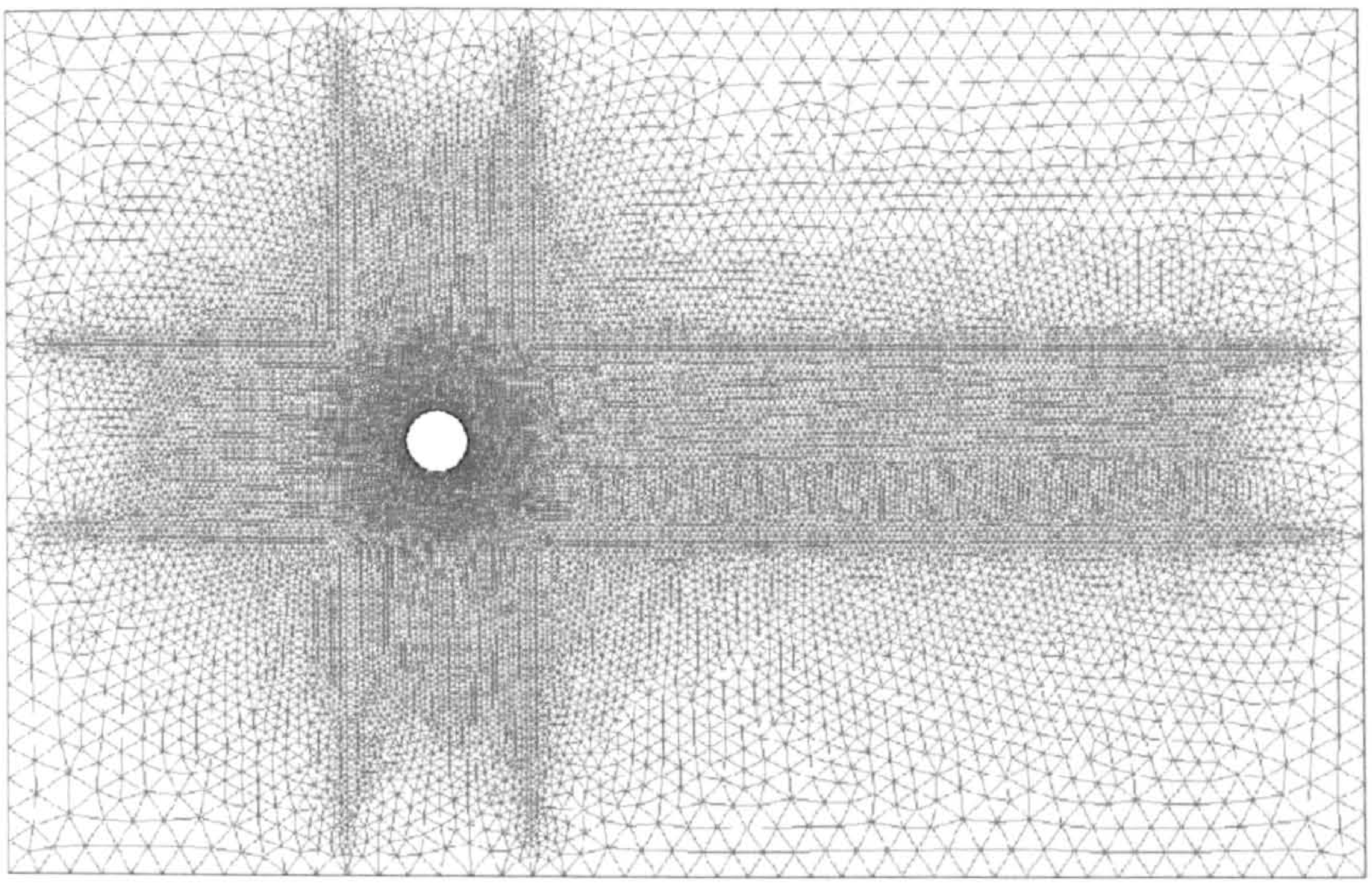

(a) Mesh

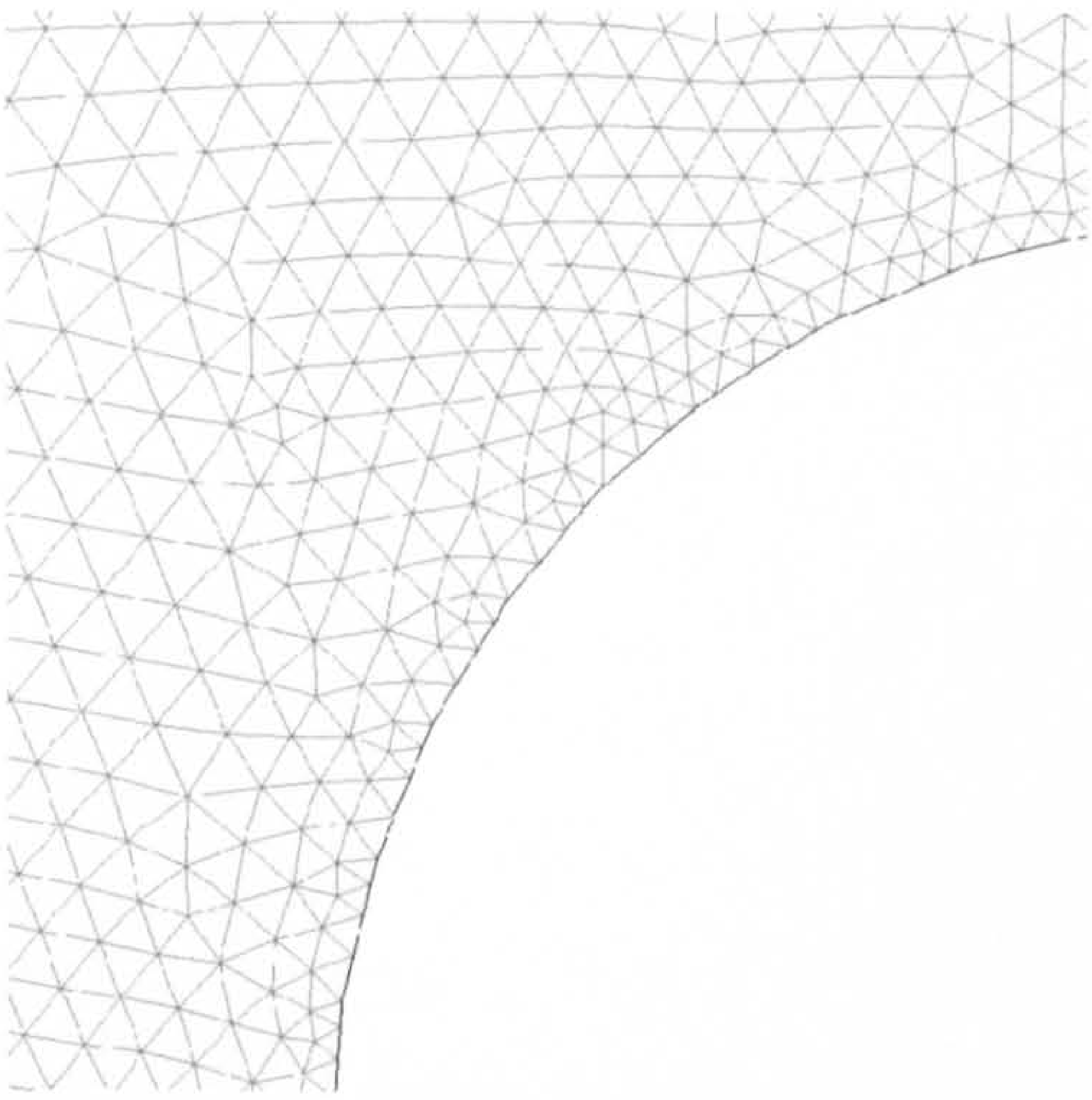

(b) Mesh adjacent to the wall

Figure 4.2: Conventional mesh containing 18,000 nodes. The mesh in concentrated on the area adjacent to the wall and the downstream region. In the region near to the outer boundaries of the numerical domain a coarser mesh is applied.

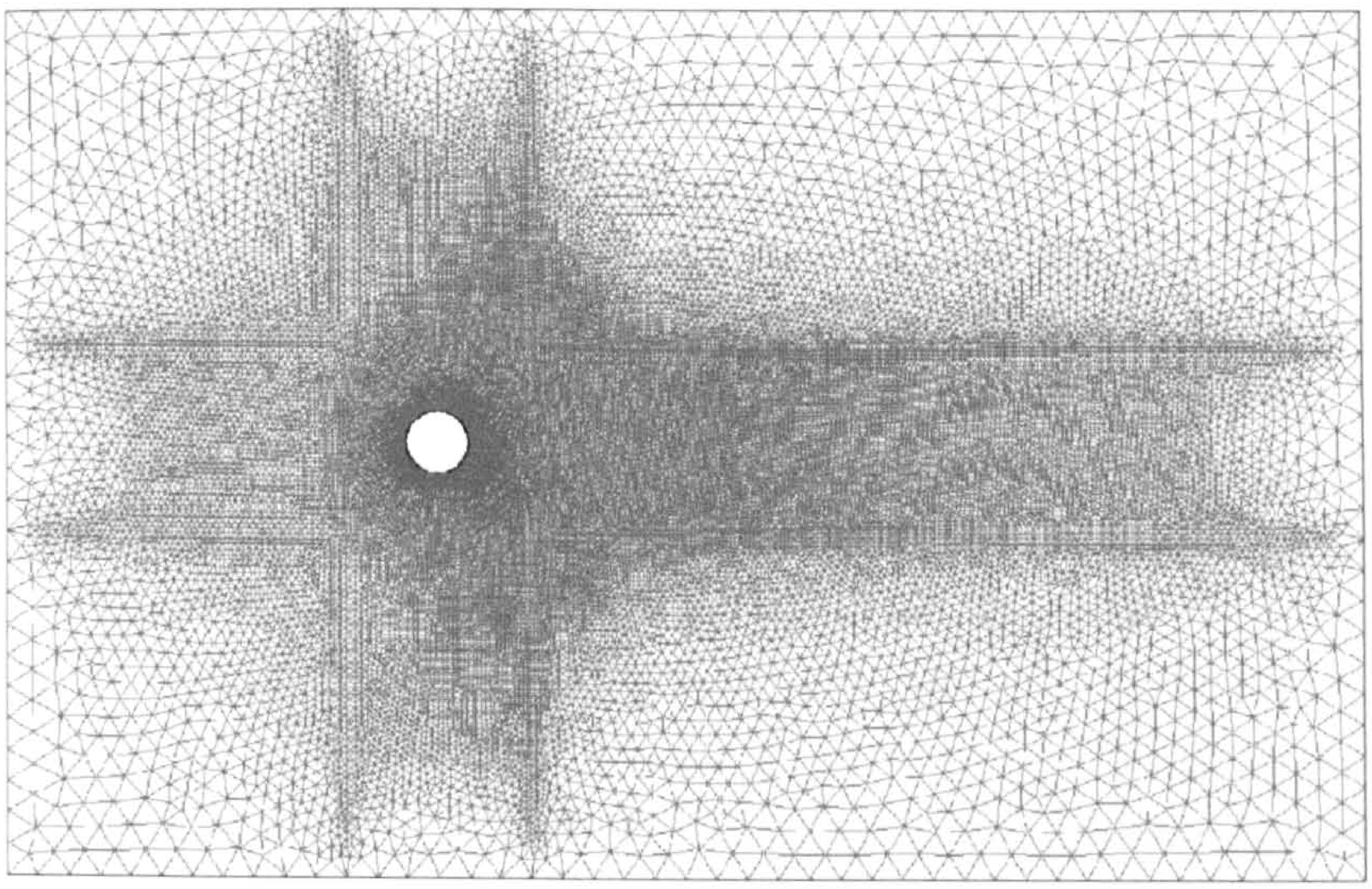

(a) Mesh

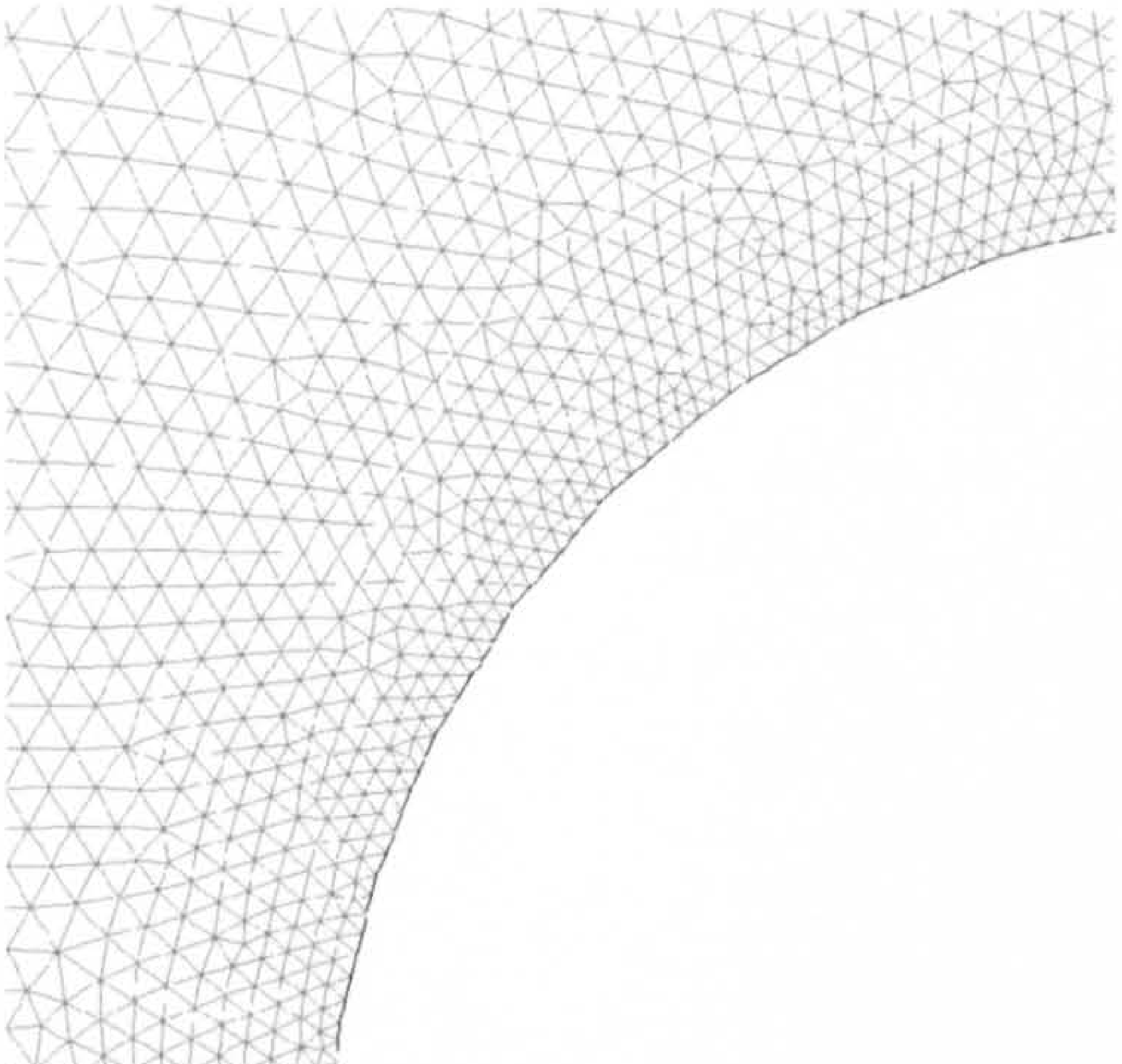

(b) Mesh adjacent to the wall

Figure 4.3: Conventional mesh containing 33,000 nodes. The mesh in concentrated on the area adjacent to the wall and the downstream region. In the region near to the outer boundaries of the numerical domain a coarser mesh is applied.

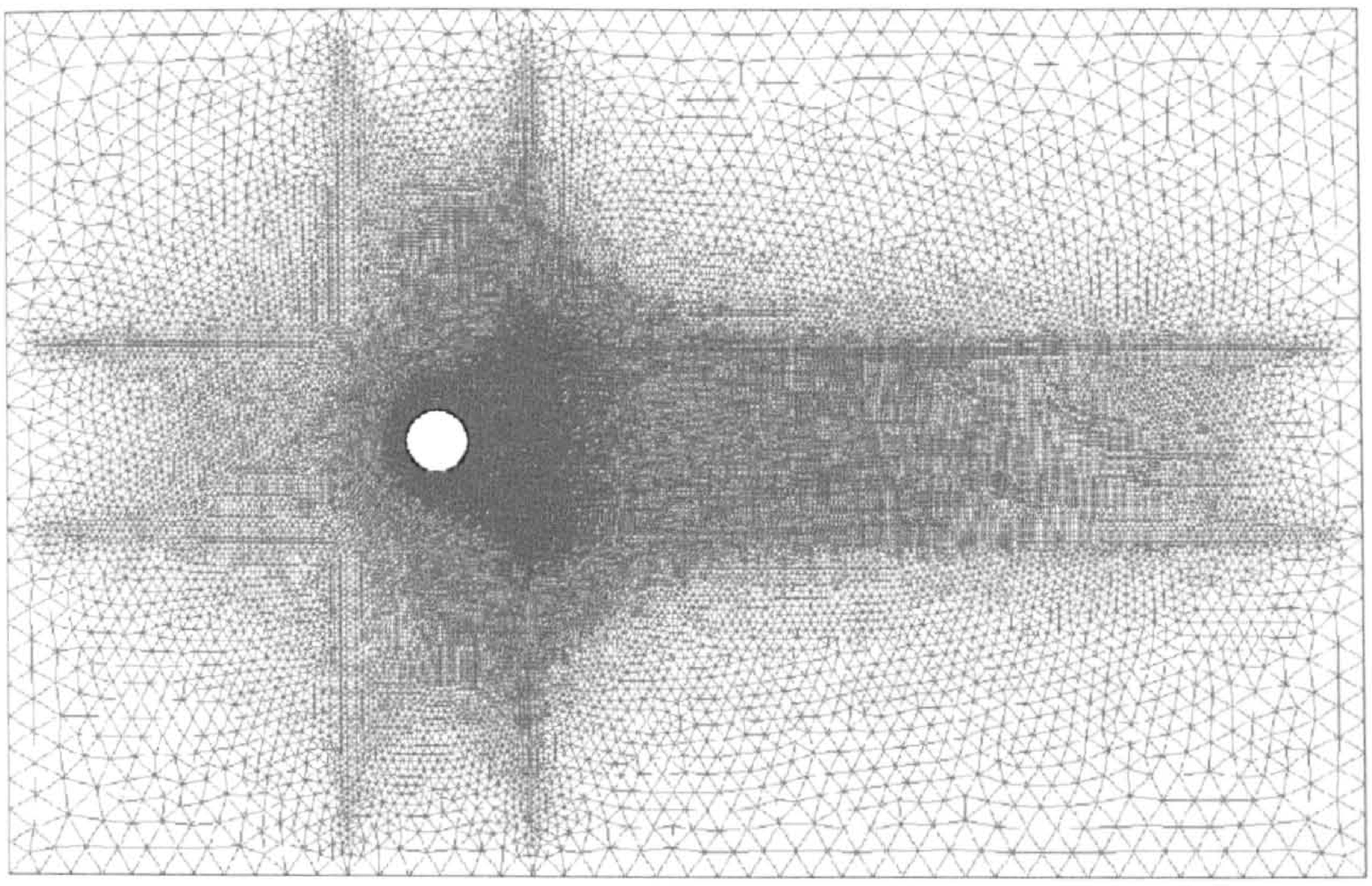

(a) Mesh

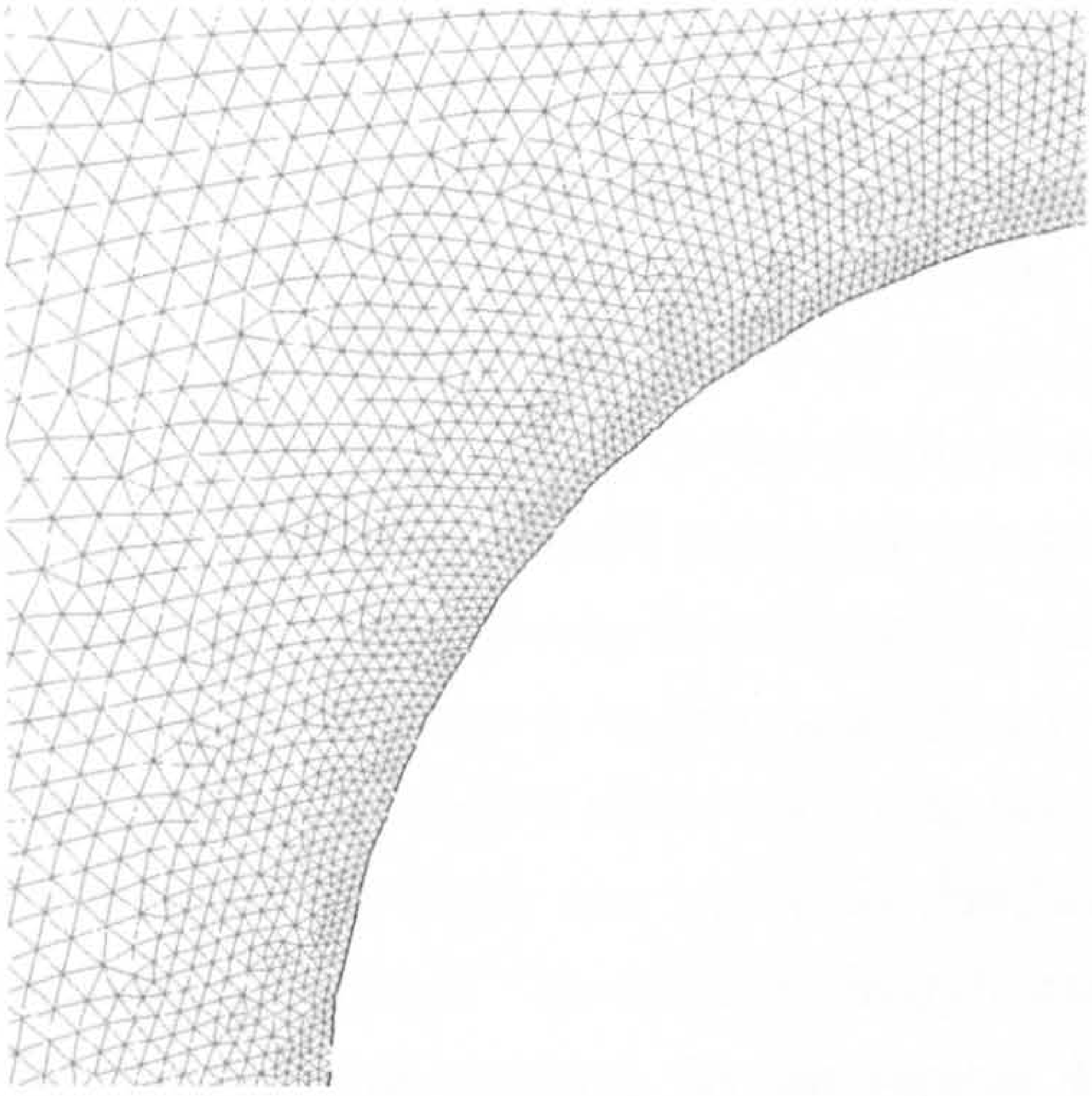

(b) Mesh adjacent to the wall

Figure 4.4: Conventional mesh containing 61,000 nodes. The mesh in concentrated on the area adjacent to the wall and the downstream region. In the region near to the outer boundaries of the numerical domain a coarser mesh is applied.

	S_t	Θ_s	L_r
Cantwell and Coles (1983)	0.179	77.0	0.5
$\Delta = \sqrt{A_{tr}}$			
$1.8 \cdot 10^4$	0.20	91.5	0.33
$3.3 \cdot 10^4$	0.22	83.0	0.00
$6.1 \cdot 10^4$	0.20	86.0	0.53
$\Delta = \sqrt{2A_{tr}}$			
$1.8 \cdot 10^4$	0.22	96.0	0.25
$3.3 \cdot 10^4$	0.20	83.5	0.67
$6.1 \cdot 10^4$	0.16	90.0	0.51

Table 4.3: Time integrated flow parameters, Strouhal number S_t, separation angle Θ_s and recirculation length L_r, for simulations with conventional mesh and subgrid length scale $\Delta = \sqrt{A_{tr}}$ and $\Delta = \sqrt{2A_{tr}}$ respectively.

4.1 Modelling vortex shedding behind a cylinder with conventional mesh

With the LES Smagorinsky model, subgrid scales have to be distinguished from the large resolved scales by a length scale. This length scale is related to the mesh size as suggested in equation 2.32 and plays a dominant role in the determination of the turbulent viscosity.

In this work two definitions for the subgrid length scale are proposed; the first definition for length scale is based on the surface area of the element and reads $\Delta = \sqrt{\frac{\Delta_x\Delta_y}{2}} = \sqrt{A_{tr}}$, while in the second definition a conventional definition is proposed which reads $\Delta = \sqrt{\Delta_x\Delta_y} = \sqrt{2A_{tr}}$ and in which it is suggested that two elements are required for resolving a turbulent scale. Compared with results produced using $\Delta = \sqrt{A_{tr}}$, LES results obtained with $\Delta = \sqrt{2A_{tr}}$ are less sensitive to discretisation errors. A larger $\frac{\Delta}{\sqrt{A_{tr}}}$ ratio leads to smaller discretisation errors, but on the other hand, the $\frac{\Delta}{\sqrt{A_{tr}}}$ ratio is required to be as small as possible in order to retain a maximum amount of information in the resolved scales.

In the LES Smagorinsky model the subgrid scales are assumed to be isotropic and therefore the smallest resolved scales should be of isotropic nature. The definition for Smagorinsky constant C_s and subgrid length scale Δ will only hold ideally for subgrid scales that fulfill the LES subgrid scale requirements. This, however, leads to considerable mesh requirements which are not easily fulfilled in a high turbulent flow. For this reason, the impact of the subgrid length scale on the flow field will be investigated for a variety of meshes. In the figures 4.2 to 4.4 the highest mesh resolution in the numerical domain is applied in the vicinity of the cylinder wall where small scale vortices are expected to develop while downstream the mesh resolution is progressively reduced.

4.1.1 Vortex shedding patterns

The results obtained from the simulations using these conventional meshes show substantial variation in the time integrated data as shown in table 4.3. A far

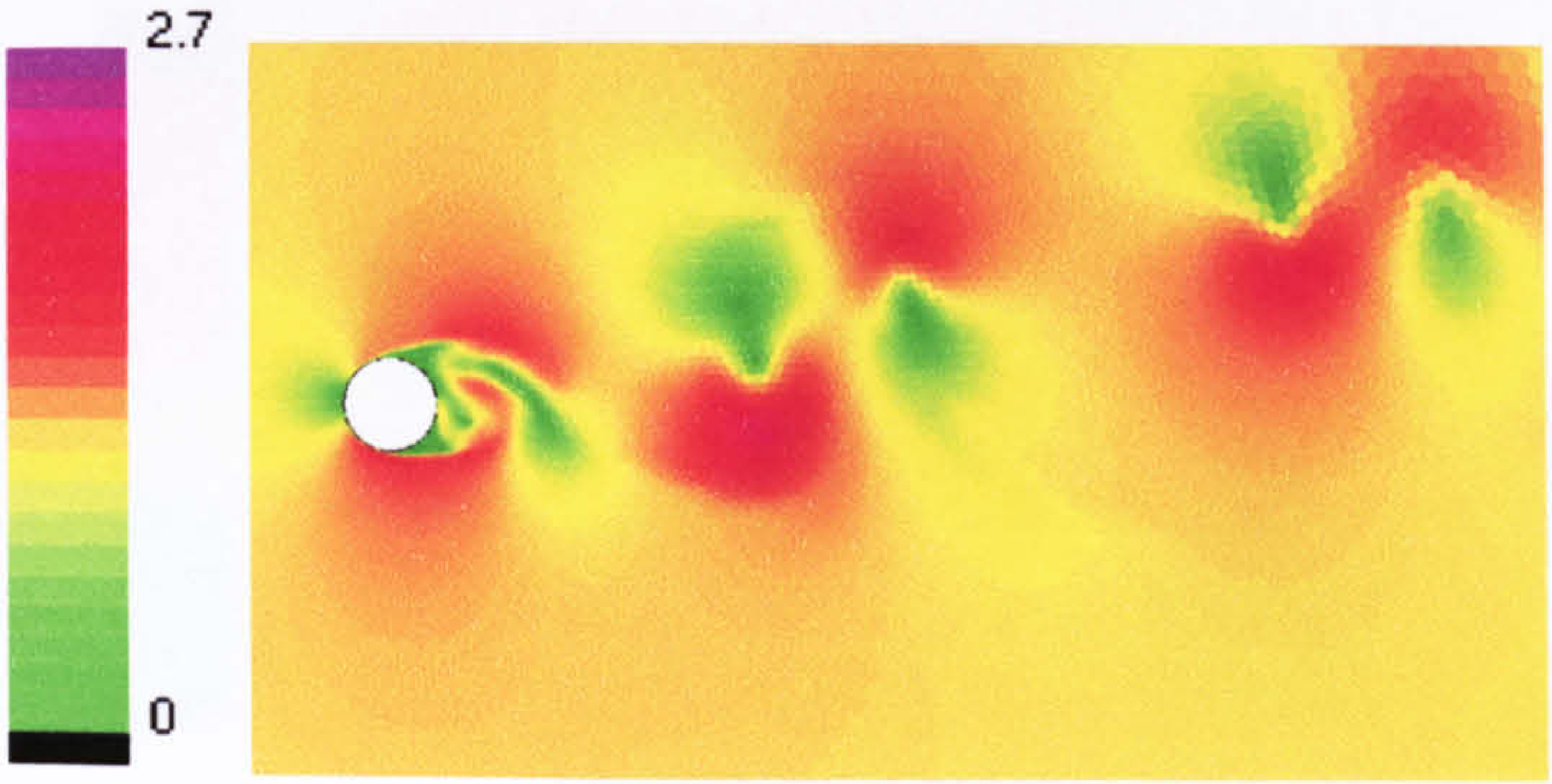

(a) 18,000 nodes

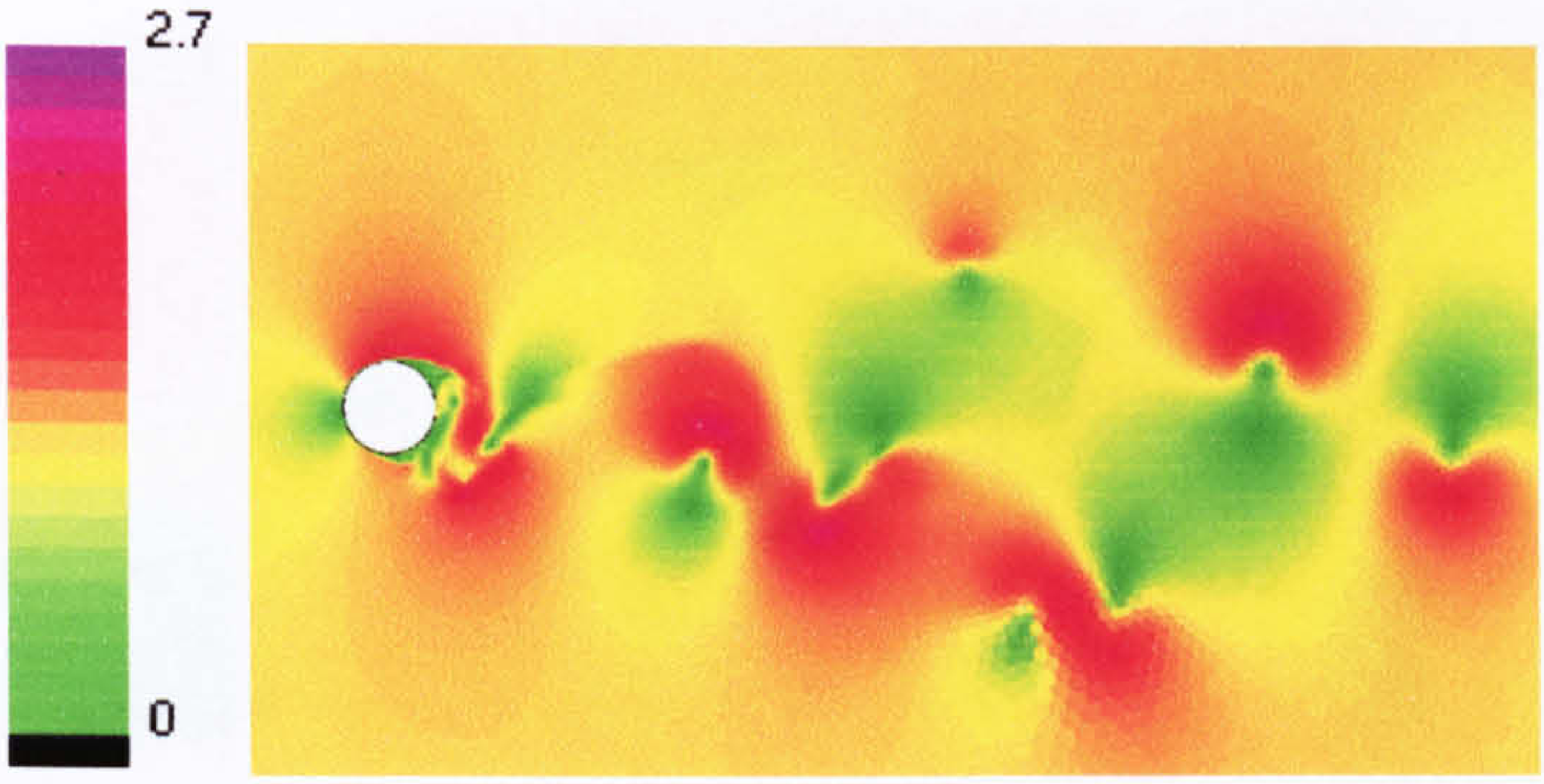

(b) 33,000 nodes

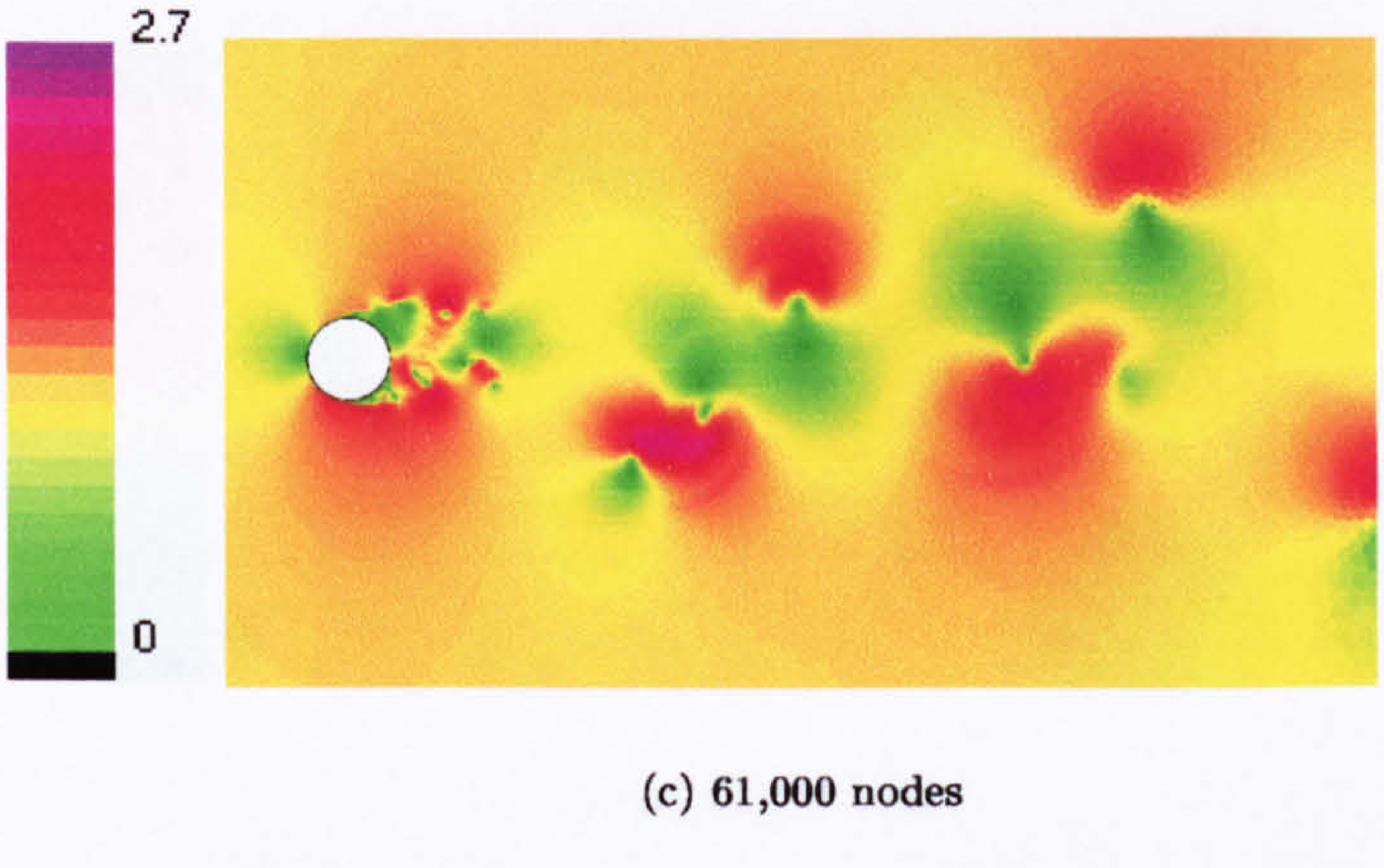

(c) 61,000 nodes

Figure 4.5: Snap shot of the velocity field at $t = 30$ for simulations with conventional mesh and a subgrid length of $\Delta = \sqrt{A_{tr}}$. A wider range of small scale vortices is observed in the shear layers with increasing mesh resolution.

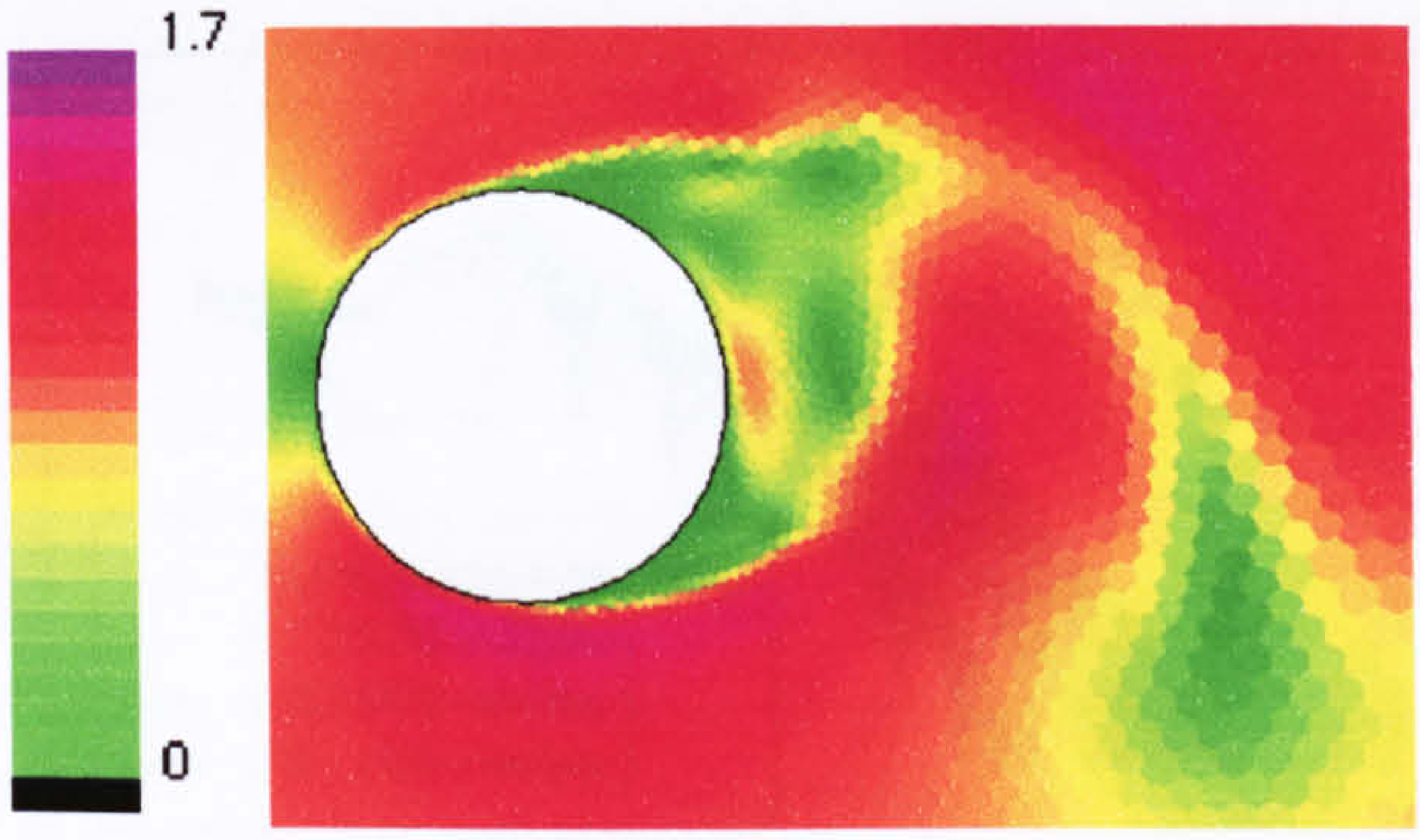

(a) 18,000 nodes

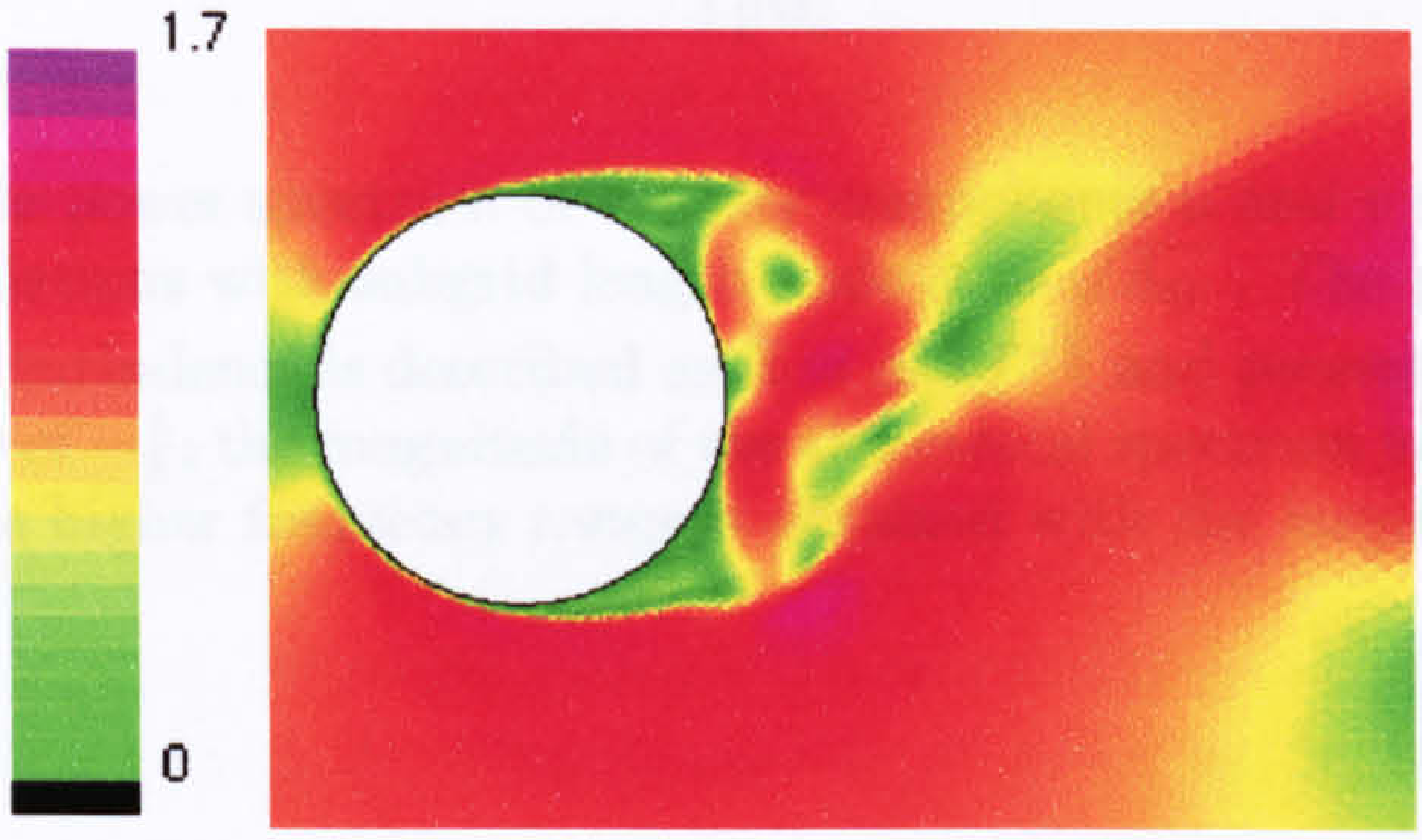

(b) 33,000 nodes

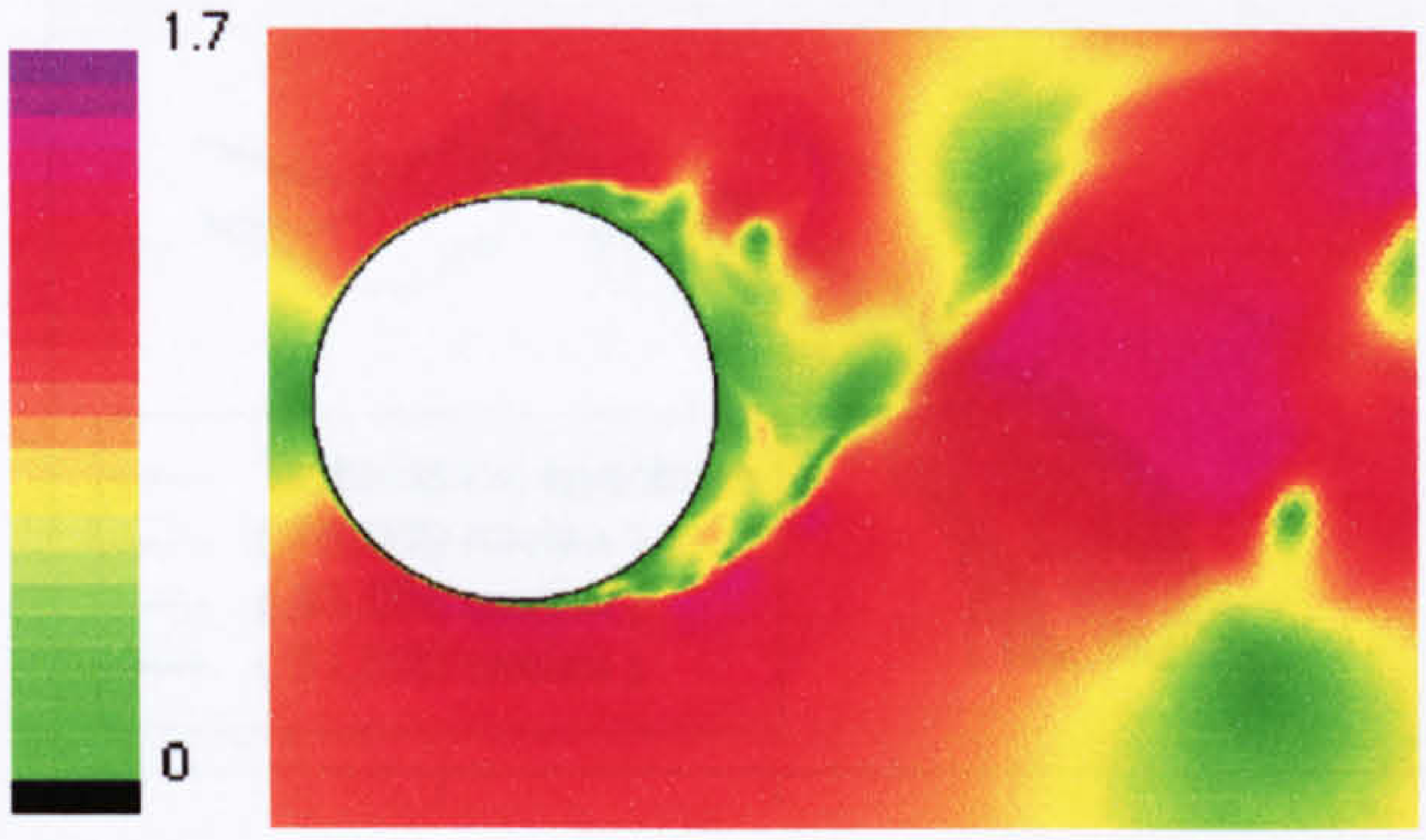

(c) 61,000 nodes

Figure 4.6: Snap shot of the velocity field at $t = 30$ of the transitional region, for simulations with conventional mesh and a subgrid length scale of $\Delta = \sqrt{A_{tr}}$. A wider range of small scale vortices is observed in the shear layers with increasing mesh resolution.

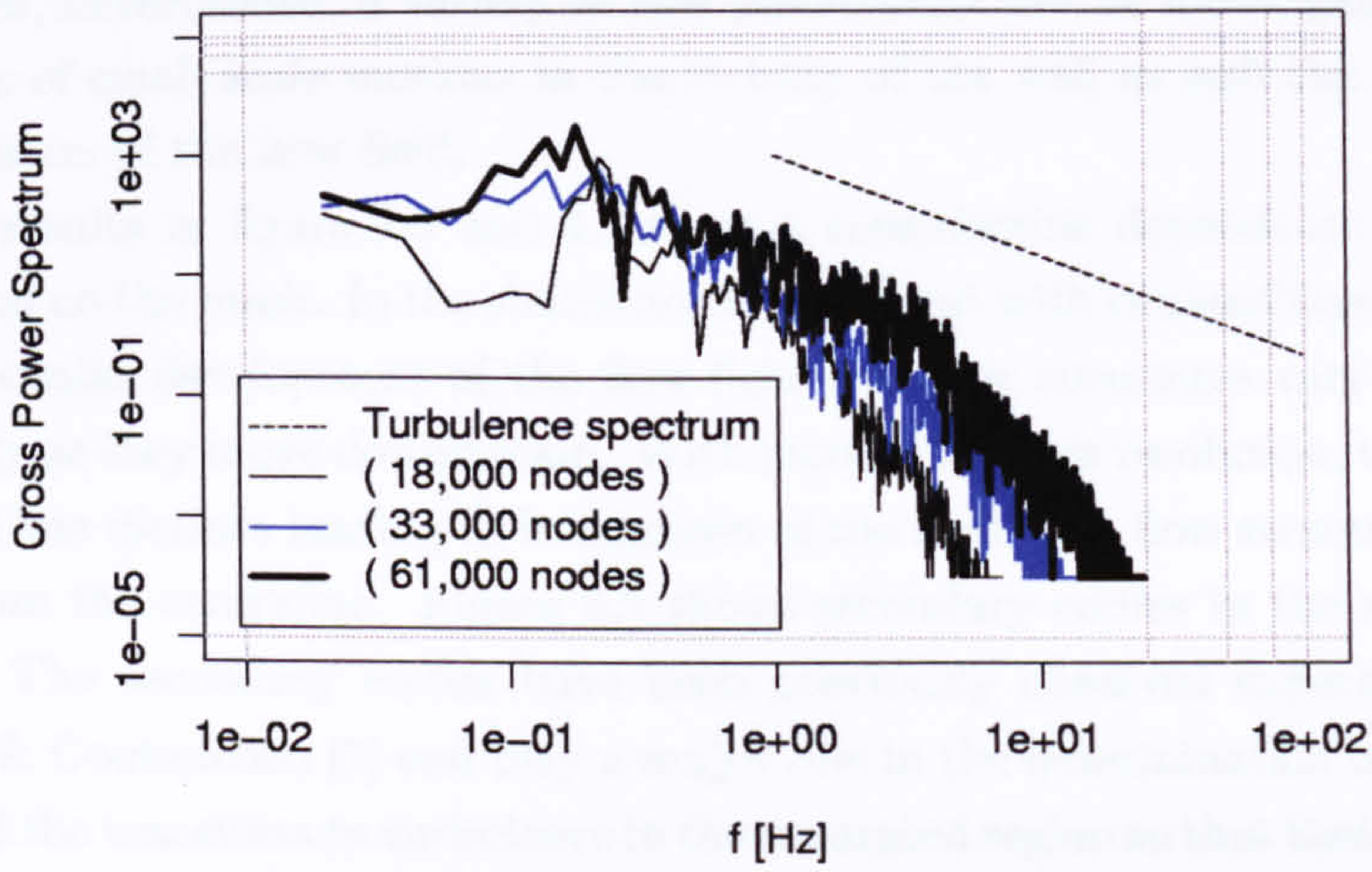

Figure 4.7: Cross-power spectrum of velocity components u and v at point $\frac{x}{D} = 1$, $\frac{y}{D} = 0$, for simulations with subgrid length scale $\Delta = \sqrt{A_{tr}}$. The power spectrum of homogeneous turbulence is described as $E = \alpha\varepsilon^{\frac{2}{3}} f^{-\frac{5}{3}}$ and presented as a straight line with a slope of $-\frac{5}{3}$; the magnitude of the theoretical spectrum is arbitrary. Best agreement in the higher frequency range is obtained with the largest mesh size.

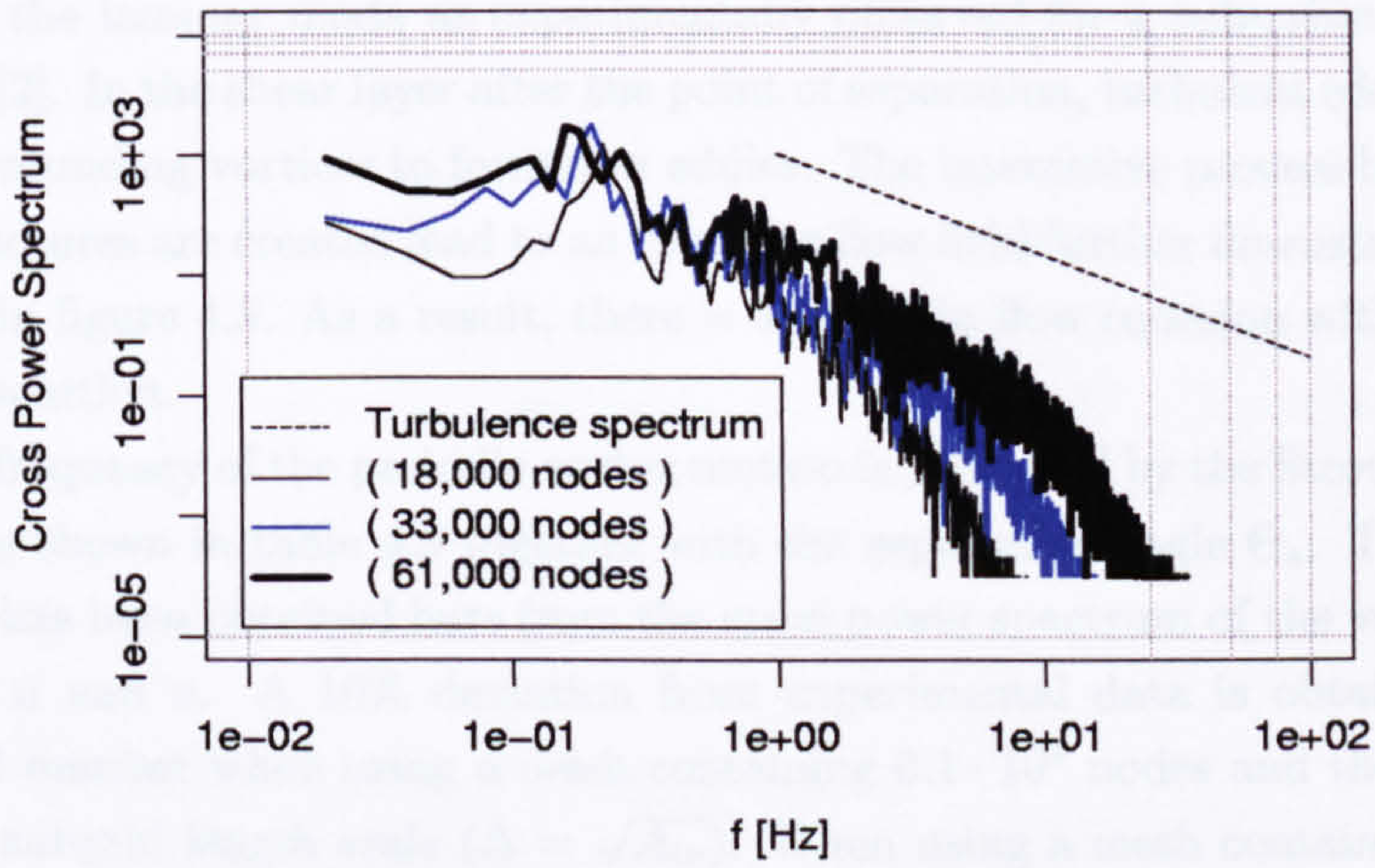

Figure 4.8: Cross-power spectrum of velocity components u and v at point $\frac{x}{D} = 1$, $\frac{y}{D} = 0$, for simulations with subgrid length scale $\Delta = \sqrt{2A_{tr}}$. The power spectrum of homogeneous turbulence is described as $E = \alpha\varepsilon^{\frac{2}{3}} f^{-\frac{5}{3}}$ and presented as a straight line with a slope of $-\frac{5}{3}$; the magnitude of the theoretical spectrum is arbitrary. Best agreement in the higher frequency range is obtained with the largest mesh size.

stronger variation in the flow prediction is shown when viewing the flow field at an instant, as shown in figures 4.5 and 4.6. Such a view can be considered as a snap shot and consequently such flow field thus not present any time integrated flow quantities, nevertheless, a variety of flow phenomena can be investigated, e.g. the existence of small scale motions in the vicinity of the wall as well the break down and cohesion of the flow field.

The results in figure 4.5 and 4.6 show a considerable dependence of the flow prediction on the mesh. In the simulations carried out with conventional mesh there is an irregular development of the flow field and flow structures vary in size and frequency as they move downstream. With increasing mesh resolution, the flow field becomes less distinct leading to breakdown of the field with flow structures drifting away from the centreline. Figure 4.6 shows secondary eddies in the recirculation region. The secondary eddies have been previously observed experimentally by Bouard & Coutanceau [7] and play a major role in the determination of turbulence level and the transition to turbulence in the separated region so that their calculation becomes very important. The prediction of secondary vortices confirms the LES results obtained by Tutar & Holdø [60] who suggested that the LES turbulence model is superior to any RANS turbulence model for modelling separating flows. With the highest mesh resolution ($6.1 \cdot 10^4$ nodes) a wider spectrum of small scale eddies has been resolved, as can be seen in figure 4.6. As a consequence, a wide variety of turbulent eddies exist in the shear layer. Nevertheless, for all simulations with conventional mesh, turbulent eddies start to build up in the shear layer away from the separation point and behind the cylinder in the recirculation region. Before the separation point, where a thin boundary layer has developed, no turbulent eddies are apparent which confirms that for Reynolds numbers of $1.4 \cdot 10^5$ separation takes place in the laminar mode as experimentally observed for a sub-critical Reynolds number [2]. In the shear layer after the point of separation, turbulent eddies interact with surrounding vortices to form new eddies. The interactive process by which the flow structures are created lead to an irregular flow field further downstream, as can be seen in figure 4.5. As a result, there is a decay in flow cohesion with increasing mesh resolution.

The frequency of the periodic vortex motion is presented by the Strouhal number S_t and is shown in table 4.3 together with the separation angle Θ_s. The Strouhal number has been obtained here from the cross-power spectrum of the velocity components u and v. A 10% deviation from experimental data is obtained for the Strouhal number when using a mesh containing $6.1 \cdot 10^4$ nodes and the first equation for subgrid length scale ($\Delta = \sqrt{A_{tr}}$). When using a mesh containing $6.1 \cdot 10^4$ nodes in combination with the second equation for subgrid length scale ($\Delta = \sqrt{2A_{tr}}$) Strouhal number is under-predicted, while in all other simulations Strouhal number is over-predicted. Tutar & Holdø [60] and Breuer [8] also discovered an over-prediction of the Strouhal number when using the LES turbulence model.

Figure 4.7 and 4.8 show the cross power spectrum on the centreline at $\frac{x}{D} = 1$. The simulations show a peak corresponding to the Strouhal number and a steady

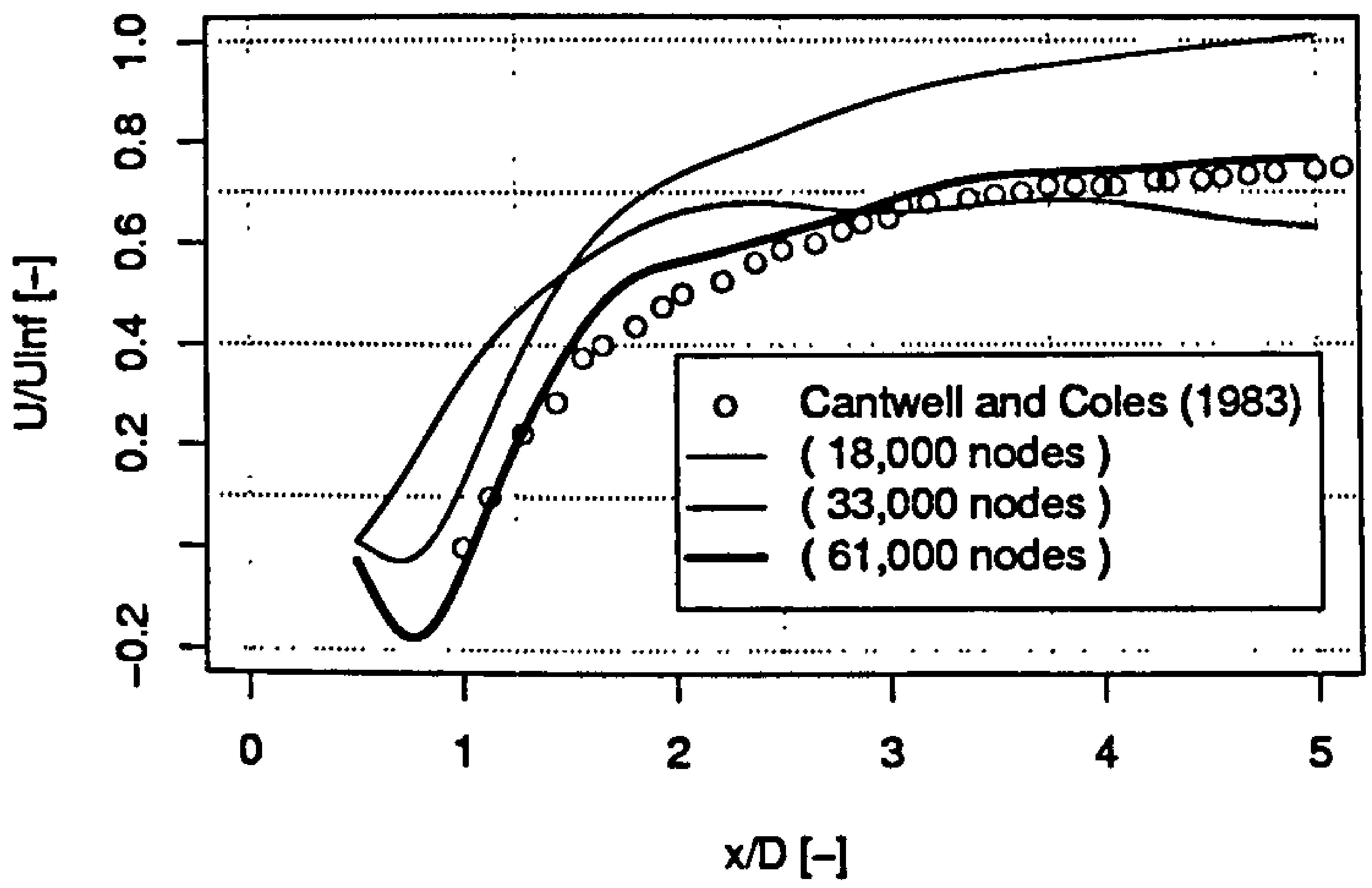

Figure 4.9: Time integrated normalised velocity along streamwise axis at $\frac{y}{D} = 0$, for simulations with conventional mesh and the subgrid length scale $\Delta = \sqrt{A_{tr}}$.

decay in energy for frequencies above 1 Hz. With increasing mesh resolution, more energy is maintained in the smaller scales above 1 Hz and better agreement is obtained with the theoretical energy spectrum for homogeneous turbulence. The slope of energy spectrum for homogeneous turbulence is based on the $-\frac{5}{3}$ constant in equation 2.34. The decay in energy at end of the spectrum at frequencies above 5 Hz suggests that the turbulence is not fully homogeneous. The sharp energy decay obtained with coarse mesh ($1.8 \cdot 10^4$ nodes) indicates that the mesh lacks sufficient mesh resolution to maintain an energy spectrum for higher frequencies above 2 Hz in accordance with the requirements for homogeneous turbulence.

The boundary layer development and the location of separation point as well the mechanism of separation are illustrated in the movie $\sqrt{A_{tr}} - 1.8 \cdot 10^4 - 1.avi$ to $\sqrt{2A_{tr}} - 6.1 \cdot 10^4 - 2.avi$ contained in the appendix. The reference names used in the text for the animation are explained in table 4.2. The separation point shows oscillatory behaviour and requires integration over time to obtain the average separation angle. The time integrated separation angles vary between 83° and 96° while it is determined by the experimental work of Cantwell & Coles [9] to be 77°.

4.1.2 Time integrated velocity field

The time integrated flow field is predicted with varying success. The average velocity in both downstream and transverse directions is in good agreement with experimental data [9] with a mesh containing $6.1 \cdot 10^4$ nodes. Here the dimensions of the recirculation region are also in good agreement, as well the average velocity field further downstream. The simulations using a mesh with $1.8 \cdot 10^4$ and $3.3 \cdot 10^4$ nodes respectively, in combination with the first equation for subgrid length scale

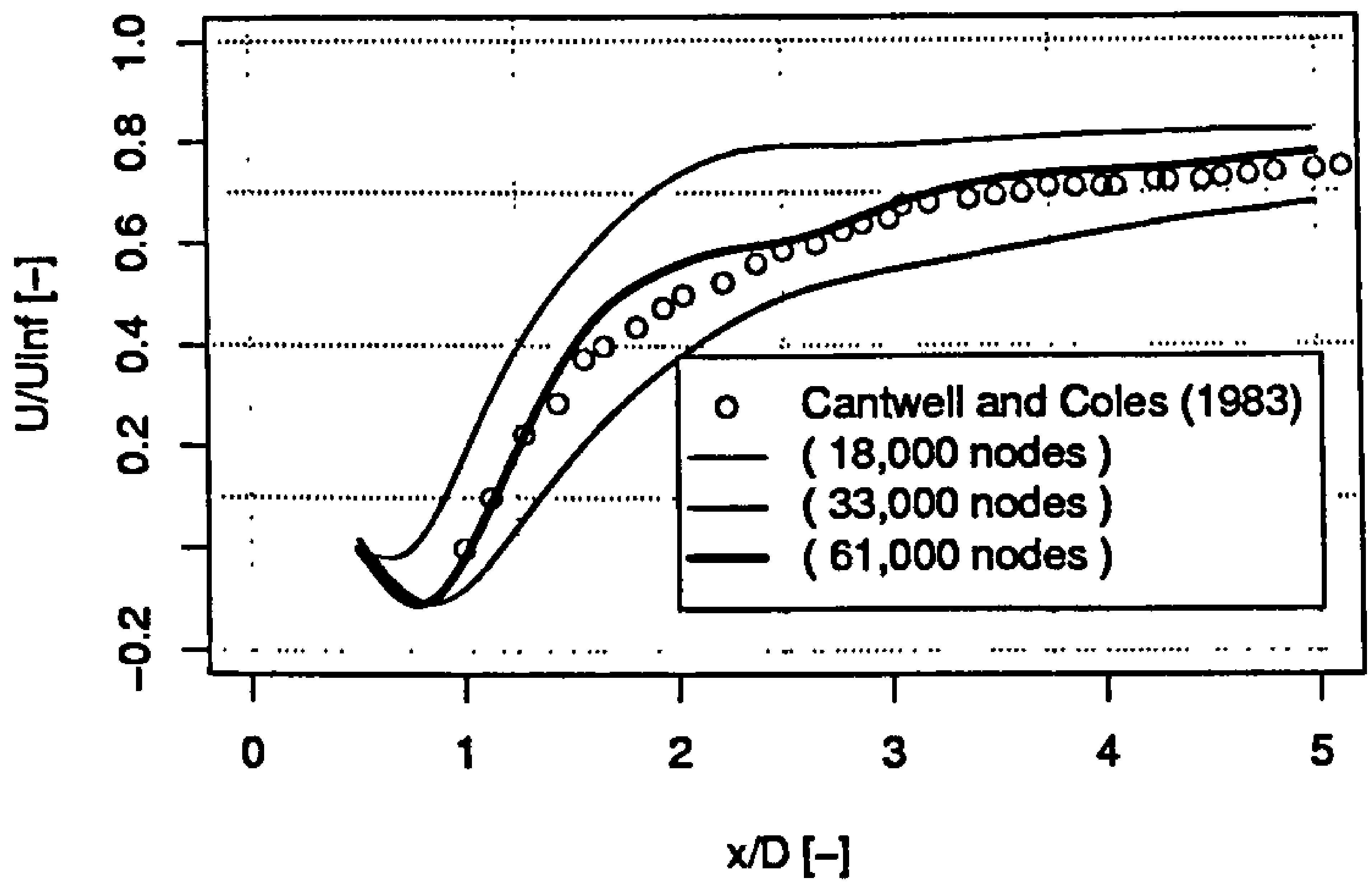

Figure 4.10: Time integrated normalised velocity along streamwise axis at $\frac{y}{D} = 0$, for simulations with conventional mesh and the subgrid length scale $\Delta = \sqrt{2A_{tr}}$.

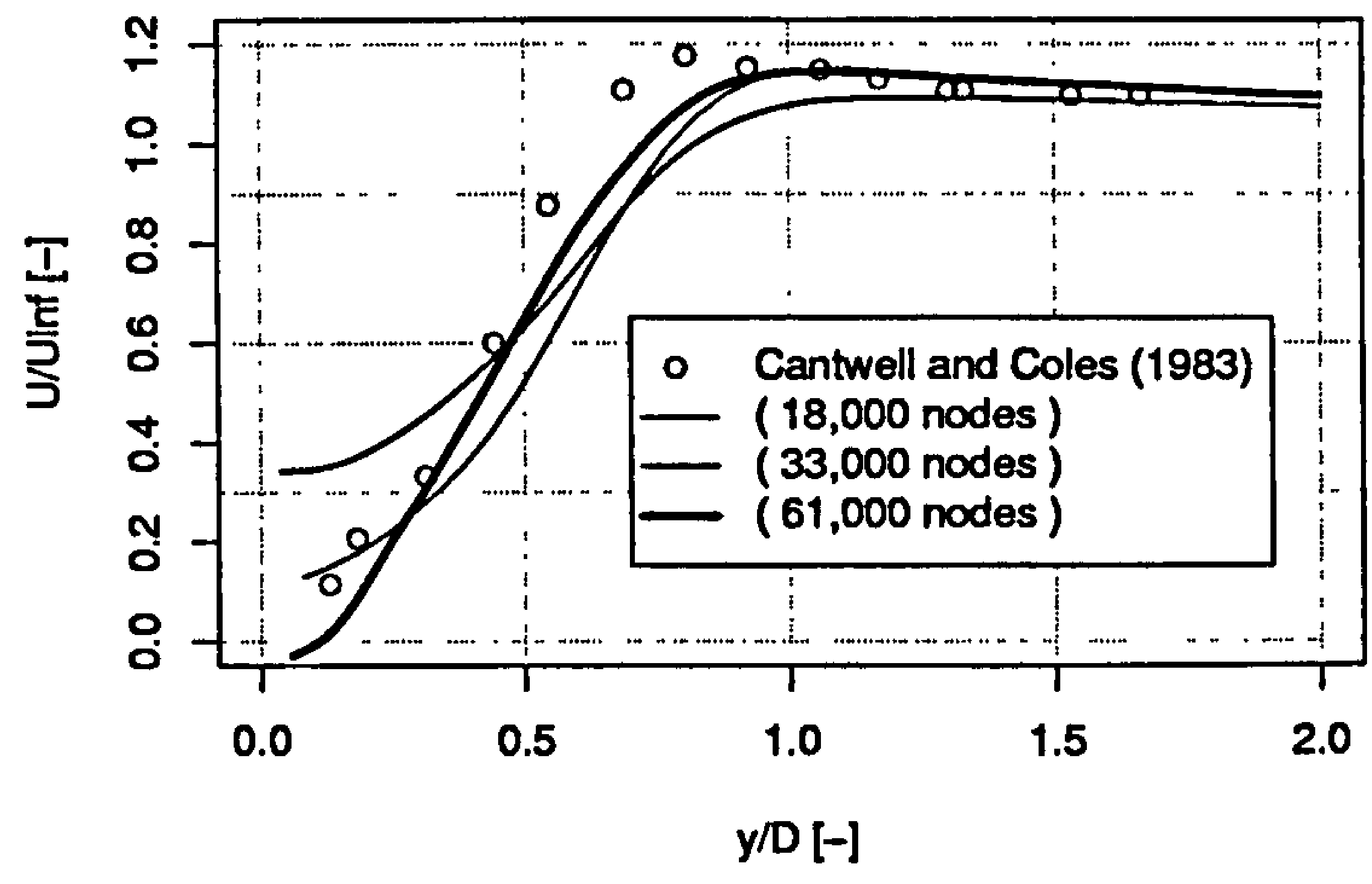

Figure 4.11: Time integrated normalised velocity along transverse axis at $\frac{x}{D} = 1$, for simulations with conventional mesh and the subgrid length scale $\Delta = \sqrt{A_{tr}}$.

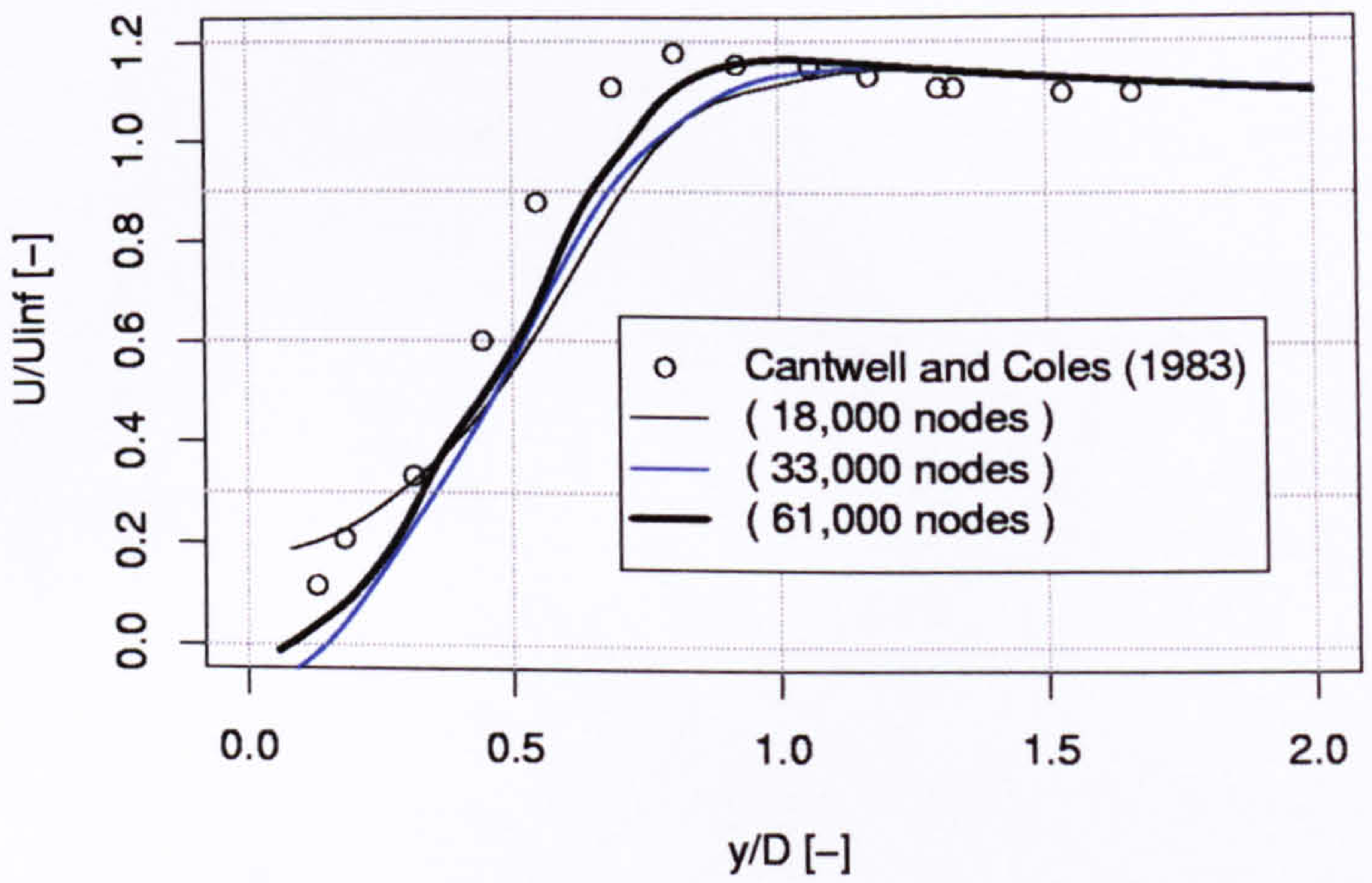

Figure 4.12: Time integrated normalised velocity along transverse axis at $\frac{x}{D} = 1$, for simulations with conventional mesh and the subgrid length scale $\Delta = \sqrt{2A_{tr}}$.

($\Delta = \sqrt{A_{tr}}$) under-predict the recirculation in the downstream region. The non-existence of the recirculation region in the second simulation ($3.3 \cdot 10^4$ nodes) is curious. It is surprising that better agreement is obtained with a mesh containing $1.8 \cdot 10^4$ nodes and that an increase in mesh resolution does not automatically lead to an improvement of the flow prediction.

In the simulations using the second definition for subgrid length scale ($\Delta = \sqrt{2A_{tr}}$) turbulent viscosity is twice as big as with the first definition. For high mesh resolution ($6.1 \cdot 10^4$ nodes) where turbulent viscosity is relatively small, the time integrated velocity field is nearly independent of the selected length scale definition. In the simulations where a coarser mesh is utilised, a significant effect of the chosen subgrid length scale is apparent. In the mesh containing $3.3 \cdot 10^4$ nodes the enlargement of the subgrid length scale leads to an increase of the recirculation region by 0.67 cylinder diameters.

The streamwise velocity component along the transverse axis does show the width of the wake region with a peak velocity at 0.8 cylinder diameters from the centreline. The peak velocity of 1.18 m/s is not predicted by any of the simulations. Similar flow profiles for the streamwise velocity component along the transverse axis are seen in the results of Breuer [8].

4.1.3 Turbulent shear stress along transverse axis

The simulations with conventional mesh show a clear lack of turbulent shear stress along the transverse axis. The results presented in figure 4.13 indicate that with increasing mesh resolution more turbulence is resolved. By increasing turbulent viscosity, i.e. the second definition for subgrid length scale ($\Delta = \sqrt{2A_{tr}}$) being

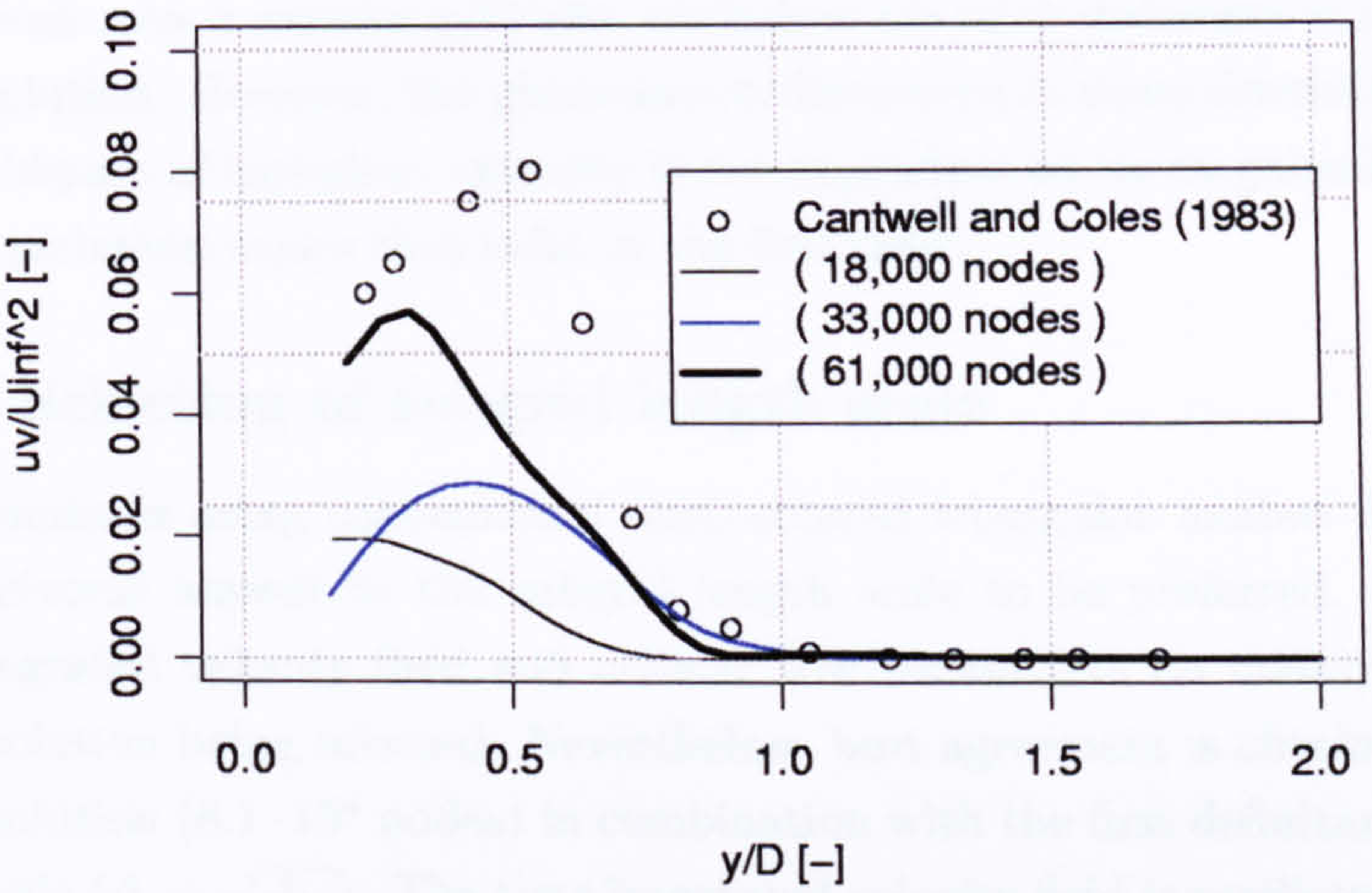

Figure 4.13: Time integrated normalised turbulent shear stress due to turbulence along transverse axis at $\frac{x}{D} = 1$, for simulations with conventional mesh and the subgrid length scale $\Delta = \sqrt{A_{tr}}$.

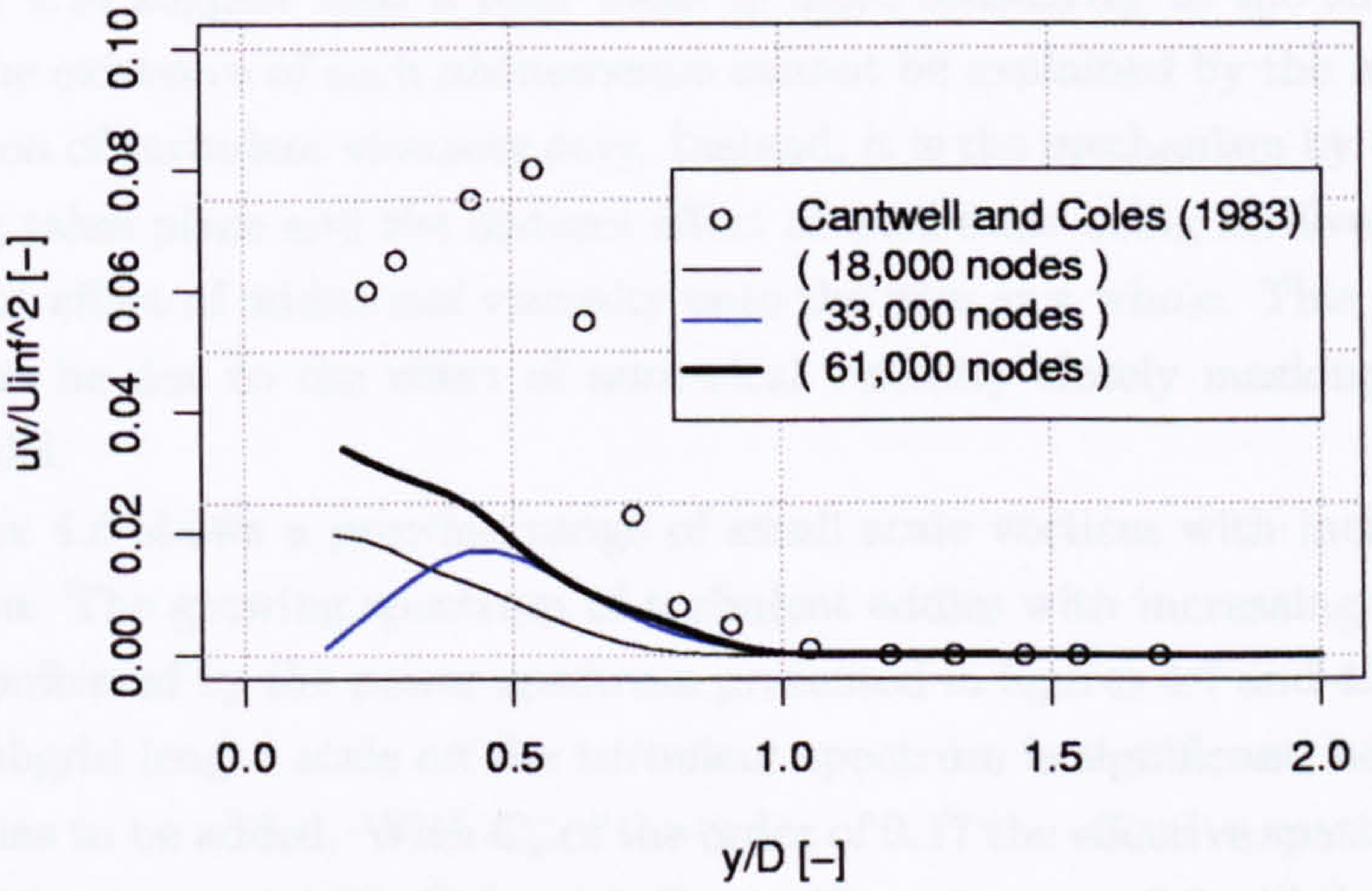

Figure 4.14: Time integrated normalised turbulent shear stress due to turbulence along transverse axis at $\frac{x}{D} = 1$, for simulations with conventional mesh and the subgrid length scale $\Delta = \sqrt{2A_{tr}}$.

selected, turbulence is suppressed as shown in figure 4.13 and 4.14. From the definition of the LES method described in section 3.2 and used here, it is known that turbulent viscosity is proportional to $(C_s\Delta)^2$. However, the effect of turbulent viscosity to the turbulent shear stress decreases with coarser mesh resolution. Since a finer mesh uses a smaller grid size, turbulent viscosity decreases with increasing mesh resolution. However, the phenomenon discovered in these simulations indicate that the impact of turbulent viscosity is not dependent on its magnitude but on the range of turbulent scales that exist in the flow field.

4.1.4 Selection of subgrid length scale

The simulations using conventional unstructured triangular meshes does not give an unequivocal answer to the subgrid length scale to be preferred. Instead, the time integrated velocity field and critical flow parameters do mainly rely on the mesh resolution being selected. Nevertheless, best agreement is obtained with high mesh resolution ($6.1 \cdot 10^4$ nodes) in combination with the first definition for subgrid length scale ($\Delta = \sqrt{A_{tr}}$). The time integrated velocity field is predicted with minor deviation while turbulent shear stress agrees very closely with experimental data.

The predictions for time integrated velocity profiles do tend to be insensitive to the subgrid length scale used with both high mesh resolution ($6.1 \cdot 10^4$ nodes) and coarse mesh resolution ($1.8 \cdot 10^4$ nodes). In contrast, a strong sensitivity to the subgrid length scale is shown for a mesh containing $3.3 \cdot 10^4$ nodes.

It is already stated that turbulent viscosity is proportional to mesh resolution and therefore the magnitude of turbulent viscosity decreases with increasing mesh resolution. However, the results presented suggest that the impact of turbulent viscosity on the flow prediction is not proportional to the mesh resolution. Figures 4.13 and 4.14 suggest that a finer mesh is more sensitivity to the subgrid length scale. The existence of such phenomenon cannot be explained by the mathematical description of turbulent viscosity only. Instead, it is the mechanism by which vortex shedding takes place and the distinct effect of each scale being involved, leading to a different effect of additional viscosity onto the flow as a whole. This phenomenon could also be due to the effect of numerical viscosity closely masking that of the LES model.

Figure 4.6 shows a growing range of small scale vortices with increasing mesh resolution. The growing spectrum of turbulent eddies with increasing mesh resolution is confirmed by the power spectrum presented in figures 4.7 and 4.8. The effect of the subgrid length scale on the turbulent spectrum is significant; nevertheless, a remark has to be added. With C_s of the order of 0.17 the effective spatial filter is determined by the mesh [46]. Only with C_s significantly above 0.5 will the length scale $l_s = C_s\Delta$ determine the width of the power spectrum. With other words, the cut-off frequency in the power spectrum is determined by the mesh resolution and not by the selected subgrid length scale. As a consequence, turbulent eddies in the flow field are only suppressed by the turbulence model but not eliminated. The impact

	Re_{LES}
Cantwell and Coles (1983)	$1.4 \cdot 10^5$
$1.8 \cdot 10^4$	$5.4 \cdot 10^3$
$3.3 \cdot 10^4$	$1.0 \cdot 10^4$
$6.1 \cdot 10^4$	$2.2 \cdot 10^4$

Table 4.4: $Re_{LES} = \left(\frac{\eta}{C_s\Delta}\right)^{\frac{4}{3}} Re$, based on the smallest element in the numerical domain.

of the chosen subgrid length scale on the resulting power spectrum is not uniform over the whole frequency spectrum. Instead, each spectrum bends in its own way under the effects of additional turbulent viscosity. Nevertheless, with increasing mesh resolution it is a priori the smaller scales that are dominated by the turbulent viscosity. Larger scales are affected by the turbulent viscosity in an indirect manner via an intermediate range of resolved scales. The sensitivity of the time integrated flow field to the turbulent viscosity depends on the intermediate range of turbulent scales and their sensitivity to the turbulent viscosity. For this reason, the impact of turbulent viscosity can grow with increasing mesh resolution. Nevertheless, this does not mean that the flow field is represented better by a coarser mesh. Although some of the flow characteristics are predicted reasonable well with a coarse mesh ($1.8 \cdot 10^4$ nodes), it is very unlikely that the predicted flow field is in accordance with the physical behaviour of the flow. The transition in the shear layer from laminar to turbulent flow conditions is unlikely to occur when small disturbances cannot develop in this region due to limited mesh resolution. Another problem of the LES technique is the effective Reynolds number of the LES-generated turbulence. With the technique the dissipation length η is replaced with $l_s = C_s\Delta$. Thus:

$$Re_{LES} = \left(\frac{\eta}{l_s}\right)^{\frac{4}{3}} Re \tag{4.1}$$

As a consequence Re_{LES} can be significantly smaller than the Reynolds number of the turbulence to be modelled. Therefore one must be careful that Re_{LES} remains sufficiently large otherwise the Reynolds number similarity might not be fulfilled and the results could not be considered representative for a large Reynolds flow [45]. The turbulent viscosity applied in the coarse mesh ($1.8 \cdot 10^4$ nodes) varies in time and space but can exceed the dynamic viscosity by a factor of 10. The reduction in Reynolds numbers due to the addition of a turbulence model is shown in table 4.4. The LES generated Reynolds number is based on the smallest element in the numerical domain and leads to an 80% reduction of the original Reynolds number.

The selection of a subgrid length scale should be based on computational results which represent the physical flow features best. It is undeniable that the time integrated velocity field as well critical flow parameters and turbulent shear stress is best predicted with the highest mesh resolution ($6.1 \cdot 10^4$ nodes) used in this investigation. The results obtained with coarser mesh do not only show a stronger

	$\overline{C_D}$	S_t	Θ_s	L_r	Micro scale $[m]$
Cantwell and Coles (1983)	1.24	0.179	77	0.5	$\eta = 1.38 \cdot 10^{-4}$
$6.1 \cdot 10^4 \mid \Delta = \sqrt{A_{tr}}$	-	0.20	86.0	0.53	$3.73 \cdot 10^{-3}$
DGA variables $C_m = 1 \mid C_{str} = 1$					
$2.8 \cdot 10^4 \mid$ superbee	1.71	0.18	96	0.15	$2.91 \cdot 10^{-3}$
$4.3 \cdot 10^4 \mid$ superbee	1.73	0.16	89	0.25	$2.54 \cdot 10^{-3}$
$4.5 \cdot 10^4 \mid$ superbee	1.59	0.15	95	0.48	$1.46 \cdot 10^{-3}$
DGA variables $C_m = 1 \mid C_{str} = 1.5$					
$3.5 \cdot 10^4 \mid$ superbee	1.64	0.19	81	0.47	$2.51 \cdot 10^{-3}$
$5.0 \cdot 10^4 \mid$ superbee	1.70	0.20	85	0.60	$2.51 \cdot 10^{-3}$
DGA variables $C_m = 1 \mid C_{str} = 2$					
$1.4 \cdot 10^4 \mid$ superbee	1.72	0.20	81	0.36	$2.54 \cdot 10^{-3}$
$2.8 \cdot 10^4 \mid$ superbee	1.63	0.16	85	0.36	$2.52 \cdot 10^{-3}$
$2.4 \cdot 10^4 \mid$ minmod	1.40	0.13	89	0.67	$2.91 \cdot 10^{-3}$

Table 4.5: Time integrated flow parameters, drag coefficient $\overline{C_D}$, Strouhal number S_t, separation angle Θ_s, recirculation length L_r and micro scale, for simulations using the DGA algorithm plus the simulation using conventional mesh $6.1 \cdot 10^4$ and length scale $\Delta = \sqrt{A_{tr}}$.

deviation from the experimental data of Cantwell & Coles [9], but are unable to maintain a turbulent energy spectrum for higher frequencies due to insufficient mesh resolution.

The results obtained with the final mesh ($6.1 \cdot 10^4$ nodes) present a time integrated velocity field independent of the selected subgrid length scale, while differences between the two simulations are present for the magnitude of turbulent shear stress, Strouhal number and separation angle and best agreement is obtained with the first subgrid length scale ($\Delta = \sqrt{A_{tr}}$). It is the turbulent shear stress profile which indicates that with the mesh resolution used in this work, turbulence is strongly suppressed with the second subgrid length scale ($\Delta = \sqrt{2A_{tr}}$). With the use of the first subgrid length scale ($\Delta = \sqrt{A_{tr}}$) a more realistic turbulent shear stress profile and separation angle Θ_s is predicted which hold better agreement. For this reason, the first subgrid length scale will be used throughout the rest of the work. The first subgrid length scale reads:

$$\Delta = \sqrt{A_{tr}} \tag{4.2}$$

4.2 Modelling vortex shedding behind a cylinder with Dynamic Grid Adaptation

The conventional meshes used in the previous section have used pre-selected levels of resolution in the regions around the cylinder. However, it is the narrow region around the cylinder where a complex flow field is expected to develop and the pre-

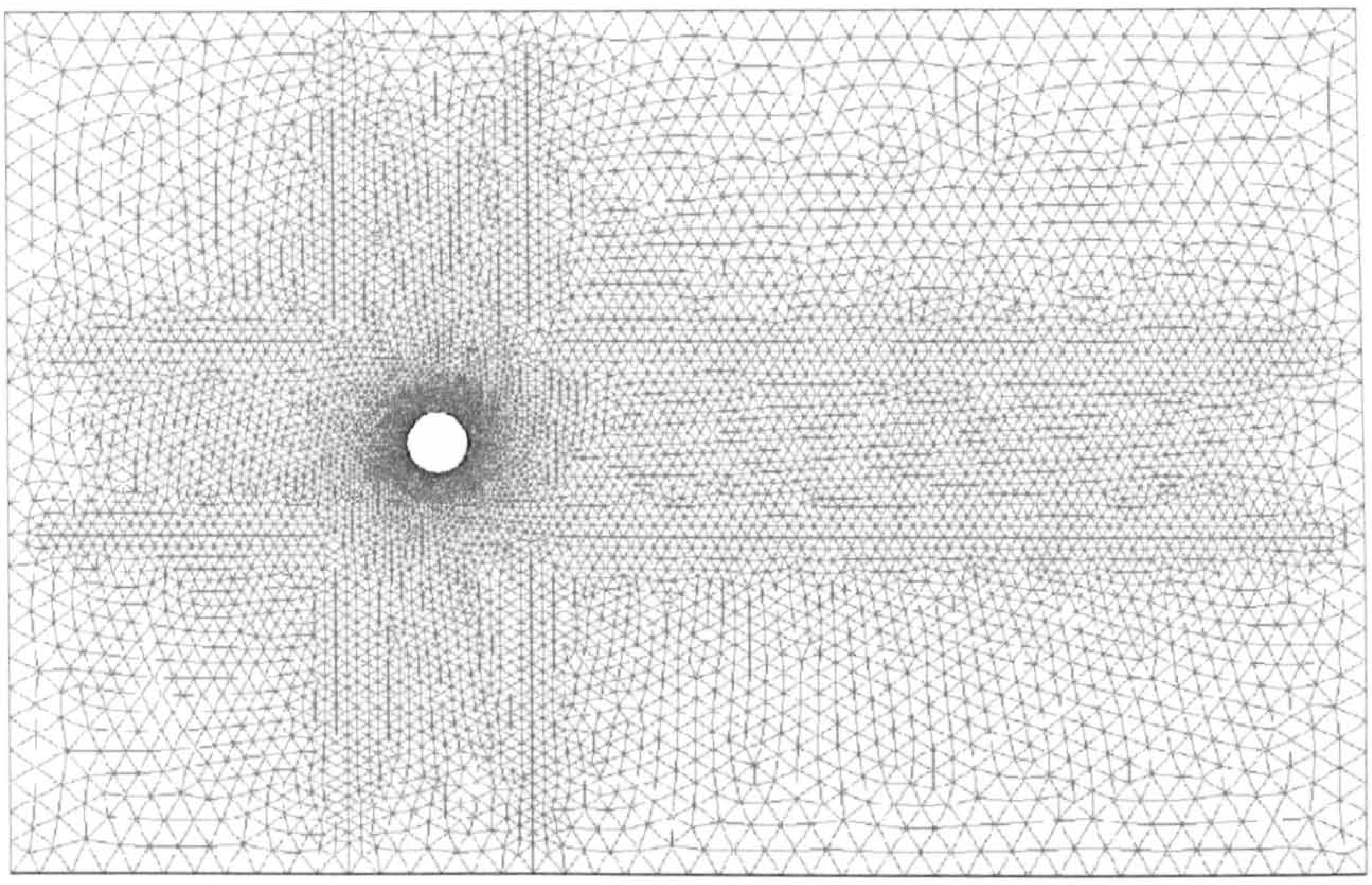

(a) Initial mesh containing 7500 nodes

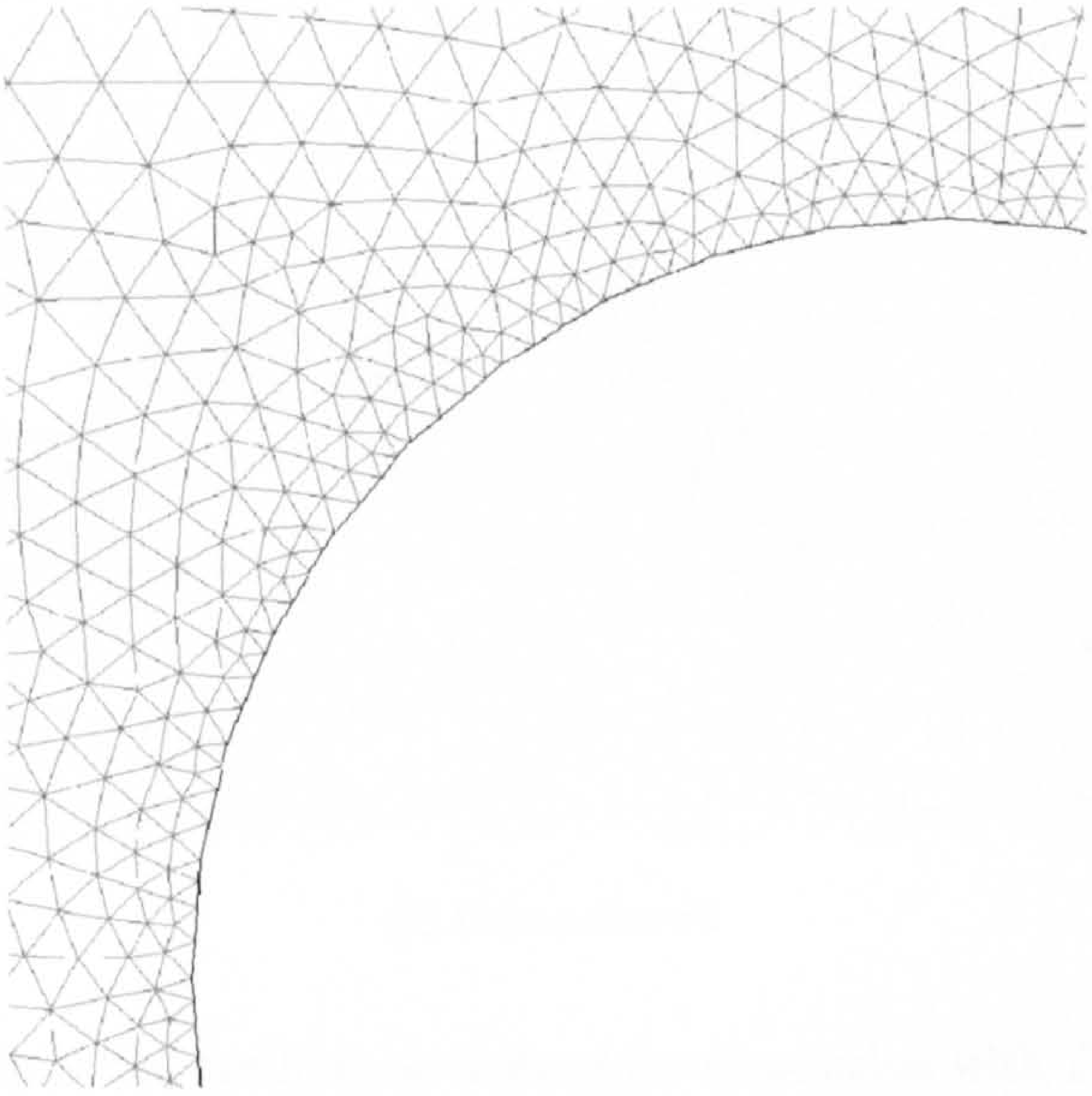

(b) Initial mesh near the wall

Figure 4.15: Mesh containing $7.5 \cdot 10^3$ nodes and created by a conventional mesh generator. The mesh holds a moderate resolution in the vicinity of the wall and the region further downstream while the area near the outer boundaries is kept coarse.

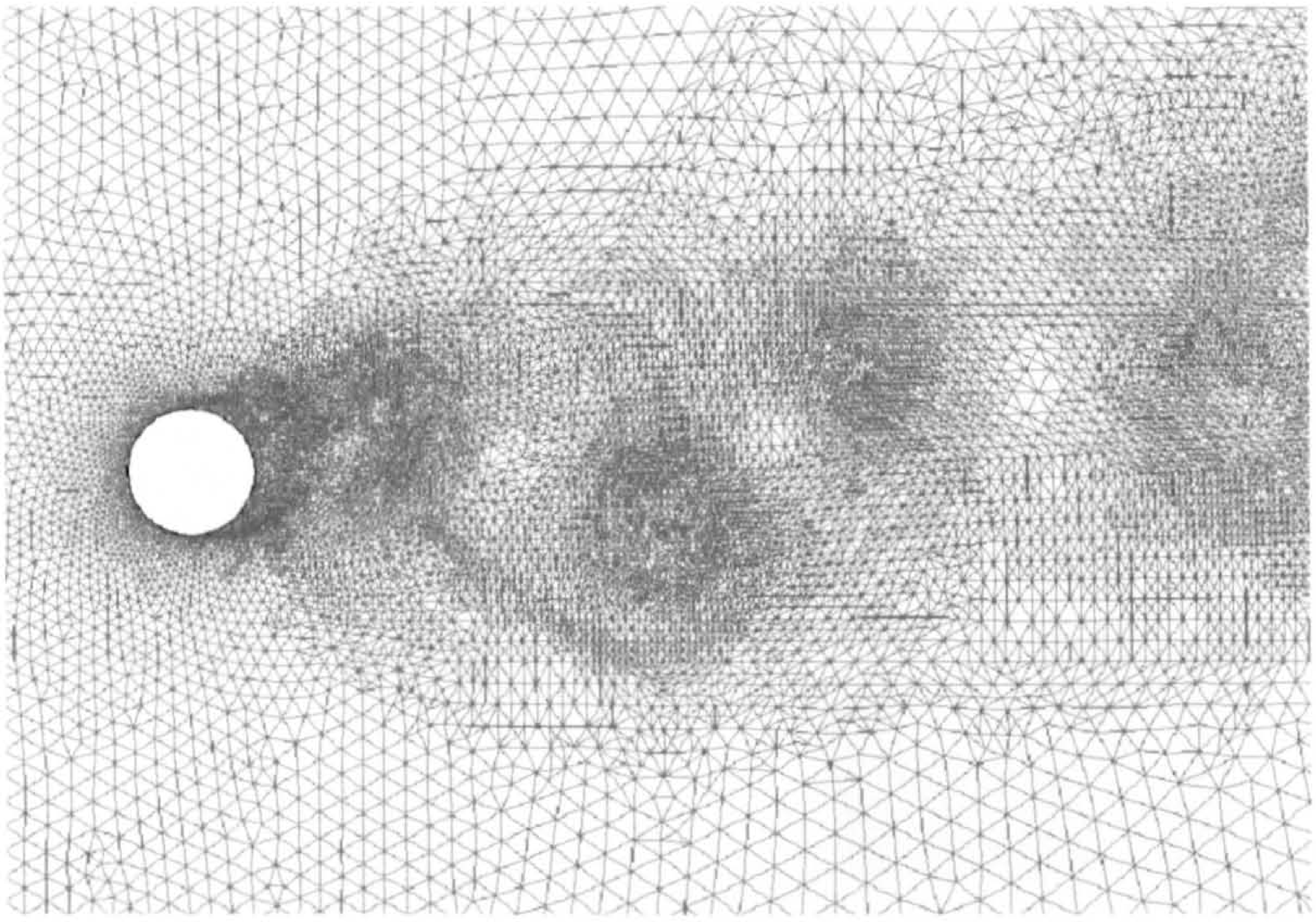

(a) Cm=1 Cstr=1

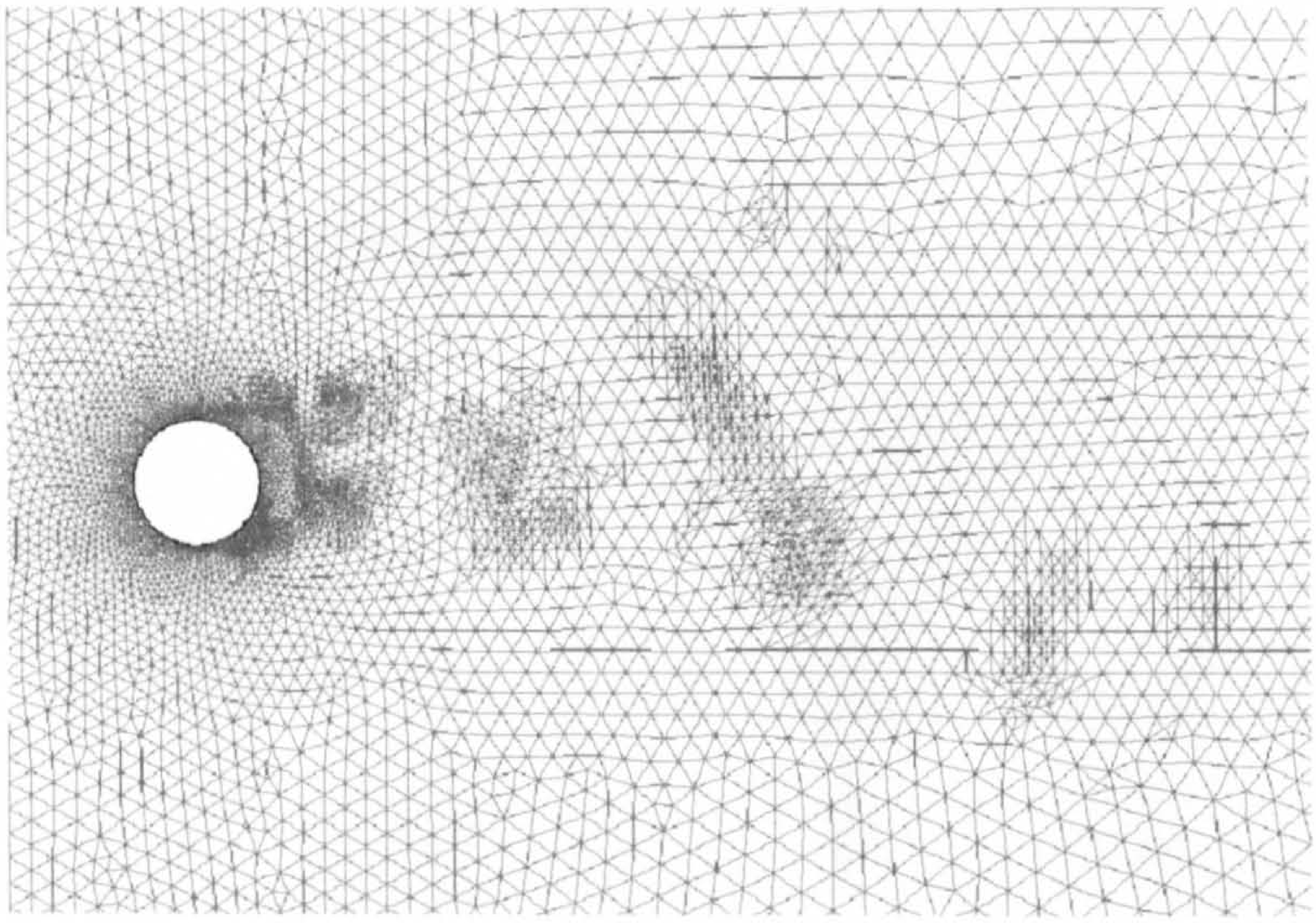

(b) Cm=1 Cstr=2

Figure 4.16: Plot of the mesh at an instant for simulation with $C_m = 1$, $C_{str} = 1$ and $2.8 \cdot 10^4$nodes and the simulation with $C_m = 1$, $C_{str} = 2$ and $1.4 \cdot 10^4$ nodes. With $C_m = 1$ and $C_{str} = 1$ cell size and strain rate are equally important leading to a smooth flow dependent mesh refinement. With $C_m = 1$ and $C_{str} = 2$ weight is given to strain rate leading to a sharper mesh refinement. The structures in the mesh reflect the coherent flow structures in the flow field.

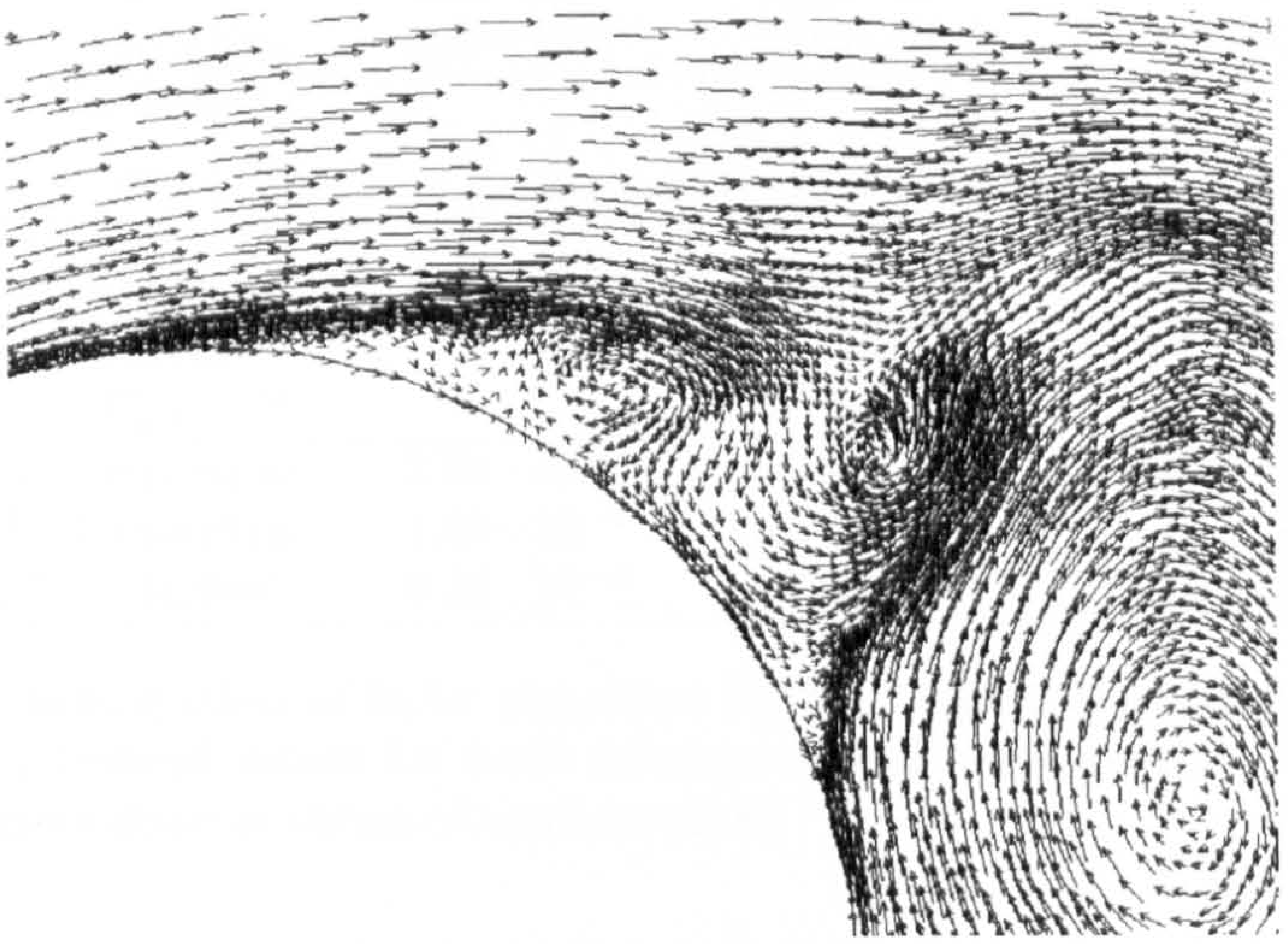

(a) Cm=1 Cstr=1

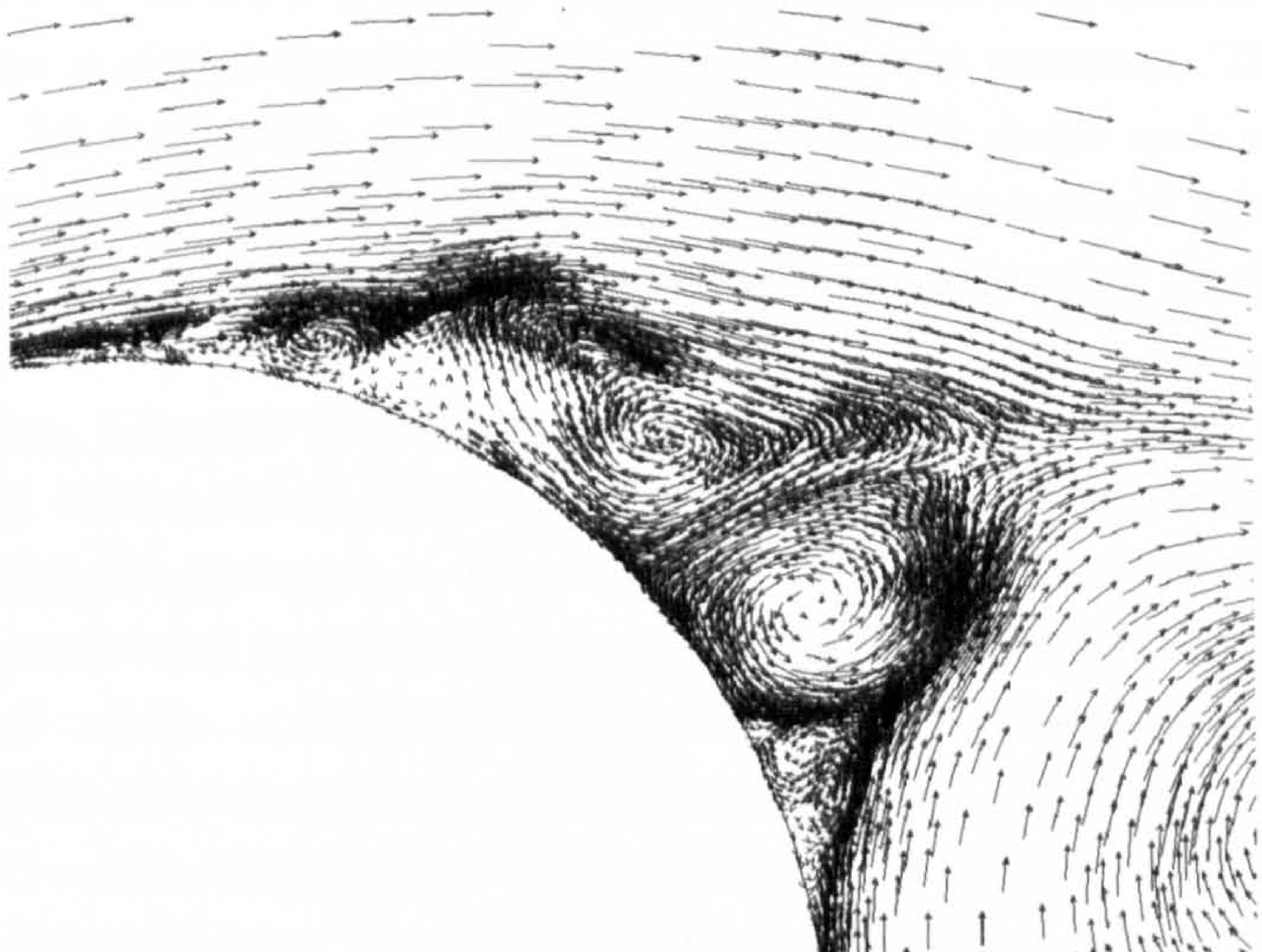

(b) Cm=1 Cstr=2

Figure 4.17: Vector plot of the flow at an instant in the vicinity of the wall for simulation with $C_m = 1$, $C_{str} = 1$ and $4.5 \cdot 10^4$nodes and the simulation with $C_m = 1$, $C_{str} = 2$ and $2.8 \cdot 10^4$ nodes. With $C_m = 1$ and $C_{str} = 1$ cell size and strain rate are equally important leading to a smooth flow dependent mesh refinement. With $C_m = 1$ and $C_{str} = 2$ weight is given to strain rate leading to a sharper mesh refinement.

	Refinement e_i	Coarsening e_i	Micro scale $[m]$
DGA variables $C_m = 1 \mid C_{str} = 1$			
$2.8 \cdot 10^4 \mid$ superbee	$2.00 \cdot 10^{-3}$	$1.00 \cdot 10^{-3}$	$2.0 \cdot 10^{-3}$
$4.3 \cdot 10^4 \mid$ superbee	$1.00 \cdot 10^{-3}$	$5.00 \cdot 10^{-4}$	$2.0 \cdot 10^{-3}$
$4.5 \cdot 10^4 \mid$ superbee	$1.00 \cdot 10^{-3}$	$5.00 \cdot 10^{-4}$	$1.0 \cdot 10^{-3}$
DGA variables $C_m = 1 \mid C_{str} = 1.5$			
$3.5 \cdot 10^4 \mid$ superbee	$2.50 \cdot 10^{-3}$	$1.25 \cdot 10^{-3}$	$2.0 \cdot 10^{-3}$
$5.0 \cdot 10^4 \mid$ superbee	$1.25 \cdot 10^{-3}$	$6.25 \cdot 10^{-4}$	$2.0 \cdot 10^{-3}$
DGA variables $C_m = 1 \mid C_{str} = 2$			
$1.4 \cdot 10^4 \mid$ superbee	$3.20 \cdot 10^{-2}$	$1.60 \cdot 10^{-2}$	$2.0 \cdot 10^{-3}$
$2.8 \cdot 10^4 \mid$ superbee	$7.00 \cdot 10^{-3}$	$3.50 \cdot 10^{-3}$	$2.0 \cdot 10^{-3}$
$2.4 \cdot 10^4 \mid$ minmod	$3.50 \cdot 10^{-3}$	$1.75 \cdot 10^{-3}$	$2.0 \cdot 10^{-3}$

Table 4.6: Configuration of DGA algorithm for the 2 dimensional simulations, including the threshold values for mesh refinement and coarsening as well the minimum mesh resolution in terms of a micro scale.

selected mesh is unlikely to be the optimum and therefore it is probable that many nodes will be used inefficiently. The design of a conventional mesh requires a good understanding of the fluid dynamics of the system being investigated, particularly where the flow is of high complexity as in many industrial processes. The reason for the use of a DGA algorithm is twofold. Not only is each single node examined for its contribution to flow prediction but, additionally solution-based grid refinement will minimize the need to put significant effort into estimating the flow pattern beforehand.

Despite the potential of DGA to use computational power more efficiently, a reliable mesh refinement thus rely on a proper error estimation which reflects the need for additional grid points. However, it is very surprising that there exists a vast literature devoted to the development of refinement methods for adaptive grid strategies but almost nothing has been done to develop refinement variables for determining the error magnitude of numerical solutions. However, the success of adaptive grid strategies depend to a large extent on a reliable refinement variable and on the determination of acceptable error bounds with which the estimated errors are compared.

In this work a refinement variable is proposed which is a modification to the equation of turbulent viscosity and is shown in equation 3.19. By varying the importance or weight of either the cell size Δ or the strain rate $|\overline{S}|$ another refinement behaviour can be established. These two terms in the equation are controlled by the two variables C_m and C_{str} and allow a user-defined refinement behaviour. The key interest in the investigation is to obtain an insight into the location of the flow regions that dominate the flow, as well the range of turbulent scales necessary for a reliable CFD prediction. The numerical requirements for modelling separated flow reflect the physical flow complexities, i.e. the regions where mesh refinement is required and the preferable DGA configuration reflect the physical flow mechanisms.

	Reference name / Animation name
DGA variables $C_m = 1, C_{str} = 1$	
$2.8 \cdot 10^4 \mid$ superbee	$C_m = 1 - C_{str} = 1 - 2.8 \cdot 10^4 - 1.avi$ E:\DGA\Cm=1-Cstr=1-nodes=28e3_PIC01.avi $C_m = 1 - C_{str} = 1 - 2.8 \cdot 10^4 - 2.avi$ E:\DGA\Cm=1-Cstr=1-nodes=28e3_PIC02.avi
$4.3 \cdot 10^4 \mid$ superbee	$C_m = 1 - C_{str} = 1 - 4.3 \cdot 10^4 - 1.avi$ E:\DGA\Cm=1-Cstr=1-nodes=43e3_PIC01.avi $C_m = 1 - C_{str} = 1 - 4.3 \cdot 10^4 - 2.avi$ E:\DGA\Cm=1-Cstr=1-nodes=43e3_PIC02.avi
$4.5 \cdot 10^4 \mid$ superbee	$C_m = 1 - C_{str} = 1 - 4.5 \cdot 10^4 - 1.avi$ E:\DGA\Cm=1-Cstr=1-nodes=45e3_PIC01.avi $C_m = 1 - C_{str} = 1 - 4.5 \cdot 10^4 - 2.avi$ E:\DGA\Cm=1-Cstr=1-nodes=45e3_PIC02.avi
DGA variables $C_m = 1, C_{str} = 1.5$	
$3.5 \cdot 10^4 \mid$ superbee	$C_m = 1 - C_{str} = 1.5 - 3.5 \cdot 10^4 - 1.avi$ E:\DGA\Cm=1-Cstr=15-nodes=35e3_PIC01.avi $C_m = 1 - C_{str} = 1.5 - 3.5 \cdot 10^4 - 2.avi$ E:\DGA\Cm=1-Cstr=15-nodes=35e3_PIC02.avi
$5.0 \cdot 10^4 \mid$ superbee	$C_m = 1 - C_{str} = 1.5 - 5.0 \cdot 10^4 - 1.avi$ E:\DGA\Cm=1-Cstr=15-nodes=50e3_PIC01.avi $C_m = 1 - C_{str} = 1.5 - 5.0 \cdot 10^4 - 2.avi$ E:\DGA\Cm=1-Cstr=15-nodes=50e3_PIC02.avi
DGA variables $C_m = 1, C_{str} = 2$	
$1.4 \cdot 10^4 \mid$ superbee	$C_m = 1 - C_{str} = 2 - 1.4 \cdot 10^4 - 1.avi$ E:\DGA\Cm=1-Cstr=2-nodes=14e3_PIC01.avi $C_m = 1 - C_{str} = 2 - 1.4 \cdot 10^4 - 2.avi$ E:\DGA\Cm=1-Cstr=2-nodes=14e3_PIC02.avi
$2.8 \cdot 10^4 \mid$ superbee	$C_m = 1 - C_{str} = 2 - 2.8 \cdot 10^4 - 1.avi$ E:\DGA\Cm=1-Cstr=2-nodes=28e3_PIC01.avi $C_m = 1 - C_{str} = 2 - 2.8 \cdot 10^4 - 2.avi$ E:\DGA\Cm=1-Cstr=2-nodes=28e3_PIC02.avi
$2.4 \cdot 10^4 \mid$ minmod	$C_m = 1 - C_{str} = 2 - 2.4 \cdot 10^4 - 1.avi$ E:\DGA\Cm=1-Cstr=2-nodes=24e3_PIC01.avi $C_m = 1 - C_{str} = 2 - 2.4 \cdot 10^4 - 2.avi$ E:\DGA\Cm=1-Cstr=2-nodes=24e3_PIC02.avi

Table 4.7: The animation file name and the reference name used in the thesis for the animations obtained from simulations with DGA algorithm. The first animation indicated by a 1 gives a view of the general flow field, while the animation indicated by a 2 gives a detailed view of the flow in the vicinity of the wall near the point of separation.

The purpose of the DGA algorithm is to generate a mesh under its own evolutionary flow tendencies. Therefore, a relatively coarse mesh is utilised at the start of the simulation as shown in figure 4.15. Here, this initial mesh contains $7.5 \cdot 10^3$ nodes and uses the same dimensions as the conventional mesh described in figure 4.1.

The introduction of the two variables C_m and C_{str} in the refinement variable gives user control of the refinement process. A view of the mesh towards the end of the simulation is shown in figure 4.16 the simulation is carried out with the DGA variables C_m and C_{str} both set to 1. The use of these constants is clearly shown in figure 4.17. In the first picture a smooth mesh refinement has taken place in the shear layers and along the cylinder, while in the latter the refinement is sharp and narrow and more focussed on areas that maintain a high strain rate. Therefore, despite the limited number of nodes in the simulation with a dominance of the strain rate in the refinement variable ($C_m = 1$, $C_{str} = 2$) and a mesh containing $1.4 \cdot 10^4$ nodes, its smallest element of size $2.54 \cdot 10^{-3}$ [m] is still smaller then the equivalent element of size $2.91 \cdot 10^{-3}$ [m] in the simulation where equal weight is given to cell size and strain rate ($C_m = 1$, $C_{str} = 1$) and a mesh containing $2.8 \cdot 10^4$ nodes. This is shown in table 4.5. The effect of the refinement variables is seen in particularly well in the vicinity of the wall before the point of separation. In this region, strong velocity gradients are maintained and, as a consequence, significant difference in mesh resolution is apparent. The difference in flow prediction between that of figure 4.17 (a) and (b) is primarily due to mesh refinement and confirms the complexity of the physical processes in which certain flow regions and vortex scales in the flow field are over-proportionately important. This means that the determination of a proper refinement variable cannot be decoupled from the physics that is under investigation. With other words, flow prediction and mesh resolution are unequivocally connected and cannot be treated in isolation.

The results presented in this section have been all obtained using LES simulations together with the DGA algorithm. The majority of the simulations have been carried out with Roe's superbee flux limiter. To investigate the effect of the TVD flux limiter on the flow prediction, a study has been carried out in which the minmod flux limiter is used. The threshold values for mesh refinement and coarsening, as well the maximum mesh resolution to overcome excessive mesh refinement, are presented in table 4.6 for all simulations.

4.2.1 Velocity patterns

The simulations carried out with a DGA algorithm present a vortex street as shown in appendix, movie $C_m = 1 - C_{str} = 1 - 2.8 \cdot 10^4 - 1.avi$ to $C_m = 1 - C_{str} = 2 - 2.4 \cdot 10^4 - 2.avi$. The reference names used in the text for the flow animations are explained in table 4.7. A wide variety of turbulent eddies is apparent in the vortex street as well secondary eddies exist in the recirculation region as observed experimentally by Bouard & Coutanceau [7]. Due to mesh refinement, mesh resolu-

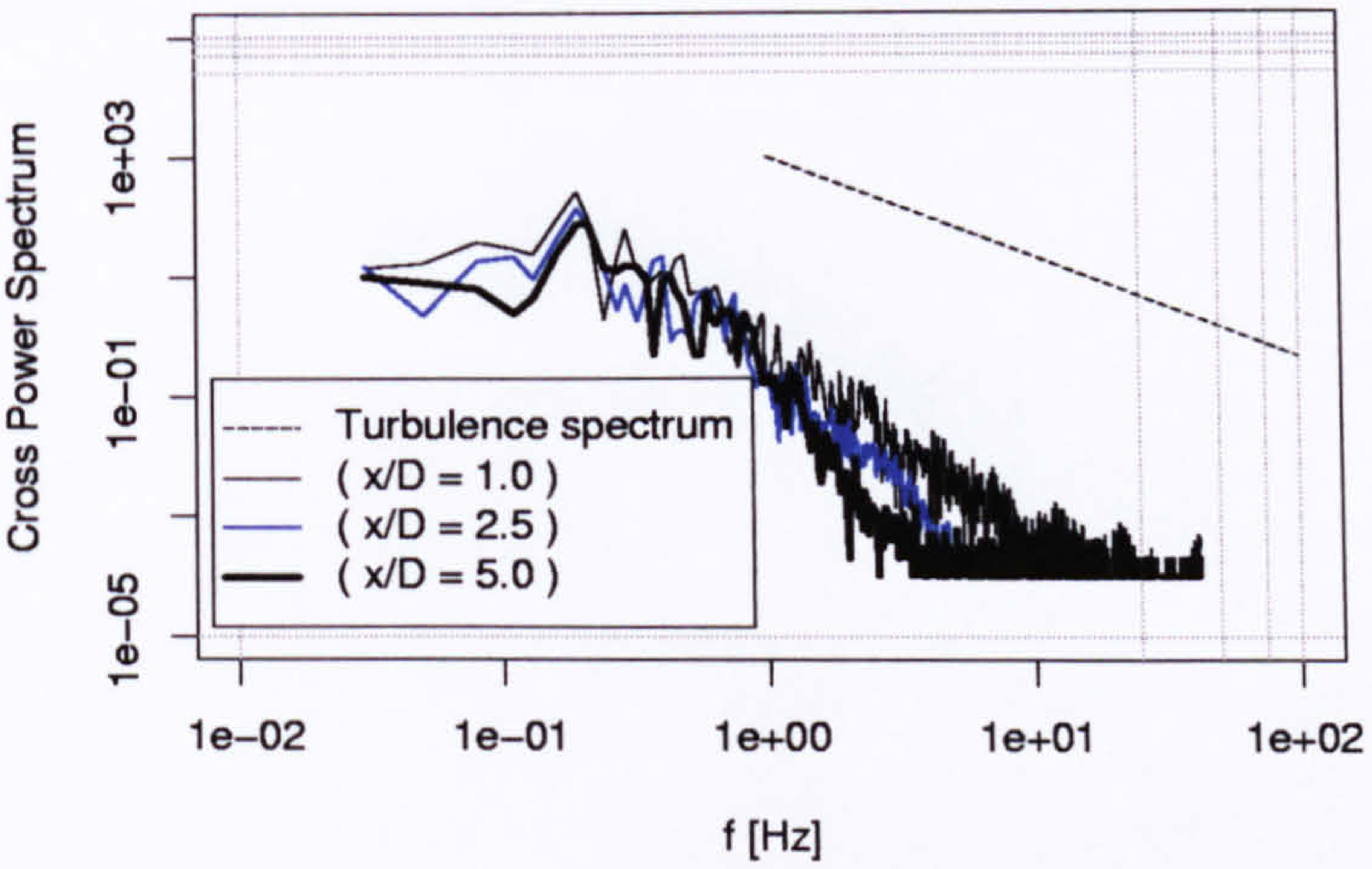

Figure 4.18: Cross power spectrum of velocity components u and v at $\frac{y}{D} = 0$, for simulation $C_m = 1$, $C_{str} = 1$, $2.8 \cdot 10^4$nodes and the superbee TVD flux limiter. The power spectrum of homogeneous turbulence is described as $E = \alpha\varepsilon^{\frac{2}{3}} f^{-\frac{5}{3}}$ and presented as a straight line with a slope of $-\frac{5}{3}$; the magnitude of the theoretical spectrum is arbitrary. Best agreement in the higher frequency range is obtained in the region with the highest mesh resolution.

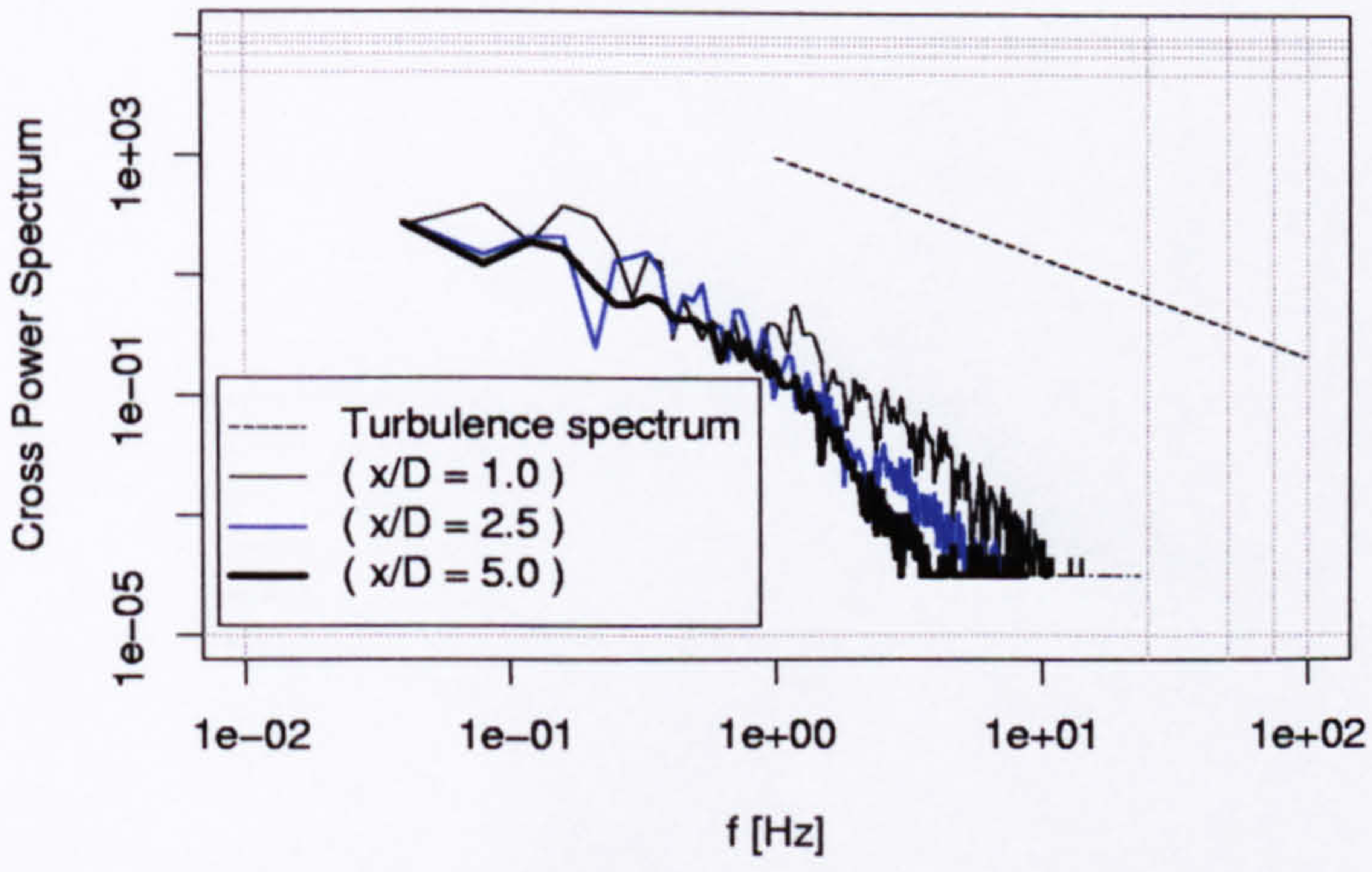

Figure 4.19: Cross power spectrum of velocity components u and v at $\frac{y}{D} = 0$, for simulation with $C_m = 1$, $C_{str} = 1$, $4.3 \cdot 10^4$ nodes and the superbee TVD flux limiter. The power spectrum of homogeneous turbulence is described as $E = \alpha\varepsilon^{\frac{2}{3}} f^{-\frac{5}{3}}$ and presented as a straight line with a slope of $-\frac{5}{3}$; the magnitude of the theoretical spectrum is arbitrary. Best agreement in the higher frequency range is obtained in the region with the highest mesh resolution.

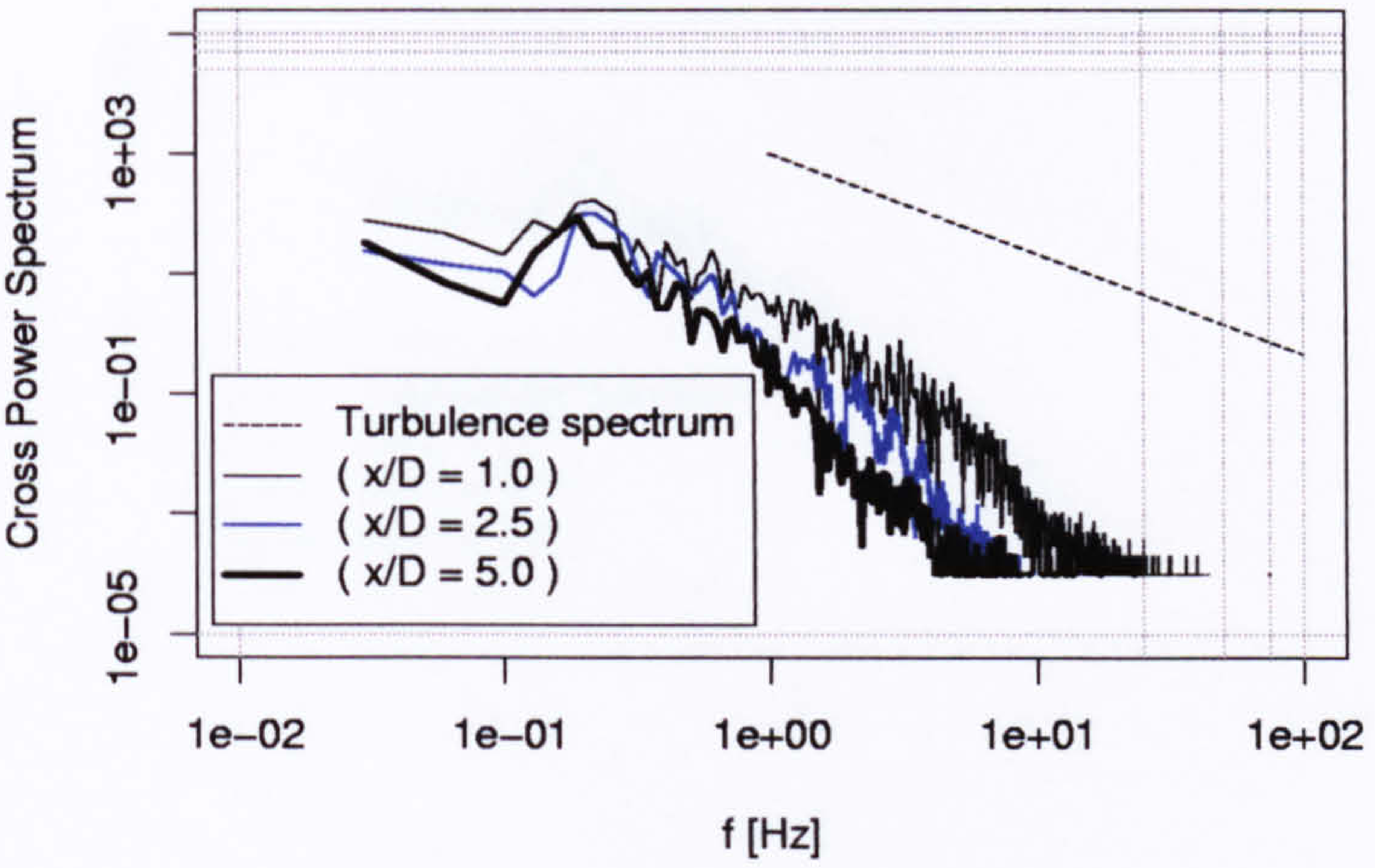

Figure 4.20: Cross power spectrum of velocity components u and v at $\frac{y}{D} = 0$, for simulation with $C_m = 1$, $C_{str} = 1$, $4.5 \cdot 10^4$nodes and the superbee TVD flux limiter. The power spectrum of homogeneous turbulence is described as $E = \alpha\varepsilon^{\frac{2}{3}} f^{-\frac{5}{3}}$ and presented as a straight line with a slope of $-\frac{5}{3}$; the magnitude of the theoretical spectrum is arbitrary. Best agreement in the higher frequency range is obtained in the region with the highest mesh resolution.

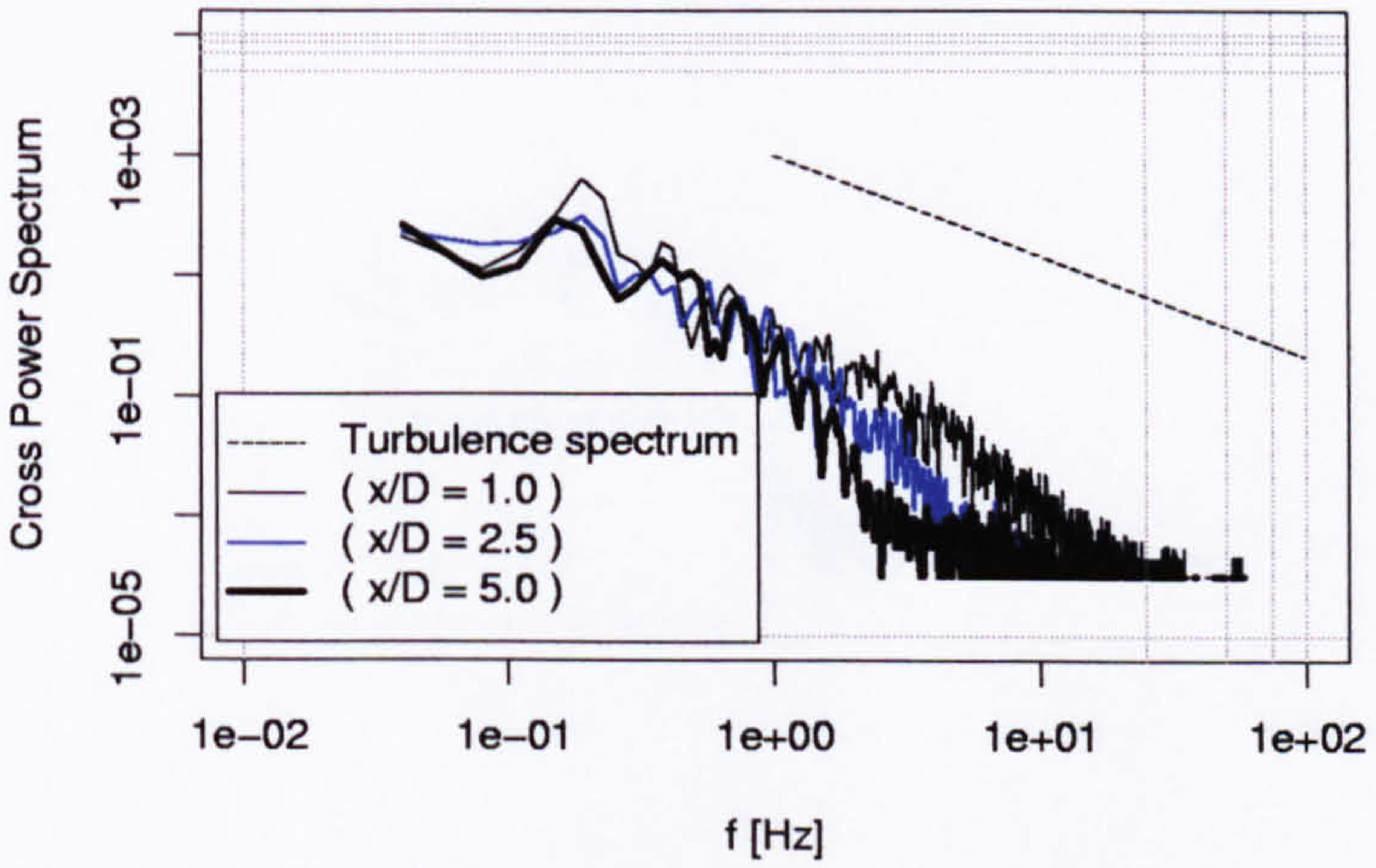

Figure 4.21: Cross power spectrum of velocity components u and v at $\frac{y}{D} = 0$, for simulation with $C_m = 1$, $C_{str} = 1.5$, $3.5 \cdot 10^4$ nodes and the superbee TVD flux limiter. The power spectrum of homogeneous turbulence is described as $E = \alpha\varepsilon^{\frac{2}{3}} f^{-\frac{5}{3}}$ and presented as a straight line with a slope of $-\frac{5}{3}$; the magnitude of the theoretical spectrum is arbitrary. Best agreement in the higher frequency range is obtained in the region with the highest mesh resolution.

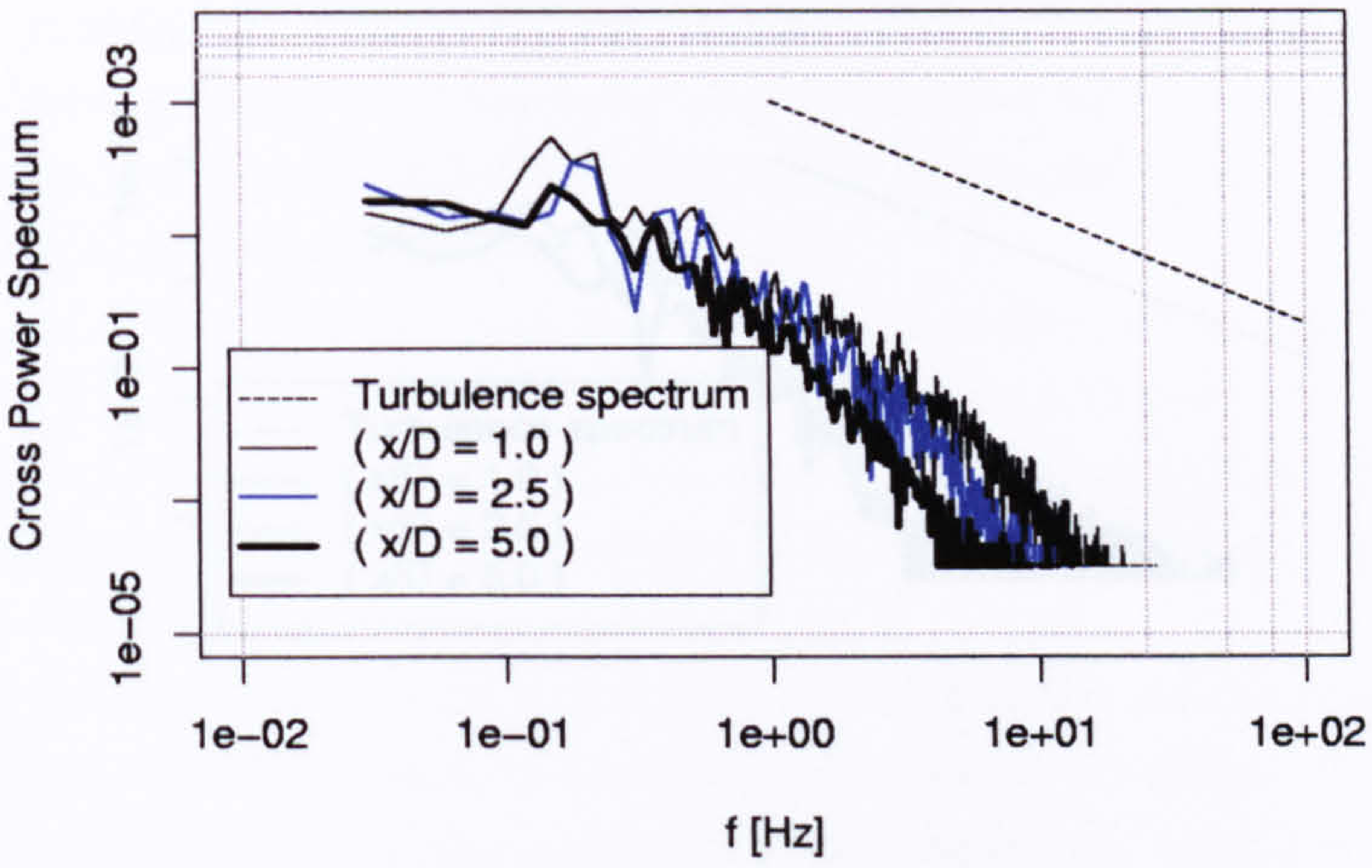

Figure 4.22: Cross power spectrum of velocity components u and v at $\frac{y}{D} = 0$, for simulation with $C_m = 1$, $C_{str} = 1.5$, $5.0 \cdot 10^4$nodes and the superbee TVD flux limiter. The power spectrum of homogeneous turbulence is described as $E = \alpha\varepsilon^{\frac{2}{3}} f^{-\frac{5}{3}}$ and presented as a straight line with a slope of $-\frac{5}{3}$; the magnitude of the theoretical spectrum is arbitrary. Best agreement in the higher frequency range is obtained in the region with the highest mesh resolution.

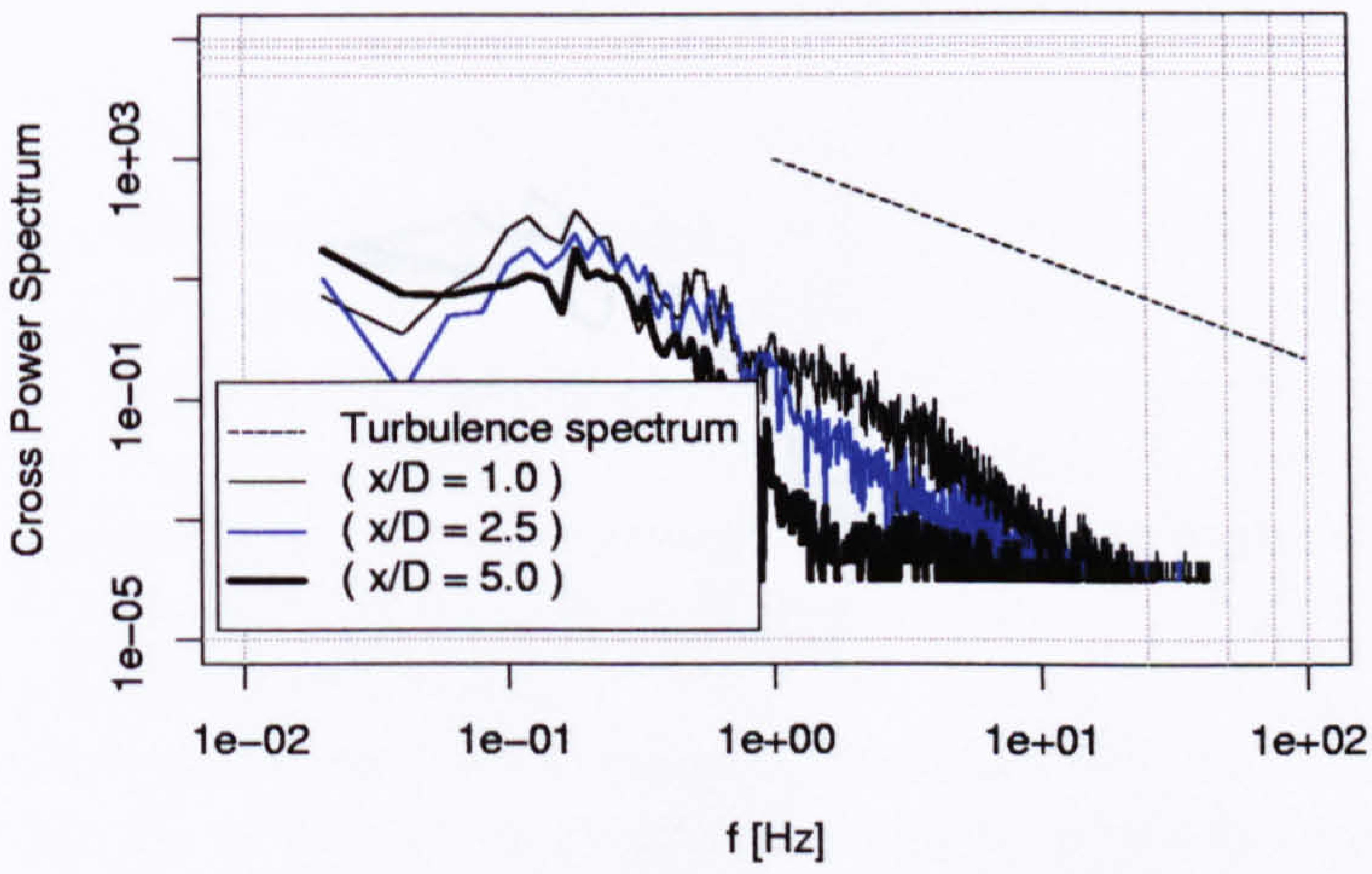

Figure 4.23: Cross power spectrum of velocity components u and v at $\frac{y}{D} = 0$, for simulation with $C_m = 1$, $C_{str} = 2$, $1.4 \cdot 10^4$ nodes and the superbee TVD flux limiter. The power spectrum of homogeneous turbulence is described as $E = \alpha\varepsilon^{\frac{2}{3}} f^{-\frac{5}{3}}$ and presented as a straight line with a slope of $-\frac{5}{3}$; the magnitude of the theoretical spectrum is arbitrary. Best agreement in the higher frequency range is obtained in the region with the highest mesh resolution.

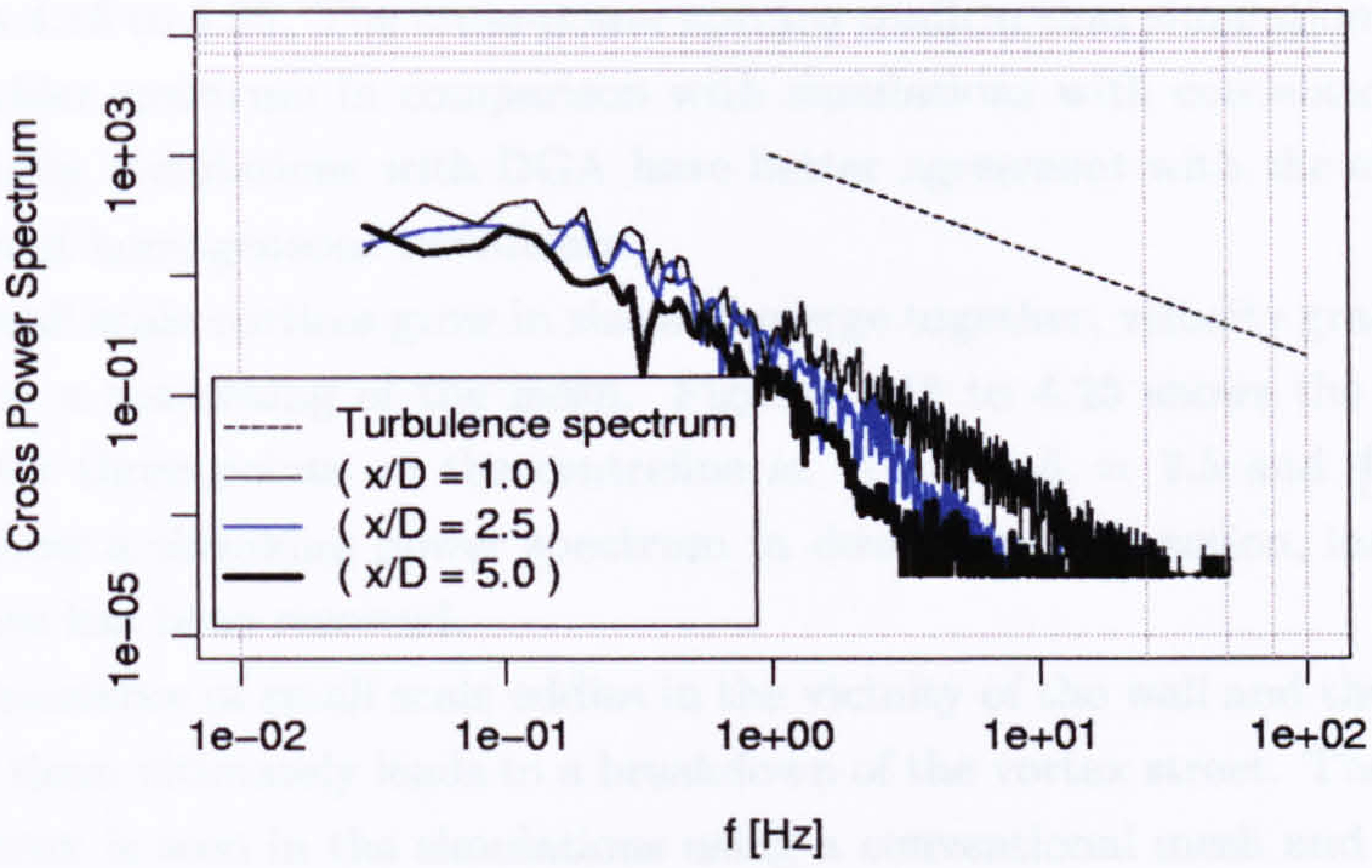

Figure 4.24: Cross power spectrum of velocity components u and v at $\frac{y}{D} = 0$, for simulation with $C_m = 1$, $C_{str} = 2$, $2.8 \cdot 10^4$ nodes and the superbee TVD flux limiter. The power spectrum of homogeneous turbulence is described as $E = \alpha \varepsilon^{\frac{2}{3}} f^{-\frac{5}{3}}$ and presented as a straight line with a slope of $-\frac{5}{3}$; the magnitude of the theoretical spectrum is arbitrary. Best agreement in the higher frequency range is obtained in the region with the highest mesh resolution.

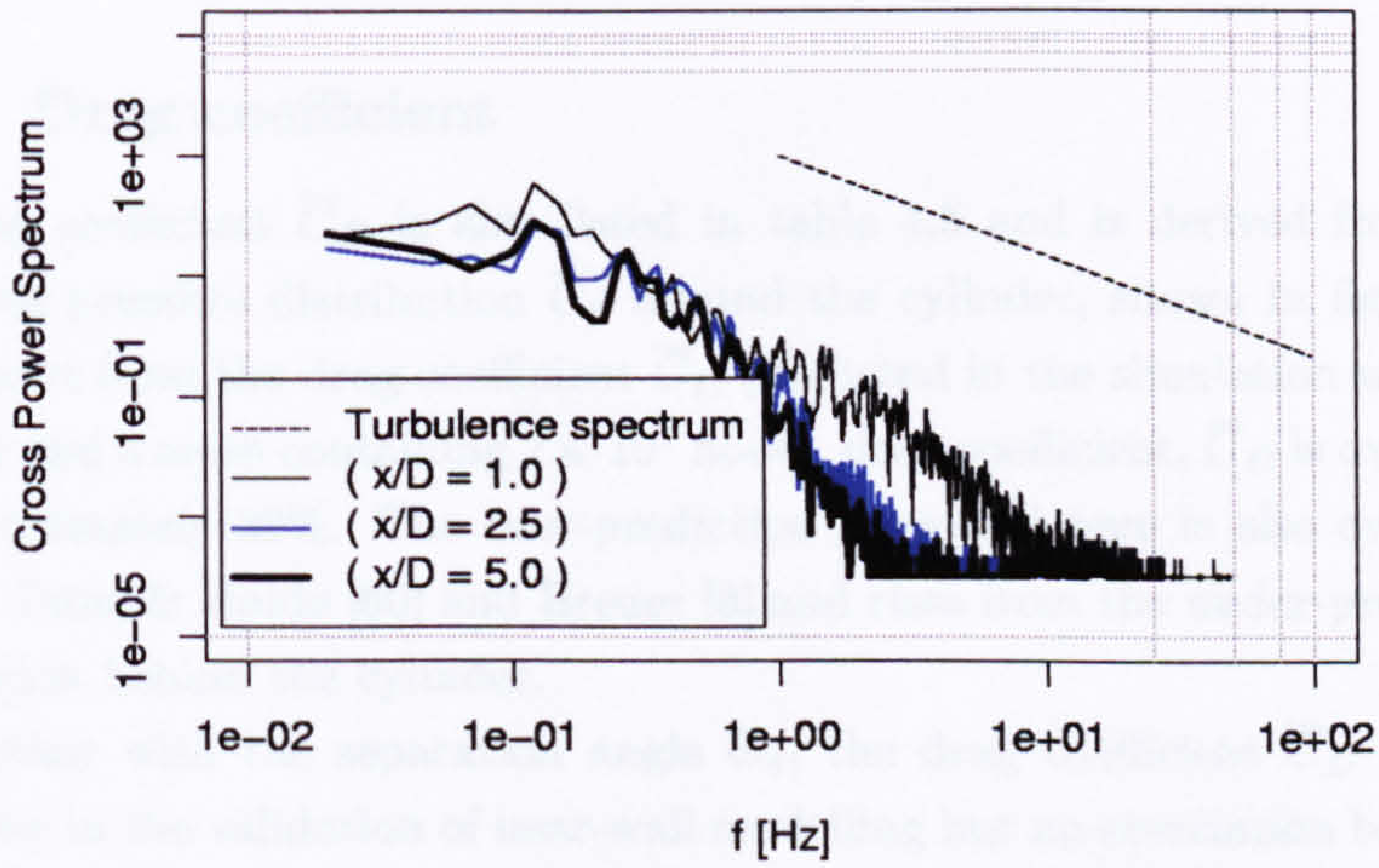

Figure 4.25: Cross power spectrum of velocity components u and v at $\frac{y}{D} = 0$, for simulation with $C_m = 1$, $C_{str} = 2$, $2.4 \cdot 10^4$nodes and the superbee TVD flux limiter. The power spectrum of homogeneous turbulence is described as $E = \alpha \varepsilon^{\frac{2}{3}} f^{-\frac{5}{3}}$ and presented as a straight line with a slope of $-\frac{5}{3}$; the magnitude of the theoretical spectrum is arbitrary. Best agreement in the higher frequency range is obtained in the region with the highest mesh resolution.

tion in the small scale vortices is significantly higher for simulations where DGA is applied, as shown in table 4.1 and 4.5. As a consequence, a wider range of vortices is resolved. The cross-power spectra at the location $\frac{x}{D} = 1$ and $\frac{y}{D} = 0$ are presented in figures 4.18 to 4.25. The cross-power spectra confirm that simulations with DGA have a wider spectrum in comparison with simulations with conventional meshes. Additionally, simulations with DGA have better agreement with the energy decay processes of homogeneous turbulence.

As small scale vortices grow in size and merge together, velocity gradients decay leading to a coarsening of the mesh. Figures 4.18 to 4.25 shows the cross-power spectra for three points on the centreline at $\frac{x}{D} = 1$, $\frac{x}{D} = 2.5$ and $\frac{x}{D} = 5$. The figures show a shrinking power spectrum in downstream direction, indicating less turbulence has been resolved.

The existence of small scale eddies in the vicinity of the wall and the interaction between them ultimately leads to a breakdown of the vortex street. The breakdown of the street is seen in the simulations using a conventional mesh and leads at the same time to a reduction in the cohesion of the flow field.

The Strouhal number S_t is obtained from the lift coefficient C_L. The dominating peak in the power spectrum for lift is obtained from a FFT frequency analysis and the results for Strouhal number S_t are presented in table 4.5. The prediction for Strouhal number S_t shows good agreement with experimental data of Cantwell & Coles [9]. Apart from the simulation with $C_m = 1$, $C_{str} = 1$ and a mesh containing $4.5 \cdot 10^4$ nodes and $C_m = 1$, $C_{str} = 2$, and a mesh containing $2.4 \cdot 10^4$ nodes, the Strouhal number is predicted with less then 12% error. Similar to the simulations with conventional mesh separation angle Θ_s is clearly over-predicted, varying between 81° and 96°.

4.2.2 Drag coefficient

The drag coefficient $\overline{C}_D$ is also listed in table 4.5 and is derived from the time integrated pressure distribution $\overline{C}_p$ around the cylinder, shown in figures 4.26 to 4.28. Apart from the drag coefficient $\overline{C}_D$ predicted in the simulation with $C_m = 1$, $C_{str} = 2$ and a mesh containing $2.4 \cdot 10^4$ nodes, drag coefficient, $\overline{C}_D$ is over-predicted by approximately 30%. The over-prediction presented here is also evident in the work of Tutar & Holdø [60] and Breuer [8] and rises from the under-pressure in the wake region behind the cylinder.

Together with the separation angle Θ_s, the drag coefficient $\overline{C}_D$ forms a key parameter in the validation of near-wall modelling but no correlation between separation angle and drag coefficient is apparent ($R_{(\overline{C}_D - \Theta_s)}$=15%). However, a decrease in drag would have been expected with increasing separation angle Θ_s [40] due to decrease of the width of the wake region. Nevertheless, it should be stated that this correlation between separation angle Θ_s and the drag coefficient $\overline{C}_D$ is due to indirect effects in the flow field. The change of the pressure profile near the point of separation has got nearly any effect on the pressure drag due to the curvature of

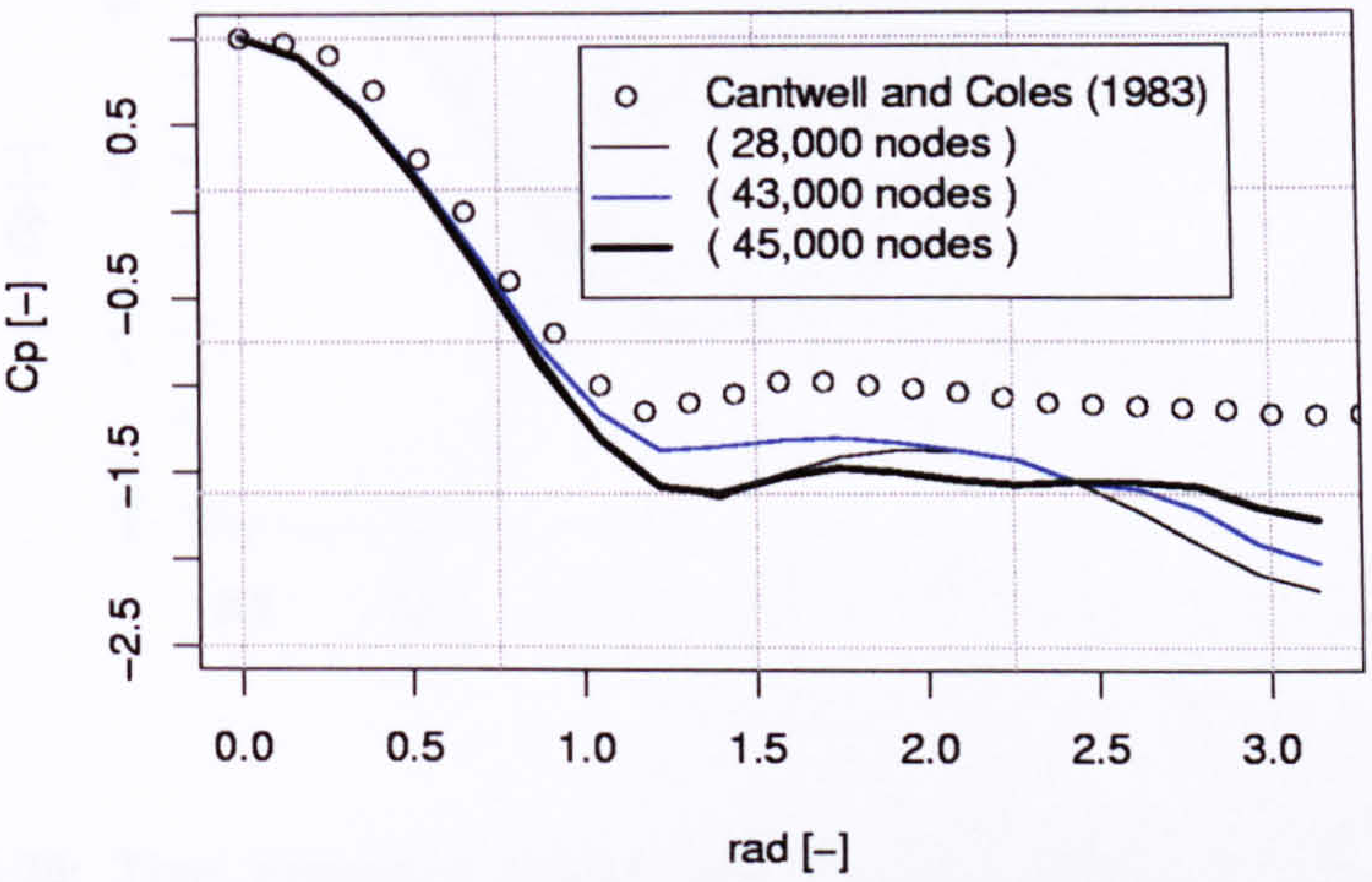

Figure 4.26: Time integrated pressure distribution $\overline{C}_p$ for a cylinder from 0 to π radials, for simulations using DGA variables $C_m = 1$, $C_{str} = 1$ and the superbee TVD flux limiter.

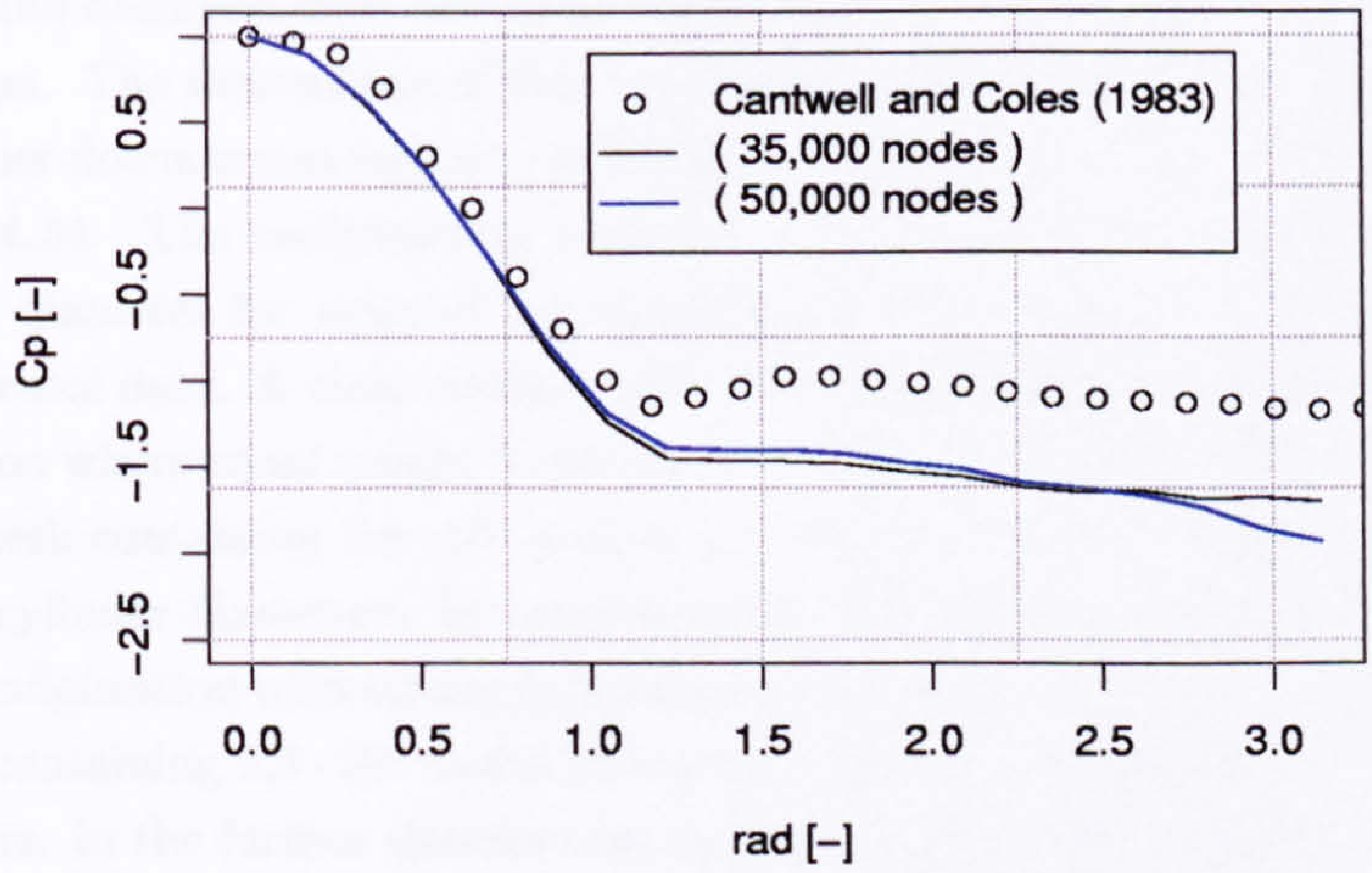

Figure 4.27: Time integrated pressure distribution $\overline{C}_p$ for a cylinder from 0 to π radials, for simulations using DGA variables $C_m = 1$, $C_{str} = 1.5$ and the superbee TVD flux limiter.

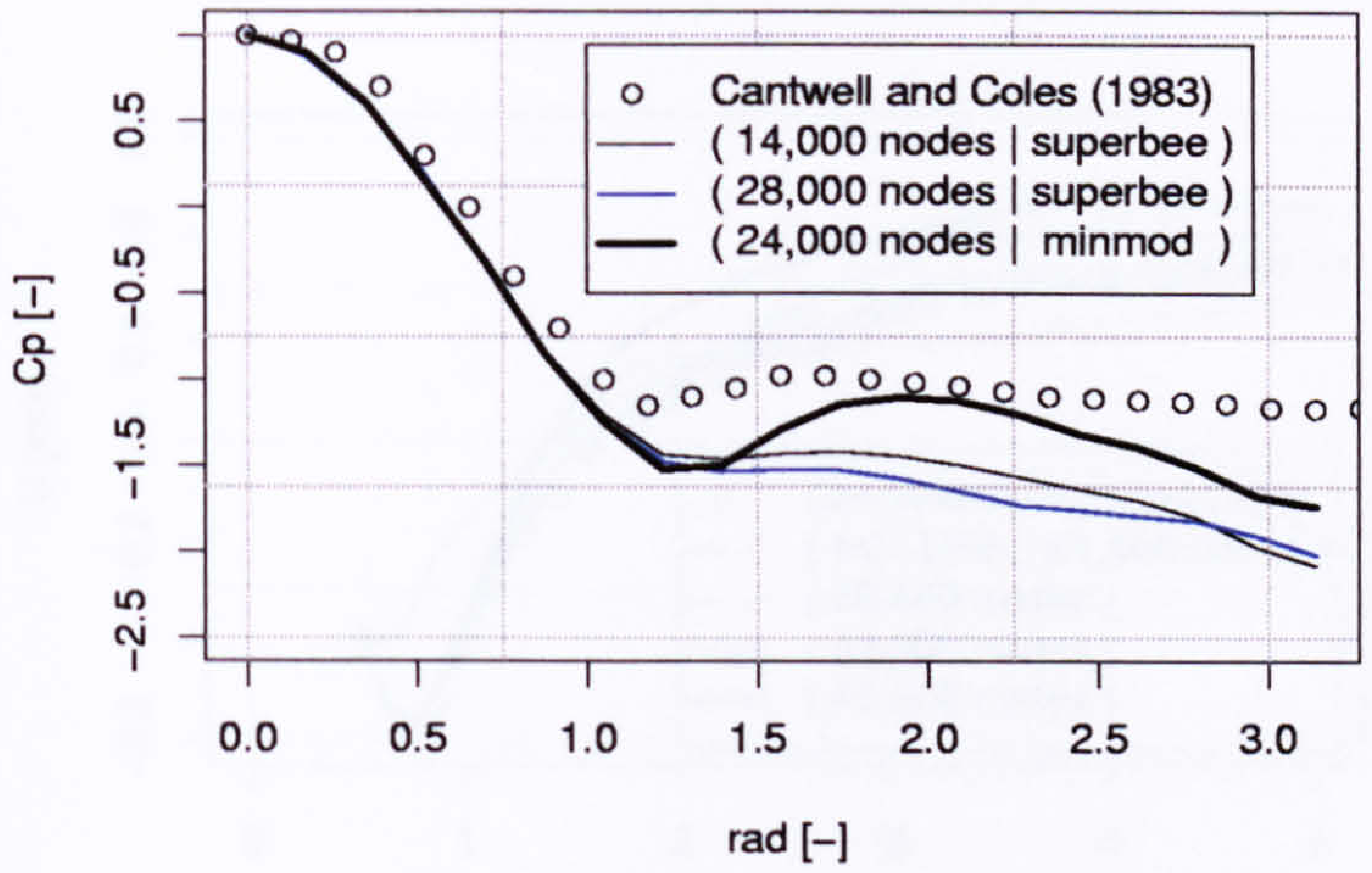

Figure 4.28: Time integrated pressure distribution $\overline{C}_p$ for a cylinder from 0 to π radials, for simulations using DGA variables $C_m = 1$ and $C_{str} = 2$.

the cylinder. Drag is dominated by the pressure distribution in the region behind the cylinder where the tangent maintains a high slope, direct effects on the pressure distribution due to separation occur in the region aside the cylinder where the tangent has a limited slope. As a consequence, direct effects of the separation have got marginal influence on the prediction of the drag coefficient $\overline{C}_D$.

4.2.3 Time integrated velocity field

The results obtained from the simulations using DGA show large variation in flow prediction. The dimensions of the recirculation region behind the cylinder as well the further downstream region is predicted with varying success, as shown in figures 4.29 to 4.34. The recirculation region is predicted to be approximately half the cylinder diameter for most of the simulations, and this is in agreement with the experimental data. A clear conflict with experimental data is apparent in the DGA simulation where equal weight is given to cell size and strain rate ($C_m = 1$, $C_{str} = 1$) and a mesh containing $2.8 \cdot 10^4$ nodes, here the recirculation region is predicted to be 0.15 cylinder diameters. In the simulation with minmod TVD flux limiter and a DGA configuration with strong dominance of the strain rate ($C_m = 1$, $C_{str} = 2$) and a mesh containing $2.4 \cdot 10^4$ nodes shows the recirculation region to be 0.67 cylinder diameters. In the further downstream region, the flow field is mostly over-predicted but, very good agreement is obtained in the simulation with $C_m = 1$, $C_{str} = 2$ and a mesh containing $1.4 \cdot 10^4$ nodes.

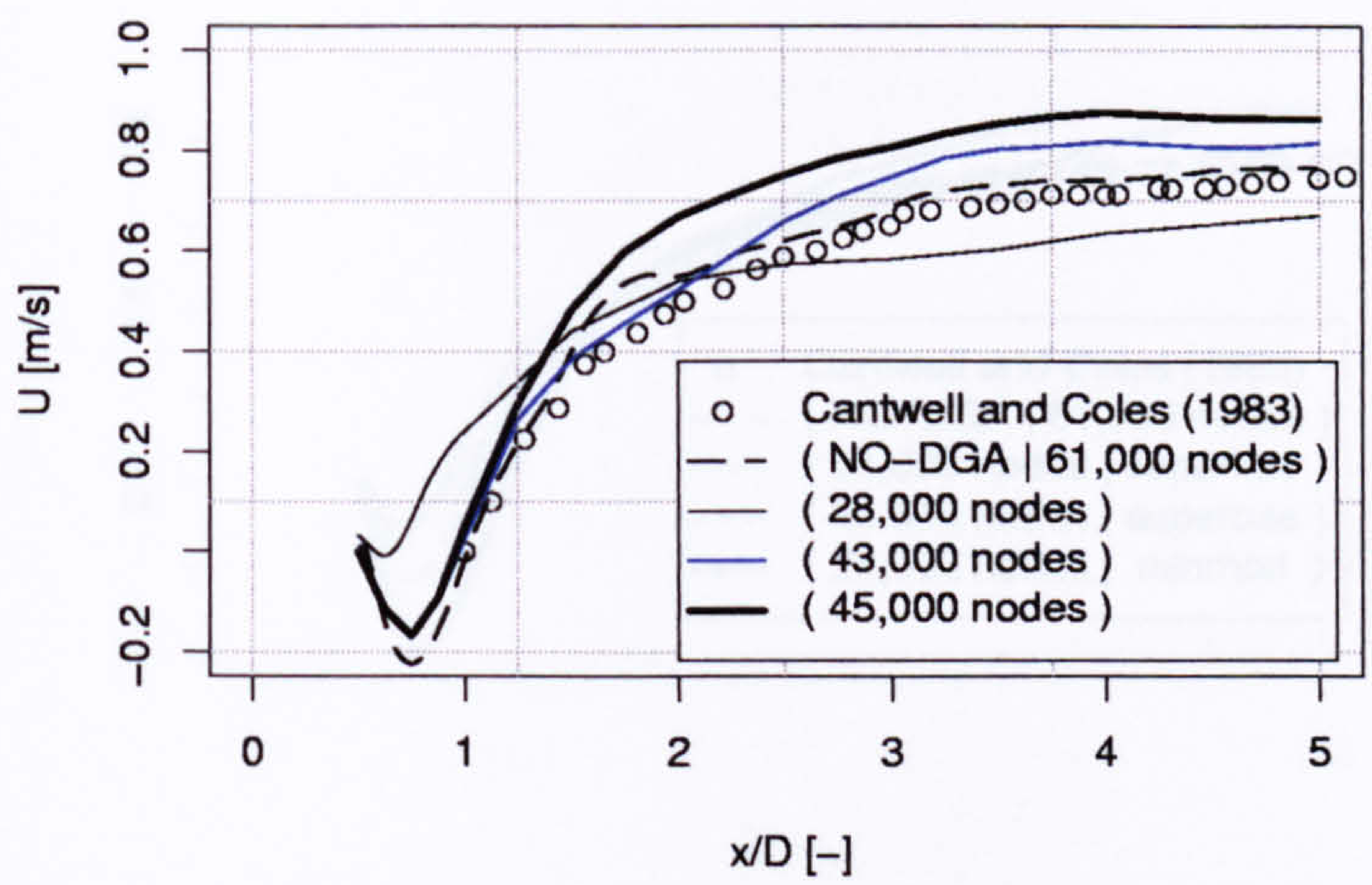

Figure 4.29: Time integrated normalised velocity along streamwise axis at $\frac{y}{D} = 0$, for simulations using DGA variables $C_m = 1$, $C_{str} = 1$ and the superbee TVD flux limiter. To allow a comparison with conventional mesh the simulation with $6.1 \cdot 10^4$ nodes and the subgrid length scale $\Delta = \sqrt{A_{tr}}$ is add.

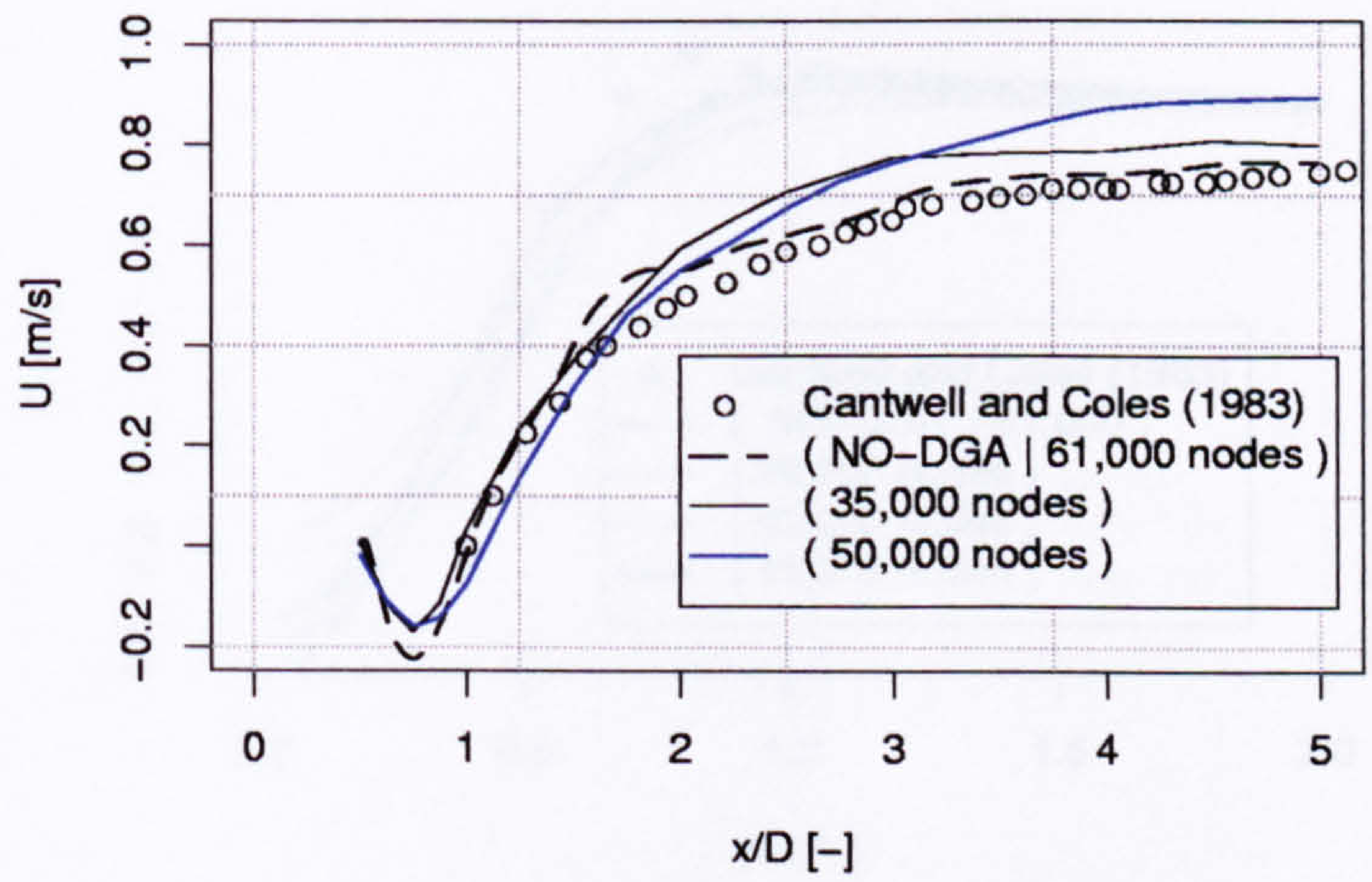

Figure 4.30: Time integrated normalised velocity along streamwise axis at $\frac{y}{D} = 0$, for simulations using DGA variables $C_m = 1$, $C_{str} = 1.5$ and the superbee TVD flux limiter. To allow a comparison with conventional mesh the simulation with $6.1 \cdot 10^4$ nodes and the subgrid length scale $\Delta = \sqrt{A_{tr}}$ is add.

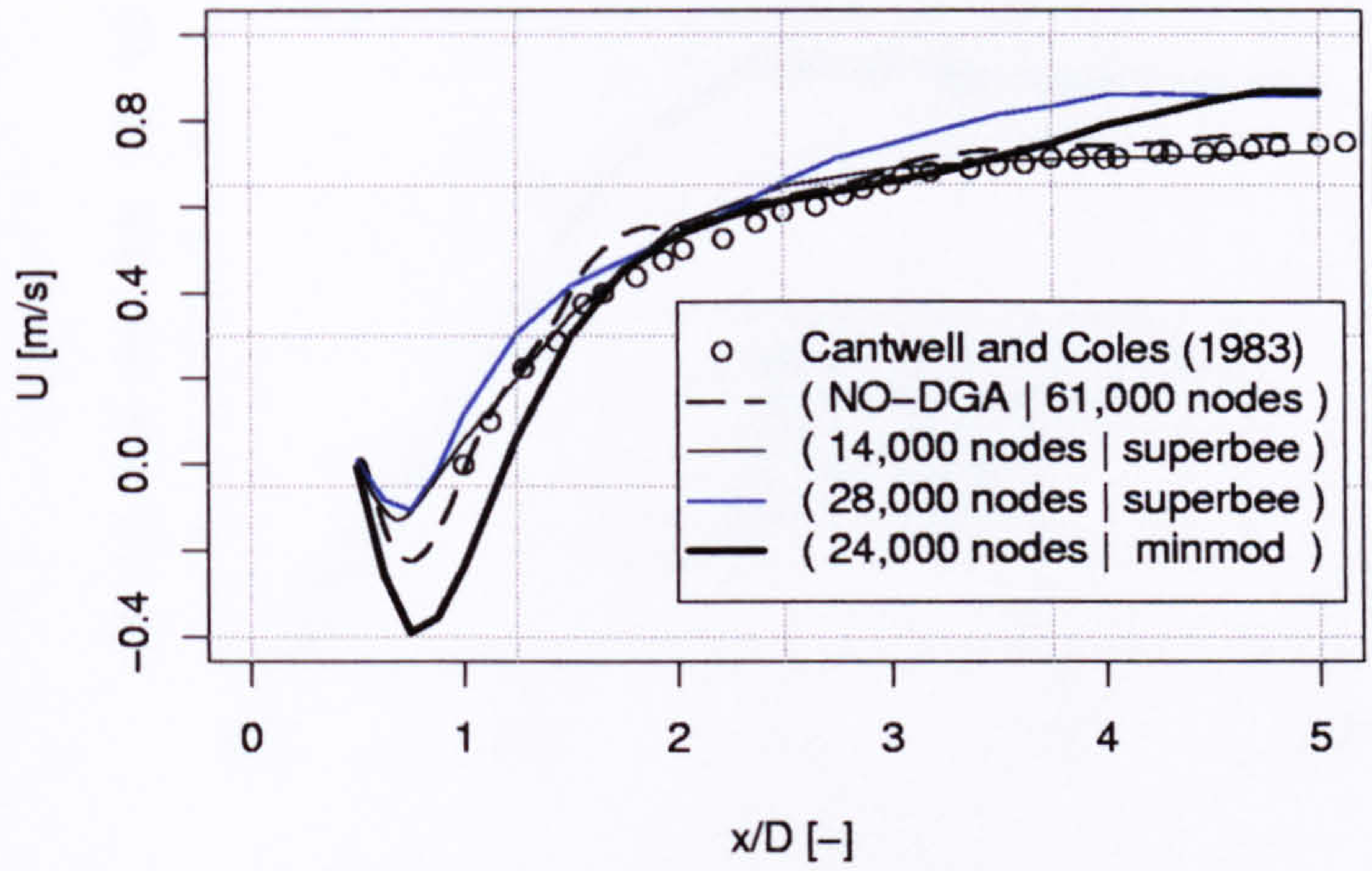

Figure 4.31: Time integrated normalised velocity along streamwise axis at $\frac{y}{D} = 0$, for simulations using DGA variables $C_m = 1$, $C_{str} = 2$. To allow a comparison with conventional mesh the simulation with $6.1 \cdot 10^4$ nodes and the subgrid length scale $\Delta = \sqrt{A_{tr}}$ is add.

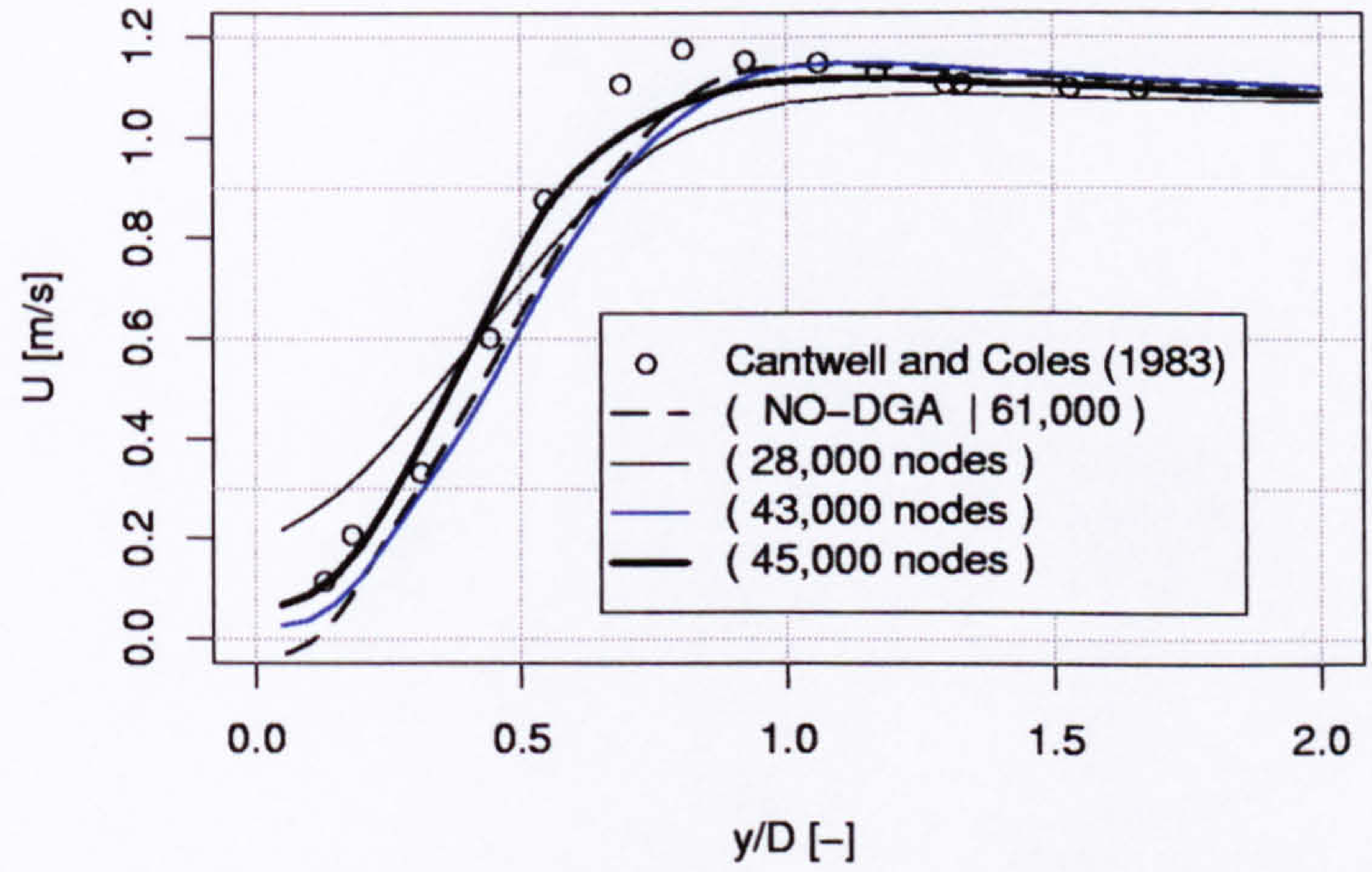

Figure 4.32: Time integrated normalised velocity along transverse axis at $\frac{x}{D} = 1$, for simulations using DGA variables $C_m = 1$, $C_{str} = 1$ and the superbee TVD flux limiter. To allow a comparison with conventional mesh the simulation with $6.1 \cdot 10^4$ nodes and the subgrid length scale $\Delta = \sqrt{A_{tr}}$ is add.

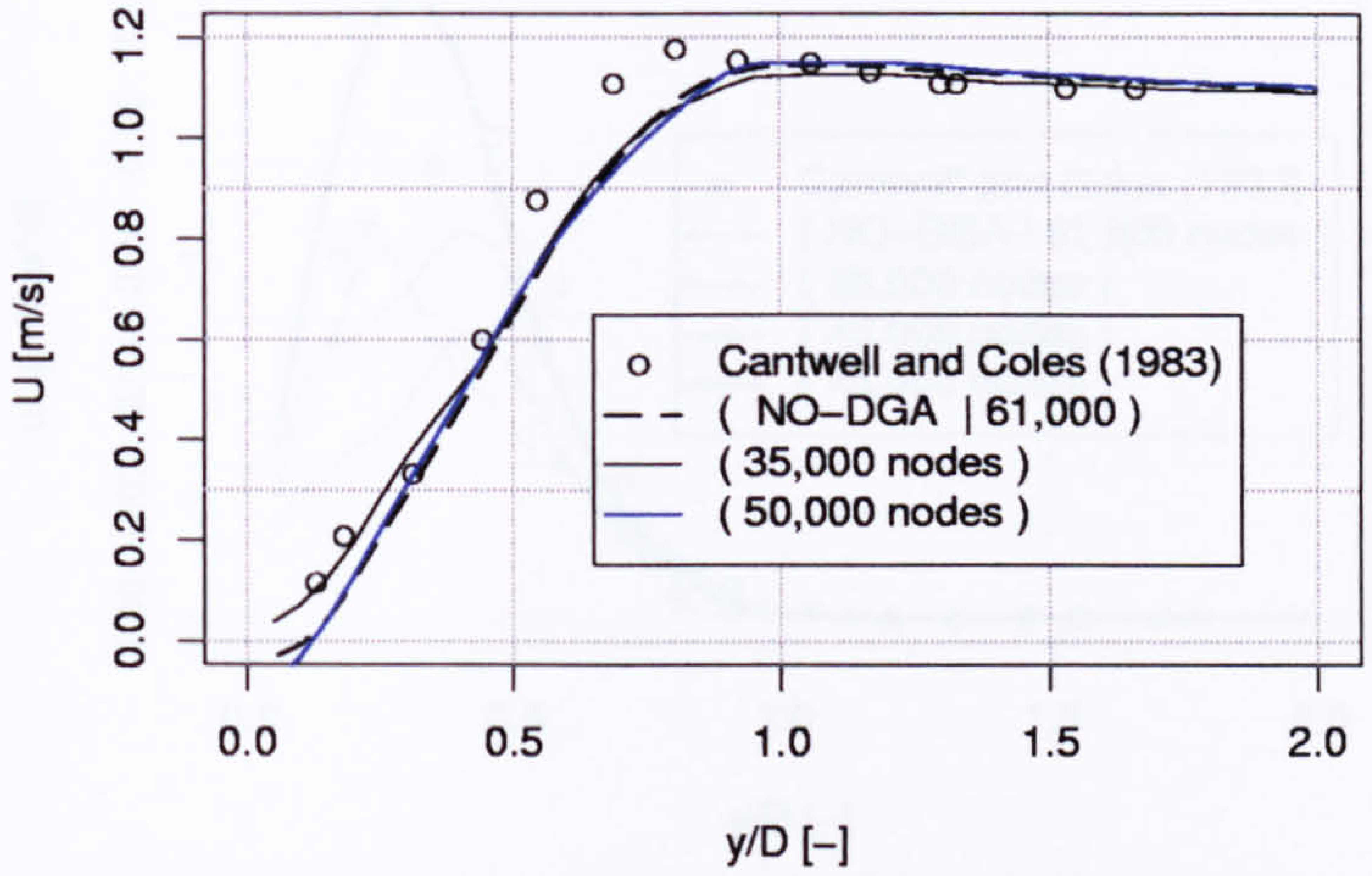

Figure 4.33: Time integrated normalised velocity along transverse axis at $\frac{x}{D} = 1$, for simulations using DGA variables $C_m = 1$, $C_{str} = 1.5$ and the superbee TVD flux limiter. To allow a comparison with conventional mesh the simulation with $6.1 \cdot 10^4$ nodes and the subgrid length scale $\Delta = \sqrt{A_{tr}}$ is add.

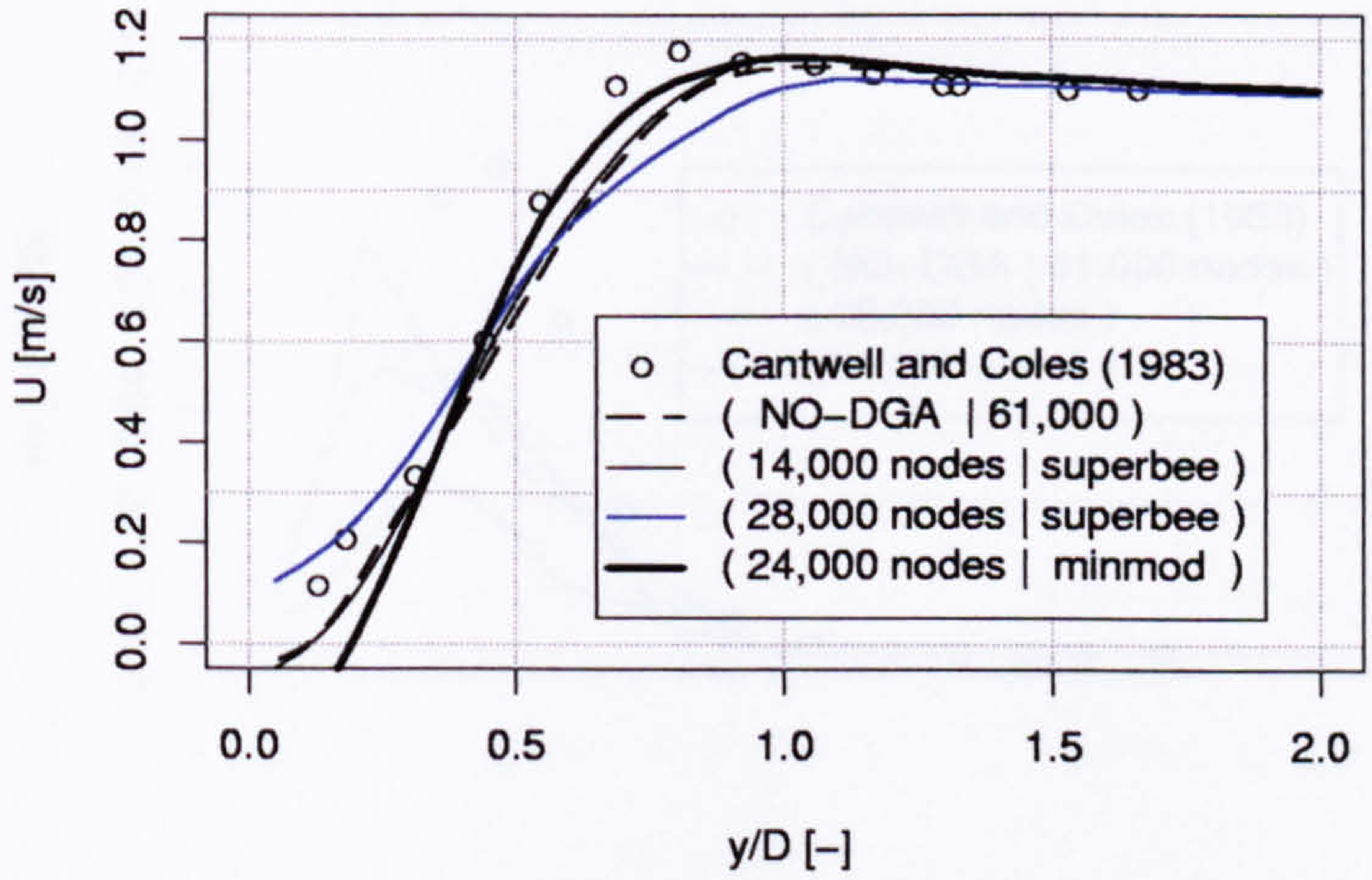

Figure 4.34: Time integrated normalised velocity along transverse axis at $\frac{x}{D} = 1$, for simulations using DGA variables $C_m = 1$ and $C_{str} = 2$. To allow a comparison with conventional mesh the simulation with $6.1 \cdot 10^4$ nodes and the subgrid length scale $\Delta = \sqrt{A_{tr}}$ is add.

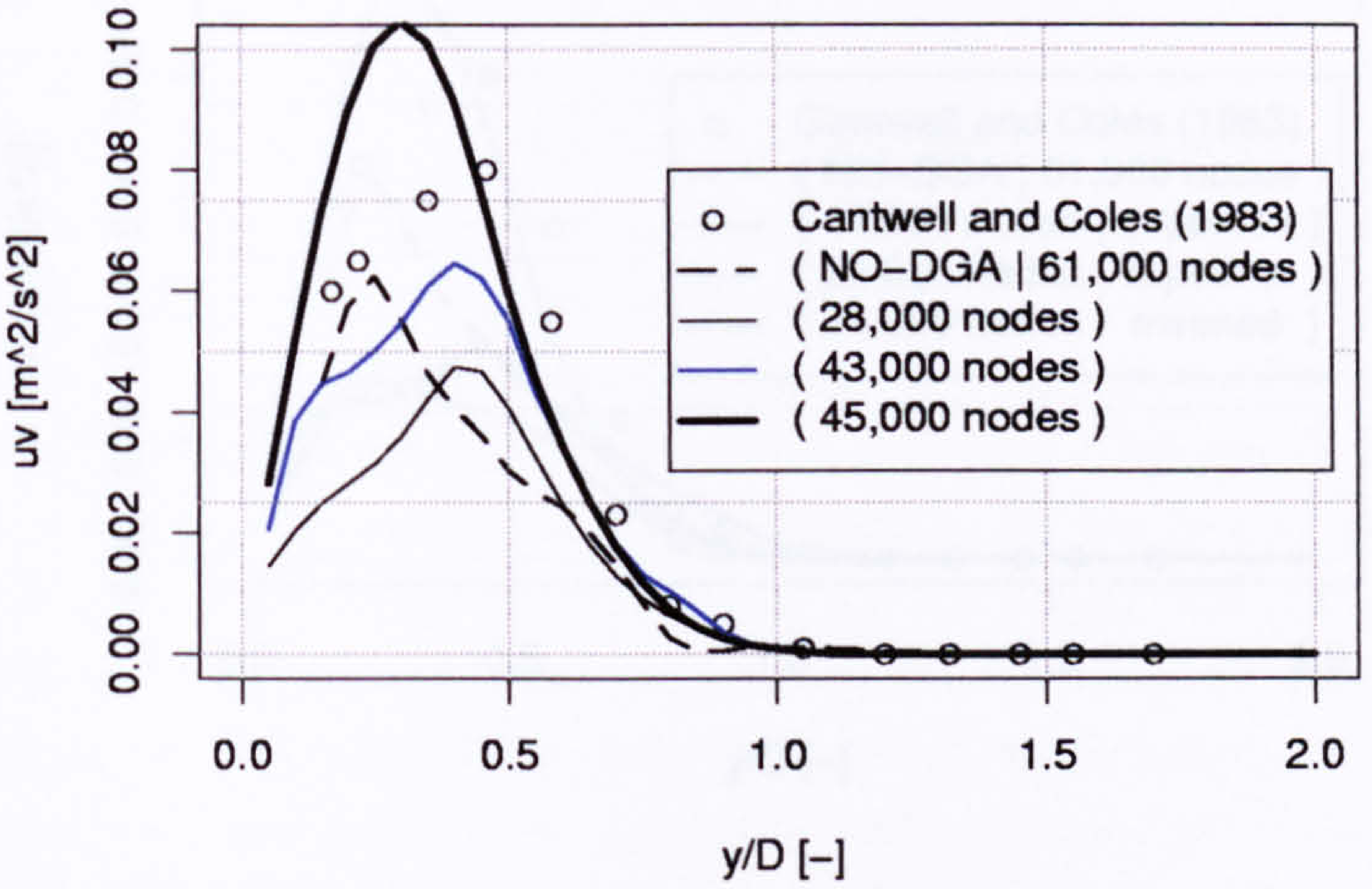

Figure 4.35: Time integrated normalised turbulent shear stress due to turbulence along transverse axis at $\frac{x}{D} = 1$, for simulations using for simulations using DGA variables $C_m = 1$, $C_{str} = 1$ and the superbee TVD flux limiter. To allow a comparison with conventional mesh the simulation with $6.1 \cdot 10^4$ nodes and the subgrid length scale $\Delta = \sqrt{A_{tr}}$ is add.

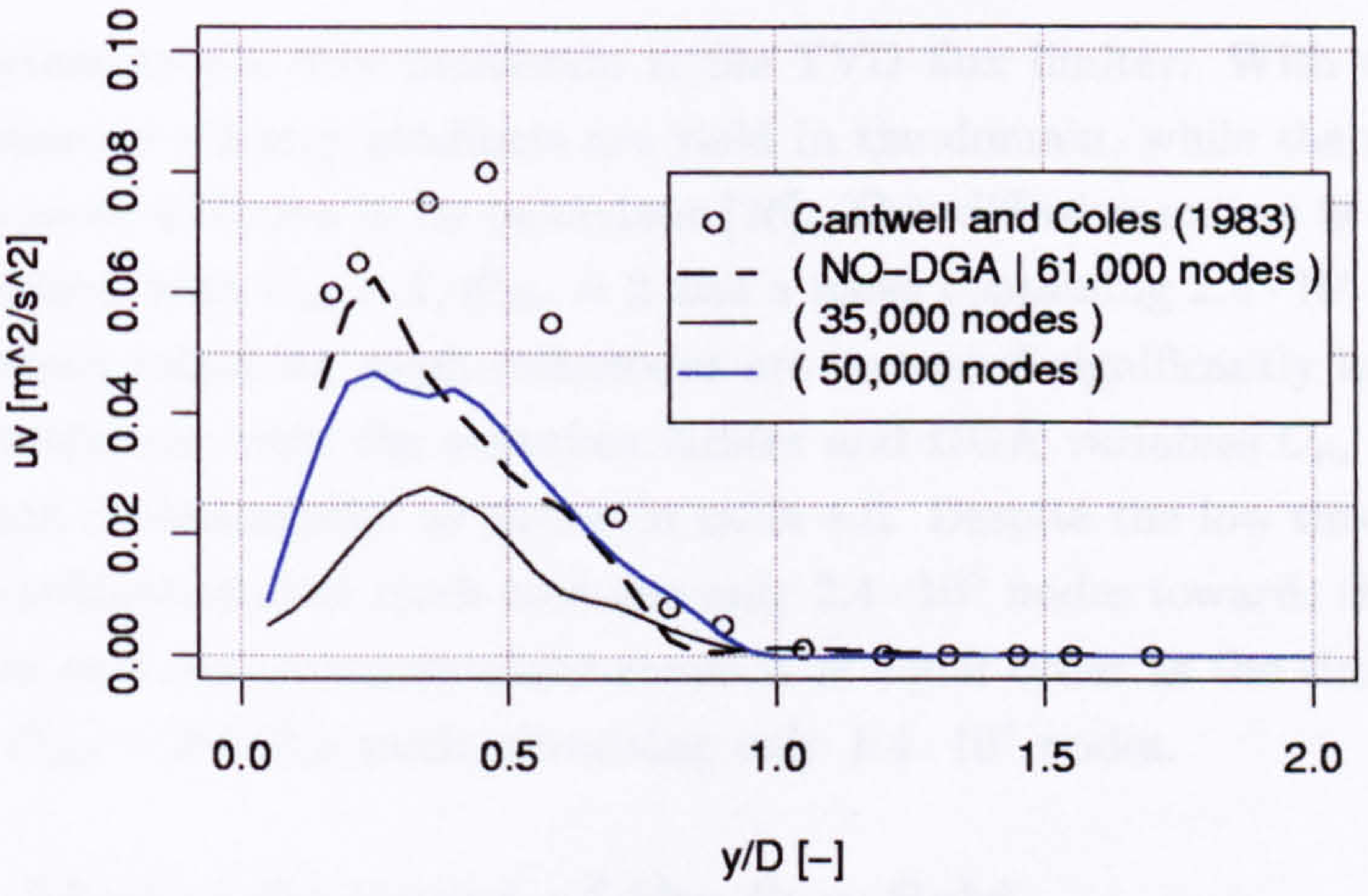

Figure 4.36: Time integrated normalised turbulent shear stress due to turbulence along transverse axis at $\frac{x}{D} = 1$, for simulations using for simulations using DGA variables $C_m = 1\text{-}C_{str} = 1.5$. To allow a comparison with conventional mesh the simulation with $6.1 \cdot 10^4$ nodes and the subgrid length scale $\Delta = \sqrt{A_{tr}}$ is add.

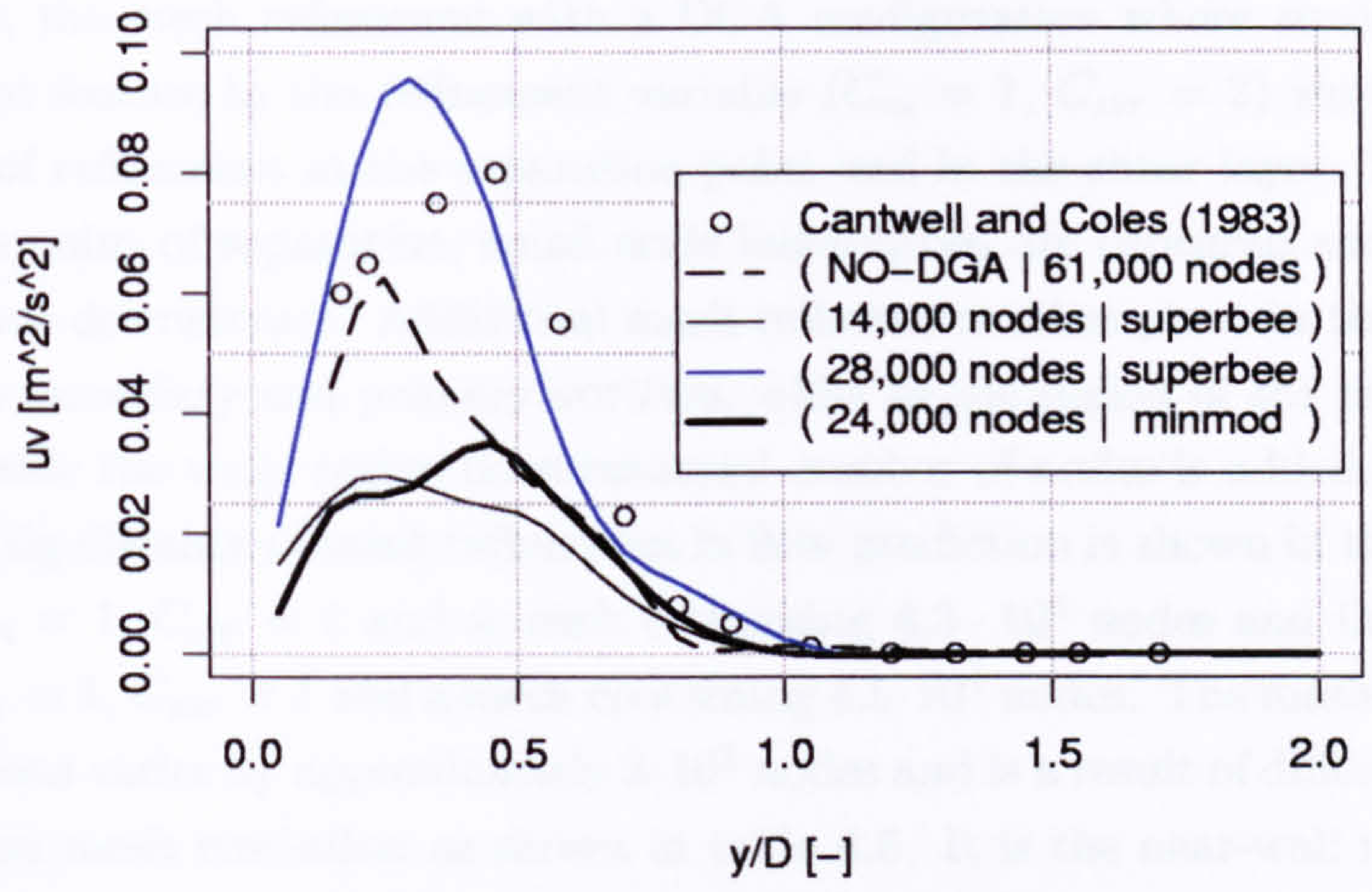

Figure 4.37: Time integrated normalised turbulent shear stress due to turbulence along transverse axis at $\frac{x}{D} = 1$, for simulations using for simulations using DGA variables C_m = 1-C_{str} = 2. To allow a comparison with conventional mesh the simulation with $6.1 \cdot 10^4$ nodes and the subgrid length scale $\Delta = \sqrt{A_{tr}}$ is add.

4.2.4 Turbulent shear stress along transverse axis

The turbulent shear stress profiles obtained from simulations with DGA show better agreement in shape and magnitude compared to the simulations with a conventional mesh. A feature that both simulation sessions have in common is the increase in turbulent shear stress with increasing mesh resolution as shown in figures 4.35 to 4.37.

Important to the flow prediction is the TVD flux limiter. With the superbee limiter, sharper velocity gradients are yield in the domain, while the minmod flux limiter is more diffusive in its behaviour [26]. This diffusive nature is confirmed in the simulation with $C_m = 1$, $C_{str} = 2$ and a mesh containing $2.4 \cdot 10^4$ nodes. Here the threshold values for mesh refinement are increased significantly in comparison to the simulations with the superbee limiter and DGA variables C_m and C_{str} set to be 1 and 2 respectively, as shown in table 4.6. Despite the low threshold values for mesh refinement, the mesh contains only $2.4 \cdot 10^4$ nodes towards the end of the simulation and the turbulent shear stress is of equal order as the simulation with $C_m = 1$, $C_{str} = 2$ and a mesh containing only $1.4 \cdot 10^4$ nodes.

4.2.5 Mesh refinement of the flow field

The mesh refinement which takes place in the flow structures is therefore heavily dependent on the values chosen for the DGA variables C_m and C_{str}, as shown in figure 4.17. With the variables C_m and C_{str} both set to 1, cell size and strain rate are weighted equally in the refinement variable and there is clear refinement at the separation point and in the shear layer. The refinement in the region of the larger vortices behind the cylinder is smooth and the nodes are equally distributed. In contrast, the mesh refinement with a DGA configuration where strain rate is the dominant feature in the refinement variable ($C_m = 1$, $C_{str} = 2$) shows a concentration of refinement at the separation point and in the shear layer. In this layer, near the point of separation, small scale instabilities are captured and followed as they move downstream. Additional mesh refinement takes place in the shear layer between secondary and primary vortices, while in the region of the larger vortices and outside the wake region no substantial number of nodes is added.

The significance of mesh refinement in flow prediction is shown in the simulation with $C_m = 1$, $C_{str} = 1$ and a mesh containing $4.3 \cdot 10^4$ nodes and the simulation with $C_m = 1$, $C_{str} = 1$ and a mesh containing $4.5 \cdot 10^4$ nodes. The mesh used in both simulations varies by approximately $2 \cdot 10^3$ nodes and is a result of different limits for maximum mesh resolution as shown in table 4.6. It is the near-wall region, where separation occurs and shear layers exist which are affected by the mesh resolution limit. The substantial variation in flow prediction proves the numerical impact of the nodes in the near wall region. As the numerics are inextricable bound up with the physics to be modelled, there is an indication that the flow in the downstream direction is to a high extent determined by the flow in the near-wall region.

The existence of nodes in the numerical domain which have a large influence on flow prediction imply that the numerical scheme applied to these nodes is of considerable importance. The results presented in the simulation with $C_m = 1$, $C_{str} = 2$ and a mesh containing $2.8 \cdot 10^4$ nodes and the simulation with $C_m = 1$, $C_{str} = 2$ and a mesh containing $2.4 \cdot 10^4$ nodes confirm the dependence of the flow prediction on the numerical scheme used. The choice of the minmod TVD flux limiter leads to a more diffusive flow and threshold values for mesh refinement have to be significantly increased; however, even with an approximately equal number of nodes there is a distinct difference with the other simulations that use equal values for C_m and C_{str}.

Despite the generally good agreement with experimental data there are drawbacks in the prediction due to imperfections inherent in any numerical scheme, like numerical diffusion and dispersion and the 2-dimensional simplification. An additional weakness in prediction is the physical representation of the small scale flow phenomena, i.e. the modelling of the full range of flow motions up to the Kolmogorov scale η. Despite substantial mesh refinement in the shear layers and in the vicinity of the wall, the smallest scale modelled in the numerical domain is still a factor 10 larger then the Kolmogorov scale η associated to the flow problem. The so-called 'micro scale' in the flow field is obtained from the smallest element in the numerical domain and is given in table 4.5 together with the Kolmogorov scale η.

Chapter 5

General discussion

5.1 Modelling of vortex shedding with Dynamic Grid Adaptation

The essential feature of this thesis is the proposed link between turbulence a model and a DGA algorithm for significantly more effective modelling of turbulence. Potentially turbulent regions are detected by the LES turbulence model and treated via the LES model assumptions when the SGS structures are sufficiently small. When the variation in turbulent viscosity exceeds a pre-defined level, the mesh will be locally refined to resolve the larger turbulent motions.

The results in section 4.2 have shown substantial sensitivity of flow prediction to the mesh used. Not only do the properties of the local turbulence depend on the mesh resolution in the numerical domain, but also time integrated flow features as velocity profiles are similarly and significantly sensitive. The variation in flow prediction is primarily due to mesh refinement and confirms the complexity of the physical processes in which certain flow regions and vortex scales in the flow field are over-proportionately important. This means that the determination of a proper refinement variable cannot be decoupled from the physics that are under investigation.

The DGA variables C_m and C_{str} can be considered to be an engineering tool to keep control over the refinement behaviour of the DGA algorithm. An increase of either one of these variables will have a substantial effect on the refinement behaviour. This aspect of the refinement strategy has a significant implication which is that a modification to the DGA variables C_m and C_{str} implies a modification to the physical flow features which are monitored according to the following equation $q_i = \rho C_s^2 \Delta^{2C_m} \left|\overline{S}\right|^{C_{str}}$. An increase of C_m gives extra weight to the cell size and leads to a smooth mesh refinement and refinement is likely to occur in regions where the mesh is coarse. By increasing C_{str} extra weight is given to the strain rate and the mesh refinement will be sharp and strongly dependent on the instantaneous flow field. In the first set of simulations C_m and C_{str} are equally weighted with values of 1 giving the refinement variable the dimensions of dynamic viscosity $\left(\frac{Ns}{m^2}\right)$. With C_m and C_{str} to be 1 and 2 respectively, extra weight is given to the strain rate and the refinement variable has the dimensions of dynamic viscosity per unit time, or dynamic pressure $\left(\frac{N}{m^2}\right)$. The simulations using DGA variables C_m and C_{str} set to be 1 and 1.5 respectively can be considered as an hybrid between both methods, with the dimensions for refinement being $\left(\frac{N\sqrt{s}}{m^2}\right)$.

The use of a viscosity term for both the turbulence modelling and mesh refinement is an extension of the classical approach for modelling unsteady turbulent flow. However, in a flow field where separation occurs due to an adverse pressure gradient as a result of decreasing dynamic pressure, the use of a dynamic pressure as a refinement variable is preferable. Although the author does not want to draw a final conclusion regarding the preferred method for unsteady flow around a circular cylinder, simulations have shown a higher rate of mesh refinement near the separation point and in the shear layer when using values of 1 and 2 respectively for the DGA variables C_m and C_{str}. The results presented for separation angle in table 4.5 confirm that good agreement is obtained with a DGA configuration where strain rate is the dominant flow feature ($C_m = 1$, $C_{str} = 2$). By choosing the DGA variables C_m and C_{str} to be 1 and 2 respectively, extra weight is given to the strain rate term in the equation for error indication leading to a comparatively low number of nodes in domain.

The importance of the DGA variables in the prediction of the flow field is also shown in movie $C_m = 1 - C_{str} = 1 - 2.8 \cdot 10^4 - 1.avi$ to $C_m = 1 - C_{str} = 2 - 2.4 \cdot 10^4 - 2.avi$ included in the appendix. Movie $C_m = 1 - C_{str} = 2 - 2.8 \cdot 10^4 - 2.avi$ shows the existence of small scale vortices in the vicinity of the wall. The interaction of these vortices with the surrounding flow field leads to a complex flow field in which vortices are predominantly moving in downstream direction with occasional vortices moving in upstream direction penetrating into the separation point leading to an upstream movement of the separation point. Upstream moving vortices are seen throughout all simulations with the variables C_m and C_{str} set to be 1 and 2 respectively, while with C_m and C_{str} set both to be 1 a high number of nodes is required before upstream flow motions are resolved in sufficient detail. Based on the mesh structures generated by the DGA algorithm, there is a clear indication that instabilities in the flow field leading to small scale vortices are generated in the regions where a high rate of strain is maintained. These are typically in the shear layer and the layers separating the larger vortices. It is seen that the simulations with C_m and C_{str} set to be 1 and 2 respectively focus mesh refinement on the regions where a high rate of strain is maintained. The importance of the upstream moving vortices onto a nonlinear elliptic flow field is a subject for discussion but, nevertheless, it is known that the small scale vortices play a major role in the determination of turbulence level and the transition to turbulence [62].

The 2-dimensional simulations show the number of nodes needed to obtain good agreement for turbulent shear stress $\overline{u'v'}$ is decreasing, with increasing values for C_{str}. The reduction in number of nodes with increasing values of the DGA constant

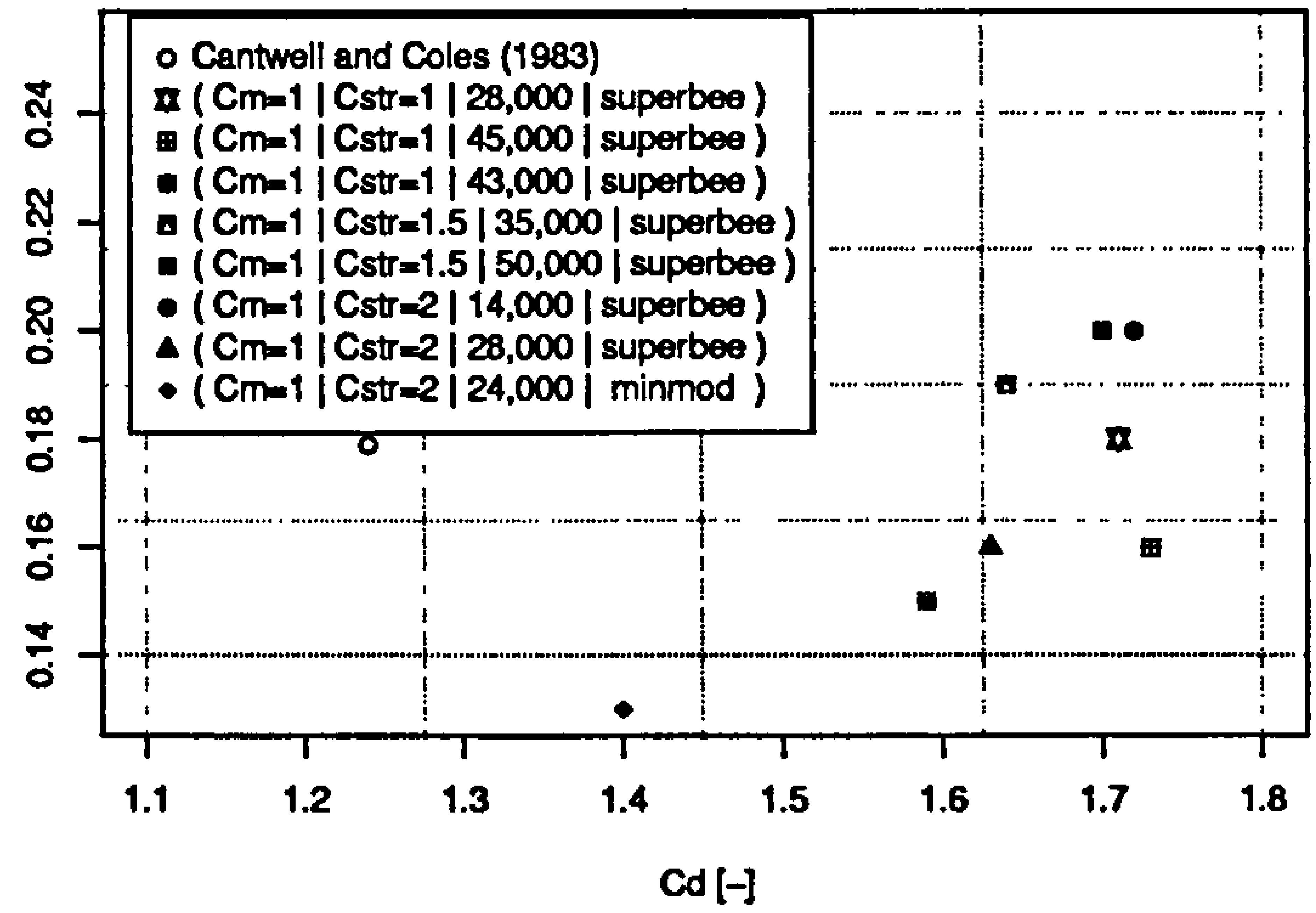

Figure 5.1: Scatter diagram for drag coefficient $\overline{C}_D$ and Strouhal number S_t for simulations using DGA. The drag coefficient $\overline{C}_D$ and Strouhal number S_t have a 76% correlation.

C_{str} indicates that the requirements for predicting the turbulent shear stress $\overline{u'v'}$ are fulfilled more efficiently with a strain rate sensitive refinement variable. The results suggest that it is the narrow region dominated by rate of strain which require high mesh resolution for proper prediction of the turbulent shear stress $\overline{u'v'}$. The importance of small scale vortices to the turbulent shear stress $\overline{u'v'}$, is also shown in the simulation where cell size and strain rate are equally weighted ($C_m = 1$, $C_{str} = 1$) and a mesh containing $4.5 \cdot 10^4$ nodes. Here, an increase in the number of nodes is accomplished by increasing the maximum mesh resolution as set in the REACFLOW input file. The relatively small number of nodes allocated in the vicinity of the wall leads to a substantial increase in turbulence level at a distance of one cylinder diameter from the centre of the cylinder. These results again confirm the sensitivity of the turbulent shear stress $\overline{u'v'}$ on the mesh used in the vicinity of the wall. It is important to state that an increase in mesh resolution leads to an increase in turbulent shear stress $\overline{u'v'}$ as shown in figures 4.35 to 4.37. A similar trend is not apparent for any of the other time integrated flow profiles and parameters.

Despite substantial mesh refinement the micro scale is still large in comparison to the Kolmogorov scale η, as shown in table 4.5. The lack of turbulent flow motions is an important reason for the irregular sensitivity of each flow variable in relation to the mesh used. This indicates that flow motions and flow mechanism in the flow field have got a unique effect on each critical flow parameter and flow profile.

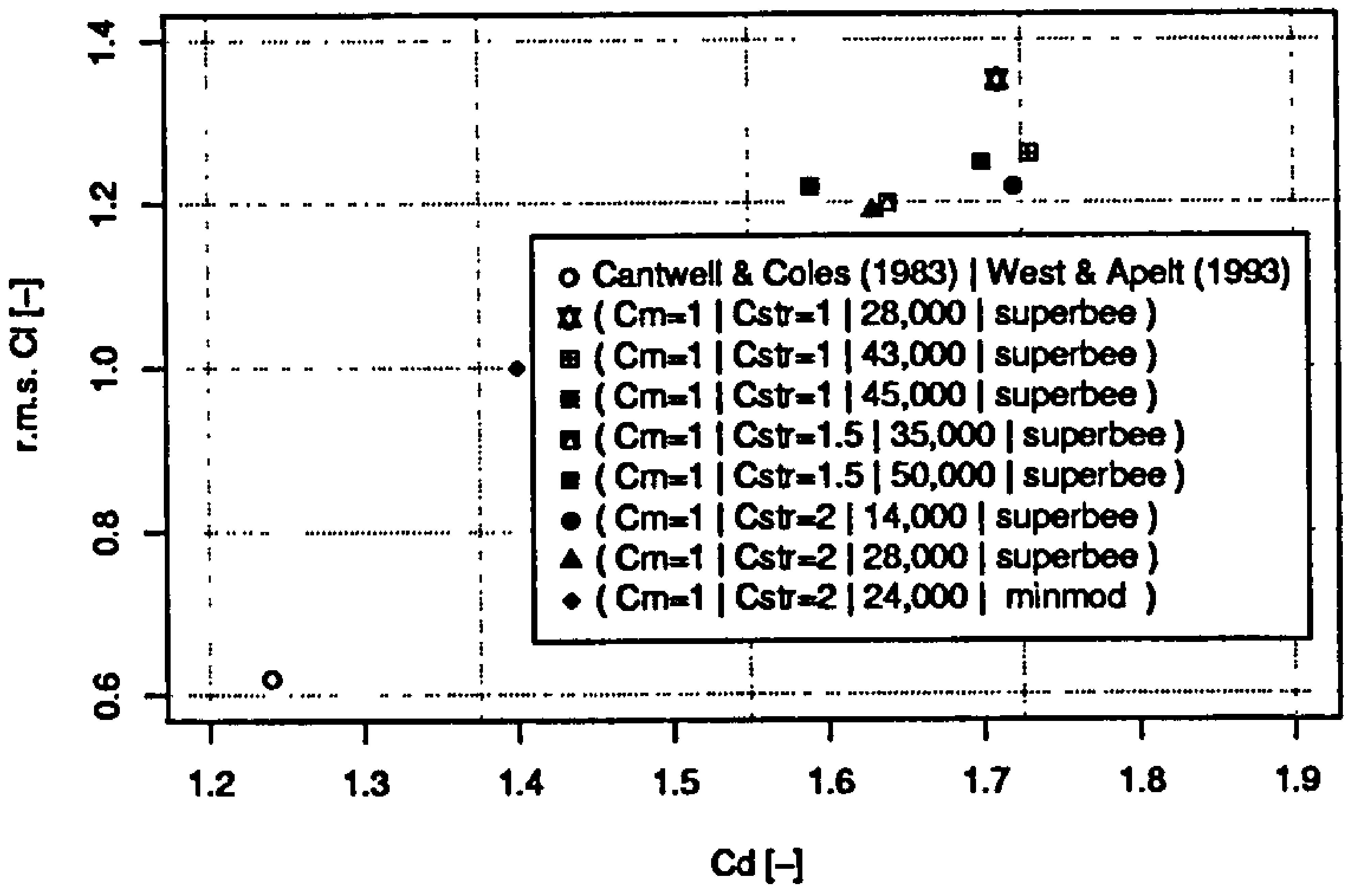

Figure 5.2: Scatter diagram for drag coefficient $\overline{C}_D$ and r.m.s. lift coefficient $\tilde{C}_L$ for simulations using DGA. The drag coefficient $\overline{C}_D$ and r.m.s. lift coefficient $\tilde{C}_L$ have a 90% correlation.

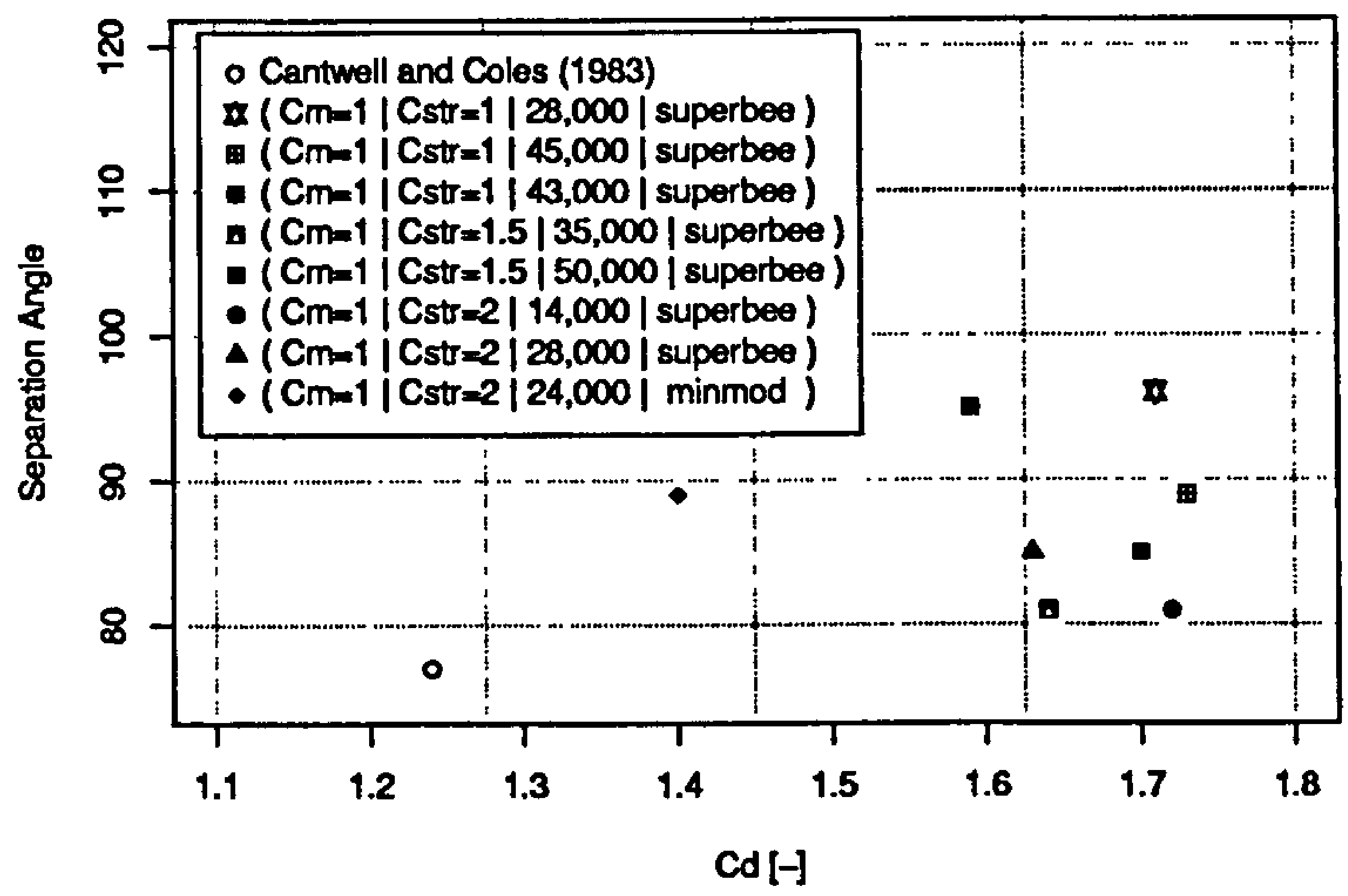

Figure 5.3: Scatter diagram for drag coefficient $\overline{C}_D$ and separation angle Θ_S for simulations using DGA. The drag coefficient $\overline{C}_D$ and separation angle Θ_s have a 15% correlation.

	$R_{(\overline{C}_D-\Theta_s)}$	$R_{(S_t-\Theta_s)}$	$R_{(S_t-L_r)}$
De With	0.15	0.51	0.23

Table 5.1: Correlation coefficients obtained from the simulations for drag coefficient $\overline{C}_D$ against separation angle Θ_s, Strouhal number S_t against separation angle Θ_s and Strouhal number S_t against recirculation length L_r. The correlation coefficients presented indicate no significant correlation is apparent in any of the flow parameter relations.

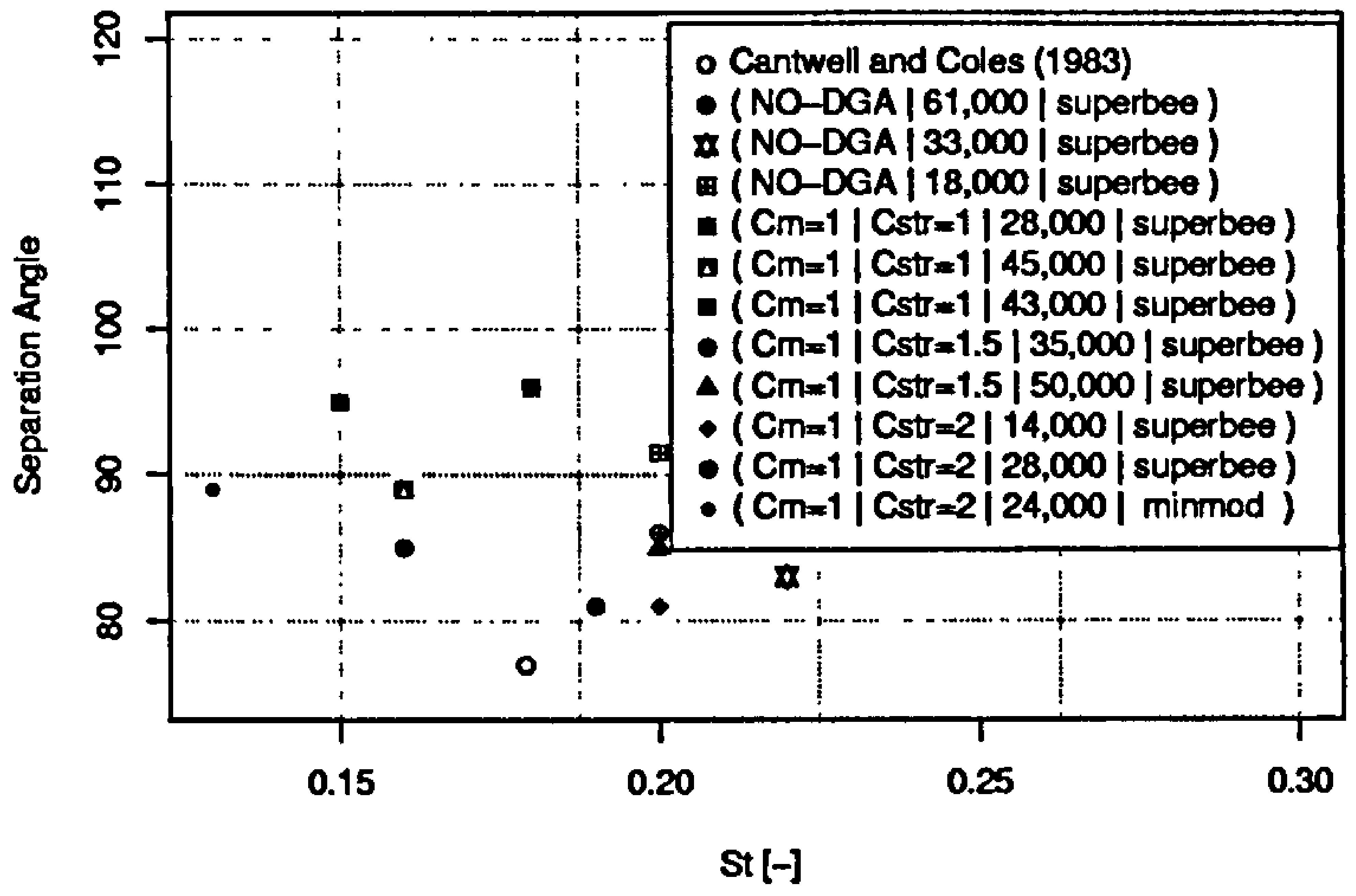

Figure 5.4: Scatter diagram for Strouhal number S_t and separation angle Θ_S for simulations using DGA and conventional mesh. The Strouhal number S_t and separation angle Θ_S have a 51% correlation.

	$R_{(\overline{C}_D-\tilde{C}_L)}$	$R_{(\overline{C}_D-S_t)}$	$R_{(\tilde{C}_L-S_t)}$	$R_{(\overline{C}_D-\Theta_s)}$	$R_{(\tilde{C}_L-\Theta_s)}$
De With	0.90	0.76	0.60	0.15	0.25
Tutar [59]	0.91	0.99	0.90	-	-
Travin et al. [58]	0.89	−0.97	−0.79	−0.51	−0.71
Breuer [8]	-	−0.89	-	−0.68	-

Table 5.2: Correlation coefficients obtained from the simulations with DGA and data presented in literature. Correlation coefficients are given for drag coefficient $\overline{C}_D$ against lift coefficient $\tilde{C}_L$, drag coefficient $\overline{C}_D$ against Strouhal number S_t, lift coefficient $\tilde{C}_L$ against Strouhal number S_t, drag coefficient $\overline{C}_D$ against separation angle Θ_s and lift coefficient $\tilde{C}_L$ against separation angle Θ_s. The coefficients show a significant correlation for drag coefficient $\overline{C}_D$ against lift coefficient $\tilde{C}_L$and drag coefficient $\overline{C}_D$ against Strouhal number S_t.

Correlations within the flow field

The mechanism by which vortex shedding takes places and the complex procedures which determine the characteristics of the vortex street have been subject to many speculations. Despite all of this, the foundations of vortex shedding have not been exposed so far . In this respect, it is of value to investigate the potential correlations between the different flow features. A comparison of the critical flow parameters $\overline{C}_D$, S_t and Θ_s is presented in figures 5.1 to 5.4. The data presented in table 5.1 indicates that no correlation is apparent between Strouhal number S_t and separation angle Θ_s nor between the drag coefficient $\overline{C}_D$ and the separation angle Θ_s. The lack of correlation between Strouhal number S_t and separation angle Θ_s indicates that the shedding frequency S_t is not a function of the geometry of the recirculation region or the curvature of the shear layer and vice versa. This conjecture is confirmed by the recirculation length L_r which shows no correlation with the shedding frequency S_t ($R_{(S_t-L_r)}$=23%).

Flow features which have better correlation are the drag coefficient $\overline{C}_D$ with the lift coefficient $\tilde{C}_L$, and the drag coefficient $\overline{C}_D$ with the Strouhal number S_t. The existence of a significant correlation between these three flow features is confirmed by numerical data as shown in table 5.2.

The connection between drag coefficient $\overline{C}_D$ and Strouhal number S_t gives a 76% correlation as shown in figure 5.1; additionally, a 90% correlation is found between drag coefficient $\overline{C}_D$ and Strouhal number S_t. Such a correlation indicates the over-predicted drag coefficient $\overline{C}_D$ has a relation with the mechanism by which vortex shedding takes place. Apart from the correlation with Strouhal number S_t, no further correlation with the drag coefficient $\overline{C}_D$ has been discovered with any of the other time integrated flow features, like recirculation length L_r, maximum turbulent shear stress $\overline{u'v'}$ or separation angle...

It is widely accepted that the amount of drag on the cylinder is to large extent dependent on the time integrated width of the wake region. The decrease in drag forces from the sub-critical to the super-critical flow regime is a clear consequence of this. Nevertheless, the weak correlation of any of the time integrated flow features with the drag coefficient $\overline{C}_D$ suggests that the average pressure field around the cylinder is not only dependent on the unsteady flow field but, to some extent dependent upon the dynamic features in the flow field.

Time integrated drag coefficient $\overline{C}_D$ versus r.m.s. lift coefficient $\tilde{C}_L$

A significant part of the drag rises from the low pressure in the wake behind the cylinder, while the decay of this low pressure occurs due to energy dissipation by the turbulent motion [40], i.e. the magnitude of drag is also related to instantaneous flow effects rather than only the unsteady flow features. Support for the hypothesis in which over-prediction of drag coefficient $\overline{C}_D$ occurs due to dynamic flow behaviour, is given by the r.m.s. drag coefficient $\tilde{C}_D$ and r.m.s. lift coefficient $\tilde{C}_L$. The r.m.s. drag coefficient $\tilde{C}_D$ and r.m.s. lift coefficient $\tilde{C}_L$ are calculated from the

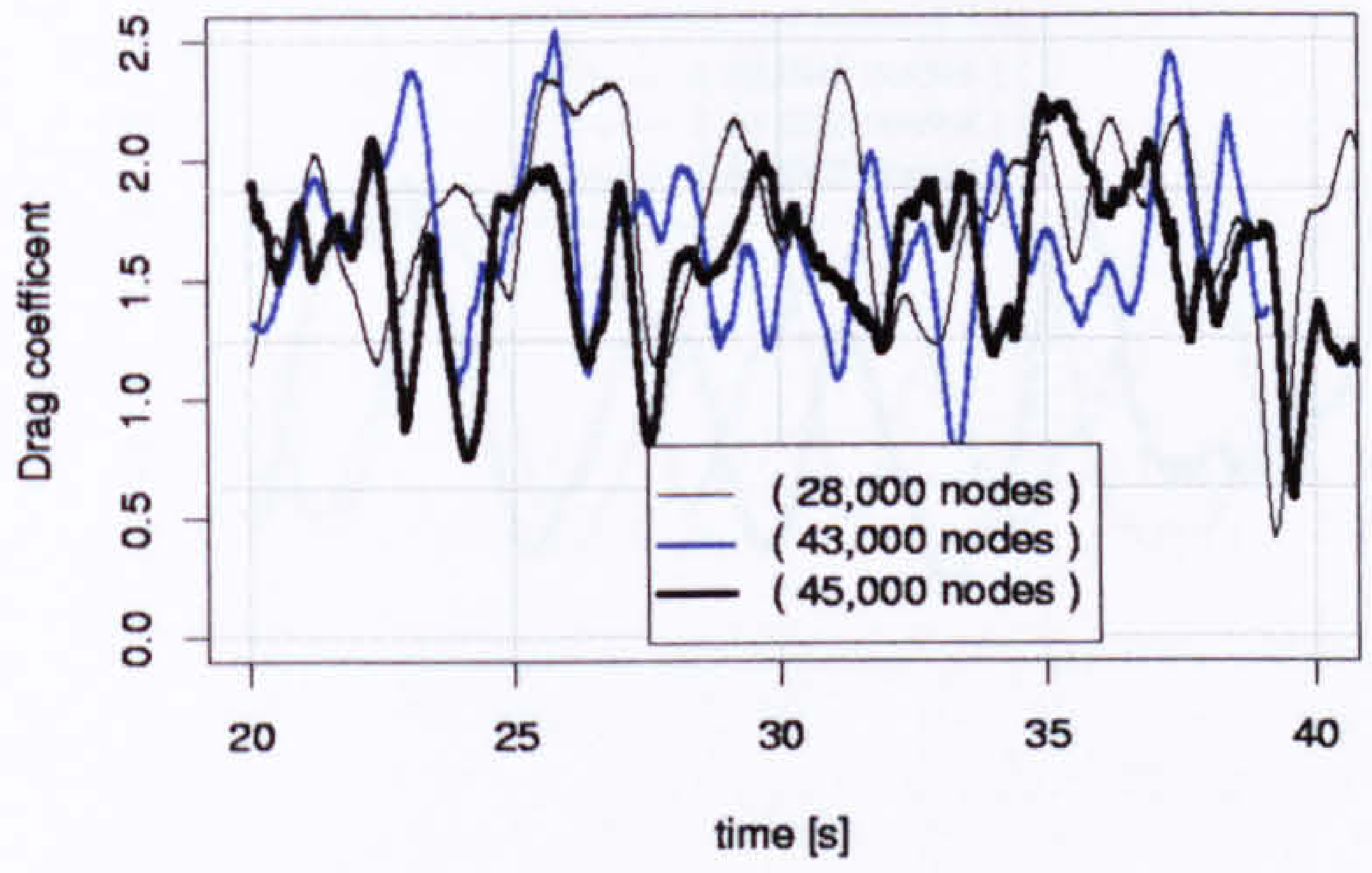

(a) DGA variables Cm=1, Cstr=1 and the superbee TVD flux limiter

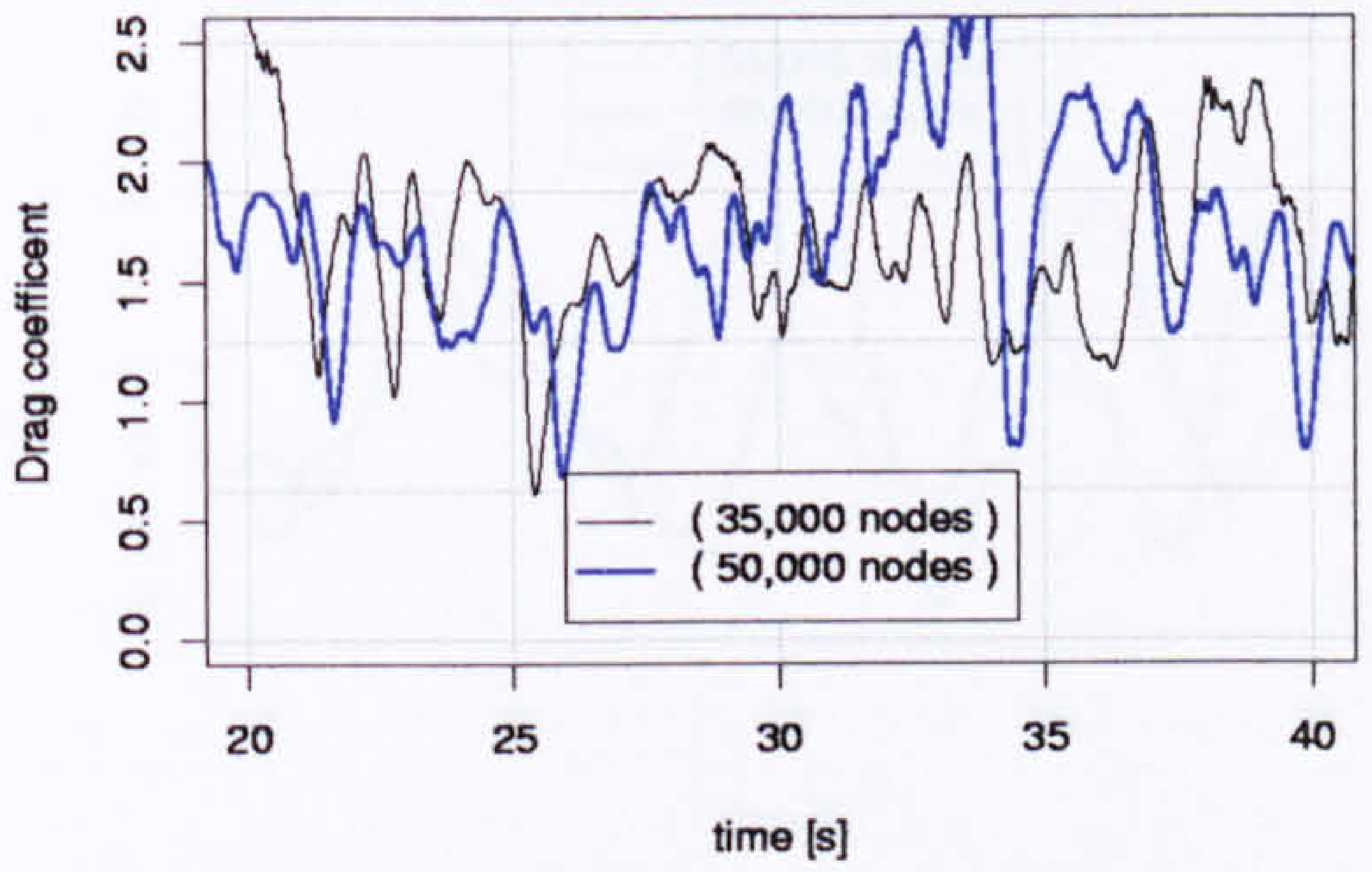

(b) DGA variables Cm=1, Cstr=1.5 and the superbee TVD flux limiter

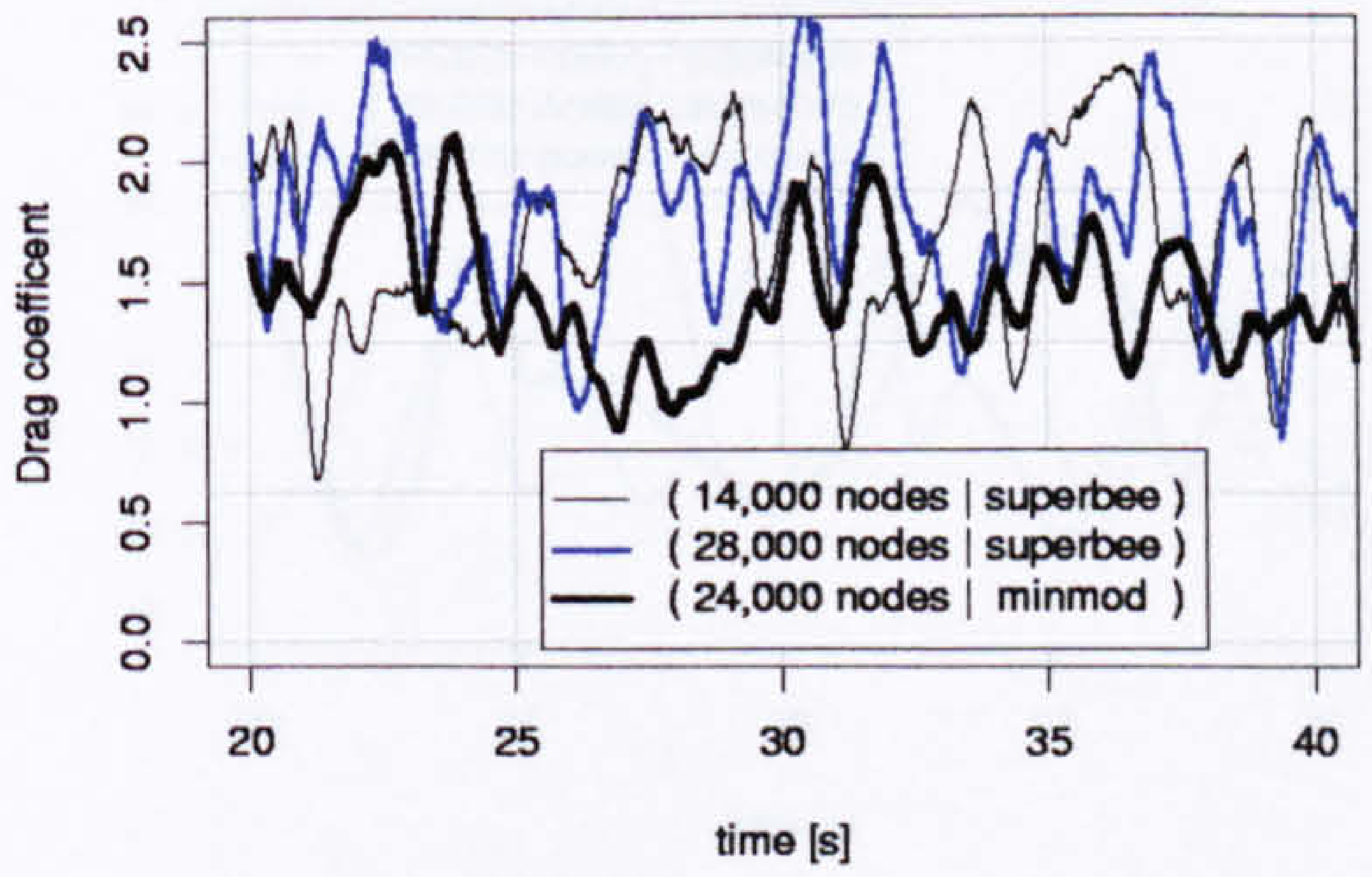

(c) DGA variables Cm=1, Cstr=2

Figure 5.5: Time history of drag coefficient C_D for simulations with DGA. The r.m.s. drag coefficient $\widetilde{C}_D$ suggests fluctuations in the drag coefficient C_D are more intense and higher than that discovered experimentally.

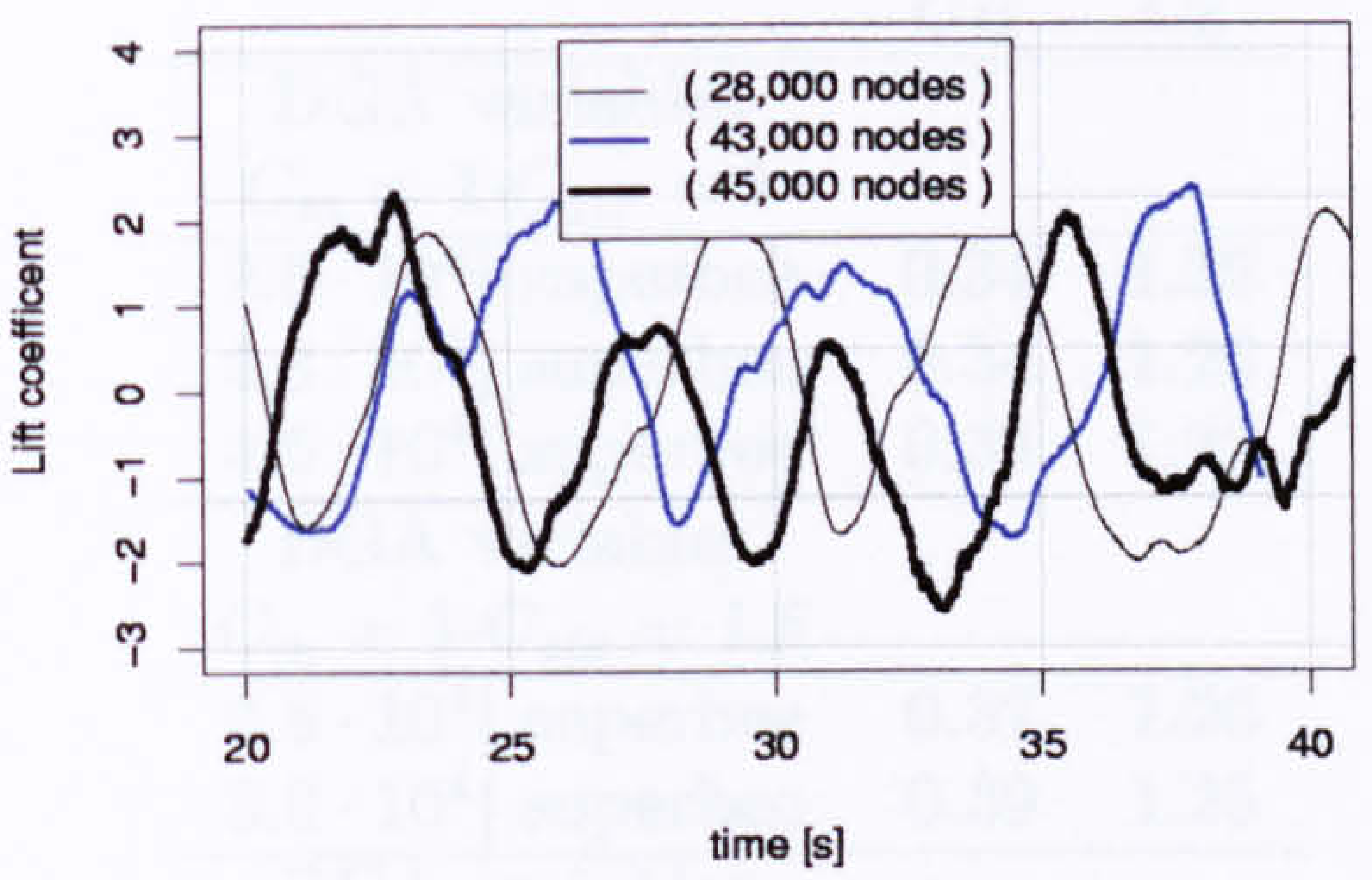

(a) DGA variables Cm=1, Cstr=1and the superbee TVD flux limiter

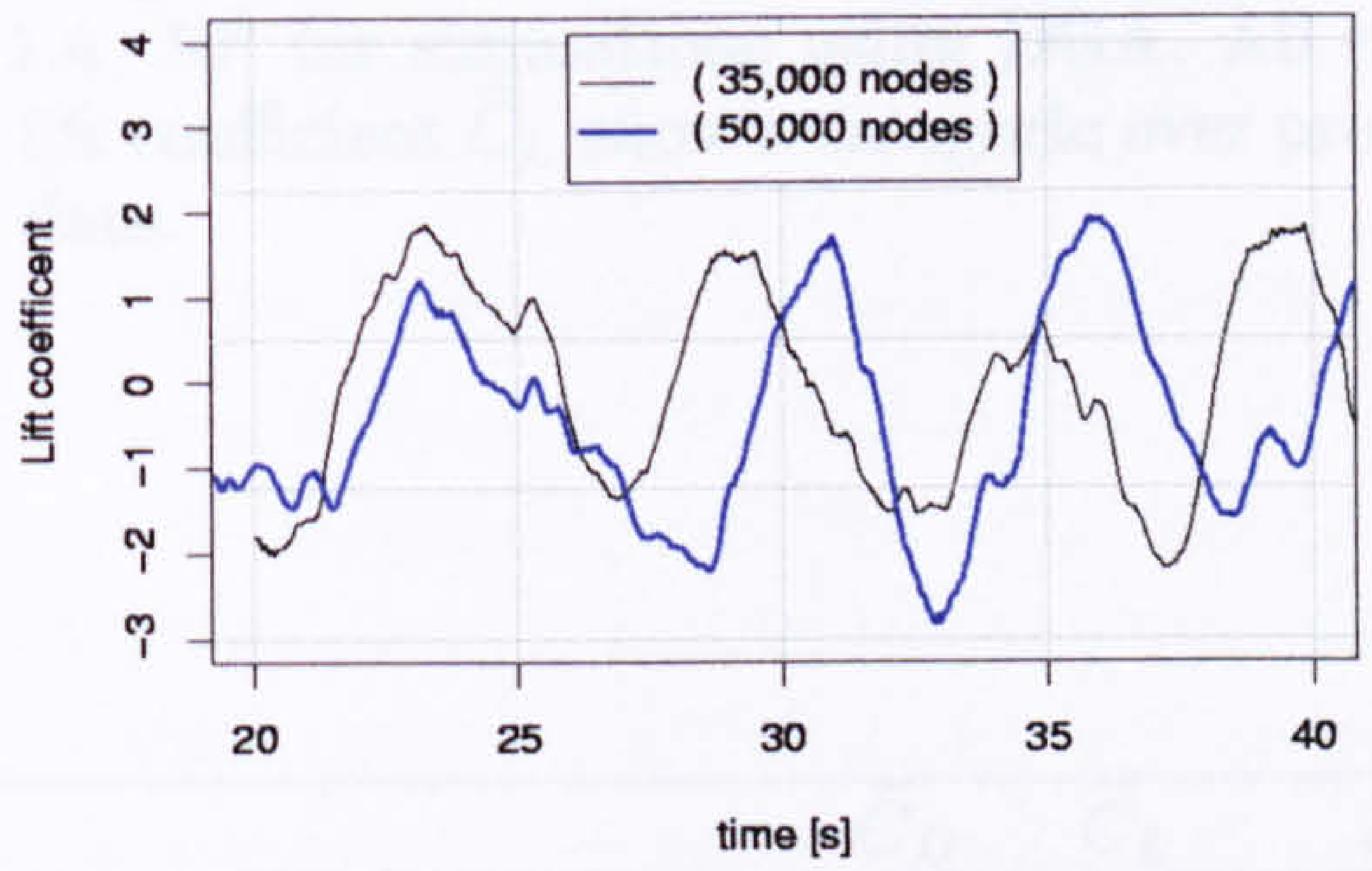

(b) DGA variables Cm=1, Cstr=1.5 and the superbee TVD flux limiter

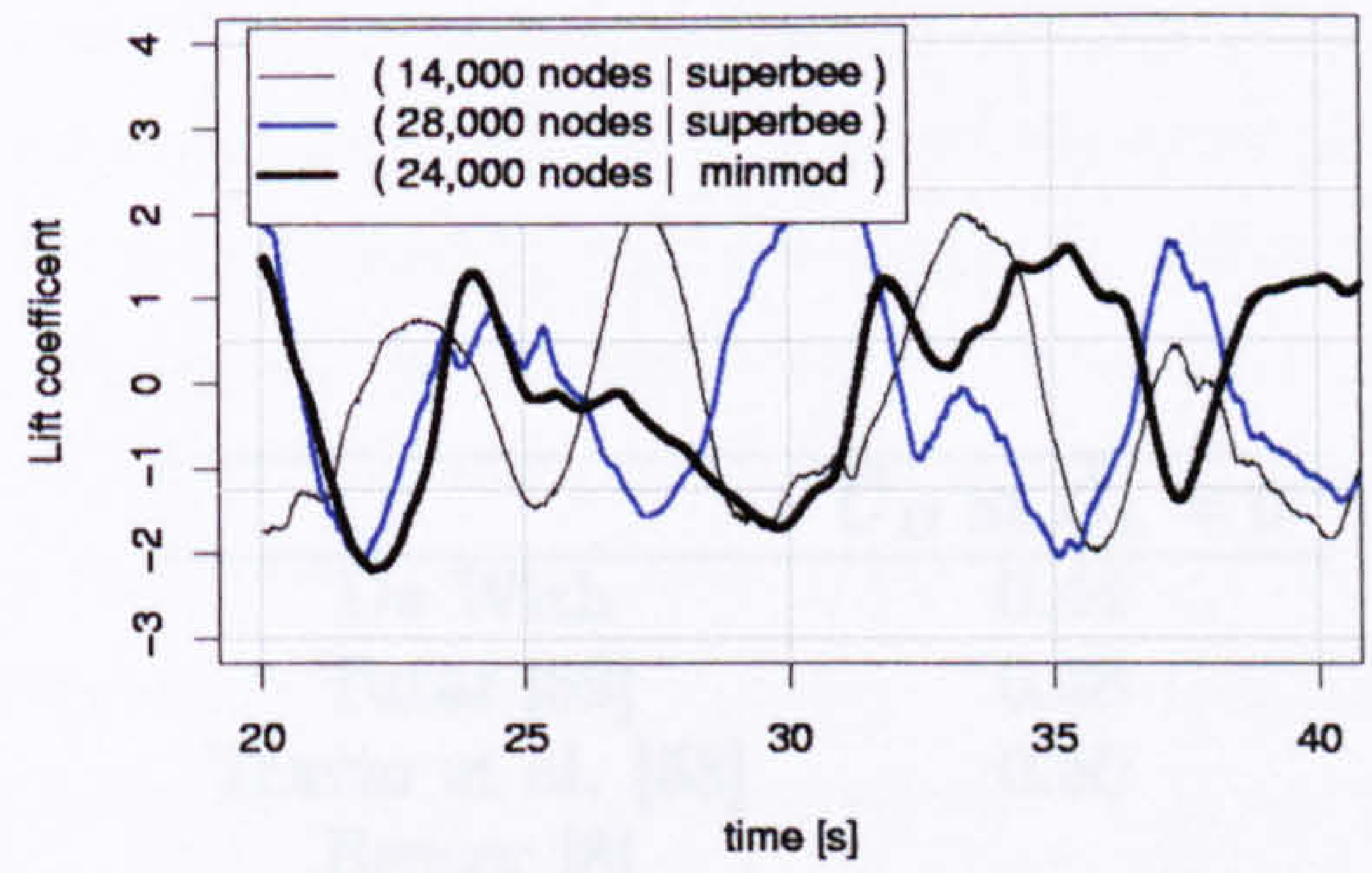

(c) DGA variables Cm=1, Cstr=2

Figure 5.6: Time history of drag coefficient C_D for simulations with DGA. The r.m.s. drag coefficient $\widetilde{C}_D$ suggests fluctuations in the drag coefficient C_D are more intense and higher than that discovered experimentally.

		$\widetilde{C}_D$	$\widetilde{C}_L$
DGA variables			
$C_m = 1\text{-}C_{str} = 1$			
$2.8 \cdot 10^4$	superbee	0.34	1.35
$4.3 \cdot 10^4$	superbee	0.34	1.26
$4.5 \cdot 10^4$	superbee	0.33	1.22
DGA variables			
$C_m = 1\text{-}C_{str} = 1.5$			
$3.5 \cdot 10^4$	superbee	0.37	1.20
$5.0 \cdot 10^4$	superbee	0.39	1.25
DGA variables			
$C_m = 1\text{-}C_{str} = 2$			
$1.4 \cdot 10^4$	superbee	0.37	1.22
$2.8 \cdot 10^4$	superbee	0.38	1.19
$2.4 \cdot 10^4$	minmod	0.29	1.00

Table 5.3: R.m.s. drag coefficient $\widetilde{C}_D$ and r.m.s. lift coefficient $\widetilde{C}_L$ for a circular cylinder at $Re = 1.4 \cdot 10^5$ for simulations using DGA. All r.m.s. values for drag coefficient $\widetilde{C}_D$ and lift coefficient $\widetilde{C}_L$ show a categoric over prediction in comparison with experimental data.

	$\widetilde{C}_D$	$\widetilde{C}_L$	Re
West & Apelt [66]	-	0.62	$1.4 \cdot 10^5$
Nishimura & Taniike [48]	0.14	0.56	$6.1 \cdot 10^4$
Norberg [49]	-	0.51	$2.0 \cdot 10^5$

Table 5.4: Experimentally obtained data for r.m.s. drag coefficient $\widetilde{C}_D$ and r.m.s. lift coefficient $\widetilde{C}_L$ at different Reynolds numbers.

	$\overline{C}_D$ at $\widetilde{C}_L = 0$
De With	0.44
Tutar [59]	0.38
Travin et al. [58]	0.50
Breuer [8]	-

Table 5.5: Based on the trend in drag coefficient $\overline{C}_D$ and lift coefficient $\widetilde{C}_L$ shown in figure 5.7 a drag coefficient $\overline{C}_D$ at lift coefficient $\widetilde{C}_L = 0$ is obtained via extrapolation.

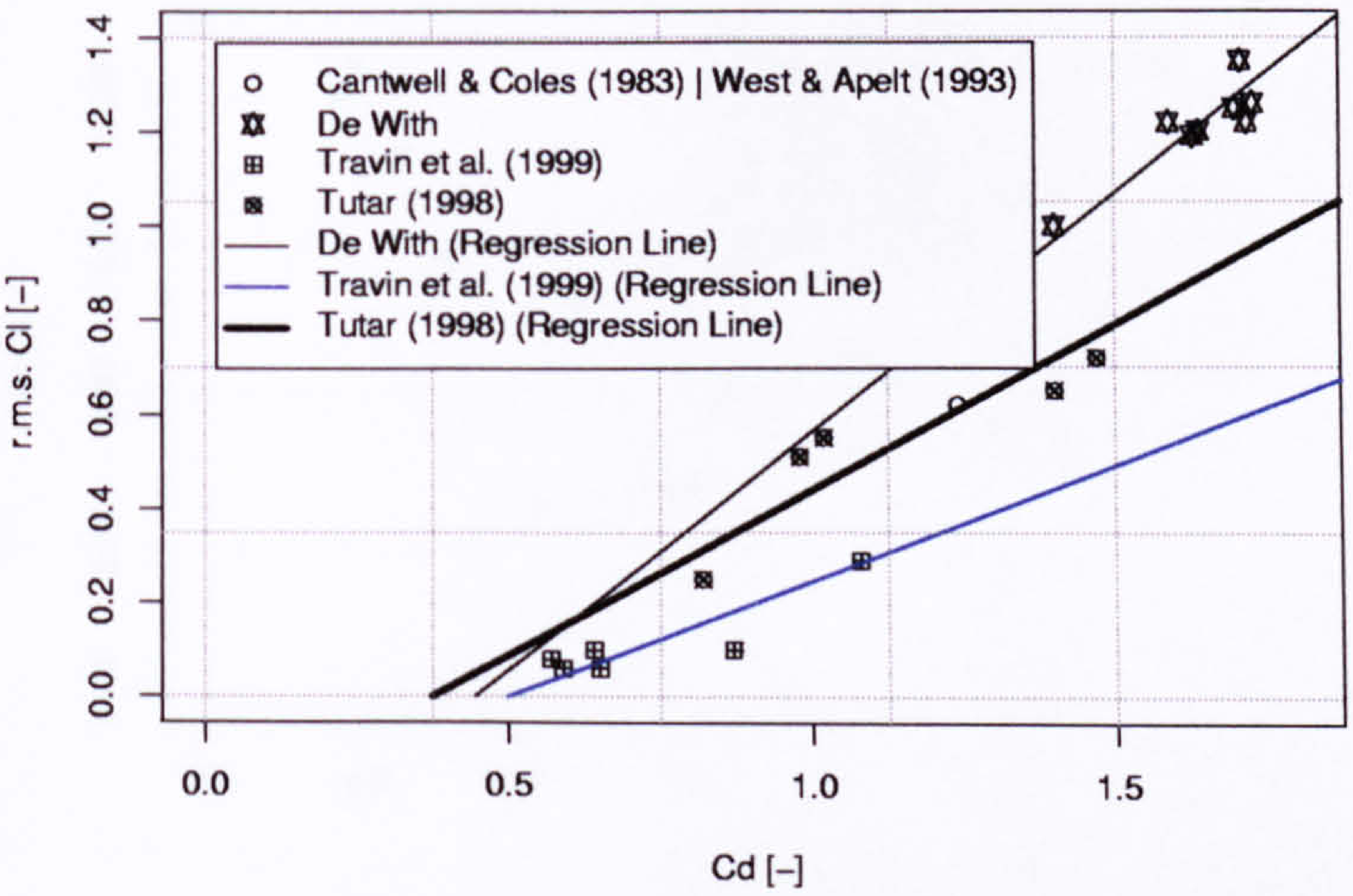

Figure 5.7: Scatter diagram for drag coefficient $\overline{C}_D$ and r.m.s. lift coefficient $\widetilde{C}_L$, with data from De With, Tutar [59] and Travin et al. [58].

drag coefficient C_D and lift coefficient C_L as shown in figures 5.5 and 5.6. The r.m.s. drag coefficient $\widetilde{C}_D$ and r.m.s. lift coefficient $\widetilde{C}_L$ are presented in table 5.3. Experimental work on the r.m.s. drag coefficient $\widetilde{C}_D$ and r.m.s. lift coefficient $\widetilde{C}_L$, by West & Apelt [66], Nishimura & Taniike [48] and Norberg [49] has given values for $\widetilde{C}_D$ and $\widetilde{C}_L$ of the order of 0.14 and 0.6 respectively, as shown in table 5.4. The values for $\widetilde{C}_D$ and $\widetilde{C}_L$ obtained from experimental work are substantially smaller then the data presented in this work. The fluctuations in the drag coefficient C_D and lift coefficient C_L are due to fluctuating motions in the vortex street. The turbulent shear stress $\overline{u'v'}$ is in good agreement with the experimental data from Cantwell & Coles [9] and therefore it is suspected that the over-prediction of $\widetilde{C}_D$ and $\widetilde{C}_L$ is due to periodical motions in the lower frequency range. The power spectrum confirms the existence of low frequency periodical motions in the order of the shedding frequency. The existence of low frequency periodical motions leads to an increase in energy dissipation and consequently an increase in drag. In other words, the mechanism by which vortices are shed from the cylinder and the periodic motions influence substantially the energy dissipation in the near wake region.

The increase of drag coefficient $\overline{C}_D$ with increasing r.m.s. lift coefficient $\widetilde{C}_L$ is apparent in numerous numerical investigations. The work of Tutar [59] and Travin et al. [58] appears to give a similar trend despite the substantial deviation in drag coefficient $\overline{C}_D$ and r.m.s. lift coefficient $\widetilde{C}_L$. The results from Tutar [59] and Travin et al. [58] together with the results presented in this thesis are combined in figure 5.7. The results indicate an increase in drag coefficient $\overline{C}_D$ with increasing values for r.m.s. lift coefficient $\widetilde{C}_L$. The figure suggest that the energy dissipation in the near wake become increasingly dependent on the mechanism by which vortices are shed from the cylinder with increasing values for r.m.s. lift coefficient $\widetilde{C}_L$. For a

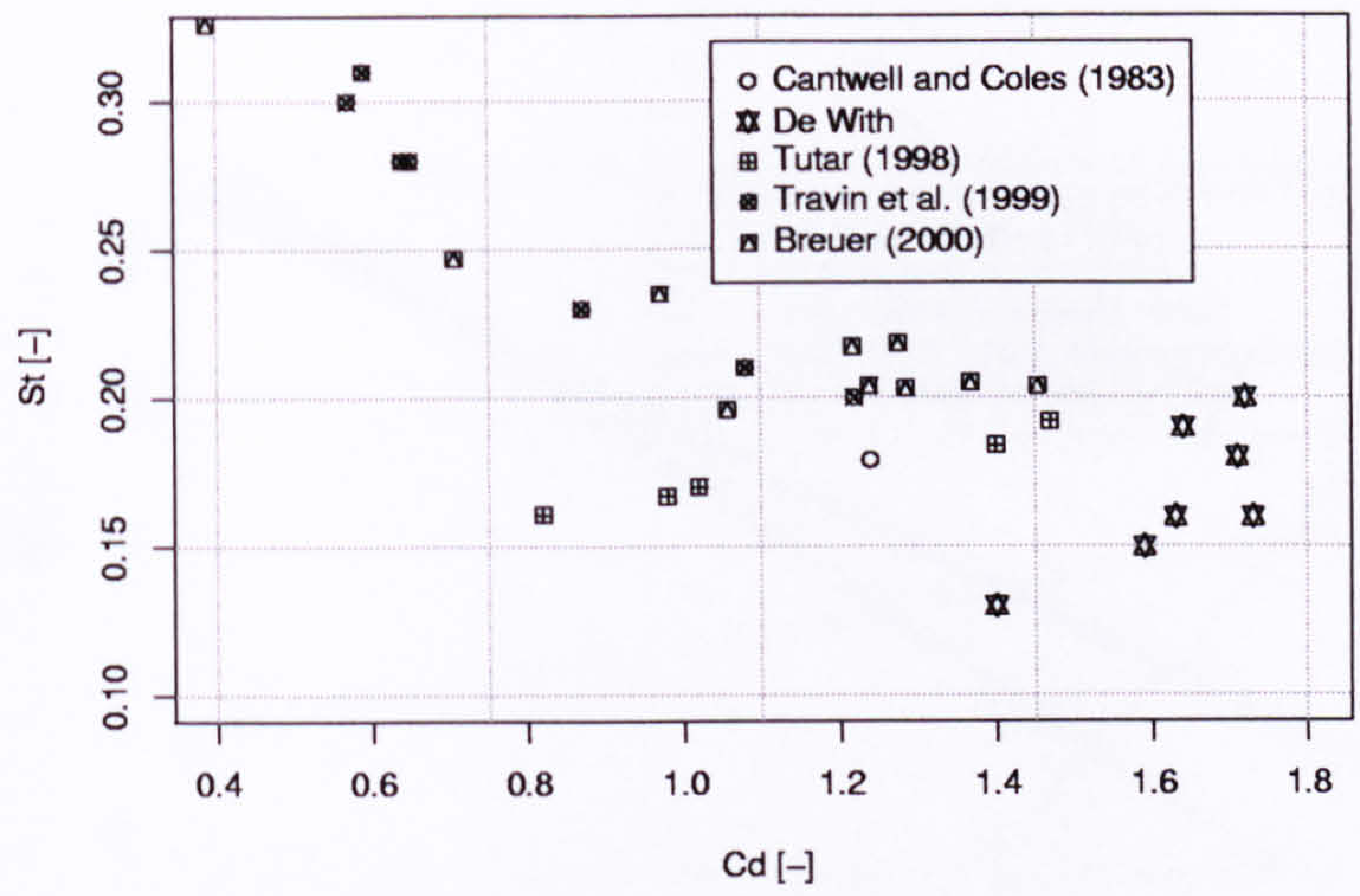

Figure 5.8: Scatter diagram for drag coefficient $\overline{C}_D$ and Strouhal number S_t, with data from De With, Tutar [59], Travin et al. [58] and Breuer [8].

flow field where the vortex shedding is less intense and lower values of r.m.s. lift coefficient $\widetilde{C}_L$ are apparent, it is most likely that the drag coefficient $\overline{C}_D$ is related to the unsteady flow field.

An extrapolation of the regression lines up to the point where the r.m.s. lift coefficient $\widetilde{C}_L$ is zero gives a hypothetical drag coefficient $\overline{C}_D$ associated to the steady flow field. The physical representation of the drag coefficient $\overline{C}_D$ at zero r.m.s. lift coefficient $\widetilde{C}_L$ is highly speculative. Nevertheless, it gives an insight into the significance of the periodical forces due to vortex shedding in relation to the drag forces. As shown in table 5.5 and figure 5.7, the drag forces due to periodic lift forces are comparatively weak in the work of Travin et al. [58], while the data presented in this work is dominated by the energy dissipation associated to the vortex shedding.

Time integrated drag coefficient $\overline{C}_D$ versus Strouhal number S_t

The consistent trends shown for drag coefficient $\overline{C}_D$ and lift coefficient $\widetilde{C}_L$ are not apparent for the Strouhal number S_t. Although there is significant correlation between the data presented here and in the numerical investigations of Tutar [59], Travin et al. [58] and Breuer [8], the corresponding regression lines have different direction, as shown in figures 5.8 and 5.9, whereby a similar trend is shown in figure 5.10. The data presented both in this thesis and in the work of Tutar [59] shows positive regression. In contrast, negative regression is shown in the work of Travin et al. [58] and Breuer [8].

The key question now centres around the physical representation of this phenomenon. It is important to note that the generally accepted negative correlation

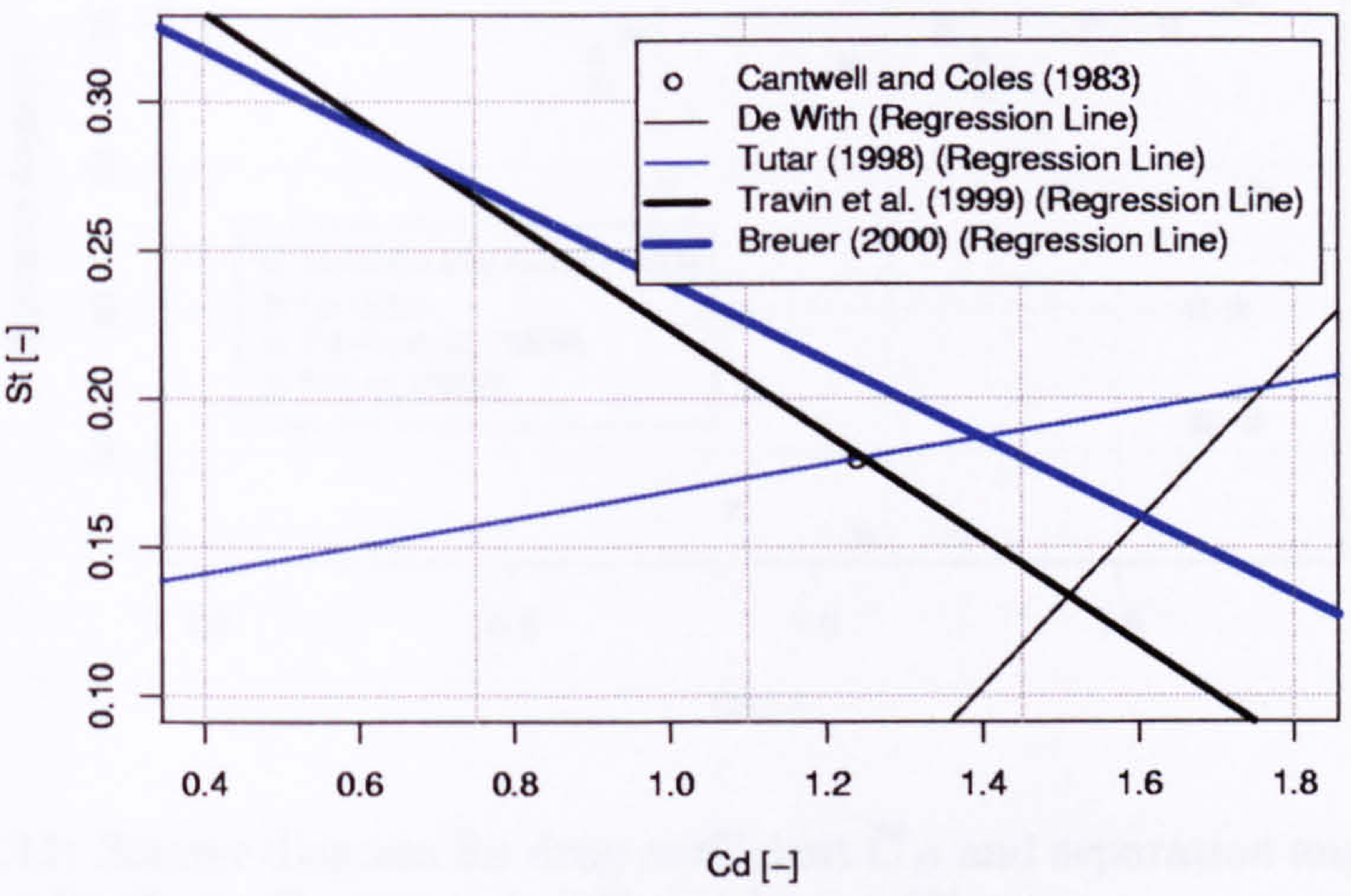

Figure 5.9: Regression lines based on figure 5.8 for drag coefficient $\overline{C}_D$ and Strouhal number S_t, with data from De With, Tutar [59], Travin et al. [58] and Breuer [8].

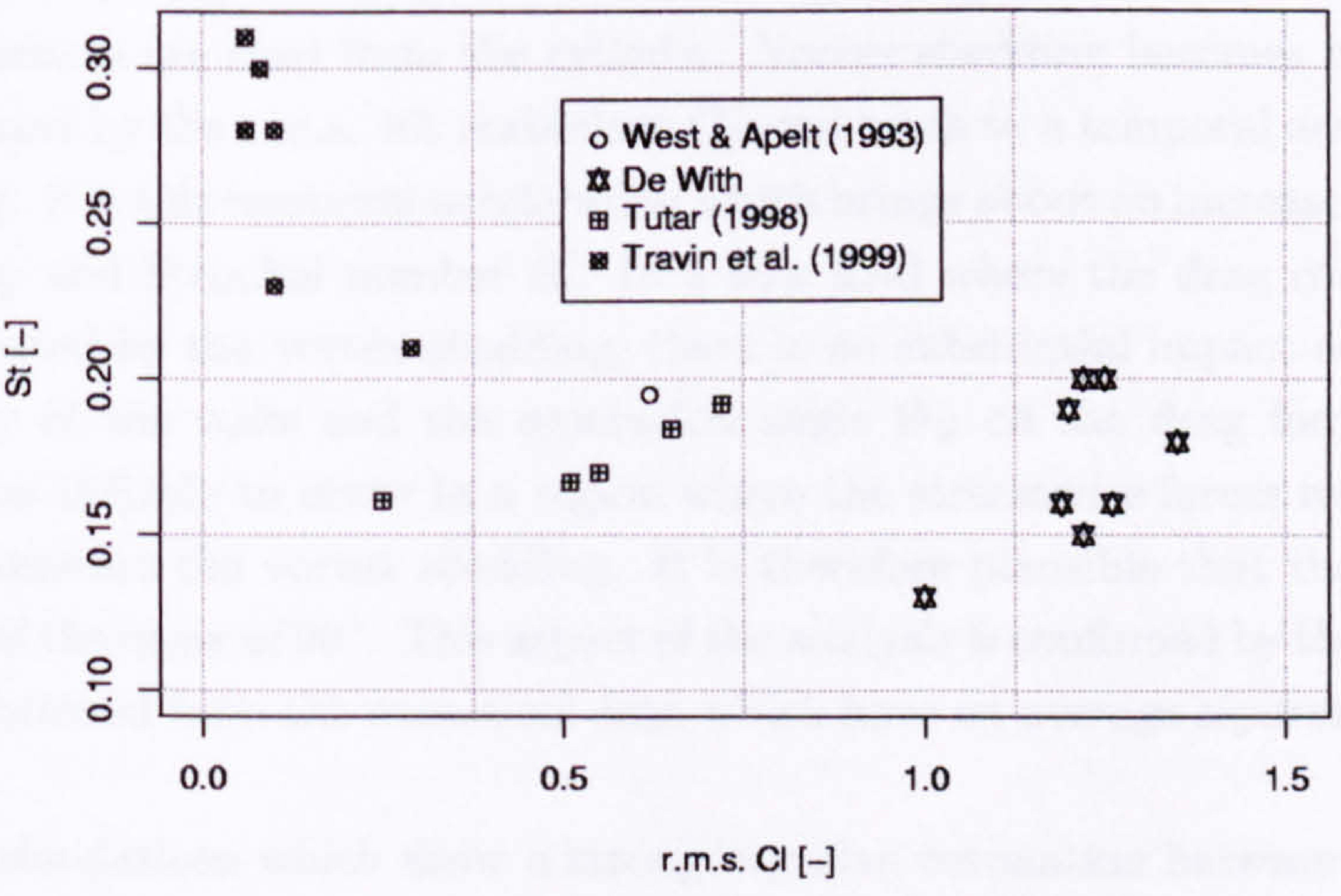

Figure 5.10: Scatter diagram for r.m.s. lift coefficient $\widetilde{C}_L$ and Strouhal number S_t, with data from De With, Tutar [59] and Travin et al. [58].

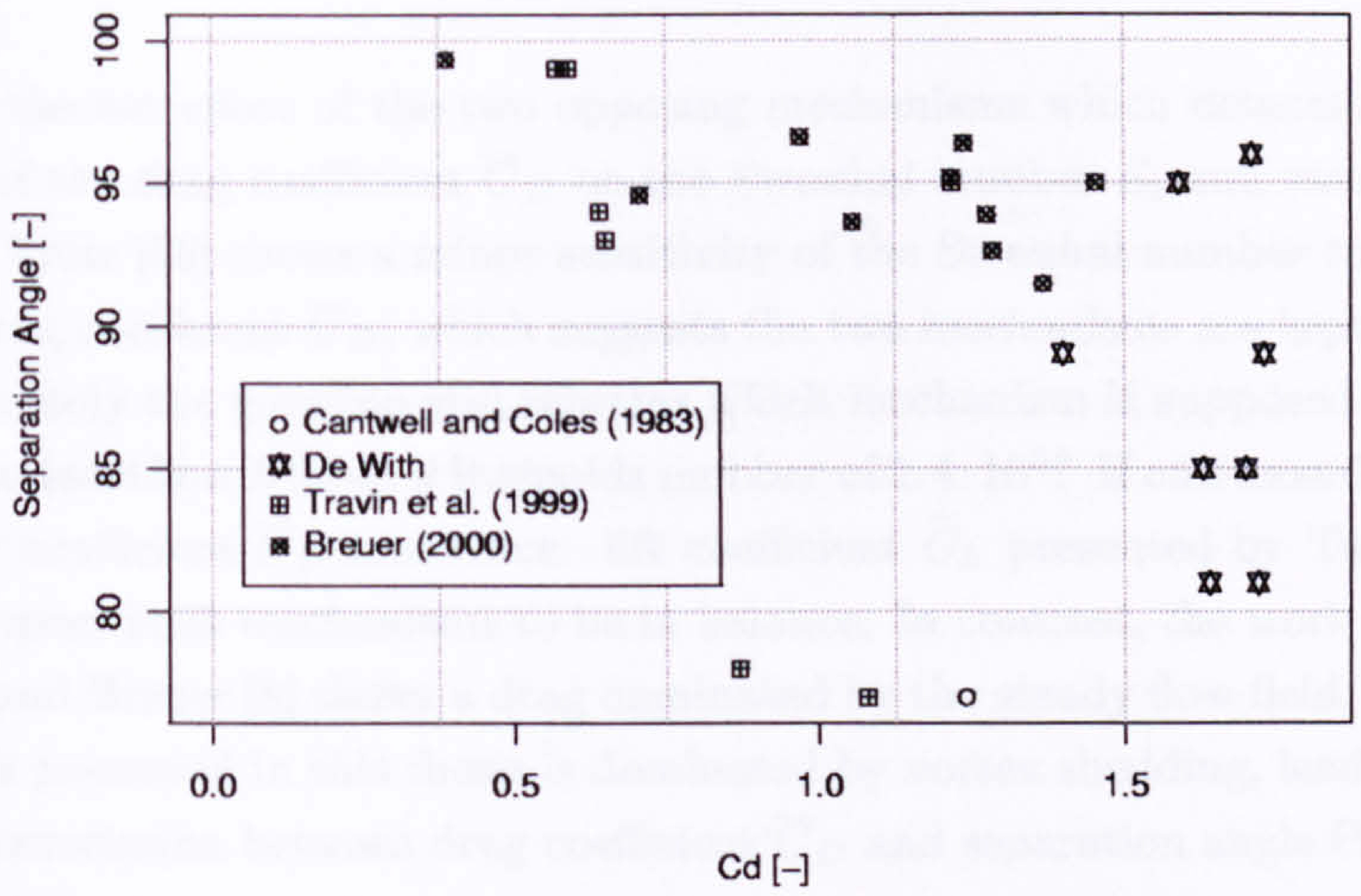

Figure 5.11: Scatter diagram for drag coefficient $\overline{C}_D$ and separation angle Θ_S, with data from De With, Travin et al. [58] and Breuer [8].

between drag coefficient $\overline{C}_D$ and Strouhal number S_t in the critical flow regime is due to the rapid transition from the sub-critical to the super-critical flow regime. The simulations presented in this work are not intended to model transition as such. Instead, a constant Reynolds number is chosen in the sub-critical flow regime. The variation in drag coefficient $\overline{C}_D$ as discovered in this work is purely due to numerics and must be seen as such.

In case of a positive regression a plausible argument is as follows: the increase in drag coefficient $\overline{C}_D$ is mainly due to increasing energy losses in the mechanism by which vortices are shed from the cylinder. Vortex shedding becomes more intense as indicated by the r.m.s. lift coefficient $\widetilde{C}_L$ and leads to a temporal acceleration of shedding. It is this temporal acceleration which brings about an increase in shedding frequency and Strouhal number S_t. In a flow field where the drag coefficient $\overline{C}_D$ is dominated by the vortex shedding, there is no substantial impact of the steady geometry of the wake and the separation angle Θ_S on the drag force. Instead, separation is likely to occur in a region where the streamwise forces remain low so as to accelerate the vortex shedding. It is therefore plausible that the separation angle is of the order of 90°. This aspect of the analysis is confirmed by the separation angles obtained from the numerical data which have an average separation angle of 88°.

The simulations which show a strong negative correlation between drag coefficient $\overline{C}_D$ and Strouhal number S_t show values for the r.m.s. lift coefficient $\widetilde{C}_L$which are substantially smaller compared to the experimental data of West & Apelt [66], Nishimura & Taniike [48] and Norberg [49]. The drag is dominated by the steady flow field and an increase in separation angle confines the width of the wake region leading to a reduction of both drag coefficient $\overline{C}_D$ and r.m.s. lift coefficient $\widetilde{C}_L$. A reduction in the dimensions of the wake leads to a reduction in Strouhal number S_t, as also seen in bluff body flow for Reynolds numbers in the super-critical flow regime.

It is the net effect of the two opposing mechanisms which determines the sensitivity of the drag coefficient $\overline{C}_D$ on the Strouhal number S_t and vice versa. The data of Tutar [59] shows a minor sensitivity of the Strouhal number to a variation in the drag coefficient $\overline{C}_D$, which suggests the two mechanisms are kept in balance. Unfortunately the question still remains which mechanism is supposed to be dominant in a wake flow field at a Reynolds number of $1.4 \cdot 10^5$? If one considers the data for drag coefficient $\overline{C}_D$ and r.m.s. lift coefficient $\widetilde{C}_L$ presented by Tutar [59] one would expect both mechanisms to be in balance. In contrast, the work of Travin et al. [58] and Breuer [8] shows a drag dominated by the steady flow field. Conversely, the work presented in this thesis is dominated by vortex shedding, leading to a low level of correlation between drag coefficient $\overline{C}_D$ and separation angle Θ_S, as shown in table 5.2.

An important remark to be added to the discussion is the importance of the separation angle Θ_S to the width of the wake. The correlation between drag coefficient $\overline{C}_D$ and separation angle Θ_S in the data of Travin et al. [58] is such that it not fully supports the analysis given in the above paragraphs. Instead, it is the drag coefficient $\overline{C}_D$ of Breuer [8] which has a better correlation with the separation angle Θ_S despite the increase of the r.m.s. lift coefficient $\widetilde{C}_L$ as shown in table 5.2 and 5.11. One reason for this phenomenon could be due to the geometrical aspects of the wake, where the separation angle does not correlate completely with the width of the wake and the pressure field around the cylinder. The reduction in correlation between separation angle Θ_S and width of the wake could reflect the quality of the mesh in the region adjacent to the wall and in the near wake region. A potential weakness in modelling the shear layers and their curvature would potentially effect the steady flow field and the drag coefficient $\overline{C}_D$, separation angle Θ_S relation.

The phenomenon investigated in the above paragraph is due to weaknesses in the numerical scheme, turbulence model and mesh. The existence of both mechanisms is difficult to validate in an experimental investigation. The simulations are set-up to resolve an identical flow problem and numerical differences apparent in these simulations are impossible to emulate in an experimental investigation. Nevertheless, the trends discovered give an important insight into the numerical aspects of numerical scheme, turbulence model and mesh resolution. A combination of the numerical scheme, turbulence model and mesh as used in this thesis show the steady flow field features are comparatively under exposed as a consequence the steady flow features do not have the impact on the flow field as shown in the work of Travin et al. [58] and Breuer [8].

An important aspect is the dimensionality of the CFD code. The dimensionality correlates with the trend in the drag coefficient $\overline{C}_D$ versus Strouhal number S_t relation. A negative trend is seen in the work of Travin et al. [58] and Breuer [8] where both have used a 3-dimensional CFD code, whilst the work presented in this thesis and the work done by Tutar [59] is carried out with a 2-dimensional CFD code showing a positive trend in the drag coefficient $\overline{C}_D$ versus Strouhal number S_t relation. It could be argued that for 3-dimensional flow simulation an additional dissipation takes place in the spanwise direction. The magnitude of dissipation in this direction is dependent on the amount of turbulent eddies and the width of the wake. As a consequence, the flow mechanism associated to the steady flow field, as described in the paragraphs above, will become more dominant. In a 2-dimensional CFD code the energy will be scattered backwards into the main flow which perhaps leads to a more intense vortex shedding and consequently an increase in drag.

Another aspect in this analysis is the mesh design. In the work of Travin et al. [58] and Breuer [8], a body-fitted structured mesh is utilised with a mesh size per plane varying between $7 \cdot 10^3$ to $6 \cdot 10^4$ nodes. The mesh shows a high resolution in the vicinity of the wall and a graduate decay in the downstream direction. The mesh used in the work of Travin et al. [58] is of size of $1 \cdot 10^4$ nodes for most simulations. Although these simulations are carried out with a 3-dimensional solver with 50 planes in the spanwise direction the number looks insufficient for calculating the wake region in a physically correct manner. The mesh does not take account of the complex physics in the shear layers which require a high mesh resolution. Instead, it only resolves the boundary layer in a sophisticated manner. The lack of mesh resolution in the recirculation which is apparent in the work of Breuer [8] and particularly in the work of Travin et al. [58] could possibly be the cause of the negative trend in the drag coefficient $\overline{C}_D$ versus Strouhal number S_t relation. Although the work of Tutar [59] presents a positive trend in the drag coefficient $\overline{C}_D$ versus Strouhal number S_t relation, similar weaknesses in the structured mesh used are apparent. These weaknesses again give strength to the argument that DGA is an important tool in mesh design to model the necessary physics in the flow field. Nevertheless, its characteristic to link strongly its mesh design to potential flow motions in combination with the REACFLOW explicit CFD solver could lead to over-prediction of the dispersive features in the flow field.

The mechanisms presented in the above paragraphs can be used to give a further insight in some of the drawbacks in the modelling scheme that has been presented and used in the simulations. The intense vortex shedding and the drag forces associated with these both mechanisms are likely to cause breakdown of the vortex street and explains the lack of cohesion in the flow field. The results could suggest that the flow field is lacking viscosity, either numerical or turbulent. However, the replaced Reynolds numbers as presented in table 4.4 suggest there is sufficient viscosity. Instead, it is likely that the 2-dimensional simplification of the flow field is a main cause for the over-prediction in r.m.s. lift coefficient $\widetilde{C}_L$ and consequently the drag coefficient $\overline{C}_D$. Due to this simplification of the flow field, energy associated with turbulence is not dissipated in the spanwise direction but instead scattered backwards into the main flow stream leading to an intensification of vortex shedding.

The dispersion within the flow field is normally associated with the non-linear advection terms and this could indicate better modelling of these terms is required.

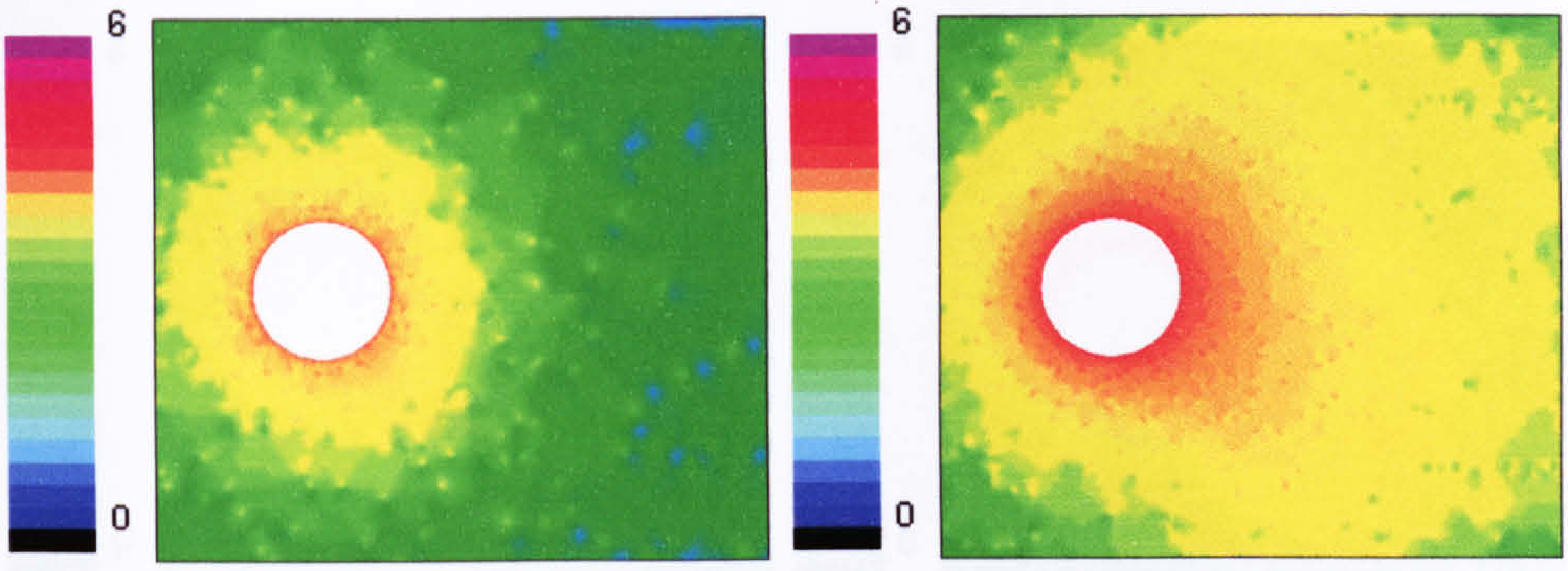

(a) 18,000 nodes

(b) 33,000 nodes

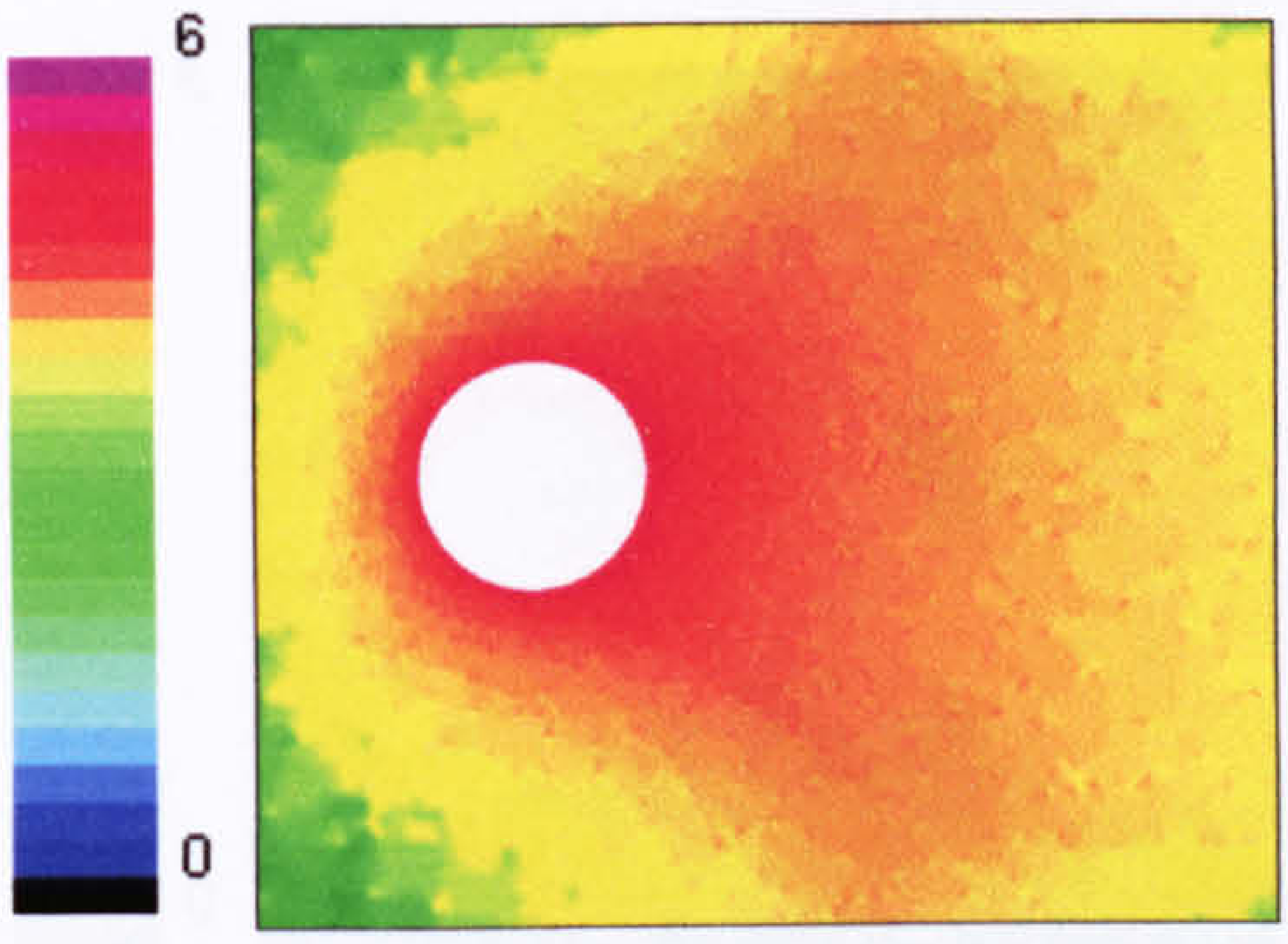

(c) 61,000 nodes

Figure 5.12: Mesh resolution $\left(\log \frac{1}{A_{tr}}\right)$ at $t = 30$ around circular cylinder for simulations using conventional mesh.

In this respect, it is important to mention the upwinding scheme and TVD flux limiter implemented in the REACFLOW code. The advective terms are discretised in a classical upwind manner which is highly dispersive when combined with a piecewise constant representation of the variables to enable an accuracy improvement. The selection of the superbee TVD flux limiter to suppress the dispersion in the advective terms in this respect maybe not the most suitable. The superbee limiter yields sharper profiles near discontinuities, but is less robust than the minmod limiter.

5.2 Effects of mesh refinement

The results obtained with the superbee flux limiter do not maintain a distinct correlation with any of the numerical features of the simulation. For example, an increase in mesh resolution can have different effects on the time integrated velocity field dependent on the selected refinement conditions. The only correlation that has been discovered in the simulations is the increase in turbulent shear stress $\overline{u'v'}$ with increasing mesh resolution. The lack of correlation between the different

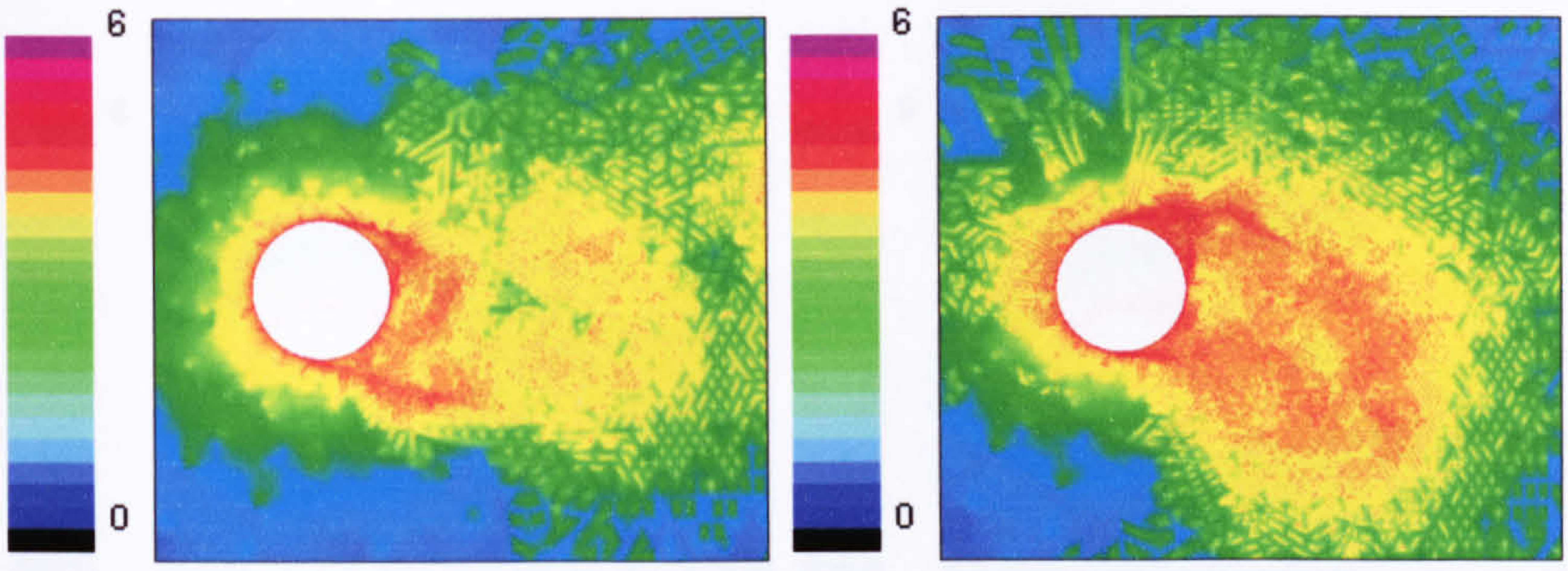

(a) 28,000 nodes

(b) 43,000 nodes

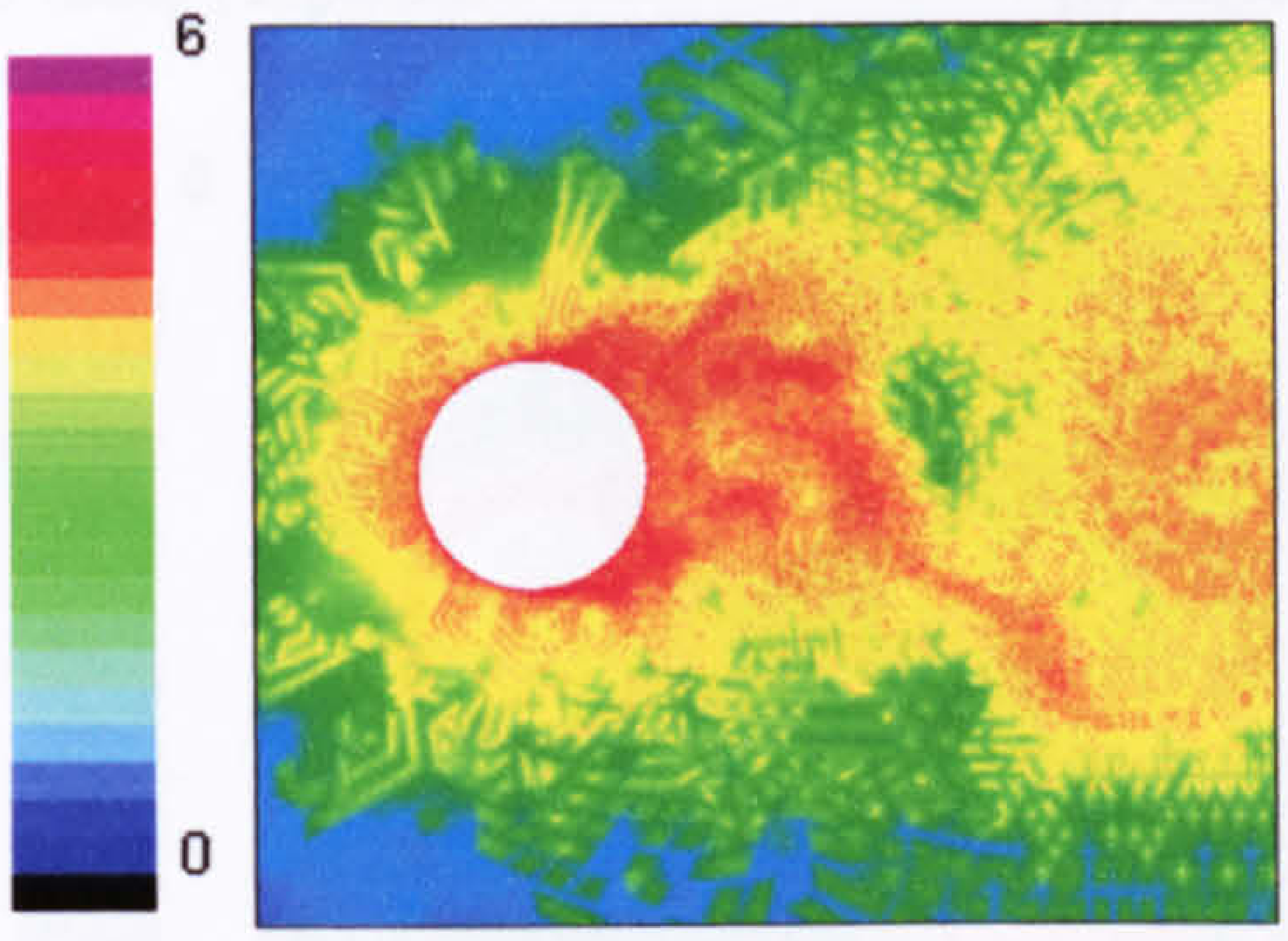

(c) 45,000 nodes

Figure 5.13: Snap shot of the mesh resolution $\left(\log \frac{1}{A_{tr}}\right)$ at $t = 30$ in fully-developed flow around circular cylinder for simulations using DGA variables C_m = 1-$C_{str} = 1$ and the superbee TVD flux limiter.

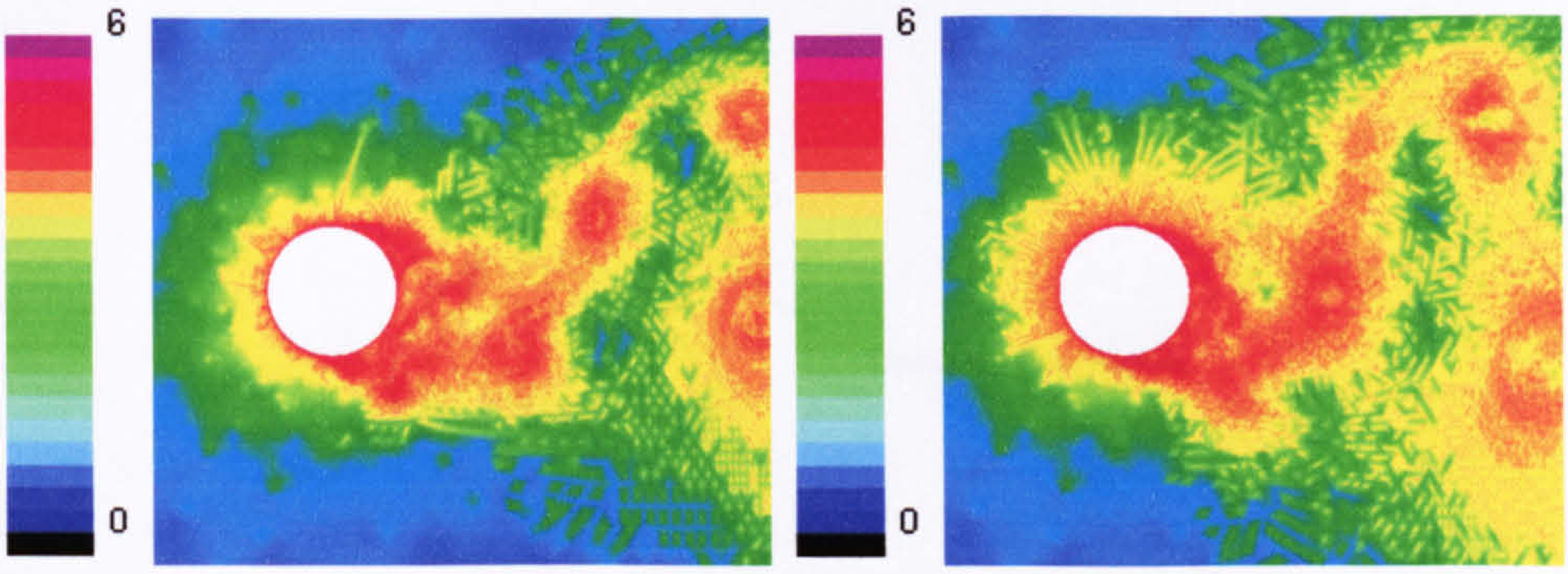

(a) 35,000 nodes

(b) 50,000 nodes

Figure 5.14: Snap shot of the mesh resolution $\left(\log \frac{1}{A_{tr}}\right)$ at $t = 30$ in fully-developed flow around circular cylinder for simulations using DGA variables C_m = 1-C_{str} = 1.5 and the superbee TVD flux limiter.

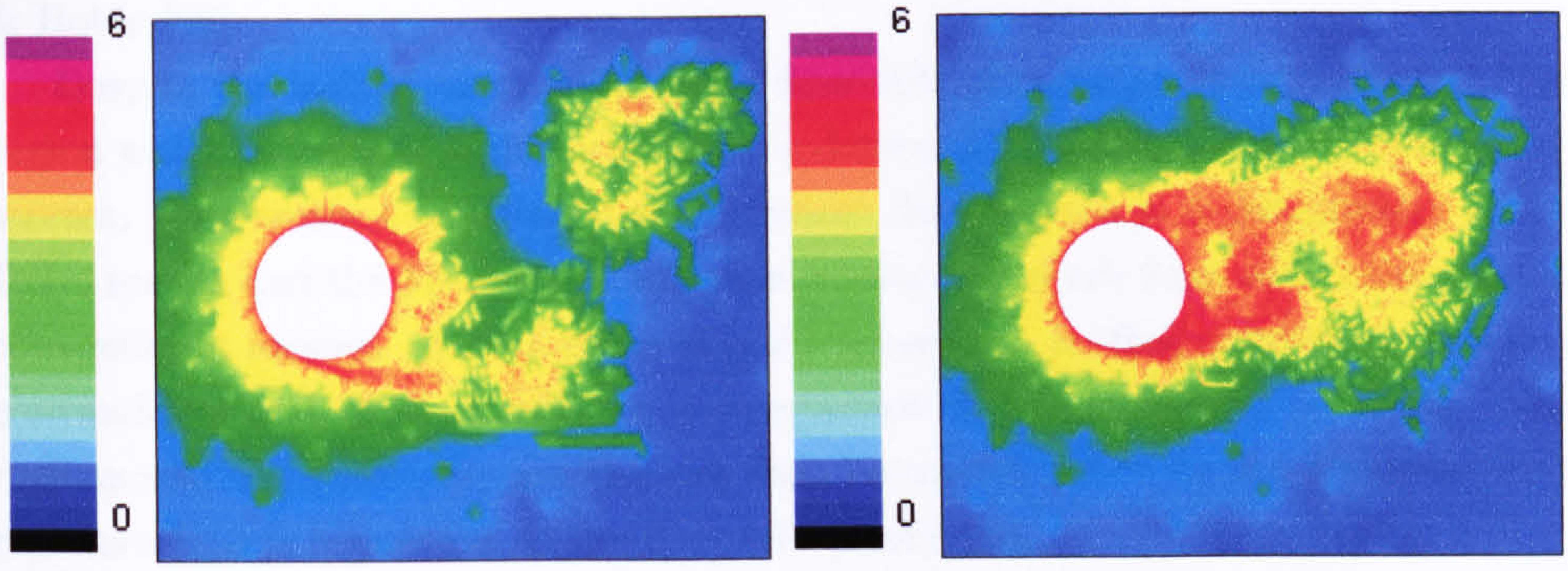

(a) 14,000 nodes | superbee

(b) 28,000 nodes | superbee

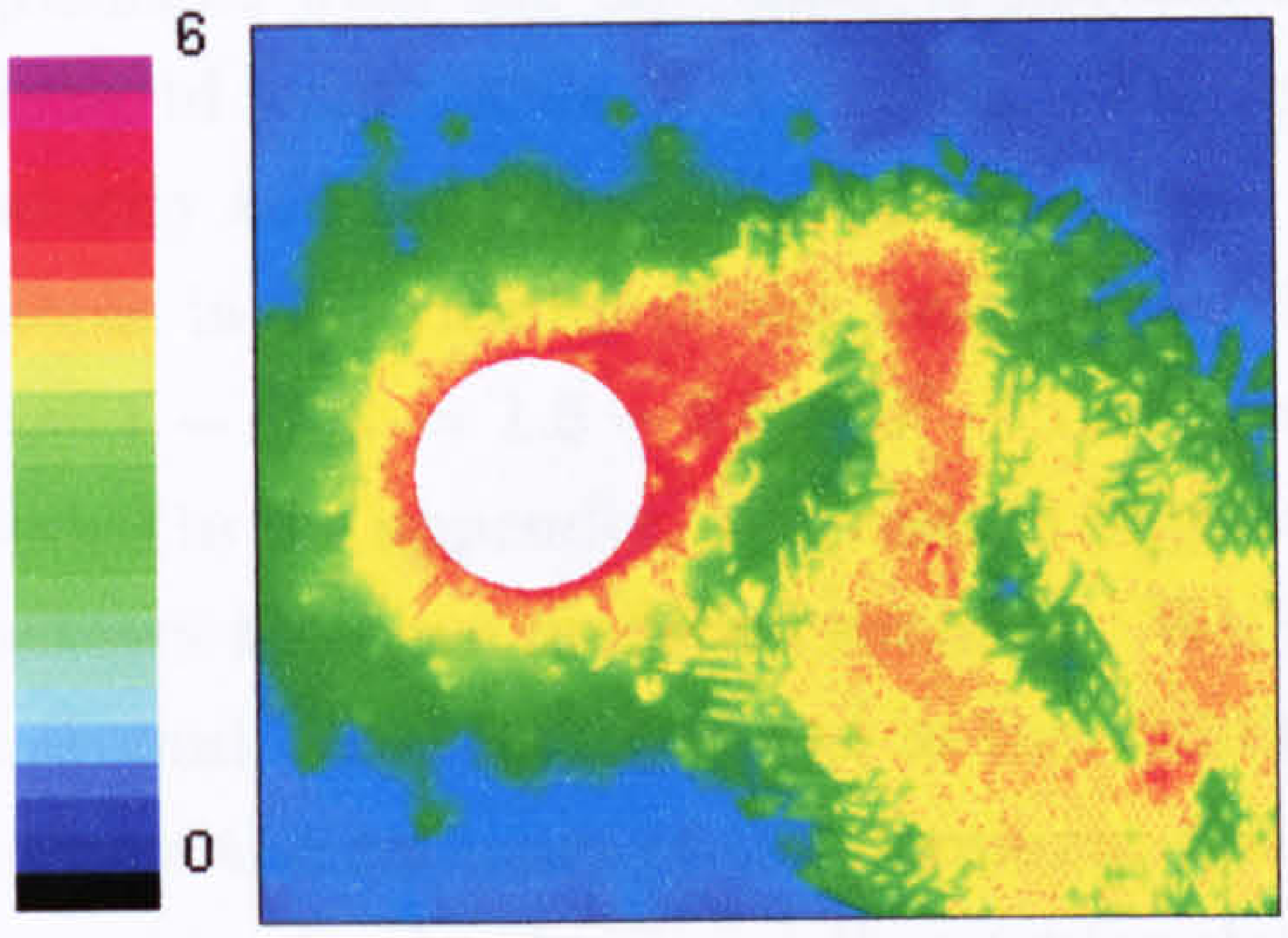

(c) 24,000 nodes | minmod

Figure 5.15: Snap shot of the mesh resolution $\left(\log \frac{1}{A_{tr}}\right)$ at $t = 30$ in fully-developed flow around circular cylinder for simulations using DGA variables $C_m = 1\text{-}C_{str} = 2$.

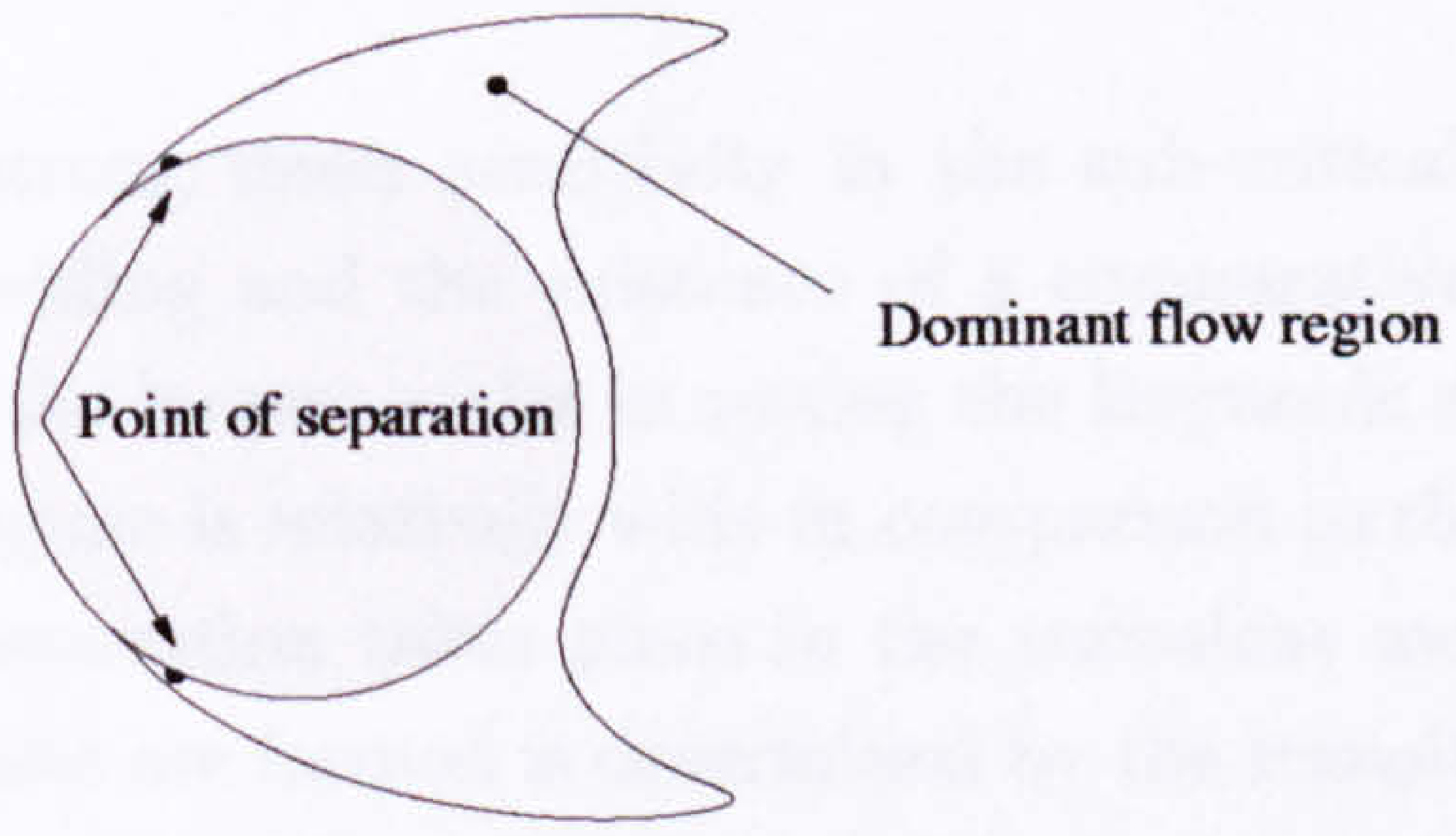

Figure 5.16: The indicated region is the dominant flow region where transition from laminar to turbulent takes place and turbulent eddies are initiated. The region is of high importance in the prediction of the flow field further downstream.

time integrated flow features and the substantial errors in the flow field prediction confirm previous numerical investigations of Travin et al. [58], Breuer [8] and Tutar & Holdø [60].

Despite the lack of correlation in the flow field parameters it is the initial flow region which remains of high importance in determining the flow field further downstream. One method to detect the important flow regions is a comparison of the DGA results and the DGA mesh with the results and mesh from simulations using conventional meshes. When there is good agreement in flow prediction between conventional and DGA simulation a comparison of the mesh can be made. The regions which are similarly meshed can then be considered to be the dominant flow regions which is important to the flow field prediction.

A comparison of the simulation with DGA variables $C_m = 1$, $C_{str} = 1.5$ and $5.0 \cdot 10^4$ nodes and the simulation with DGA variables $C_m = 1$, $C_{str} = 2$ and $1.4 \cdot 10^4$ nodes shows good agreement with the one using a conventional mesh containing $6.1 \cdot 10^4$ nodes and a subgrid length scale of $\Delta = \sqrt{A_{tr}}$. The agreement covers both the time integrated velocity and the critical flow parameters. All three simulations show similar flow patterns in the vicinity of the wall, as seen in the movie $\sqrt{A_{tr}} - 6.1 \cdot 10^4 - 1.avi$, $C_m = 1 - C_{str} = 1.5 - 5.0 \cdot 10^4 - 1.avi$ and $C_m = 1 - C_{str} = 2 - 1.4 \cdot 10^4 - 1.avi$ included in the appendix. The results suggest that flow separation and transition to turbulence has been modelled similarly. With the mesh only equal in the narrow regions around the shear layer and in the vicinity of the wall (figures 5.12 to 5.15) one can draw the contours of the dominant flow region, as shown in figure 5.16. The flow motions in the dominant flow region determine the flow field further downstream.

Travin et al. [58] concluded that a laminar separating shear layer is more mesh sensitive than a separation that takes place in the turbulent mode. The work of Herfjord et al. [24] investigated the fluid structure interaction in the case of two dependent cylinders in vortex-induced vibrations. Herfjord et al. [24] obtained better numerical agreement with experimental data for the flow field around the downstream cylinder and in this work, it is the flow around the downstream cylinder which contains a comparatively high rate of turbulence before the point of separation.

It is likely the strong mesh sensitivity in the sub-critical flow regime is due to strong vortex shedding and the existence of a comparatively wide wake which increases the role of the largest scales in setting the Reynolds stresses. The wake in a sub-critical flow regime is relatively wide in comparison to that in a super-critical flow regime where separation takes place in the turbulent mode. The process by which the largest scales are formed is determined by the transition process, starting after the point of separation. It is the lack of numerical control on the location and progression by which transition from laminar to turbulent flow conditions takes place which leads to the strong sensitivity of flow prediction on mesh resolution.

Mesh resolution and flow prediction

The underlying theme both in this work and other work dealing with the flow around a cylinder is that most attention should be paid to the regions adjacent to the cylinder and the shear layers in the wake region. Despite the obvious and general sense in this statement, one must question why a further mesh refinement in the vicinity of the wall does not improve the flow prediction. The simulation with DGA variables $C_m = 1$, $C_{str} = 1$ and $4.3 \cdot 10^4$ nodes, and the simulation DGA variables $C_m = 1$, $C_{str} = 2$ and $2.8 \cdot 10^4$ nodes respectively have a substantial increase of mesh resolution in comparison to the simulations with a mesh containing $2.8 \cdot 10^4$ and $1.4 \cdot 10^4$ nodes respectively. The reduced quality of the prediction could be due to separation taking place in turbulent mode. However, the thin boundary layer up to the point of separation is resolved by about 6 to 10 elements and this number is smaller than in the work of Tutar at al. [61] and Breuer [8] who used 15 and 25 grid points respectively. There is no turbulent kinetic energy until the point of separation, which suggests that separation takes place in the laminar mode as experimentally expected for flow around a circular cylinder in a sub-critical flow regime. It is only close to the point of separation and in the surrounding shear layers where the mesh resolution exceeds that used in the work of Tutar et al. [61] and Breuer [8]. In this region, the shear layer contains about 30 elements in radial direction, while in the circumferential direction the mesh resolution is about 3 elements per degree. In comparison, Tutar et al. [61] and Breuer [8] used 0.5 and 1 element per degree respectively. The reason for strong mesh refinement in the circumferential direction, is because mesh refinement in an element always takes place over the longest edge, giving the tendency to create equilateral shaped elements. As a consequence, small scale isotropic vortices are modelled, which do not exist neither in the simulations with $C_m = 1$, $C_{str} = 1$ and a mesh containing $2.8 \cdot 10^4$ nodes and in the simulation with $C_m = 1$, $C_{str} = 2$ and $1.4 \cdot 10^4$ nodes, nor in the work of Tutar et al. [61] and Breuer [8]. It is a plausible suggestion that the small scale vortices of this type, generated in the vicinity of the wall, lead to an increase in turbulent activity in the shear layers. As the vortices in the shear layer grow in magnitude due to coalescence with surrounding vortices there will be an increase in turbulent intensity as supported by figures 4.35 and 4.37.

The major question relevant to this conjecture is that concerning the physical representation of small scale vortices. Although the numerics are inextricable bound up with the physics to be modelled, numerical requirements have to be fulfilled to ensure numerical stability of the flow field. To ensure these criteria imperfections in the numerical scheme have to be accepted. In this respect it is important to mention the flux limiter used to ensure TVD. In comparison to the minmod and Osher-Chakravarthy limiters, the superbee limiter used in this work yields sharper profiles near discontinuities. The existence of sharp velocity profiles makes the flow field more sensitive to dispersion [26] leading to numerical dispersion. Another aspect relevant to the modelling of the flow field is the 2-dimensional simplification used in this work. As a consequence, flow motions in the spanwise direction which are to be expected in real life are not considered.

5.3 Impact of numerical scheme on the flow prediction

There are several important advantages in using the DGA algorithm in modelling flows for both industrial and academic application. Solution-based grid refinement will minimize the need to estimate the flow field beforehand. Instead, the mesh develops under its own flow evolutionary tendencies. Habashi et al. [22] concluded that the use of CFD stabilisation artifices, such as upwinding or artificial viscosity, are drastically reduced, if not altogether eliminated, in a well-posed grid refinement methodology. These two appealing features can be considered a significant step towards mesh-independent and solver-independent CFD.

Despite the ambitious conclusions of Habashi, the work in this thesis has shown the importance of a well-posed refinement variable which reflects the nature of the flow field under investigation. Even with the use of an ideal refinement method and a highly-suitable refinement variable, a potential for improving the mesh remains for as long as the mesh has not resolved the Kolmogorov scale η. An ideal mesh refinement in this context is a flow field with a numerical error defined as the deviation from the analytical solution which is the same throughout all the elements. The purpose of the DGA algorithm is to monitor the flow field to determine weaknesses in the numerical representation of the flow field and to give careful and sufficient refinement of the mesh locally. The extent to which the DGA algorithm can detect weaknesses in the numerical flow prediction determines the level of mesh-independent and solver-independent CFD. To detect weaknesses in a numerical flow field described by the Navier-Stokes, one ideally needs the Navier-Stokes equations themselves. In this work an approximation to the numerical error is presented which requires the setting of values for the DGA variables C_m and C_{str} and the refinement threshold values. The values chosen for any of these variables affects the detection of numerical errors leading to an error detection which is not universal in its application. The use of an approximation to describe the numerical error is an important reason for the significant mesh dependency of the flow prediction.

The sensitivity of the flow prediction towards the CFD solver that is used is an important aspect in this analysis. For this reason a simulation with the minmod TVD flux limiter has been carried out. Despite the substantial number of nodes ($2.4 \cdot 10^4$) generated in the simulation with minmod flux limiter, the prediction of the flow field is quite distinct from the flow prediction obtained in the simulations with the superbee flux limiter. The critical flow parameters- drag coefficient $\overline{C}_D$ and Strouhal number S_t, as well the flow profiles for average downstream velocity $\overline{u}$ and the prediction for fluctuating drag $\widetilde{C}_D$ and fluctuating lift $\widetilde{C}_L$, indicate a substantial influence of the TVD algorithm on the flow prediction. The DGA configuration described in table 4.6 shows the necessary reduction in the threshold values to ensure a range of flow motions in the flow field equivalent to the simulations with the superbee flux limiter. Despite the necessary increase in mesh resolution to obtain a turbulent shear stress profile that holds reasonable agreement with the simulations using the superbee flux limiter, drag coefficient $\overline{C}_D$, fluctuating drag $\tilde{C}_D$ and fluctuating lift $\tilde{C}_L$ have better agreement with experimental data.

The additional numerical diffusion when using the minmod flux limiter is a second order numerical error and only a refinement method sensitive to second order errors will capture such weaknesses to a full extent. Due to a decay in gradients, the mesh is refined by modifying the threshold values for mesh refinement to compensate for the increase in numerical diffusion. In case of a refinement method which does not detect second order errors, an additional mesh refinement intended to compensate for numerical diffusion will not lead to uniform reduction of the numerical error. With the refinement configuration as used in the simulations with DGA it is likely the second order errors are not captured ideally and, as a consequence, additional moderate mesh refinement will not compensate for the increase in numerical diffusion throughout the domain. Nevertheless, the level of agreement obtained from the simulations with the superbee flux limiter points to it having potential for further improvement and it would therefore be premature to reject the use of a more robust minmod flux limiter in a simulation with DGA algorithm. Nevertheless, the results presented in this work do lead to the conclusion that even with the use of a DGA algorithm there is still a need for well-formulated numerical schemes. In this respect, solver independent CFD will remain a utopia for as long as the closure problem is unresolved.

5.4 Subgrid length scale

While the smallest eddies in a fully turbulent Newtonian fluid are of the order of the Kolmogorov scale η, the size of the smallest eddies in a fully turbulent flow with LES turbulence modelling is of the order of the numerical grid length scale Δ.

In a Navier-Stokes fluid, i.e. a fluid that is described by Navier-Stokes equations, there are a priori no structures of length scales smaller than the numerical grid Δ. Even if it were possible to carry out a DNS with a grid spacing smaller than the size of the molecules, one could not expect that DNS would provide insight into the existence of individual molecules. Correspondingly, the LES equations describe the energy dissipation of the eddies smaller than l_s into the large eddies. The motion of the small eddies itself, however, is not explicitly described but is parameterized. In other words, the LES equations do not know anything about the existence of individual eddies smaller than l_s, i.e. of eddies within the inner inertial range.

The inclusion of the Smagorinsky constant C_s in the equation for turbulent viscosity is aimed at ensuring that an energy spectrum for the larger eddies is in accordance with the homogeneous turbulence. However, one could argue that a

Smagorinsky constant C_s of the order of 0.15 also implies that there is an intermediate range of subgrid scale motions which are neither resolved by the mesh nor modelled by the LES assumptions. In the simulations presented here subgrid scales with frequencies above $\frac{f_\Delta}{C_s}$ are considered to be fully diffusive, the intermediate range is considered only to be responsible for the transport of energy from the larger to the smaller eddies [17]. It should be noted that such an assumption only holds under the correct numerical and physical conditions and therefore the value should be ideally a function of Reynolds number, grid size Δ and strain rate $|\overline{S}|$, i.e. as $C_s\left(Re, \Delta, |\overline{S}|\right)$. To validate the variable C_s one ideally needs data for the turbulence spectrum obtained from an experimental investigation. However, the only characteristic of turbulence available for validating the power spectrum is the energy decay for homogeneous turbulence, which has been presented together with the numerical data in figures 4.18 to 4.25. The power spectrum obtained from the numerical data has best agreement at the point $\frac{y}{D} = 0$, $\frac{x}{D} = 1$, while further downstream there is a steeper decay of the turbulent energy. As it is expected that the vortex flow will remain a state of self-preservation, no physical argument is obvious for the deformation of the power spectrum in the higher frequency range. Therefore, it is likely that the deformation of the power spectrum is a consequence of the mesh used which tends to become coarser in the downstream direction.

Validating the Smagorinsky constant C_s and the definition for length scale Δ by the power spectrum is beyond the capabilities of the data generated in this work. Nevertheless, a reconsideration of the preferable length scale for triangular mesh, as determined in section 4.1, could be be carried out using the data obtained from simulations using the DGA algorithm.

The simulations with DGA hold reasonable agreement with the time integrated velocity profiles as well as turbulent shear stress $\overline{u'v'}$, and, although deviation from experimental data is apparent, errors are in the same order as seen with the data from conventional mesh. It is the drag coefficient $\overline{C}_D$, fluctuating drag $\widetilde{C}_D$ and fluctuating lift $\widetilde{C}_L$ which are clearly over-predicted. Suggestions for the existence of this phenomenon have been given in section 5.1 but are not discussed in the context of a suitable length scale. It is concluded that the lower scale flow motions, indicated by the fluctuating drag $\widetilde{C}_D$ and fluctuating lift $\widetilde{C}_L$, are of too high intensity and it is suggested that convective energy loss is responsible for the increase in drag. Therefore, larger scale flow motions should be suppressed and one way of doing this is to increase either the numerical or turbulent viscosity. It is the simulation with minmod flux limiter that confirms this analysis. The simulation has shown a drastic reduction in drag coefficient $\overline{C}_D$ in comparison with the simulations using the superbee flux limiter. This supports the opinion that the increase in energy dissipation due to diffusion has less impact on the drag force then the decrease in turbulent intensity due to diffusion. An increase of diffusion in effect leads to a reduction in Reynolds number. The suggestion that pressure drag is decreasing with decreasing turbulent intensity is in accordance with the Reynolds number drag relation as proposed by Roshko [52] although the drag coefficient $\overline{C}_D$ remains in the range of 1 to 1.24 for a wide range of Reynolds numbers, there is a graduate decay with decreasing Reynolds number. As a consequence, a length scale $\Delta = \sqrt{2A_{tr}}$ cannot be considered as the weaker length scale beforehand. Nevertheless, an increase of turbulent viscosity by a factor of 2 will further reduce the effective Reynolds number, leading to a suppression of the turbulent flow field.

Although the initial choice for the length scale $\Delta = \sqrt{A_{tr}}$ still remains that preferred when considering only the data available for the simulations with conventional mesh, a simulation with length scale $\Delta = \sqrt{2A_{tr}}$ would be an interesting case study. However, it is preferable to carry out this simulation in combination with an increase in mesh resolution in order to overcome large values for turbulent viscosity.

Van driest damping function for the near wall approach

The present LES simulations use a near wall approach derived from the Van Driest mixing length approach. This requires the calculation of the wall shear stress in order to determine the reduced length scale l_s in the vicinity of the wall. Thus the sensitivity of the entire process to determine the length scale l_s is dependent upon a good approximation of the wall shear stress. Since the present calculation procedure uses a linear velocity gradient assumption for very small normal distances from the wall, the success of the accurate predictions of the wall shear stress becomes highly dependent upon the particular node used close to the cylinder wall and hence the resolution in the near wall region. In this respect, it can be considered a disadvantage that equilateral triangles are maintained throughout the refinement procedure. To resolve the boundary layer sufficiently well perpendicular to the wall causes too many triangles to be added in the flow direction where little variation takes place. On the other hand and more importantly, the linear velocity gradient assumption is valid for steady boundary layer conditions and in the case of unsteady flow that is the norm in the current work, this assumption may become inappropriate.

5.5 Instantaneous flow patterns

The validation of numerical data has been limited to the use of averaged quantities. Although these quantities are of central interest from an applied CFD perspective, their use under-rates the instantaneous effects due to grid refinement. Typical are the small scale motions in the regions where the mesh has been refined strongly. Here it could be argued that either the mesh has refined due to the flow field, or a flow motion has developed as a result of mesh refinement. So, to what extent can grid refinement drive the flow field? In the downstream region this effect is unlikely to be significant as the flow has already been determined by upstream conditions. However, in the region where separation occurs, the mesh can have significant influence on the flow field. Comparison of the flow field at an instant shows radical differences in flow patterns as seen in the simulations presented in the movie $C_m = 1 - C_{str} = 1 - 2.8 \cdot 10^4 - 1.avi$ to $C_m = 1 - C_{str} = 2 - 2.4 \cdot 10^4 - 1.avi$

	$\frac{6.1 \cdot 10^4 - DGAMesh}{6.1 \cdot 10^4}$
DGA variables $C_m = 1 \mid C_{str} = 1$	
$2.8 \cdot 10^4 \mid$ superbee	54.1%
$4.3 \cdot 10^4 \mid$ superbee	29.5%
$4.5 \cdot 10^4 \mid$ superbee	26.2%
DGA variables $C_m = 1 \mid C_{str} = 1.5$	
$3.5 \cdot 10^4 \mid$ superbee	42.6%
$5.0 \cdot 10^4 \mid$ superbee	18.0%
DGA variables $C_m = 1 \mid C_{str} = 2$	
$1.4 \cdot 10^4 \mid$ superbee	77.0%
$2.8 \cdot 10^4 \mid$ superbee	54.1%
$2.4 \cdot 10^4 \mid$ minmod	60.7%

Table 5.6: Reduction in mesh size in comparison with the conventional mesh containing $6.1 \cdot 10^4$ nodes. $MeshReduction = \frac{Conv.Mesh - DGAMesh}{Conv.Mesh} * 100\%$

contained in the appendix.

It is expected that the increase in turbulent shear stress $\overline{u'v'}$ is due to an increase in mesh resolution. Nevertheless, the addition of new nodes in the numerical domain can trigger instabilities, unless the nodes are carefully initialised. For initialising the element-based variables in the new elements the ones in the original element have been used. Such a method introduces inevitably some increase in velocity gradients. However, to quantify the extent to which the DGA is driving the flow field remains a hard task as the governing equations and DGA algorithm are coupled.

Despite the spreading in the numerical data, average quantities as time integrated velocity, turbulent shear stress and critical flow parameters show reasonable agreement. The level of agreement obtained with the DGA simulations and the comparison with simulations using a conventional mesh indicates the effect of small scale vortices is not dominating the main flow properties. The increase in turbulent shear stress $\overline{u'v'}$ is likely to occur due to the increase in mesh resolution. At the same one can note that the spreading seen in the other averaged flow quantities is also apparent in the simulations with conventional mesh.

5.6 Effects of Dynamic Grid Adaptation

Substantial mesh reduction is obtained in the simulations with DGA in comparison with the simulations using conventional mesh. Nevertheless, the reduction in mesh size has not lead to a decay in flow prediction, instead the flow predictions with DGA algorithm maintain an equal level of agreement with experimental data. Therefore one can only conclude that the use of a DGA algorithm is an important tool in the context of modelling turbulent unsteady flow.

It is clear from the current work that the use of a DGA algorithm for turbulence modelling has enabled a substantial reduction in mesh size in comparison with the conventional mesh used in the first simulation session. Dependent on the configuration of the DGA algorithm, reductions in the mesh size up to 75% have been achieved, as shown in table 5.6. The core reason for this reduction is the monitoring of the flow field which enables the removal and addition of nodes on a temporary basis. The reduction in mesh size which has been accomplished in the upstream flow region and aside the circular cylinder is substantial, but could have been accomplished with conventional mesh design as well after several manual adjustments.

The most substantial reduction in mesh size has been accomplished with a DGA configuration where strain rate is the dominant flow feature in the refinement variable. The simulation with a DGA configuration where strain rate is the dominant flow feature ($C_m = 1$, $C_{str} = 2$) and a mesh containing approximately $1.4 \cdot 10^4$ nodes gives a flow field similar to the simulation with a conventional mesh containing $6.1 \cdot 10^4$ nodes and a subgrid length scale to $\Delta = \sqrt{A_{tr}}$. Despite some of the weaknesses in both the simulations with DGA and the conventional mesh, there is no decay in the quality of the flow prediction when using a DGA algorithm. A main weakness in the flow field is the lack of cohesion leading to a disturbed vortex street and an over-prediction of the drag coefficient $\overline{C}_D$, fluctuating drag $\widetilde{C}_D$ and fluctuating lift $\widetilde{C}_L$. Nevertheless, the lack of cohesion has also been discovered in the simulations with conventional meshes and it is suggested that this weakness of the flow prediction is most likely due to the 2-dimensional representation of the flow field or the modelling of the advective terms of the Navier-Stokes equations. As a consequence, the use of a DGA algorithm in the context of turbulence modelling remains a suitable tool which can be used as a next step in an attempt to resolve turbulence more realistically.

Results using different combinations of the DGA variables C_m and C_{str} have given the opportunity to validate a suitable mesh refinement process in a turbulent flow field. With the choice of C_m and C_{str} set to be both equal to 1 the cell size and strain rate are equally weighted in the refinement variable, while with the DGA variable C_{str} set to be 1.5 and 2 respectively, strain rate is made the dominant flow feature in the refinement variable. The simulation results do not automatically point to an ideal combination of the DGA variables C_m and C_{str}. The results obtained with the DGA variables $C_m = 1$ and $C_{str} = 1.5$ give good agreement in the recirculation region but here the reduction in mesh size is comparatively small. In contrast, the simulations with strain rate as its dominant flow feature in the refinement variable ($C_m = 1$, $C_{str} = 2$) gain a strong reduction in mesh size. However, by selecting a more diffusive minmod TVD flux limiter, excessive mesh refinement is required to compensate for the extra numerical diffusion indicating that second order errors in the numerical representation are not well captured.

It is difficult to suggest ideal values for the DGA variables C_m and C_{str}. Nevertheless, for the flow investigated in this work a further increase of the variable C_{str} to increase the dominance of the strain rate is unlikely to give improved results. With the choice of C_m and C_{str} to be 1 and 2 respectively, it is now clear that hardly any mesh refinement in the wake region can be carried out without reaching the minimum cell size in the vicinity of the wall. As a consequence, a further increase of the variable C_{str} together with a decrease of the threshold values to ensure mesh refinement in the wake region further away from the cylinder undeniably leads to monotonic mesh refinement in the vicinity of the wall. As a consequence, the DGA algorithm will become insensitive to small changes in the refinement variable in the region near the wall. In contrast, a further decrease of the DGA variable C_{str} to values of the order of 0.5 is unlikely to give improved results either. In such cases, the cell size will be the dominant feature in the refinement variable and it is likely the mesh will be smoothly refined throughout the whole numerical domain, but the mesh will lack focus on those areas which are of high importance in the flow field prediction.

To select 'ideal' values for the DGA variables C_m and C_{str} for the cylinder system requires further work. This should focus on a further increase of the mesh resolution in the vicinity of the wall to resolve the boundary layer and separation process in more detail. Preferably, these simulation should be 3-dimensional and to avoid excessive calculation time an implicit flow solver should be used.

Chapter 6

Conclusions

The aims of this work, as described in the introduction, were as follows:

- To establish a method for modelling turbulent unsteady flow where the large turbulent eddies are captured by a DGA algorithm and resolved by the mesh itself while smaller turbulent eddies are modelled with a LES turbulence model.
- To determine a proper DGA refinement variable for an unsteady turbulent flow field.
- To investigate the mesh requirements for turbulent unsteady flow and the sensitivity towards mesh resolution and flow solver.
- To gain a further insight into flows where turbulence is a key flow feature.

The LES turbulence model of Smagorinsky has been used and a modification to Smagorinsky's equation for turbulent viscosity is proposed as a refinement variable in the DGA algorithm. Two sets of simulations have been carried out, the first using a conventional mesh and aiming to obtain a suitable subgrid length scale for the LES turbulence model. The second used a DGA algorithm and aimed to discover a suitable refinement variable and to investigate the numerical and physical aspects of the unsteady turbulent flow.

The following conclusions can be drawn from the present study:

- The concept of modelling the vortex shedding behind a circular cylinder in the sub-critical flow regime, as proposed in this work, has shown wide potential. The results obtained from the simulations with DGA have the same level of agreement with experimental data as that obtained with conventional meshes. However, the use of a DGA algorithm enables a significant reduction in mesh size. Despite substantial variation in the flow prediction, a reduction in mesh size of 50% lies well within the capabilities of the proposed concept and 75% has been observed for some cases.

- The use of solution-based grid refinement as shown in this work will minimize the need for a sophisticated mesh generated by conventional mesh generators. Instead, the mesh will develop automatically under the influence of flow features and reflect the structures being modelled. As a consequence, there is less need to put effort into estimating the flow field beforehand and time-consuming mesh testing can be reduced.

- The variation in flow prediction is primarily due to mesh refinement and confirms the complexity of the physical processes where certain flow regions and vortex scales in the flow field are over-proportionally important. This means that the determination of a proper refinement variable cannot be decoupled from the physics under investigation.

- With the DGA variables for cell size and strain rate set to be of equal importance ($C_m = 1$, $C_{str} = 1$) in the refinement variable smooth mesh refinement around the separation point and the shear layer is accomplished, while in the larger vortex behind the cylinder, nodes are equally distributed. In contrast, the mesh refinement with strain rate being the dominant flow feature ($C_m = 1$, $C_{str} = 2$) mesh refinement in the separation point region and in the shear layer becomes distinct and sharp. In the shear layer near the point of separation, small scale instabilities are captured and followed as they move downstream. Based on the prediction of the critical flow parameters, the average velocity and turbulent shear stress $\overline{u'v'}$ profile, a near-optimum refinement variable is obtained with moderate dominance of the strain rate in the refinement variable. This has been obtained by setting the DGA variables C_m and C_{str} to 1 and 1.5 respectively.

- A comparison of the 8 simulations using the DGA simulation shows an increasing number of nodes does not lead automatically to an improvement of the flow prediction. A similar trend has been also discovered by Travin et al. [58] and Breuer [8]. Evidence for this phenomenon does not exist and no substantial contribution to the understanding of this phenomenon is presented in this thesis. However, it is suggested, that the lack of numerical control on the location and progression where transition from laminar to turbulent flow conditions takes place, leads to a strong sensitivity towards the used mesh.

- The present work shows that upwinding still has an effect on the flow prediction. This refutes a mesh-independent and solver-independent CFD as suggested by Habashi et al. [22].

- In this work, results are presented for the following critical flow parameters: drag coefficient $\overline{C}_D$, Strouhal number S_t and separation angle Θ_s, as well as time integrated velocity and turbulent shear stress $\overline{u'v'}$. Velocity, turbulent shear stress $\overline{u'v'}$, Strouhal number S_t show reasonable agreement with experimental data, but with certain variation. In contrast, the drag coefficient

$\overline{C}_D$ and separation angle Θ_s are predicted with less variation but are over-predicted. It is suggested that the over-prediction in drag coefficient $\overline{C}_D$ is due to the intense vortex shedding leading to an increase in dissipation whereby the larger scale eddies are affecting the Strouhal number S_t .

- The simulations have confirmed the existence of a so-called dominant region of the cylinder including the shear layers where the transition from laminar to turbulent flow takes place. It is suggested that the region is highly mesh sensitive and a modification of the mesh in this region will have a substantial influence on the flow field further downstream. Conversely the strong variation in the mesh further downstream suggests the downstream flow field requires less computational modelling.

- Based on the results obtained with conventional mesh and a mesh containing $6.1 \cdot 10^4$ nodes, the subgrid length scale $\Delta = \sqrt{A_{tr}}$ is to be preferred and has been used in the simulations with DGA algorithm. In the simulations with conventional mesh, the time integrated flow field has been seen to be nearly independent of the selected subgrid length scale, while better agreement was obtained for turbulent shear stress $\overline{u'v'}$, Strouhal number S_t and separation angle Θ_s, with the subgrid length scale set as $\Delta = \sqrt{A_{tr}}$. It is suggested that, based on the over-prediction for drag coefficient $\overline{C}_D$, a more diffusive length scale ($\Delta = \sqrt{2A_{tr}}$) could be preferable to suppress the large scale flow motions and to reduce drag.

Chapter 7

Recommendations for further work

It is suggested that the following improvements can be carried out in order to increase the performance of the present numerical calculation method and hence to obtain a more universal application of the concept proposed in this thesis.

- The use of an explicit CFD flow solver has shown to be very time-consuming and lead to severe limitations in the mesh resolution. A further increase in mesh resolution would have allowed the resolution of a wider range of turbulent eddy size, but with a explicit flow solver this would not only increase the calculation time for each time step but reduce the time step size as well. The implementation of an implicit incompressible CFD flow solver into the REACFLOW code would be a substantial advantage and allow the user to investigate industrial flow systems using the proposed concept.
- For further investigation of the vortex shedding behind a circular cylinder in the sub-critical flow regime, 3-dimensional simulations should be carried out with mesh adaptation carried out in the same way as that used in the 2-dimensional simulations. The 3-dimensional simulations carried out in the course of the present work but not reported in this thesis have shown the existence of 3-dimensional flow structures in the recirculation region. These structures could well be important to the exchange of momentum in the flow field and the onset of transition. Unfortunately these 3-dimensional simulations lack sufficient mesh resolution, leading to a diffusive flow field which shows a severe over-prediction of the recirculation region and poor prediction of the small scale turbulence.
- The concept of linking the DGA algorithm up with the turbulence model has been applied so far only to incompressible non-reactive flows. It would be of considerable interest to explore the application of the modelling concept proposed in this thesis to compressible flows where there is exchange of heat

as well to flows where chemical reactions are taking place.

Bibliography

[1] M B Abbott and Basco D R. *Computational Fluid Dynamics: An Introduction for Engineers*. Longman Scientific and Technical, 3rd edition, 1994.

[2] E Achenbach. Distribution of local pressure and skin friction around a circular cylinder in cross-flow up to 5e6. *J. Fluid Mech.*, 34:625–639, 1968.

[3] J D Anderson. *Computational Fluid Dynamics : The basics with applications*. Mechanical Engineering Series. McGraw-Hill International Editions, 1995.

[4] I Babuska, O C Zienkiewicz, J Gago, and E R de A Oliverira. *Accuracy Estimates and Adaptive Refinements in Finite Element Computations*. John Wiley, 1986. New York.

[5] S Balachandar, R Mittal, and F M Najjar. Properties of the mean recirculation region in the wakes of two-dimensional bluff bodies. *J. Fluid Mech.*, 351:167–199, 1997.

[6] J P Boris and D L Book. Flux corrected transport I. SHASTA a fluid transport algorithm that works. *J. Comput. Phys.*, 11:38–69, 1973.

[7] R Bouard and M Coutanceau. The early stage of development of the wake behind an impulsively started cylinder for 40 < Re < 10e4. *J. Fluid Mech.*, 101(3):583–607, 1980.

[8] M Breuer. A challenging test case for large eddy simulation: high Reynolds number circular cylinder flow. *Int. J. Heat Fluid Fl.*, 21(5):648–654, 2000.

[9] B Cantwell and D Coles. An experimental study of entrainment and transport in the turbulent near wake of a circular cylinder. *J. Fluid Mech.*, 136:321–374, 1983.

[10] S Chandrasekhar. Dynamical instability of gaseous masses approaching the Schwarzschild limit in general relativity. *Phys. Rev. Lett.*, 12:114–116, 1964.

[11] A J Chorin. Numerical solution of the Navier-Stokes equations. *Math. Comp.*, 23:341–353, 1968.

[12] M Ciafalo. Large eddy simulation: a critical survey of models and applications. *Advan. Heat Transf.*, 25:321–419, 1994.

[13] A R Diaz, N Kikuchi, and J E Taylor. A method for grid optimization for the finite element method. *Comput. Meth. Appl. Mech. Eng.*, 41:29–45, 1983.

[14] P G Drazin and W H Reid. *Hydrodynamic Stability.* Cambridge Press, 1981.

[15] E R Van Driest. On turbulent flow near a wall. *J. Aeronaut. Sc.*, 23:1007–1011, 1956.

[16] P R Eiseman. Adaptive grid adaptation. *Comput. Meth. Appl. Mech. Eng.*, 64:321–376, 1987.

[17] J H Ferziger. Large eddy numerical simulations of turbulent flows. *AIAA*, 15(9):1261–1267, 1977.

[18] J H Ferziger. Large Eddy Simulation. In T B Gatski, M Y Hussaini, and J L Lumley, editors, *Simulation and Modeling of Turbulent Flows*, chapter 3, pages 109–154. Oxford University Press, 1996.

[19] M Germano, U Piomelli, P Moin, and W H Cabot. A dynamic subgrid scale eddy viscosity model. *Proc. Summer Workshop, Center for Turbulence Research*, 1990. Stanford CA.

[20] J H Gerrard. The mechanics of the formation regions of vortices behind bluff bodies. *J. Fluid Mech.*, 25:401–413, 1966.

[21] M Gorman and H L Swinney. Recent results on instabilities and turbulence in Couette-flow. *Physica A*, 106(1-2):123–127, 1981.

[22] W G Habashi, J Dompierre, Y Bourgault, D Ait-Ali-Yahia, M Fortin, and M G Vallet. Anisotropic mesh adaptation: towards user-independent, mesh-independent and solver-independent CFD. Part 1: general principles. *Int. J. Numer. Meth. Fluids*, 32:725–744, 2000.

[23] A Harten. High resolution schemes for hyperbolic conservation laws. *J. Comput. Phys.*, 49:357–393, 1983.

[24] K Herfjord, T Kvamsdal, K M Okstad, and G Olsen. Fluid-structure interaction of two cylinders in vortex induced vibrations. In B Skallerud and H I Andersson, editors, *First National Conference on Computation Mechanics*, pages 169–190. NTNU Trondheim, May 3-4 2001.

[25] J O Hinze. *Turbulence, an introduction to its mechanism and theory.* McGraw-Hill book company, inc., 1959.

[26] C Hirsch. *Numerical Computation of Internal and External Flows*, volume 1. Wiley, 1988.

[27] T Huld and H Wilkening. *Adaptive grid methods for unsteady CFD problems.* Joint Research Centre of the European Commission, T.P. 723, I-21023 Ispra, 1998.

[28] D D Joseph. *Stability of Fluid Motions*, volume I and II. Springer-Verlag, 1976.

[29] A N Kolmogorov. Dissipation of energy in a locally isotropic turbulence. *Doklady Akad. Nauk SSSR*, 32:141, 1941.

[30] B Van Leer. Towards the ultimate conservative difference scheme. V. a second order sequel to Godunov's method. *J. Comput. Phys.*, 32:101–136, 1979.

[31] D K Lilly. The representation of small-scale turbulence in numerical simulation experiments. *Proc. IBM Sci. Comput. Symp. Environm. Sci.*, pages 195–210, November 1967.

[32] C A Lin and M A Leschziner. Computation of three-dimensional injection into swirling combustor-model flow with second-moment closure. In C Taylor, P Gresho, R L Sani, and J Hauser, editors, *Numerical methods in laminar and turbulent flow*. Pineridge Press, Swansea, 1989.

[33] C C Lin. *On the Theory of Hydrodynamic Stability*. Cambridge University Press, 1955.

[34] R Lohner. An adaptive finite element solver for transient problems with moving bodies. *Comput. Struct.*, 30:303–317, 1988.

[35] R Lohner. Mesh adaptation in fluid mechanics. *Eng. Fract. Mech.*, 50(5/6):819–847, 1995.

[36] R Lohner and J D Baum. Adaptive H refinement on 3-D unstructered grids for transient problems. *Int. J. Numer. Meth. Fluids*, 14(12):1407–1419, 1992.

[37] R Lohner and J D Baum. Numerical-simulation of shock interaction using an adaptive finite-element scheme. *AIAA*, 32(4):682–692, 1994.

[38] T S Lund, H J Kaltenbach, and K Akselvoll. On the behaviour of centered finite difference schemes for large eddy simulation. *Proc. Sixth Intl Symp. on Computational Fluid Dynamics. Lake Tahoe*, September 1995.

[39] X Ma, G S Karamanos, and G E Karniadakis. Dynamics and low-dimensionality of a turbulent wake. *J. Fluid Mech.*, 410:29–65, 2000.

[40] B S Massey. *Mechanics of fluids*. Van Nostrand Reinhold (UK) Co. Ltd, 5 edition, 1983.

[41] C Mavriplis. A posteriori error estimators for adaptive spectral element techniques. *Proc. 8th GAMM Conf. Numer. Meth. Fluid. Mech.*, 29:333–342, 1990.

[42] J J McGuirk and W Rodi. A depth-averaged mathematical model for the near field of side discharges into open-channel flow. *J. Fluid Mech.*, 86(4):761–781, 1978.

[43] J J McGuirk, A M K P Taylor, and J H Whitelaw. The assessment of numerical diffusion in the upwind-differencing calculations. In L J S Bradbury, F Durst, B E Launder, F W Schmidt, and J H Whitelaw, editors, *Selected Papers from the Third International Symposium on Turbulent Shear Flow*, page 206. Univ. of California Press, 1983.

[44] O J McMillan and J H Ferziger. Tests of new subgrid scale models in strained turbulence. *AIAA*, 80:1339, 1980.

[45] C H Moeng and J C Wyngaard.. Spectral analysis of large-eddy simulations in the convective boundary layer. *J. Atmos. Sci.*, 45:3573–3587, 1988.

[46] A Muschinski. A similarity of locally homogeneous and isotropic turbulence generated by a Smagorinsky-type LES. *J. Fluid Mech.*, 325:239–260, 1996.

[47] S Muzaferija and D Gosman. Finite-volume CFD procedure and adaptive error control strategy for grids of arbitrary topology. *J. Comput. Phys.*, 138:766–787, 1997.

[48] H Nishimura and Y Taniike. Aerodynamics characteristics of fluctuating forces on a circular cylinder. *J. Wind Eng. Ind. Aerod.*, 89:713–723, 2001.

[49] C Norberg. Flow around a circular cylinder: aspects of fluctuating lift. *J. Fluid. Struct.*, 15:459–469, 2001.

[50] H Persillon and M Braza. Physical analysis of the transition to turbulence in the wake of a circular cylinder by three-dimensional Navier-Stokes simulation. *J. Fluid Mech.*, 365:23–88, 1998.

[51] O Reynolds. An experimental investigation of the circumstances which determine whether the motion of water shell be direct or sinous, and the law of resistance in parallel channels. *Philos. Trans. Roy. Soc. London*, 174:935–982, 1883.

[52] A Roshko. Experiments on the flow past a circular cylinder at very high Reynolds numbers. *J. Fluid Mech.*, 10:345–356, 1961.

[53] T Sarpkaya. Inviscid model of two-dimensional vortex shedding by a circular cylinder. *AIAA*, 17:1193–1200, 1979.

[54] J Smagorinsky. General circulation experiments with the primitive equations, part 1: the basic experiment. *Mon. Wea. Rev.*, 91:99, 1963.

[55] A Soria and F Ruel. *Finite volume analysis of multicomponent incompressible viscous flow.* Joint Research Centre of the European Commission, special publication no. i.94.41 edition, 1994.

[56] R Teman. Sur l' approximation de la solution des equations de Navier-Stokes par la methode des pas fractionnaires. *Arch. Ration. Mech. Anal.*, 32:377–385, 1968.

[57] H Tennekes and L J Lumley. *A first course in Turbulence.* MIT Press USA, 1972.

[58] A Travin, M Shur, M Strelets, and P Spalart. Detached-Eddy Simulations past a circular cylinder. *Flow Turbul. Combust.*, 63:293–313, 1999.

[59] M Tutar. *Computational modelling of vortex shedding from offshore risers.* PhD thesis, University of Hertfordshire, October 1998.

[60] M Tutar and A E Holdø. Computational modelling of flow around a circular cylinder in sub-critical flow regime with various turbulence models. *Int. J. Numer. Meth. Fluids*, 35:763–784, 2001.

[61] M Tutar, A E Holdø, and A P Lewis. Comparitive performance of various two equation models and LES on simulated flow past a circular cylinder. In *Proceedings of A.S.M.E. Fluids Engineering Summer Meeting on Finite Element Applications in Fluid Dynamics*, June 20-25 1998.

[62] M Tutar, A E Holdø, and A P Lewis. Simulation of vortex shedding from an oscillating circular cylinder. In *Proceedings of 29th American Institute of Aeronautics and Astronautics Fluid Dynamics Conference*, New Mexico, June 15-18 1998.

[63] B Vallès. *Computational study of vortex shedding behind bluff bodies.* PhD thesis, NTNU Trondheim, 2001. ISBN 82-471-5335-1.

[64] B Vreman, B Geurts, and H Kuerten. Comparison of numerical schemes in Large Eddy Simulation of the temporal mixing layer. *Intl J. Numer. Meth. Fluids*, 22:297–311, 1996.

[65] Z J Wang. A quadtree-based adaptive cartesian/quad grid flow solver for Navier-Stokes equations. *Comput. Fluids*, 27(4):529–549, 1998.

[66] G S West and C J Apelt. Measurements of fluctuating pressures and forces on a circular cylinder in the Reynolds number range 10e4 to 2.5*10e5. *J. Fluid Struct.*, 7:227–244, 1993.

[67] H Wilkening and T Huld. An adaptive 3-D CFD solver for modeling explosions on large industrial environmental scales. *Combust. Sci. Technol.*, 149:361–387, 1999.

[68] C H K Williamson and G L Brown. A series in 1/root Re to represent the Strouhal-Reynolds number relationship of the cylinder wake. *J. Fluid Struct.*, 12(8):1073–1085, 1998.

[69] G De With. Simulation of a free jet at low Reynolds numbers, with DGA algorithm. Technical report, University of Hertfordshire, 2001.

[70] V Yakhot and S O Orszag. Renormalization group methods in turbulence. *Phys. Rev. Lett.*, 57(14):1722–1724, 1986.

[71] D De Zeeuw and K G Powell. An adaptively refined cartesian mesh solver for the Euler equat ions. *J. Comput. Phys.*, 104:56–68, 1992.

[72] J Z Zhu and O C Zienkiewicz. A posteriori error estimation and three-dimensional automatic mesh generation. *Finite Elem. Anal. Des.*, 25:167–184, 1997.

[73] O C Zienkiewicz and J Z Zhu. A simple error estimator and adaptive procedure for practical engineering analysis. *Int. J. Numer. Meth. Eng.*, 24:337–357, 1987.

Appendixes

Appendix A

G. de With, A. E. Holdø and T. A. Huld. The use of Dynamic Grid Adaptation algorithms for modeling transitional flow. Proceedings of A.S.M.E. Emerging Technologies for Fluids, Structures and Fluid-Structure Interaction, Atlanta, Georgia, July 22-26, 2001.

Errata

- Page 7, figure 2, turbulent shear stress $\overline{u'v'}$ should be as shown in thesis figure 4.13, 4.35 and 4.37.
- Page 8, table 1, drag coefficient $\overline{C}_D$ should be multiplied by density $\rho = 1.178$.

Appendix B

G. de With, A. E. Holdø and T. A. Huld. Modeling of flow around a circular cylinder in sub-critical flow regime with the of Dynamic Grid Adaptation Algorithms, Proceedings of A.S.M.E. (accepted) 2002.

Erratum

- Page 12, table 1,drag coefficient $\overline{C}_D$ should be multiplied by density $\rho = 1.178$.

Appendix A

Proceedings of PVP-Vol. 431
Emerging Technologies for Fluids, Structures and Fluid-Structure Interaction - 2001
July 22-26, ASME 2001, Atlanta, Georgia, USA

THE USE OF DYNAMIC GRID ADAPTATION ALGORITHMS FOR MODELING TRANSITIONAL FLOW

Govert de With
Arne E. Holdø*
CFD Research Group
Dep. Aeronautical Civil and Mechanical Eng.
University of Hertfordshire
Hatfield Campus, College Lane
Hatfield, Herts AL10 9AB
Email: G.de-With@herts.ac.uk
Email: A.E.Holdo@herts.ac.uk

Thomas A. Huld
Institute for Systems, Informatics and Safety
Joint Research Centre
Ispra (Va), 21020
Italy
Email: Thomas.Huld@jrc.it

ABSTRACT

In the present study a Dynamic Grid Adaptation (DGA) algorithm is utilized for predicting flows where transition from laminar to turbulent flow conditions is taking place. The reason for adopting a DGA algorithm is the unsteadiness and transition of the flow field making a turbulence model insufficient and a conventional predefined fine mesh inefficient. The approach behind the simulations carried out, is to focus the mesh refinement on the regions where transition is taking place. In the region where the flow is fully developed a coarser mesh should develop and the turbulence will be modeled with the Large Eddy Simulation (LES) turbulence model.

So far significant work has been done in the development of adaptive methods and adaptive grid strategies (Eiseman, 1987) (Habashi et al., 2000) (Lohner, 1995) (Muzaferija and Gosman, 1997), but not much has been done to determine flow specific error magnitudes of numerical solutions. However, the success of adaptive grid methods depends well on a reliable refinement variable, and on the adequate determination of acceptable error bounds with which the estimated errors are compared. Therefore the aim of the study is to present an appropriate refinement variable for error estimation as well the determination of acceptable error bounds. The presented refinement condi-

---

*Address all correspondence to this author.

tions do focus on a mesh refinement in regions where transition is taking place.

The method utilized for DGA determines the error based on the variation in the refinement variable values, and the refinement variable is a product of the local mesh cell size and the rate of strain. The relation is derived from the equation for turbulent viscosity in the LES turbulence model and is an indication for turbulent activity. It is investigated how the focus of the DGA algorithm can be manipulated by varying the weight of either the mesh cell size or the rate of strain.

NOMENCLATURE

$A_{triangle}$	Element surface
A^+	Constant
C_d	Drag coeficient
C_m	Adaptation constant for mesh
C_s	Smagorinsky constant
C_{str}	Adaptation constant for strain
D	Cylinder diameter
D_{damp}	Damping variable
e_i	Estimated error
N	Number of neighbor elements
p	Pressure
q	Refinement variable
$\hat{q}_i$	Interpolated refinement variable
Re	Reynolds number
$\lvert\bar{S}\rvert$	Magnitude of strain
S_{ij}	Strain tensor
S_t	Strouhal number
t	Time
$\bar{u}$	Average velocity
$\bar{u}_{cl}$	Average centerline velocity
u_i	u,v,w for i=1,2,3 respectively
u	Streamwise velocity component
u'	Streamwise fluc. velocity component
u_τ	Shear friction velocity
v	Lateral velocity component
v'	Lateral fluc. velocity component
x	Space in streamwise direction
x_i	x,y,z for i=1,2,3 respectively
y	Space in lateral direction
y^+	Distance in wall shear units
Δ	Subgrid length scale
μ_{lam}	Laminar viscosity
μ_t	Turbulent viscosity
ν	Kinematic viscosity
ρ	Density

INTRODUCTION

In the present study a numerical investigation is undertaken to predict flows where transition from laminar to turbulent is taking place. The type of problem being selected for this work is the flow in the near wake of a circular cylinder at a Re number of 1.4e5. Despite all complexity associated to the transition taking place in the near wake, agreement has been found for the general behaviour of such flow structures. It is the initial instability in the boundary layer, in the vicinity of the wall, which results in a migration of vorticity to form periodic, circumferentially coherent concentrations in the shear layer. Due to wave instabilities in the flow field, a 'street' of interacting and coalescing vortices do occur.

It is generally accepted that the motions at the smallest scale of a flow tend to become independent of the large scale motions as the Re number increases. The fact is that very little is known about the coupling between the organized motion and the smaller scales, or about the mechanisms by which energy delivery and dissipation are actually accomplished. However the effect of small scales onto the main flow, in particular in transitional flow, is considered to be significant. This means that most of the model assumptions of any turbulence model do not apply. Consequently the complexity associated to transitional flow can only be modeled in a physically correct manner by the Navier-Stokes equations themself, i.o.w a fine mesh should be applied in the region where transition is taking place.

In the region further downstream, where the flow has attained a state of self-preservation, turbulence is considered to be more uniform in its behaviour and the effects of small scale motions can be estimated via the model assumptions laid down in the turbulence model. To ensure a high mesh resolution in the region where transition is taking place, without leading to an excessive increase of nodes in the whole numerical domain, due to the unsteadiness of the transitional phenomenon, requires the use of a Dynamic Grid Adaptation (DGA) algorithm. Significant work has been done in the development of adaptive methods and adaptive grid strategies (Eiseman, 1987) (Habashi et al., 2000) (Lohner, 1995) (Muzaferija and Gosman, 1997). However this work will focus on the determination of a reliable refinement variable, and acceptable error bounds. The refinement variable is obtained from the velocity field and includes both rate of strain and local mesh cell size, the variation in weighting of either one of these terms gives a control on the actual refinement behaviour and on the region where the refinement is taking place. For the flow further downstream, where a coarser mesh will develop the turbulence will mainly rely on the Large Eddy Simulation (LES) turbulence model being implemented.

In this work the Computational Fluid Dynamics (CFD) code REACFLOW has been been utilized, this code has adopted the projection method in the solution procedure and uses a triangular mesh. Due to the triangular mesh being used in the REACFLOW code the definition of the length scale in the LES turbulence model has to be considered. The LES turbulence model belongs to the eddy viscosity type of turbulence models and calculates the turbulent viscosity element wise from both the rate of strain and the cell size of the element. In this work two methods for calculating the length scale will be presented.

BACKGROUND

The work being undertaken focuses both on grid adaptation and LES turbulence modeling. The suitability of the LES turbulence model in combination with DGA lies in the concept being chosen for calculating turbulent viscosity. In this turbulence model, turbulent viscosity is proportional to the cell size of the element, therefore an increase in mesh resolution will lead to a reduction in turbulent viscosity. In case of a very fine mesh the contribution of the LES turbulence model vanishes and the flow is practically calculated without turbulence model.

Dynamic grid adaptation

The search for solutions free from numerical error has been and will be one of the main goals of CFD research. An indisputable way to reduce the numerical error is by reducing the size of the discretization elements. However an excessive increase in mesh resolution would lead to insurmountable demand for computational power. As a consequence a mesh sensitivity analyses is very usual and mostly required to find consensus in numerical error and computational demand. This however requires the user to estimate beforehand the regions of interest. Research has shown that the flow prediction is significantly sensitive to the mesh being utilized, this numerical behaviour indicates a need for dynamically generated mesh, which adapt the mesh to the flow field, to cover interesting flow phenomena in high detail. A well developed and robust DGA algorithm can lead to a reduction in both numerical error and computational power, this appealing feature has enforced the CFD society to develop a whole range of algorithms for DGA of different applicability and complexity.

Refinement Strategies Over recent years a whole series of strategies have developed, a small number of these strategies are preprocessing based and focus on a geometry based mesh refinement, however, for CFD purpose the majority of the strategies is focusing on a solution based mesh refinement. In this work we will deal with the solution based mesh refinement of which three approaches can be distinguished.

R-refinement r-refinement, or grid movement (relocation). In this approach a basically fixed number of grid points is used, but the point positions are moved in such a way so that the grid points concentrate in critical spatial areas. R-refinement plays an important and growing role in computational fluid dynamics, especially where the fluid interacts with moving walls (as in piston engines or structures yielding to an overpressure).

H-refinement in this approach a variable number of grid points is used. Points are added to, or removed from, the grid according to the local requirements, without changing the positions of the other grid points. As a result, the spatial grid step h is locally decreased or increased, while the grid is locally refined or coarsened, respectively.

P-refinement in this approach a principally fixed grid is used, but adaptive solution is obtained by locally varying the order of spatial discretization. Methods which do accomplish the addition of higher order shape functions are either the conventional polynomials (Babuska et al., 1986), spectral element functions (Mavriplis, 1990) or hierarchical shape-functions (Zienkiewicz and Zhu, 1987). P-refining methods are increasingly used in finite-element methods, often together with h-refining methods (Lohner, 1995).

Indication of error The crucial issue of grid refinement is to modify the grid and focus on the regions of interest. In flow simulations the regions of interest will naturally be regions where there is variation in one or more important properties. While regions of constant properties may be interesting from an engineer's point of view, but from which no additional accuracy is gained by calculating it with more grid points.

The information about the regions where the grid should be refined or coarsened ideally should be provided by an error estimator. Error estimation for fluid flow calculations is not an easy task. The Navier-Stokes equations, are a coupled, nonlinear system, and errors present in any one of these fields in general will effect the solutions of all others, in a nonlinear manner difficult to describe accurately. The discretization error describes the deviation from the analytical solution of the set of differential equations, but is not directly accessible. However it is possible to construct approximations to this error.

There are a number of adaptive methods in CFD which are designed to be used in combination with finite element, finite volume and finite difference schemes. The different schemes can be divided in four groups and are enumerated below:

* Jump in property variable

* Interpolation theory

* Comparison of derivatives

* Residu of partial differential equation

LES Turbulence Model

The fluctuations occurring in the flow can be associated to a range of different scales, also known as vortices. The large scales are associated to low frequency vortices and their behaviour is dominated by the main flow; in contrast the small scales have higher frequency. The small scales are more isotropic and uniform in their behaviour, consequently the effects of small scales are easier to estimate.

The idea behind LES turbulence modeling is to use a mesh fine enough to ensure that the larger scales can be resolved explicitly by the mesh, while the small scales -called subgrid scales-, which cannot be observed in the numerical domain, are estimated via the LES model assumptions. The small scales are taken into account via an extra dissipation term, which accounts for the energy dissipation which should have occurred in the small scales.

For the turbulent flow computations, space averaged Navier-Stokes equations of motion of an incompressible fluid can be written as:

$$\frac{\partial \overline{u_i}}{\partial t}+\overline{u_j}\frac{\partial \overline{u_i}}{\partial x_j}=-\frac{1}{\rho}\frac{\partial p}{\partial x_i}+\frac{(\mu_{lam}+\mu_t)}{\rho}\frac{\partial^2 \overline{u_i}}{\partial x_j \partial x_j} \quad (1)$$

Here the over bar represents the filtered variable. The term μ_t for the space averaged equation is called the subgrid scale viscosity or turbulent viscosity. (Smagorinsky, 1963) proposed a method of calculating the subgrid scale viscosity as shown in equation 2.

$$\mu_t = \rho\,(C_s\Delta)^2\,|\overline{S}| \qquad (2)$$

Here C_s is the Smagorinsky constant, which normally has a value in the range of 0.10 to 0.25, Δ is the subgrid length scale associated to the grid size. The quantity $\overline{S}_{ij}$is the resolvable strain rate given by equation 3.

$$\overline{S}_{ij} = \frac{1}{2}\left(\frac{\partial \overline{u}_i}{\partial x_j} + \frac{\partial \overline{u}_j}{\partial x_i}\right) \qquad (3)$$

In the next step the locally calculated turbulent viscosity, which for each element varies in magnitude, is added to the laminar viscosity. In the next time step, the governing equations will be resolved, including the turbulent viscosity to count for the subgrid scales.

Near Wall Treatment For the LES simulation no wall function is used, but wall effects were taken into account by reducing the Smagorinsky constant in the vicinity of the cylinder surface. A damping variable D_{damp} was introduced to reduce the Smagorinsky constant in a region of 20% of the cylinder diameter around the bluff body. The damping function has an alternative form of the Van Driest damping function as shown in equation 4. This was suggested by (Tutar et al., 1998) who indicated that the use of the van Driest wall function for separated flows, i.e. a flow passing a circular cylinder, is questionable.

$$D_{damp} = 1 - e^{-\left(\frac{y^+}{A^+}\right)^2} \qquad (4)$$

Here A^+ is a constant, which in accordance to literature, is assumed to be 25, y^+ is the distance of the element to the wall in terms of wall-shear units, i.e. $y^+ = \frac{yu_\tau}{\nu}$. The shear friction velocity u_τ is calculated from the velocity gradient at the wall, i.e. $u_\tau = \sqrt{\nu \frac{du}{dy}}$. Thus, by taking the wall effects into account, a damped value for the Smagorinsky constant is calculated in the wall region via $C_s(D_{damp}) = C_s D_{damp}$.

SOFTWARE DEVELOPMENT

Dynamic grid adaptation

The refinement strategy being used in the REACFLOW code is the so called h-refinement, where grid points are added and removed based on the error estimation and the error bounds, defined at the start of the simulation. The refinement of the mesh always takes place across the longest edge of the triangular element, meaning that the new created triangles tend to be of equilateral shape.

Method for error indication The method for error indication being implemented is an estimation of the local interpolation error. For a given variable of interest, q, an interpolated value for a grid point x_i can be defined. This value $\widehat{q}_i$ can be defined in various ways. However in the present work the arithmetical mean is defined over the neighbor grid points:

$$\widehat{q}_i \equiv \frac{1}{N}\sum_{j=1}^{N} q_j \qquad (5)$$

where q_j are the values of the variable at the j'th of the N neighbors of the grid point x_i. The interpolated value may now be compared with the actual value in that grid point, q_i. If the absolute value of the difference

$$e_i \equiv |q_i - \widehat{q}_i| \qquad (6)$$

is greater than a predefined value, a new grid point will be inserted in the vicinity.

An error estimation of this kind thus assume the solution to be smooth and will lead to mesh refinement in the region where there is a certain variation in the refinement variable. An advantage of the interpolation method is that all neighbor elements are included in the determination of a new node, leading to a smoother and averaged mesh refinement.

Refinement Variable The determination of an appropriate refinement variable to approximate the discretization error heavily relies on the physical problem investigated. Widely used refinement variables in this respect are the density, pressure and velocity gradients, as well the turbulent viscosity. However the discretization error describing the deviation from the analytical solution of the set of differential equations is not directly accessible. Therefore the refinement variable is a compromise of the quality of the error indication and the computational complexity of the refinement variable.

Modification to turbulent viscosity as a refinement variable The refinement variable used in this work is derived from the equation for turbulent viscosity in the LES turbulence model. By varying the weight of either the cell size or the strain rate an other adaptation behaviour can be established. The weighting constants C_m and C_{str} have to be defined at the start of the simulation, and are constant throughout the domain. An increase of the constant C_m will lead to a more solution independent mesh refinement, while an increase in the constant C_{str} will lead to a mesh refinement in the regions where high velocity gradients do occur.

$$\mu_t = \rho\,(C_s\Delta)^2\,|\bar{S}| \qquad (7)$$

$$e_i = \rho C_s^2 \Delta^{C_m}\,|\bar{S}|^{C_{str}} \qquad (8)$$

Turbulence model

Modeling turbulent flow with the Standard Smagorinsky LES turbulence model requires the implementation of equation 2. This equation calculates the subgrid scale viscosity by means of four parameters:

* Subgrid length scale
* Density
* Smagorinsky constant
* Rate of strain

Both density and rate of strain can be obtained from the CFD code, while the Smagorinsky constant can be set to 0.15, as suggested in literature (Smagorinsky, 1963), (Ferziger, 1996). Extra attention should been given to the definition of length scale, as the mesh is of triangular shape.

Subgrid length scale A widely used definition for the subgrid length scale for a rectangular mesh, proposed by (Smagorinsky, 1963), simply reads: $\Delta = \sqrt{\partial x \partial y}$. As the present code uses triangular grids, the definition of the subgrid length scale must be considered. In our previous work, two definitions for the subgrid length scale have been used. In the first definition, the subgrid length scale is defined in a way similar to the definition of Smagorinsky, as shown in equation 9. In the second, the subgrid length scale is defined as the square root of the triangle surface, as shown in equation 10. It is argued that the latter is consistent with the definition of subgrid length scale proposed by Smagorinsky; Smagorinsky also defined the subgrid length scale as the square root of the surface of the element.

$$\Delta = \sqrt{\partial x \partial y} = \sqrt{2A_{triangle}} \qquad (9)$$

$$\Delta = \sqrt{\frac{1}{2}\partial x \partial y} = \sqrt{A_{triangle}} \qquad (10)$$

As proposed in the work of (de With, 1999) the second definition, shown in equation 10, has given better agreement with experimental data and will be used in this work.

RESULTS

In this work a mixture of simulations have been undertaken, utilizing the DGA algorithm as well using a conventional pre-defined mesh. The two simulations using the DGA algorithm have both used an initial mesh containing 7500 nodes. In the former simulation, the refinement variable is configured with a value of 1 for both constants C_m and C_{str}, while in the latter the constant C_m and C_{str} where set to 1 and 2 respectively. In the rest of the simulations a conventional pre-defined mesh containing 6.1e4 nodes was utilized.

The simulations were performed at a Re number of 1.4e5 to allow a comparison with experimental data obtained in a study of (Cantwell and Coles, 1983). Based on the experimental data being available, a comparison is made with the velocity decay along the centerline and the shear stresses $\frac{\overline{u'v'}}{U^2}$ in cross sectional direction at a distance $\frac{x}{D} = 1$ from the center of the cylinder. The shear stresses $\frac{\overline{u'v'}}{U^2}$ are obtained via a Fast Fourier Transform (FFT) analysis to separate the shear stresses associated to the shedding frequency from the shear stresses associated to the turbulent motions. Additionally drag coefficient (C_D), vortex shedding frequency (S_t) and separation angle are obtained from the numerical data to allow a comparison with experimental data.

As shown in figure 1, good agreement in velocity decay is accomplished in the downstream region. It is the recirculation region, just behind the cylinder, where the level of agreement has decreased, and the recirculation has been under predicted. The complexity in modeling the recirculation region is confirmed by the prediction of shear stresses, shown in figure 2, which shows good agreement away from the cylinder, while towards the center shear stresses have been over predicted. Additionally to velocity decay and shear stresses, it are drag coefficient and separation angle which quantify the quality of the flow field in the region adjacent to the wall. These flow parameters, obtained from the numerical data, show an over prediction in comparison with the data of (Cantwell and Coles, 1983). The Strouhal number representing the frequency of vortex shedding shows good agreement for all simulations.

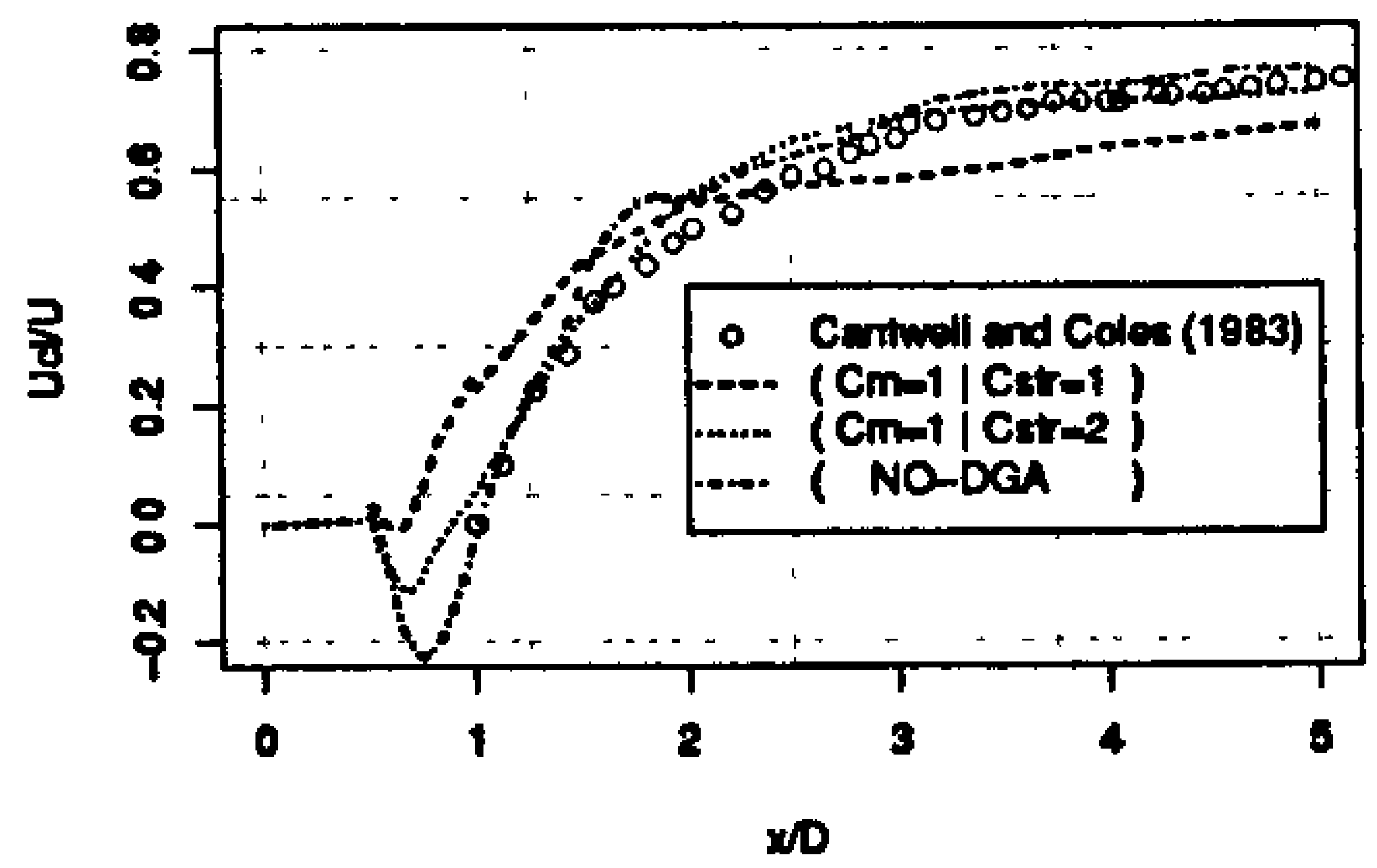

Figure 1. TIME AVERAGED VELOCITY ALONG CENTERLINE $\frac{u_d}{U}$ at $\frac{y}{D} = 0$

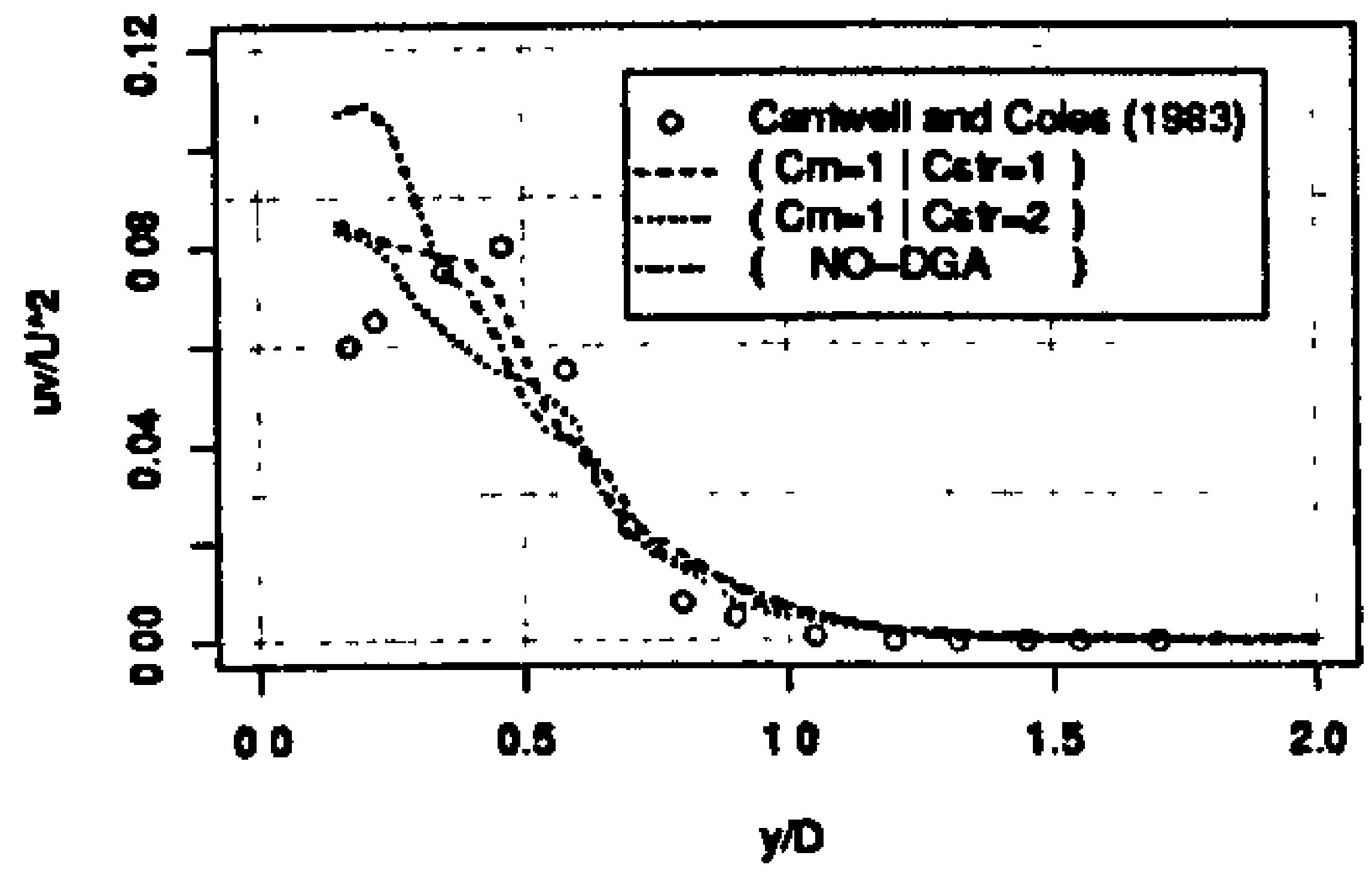

Figure 2. TIME AVERAGED SHEAR STRESSES $\frac{\overline{u'v'}}{U^2}$ AT $\frac{x}{D} = 1$

DISCUSSION

It is very surprising that there exists a vast literature devoted to the development of error estimators for adaptive grid strategies, but almost nothing has been done to develop refinement variables of determining the error magnitude of numerical solutions. However, the success of adaptive grid strategies depends well on a reliable error estimation and on the adequate determination of acceptable error bounds, with which the estimated errors are compared.

Suggestions for refinement variables in a turbulent flow field were done by (Wang, 1998) and (Zeeuw and Powell, 1992). In a comprehensive study which was conducted by (Zeeuw and Powell, 1992), they found a criterion based on compressibility and rotationality most suitable. (Wang, 1998) suggested to use the local cell Re number as a refinement variable in the vicinity of the wall instead of the divergence and curl. Despite the variety of refinement variables suitable for flow problems where turbulent flow features are of primary interest, it is the use

Table 1. FLOW PARAMETERS FOR A CIRCULAR CYLINDER AT RE=1.4e5

	C_D	S_t	Sep. [o]
Cantwell and Coles (1983)	1.24	0.179	77.0
$C_m = 1\text{-}C_{str} = 1$	1.45	0.180	96.0
$C_m = 1\text{-}C_{str} = 2$	1.46	0.173	81.0
NO-DGA	-	0.174	86.0

of velocity gradients, which they have in common. Centerline velocity variation, rotationality and local cell Re number are all obtained from the local velocity gradients. The reason for using the velocity gradient is twofold. In a flow field driven by convection, it are the complex flow patterns, which are characterized by the velocity gradient in space. From a numerical perspective, it is the local cell Re number and indirectly the velocity gradient, which is a measure for the discretization error of the convection terms. A flow parameter which incorporates all the velocity gradients, as well the mesh cell size is the turbulent viscosity, as calculated in equation 2. With the addition of the two constants C_m and C_{str} into the equation for turbulent viscosity a refinement variable is proposed, which should indicate for the error magnitude in convective driven flows, and still allow control on the refinement behaviour, by means of the two constants C_m and C_{str}. The impact of the refinement constants onto the refinement behaviour is shown in figure 3 and 4. In the former, the DGA has led to a uniform refinement in the whole region behind the cylinder, while in the latter the DGA has refined boundary layer, separation and shear layers in high depth, but not much attention has given to the wake region. A broader picture of the mesh refinement is shown in figure 5 and 6. With the constants C_m and C_{str} set to 1 the refinement is sensitive to the absolute dimensions of the mesh leading to a strong refinement in the wake region, where the velocity gradients are substantially smaller compared to the region adjacent to the cylinder. In contrast the latter simulation shows no substantial mesh refinement in the region further downstream.

As a consequence of different refinement behaviour there is a significant difference in mesh resolution towards the end of the simulation. The first simulation ($C_m = 1\text{-}C_{str} = 1$) established a mesh containing roughly 2.6e4 nodes, while in the second simulation ($C_m = 1\text{-}C_{str} = 2$) the final mesh contained around 1.4e4 nodes. The main question in both simulations is the contribution of additional refinement to the quality of prediction. A comparison of both simulations with experimental data shows that both simulations do predict the flow well, however both have got there strengths and weaknesses. In the first simulation ($C_m = 1\text{-}C_{str} = 1$) the recirculation behind the cylinder is under predicted as well the drag coefficient and separation angle deviate from the experimental data. A comparison of the second simulation ($C_m = 1\text{-}C_{str} = 2$) shows a deviation in the shear stresses towards the centerline, as well an over prediction of the drag coefficient. Based on the comparison with experimental data, it is plausible that the mesh refinement in the region further downstream does hardly contribute to the quality of the prediction. This hypothesis is confirmed by the third simulation (NO-DGA). In the third simulation, a mesh is generated with a high resolution around the cylinder, and in the region further downstream where the wake is expected to develop. In this simulation, velocity decay and Strouhal number are predicted well, but there is an over prediction of the shear stresses towards the centerline. The level of agreement obtained with such high mesh resolution, thus support the hypothesis that it is the modeling of the boundary layer and shear layers which is crucial to good flow prediction. It is the second simulation ($C_m = 1$-

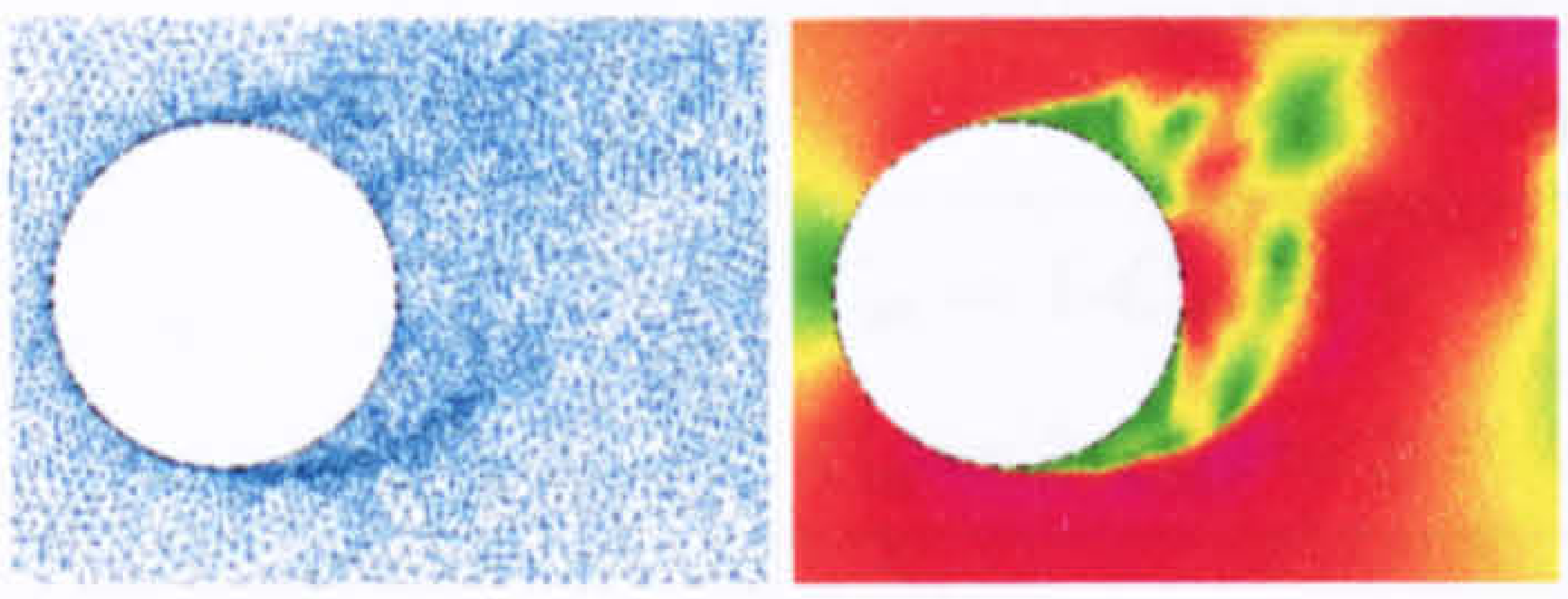

(a) MESH (b) FLOWFIELD

Figure 3. MESH AND FLOWFIELD AROUND CIRCULAR CYLINDER $C_m = 1\text{-}C_{str} = 1$

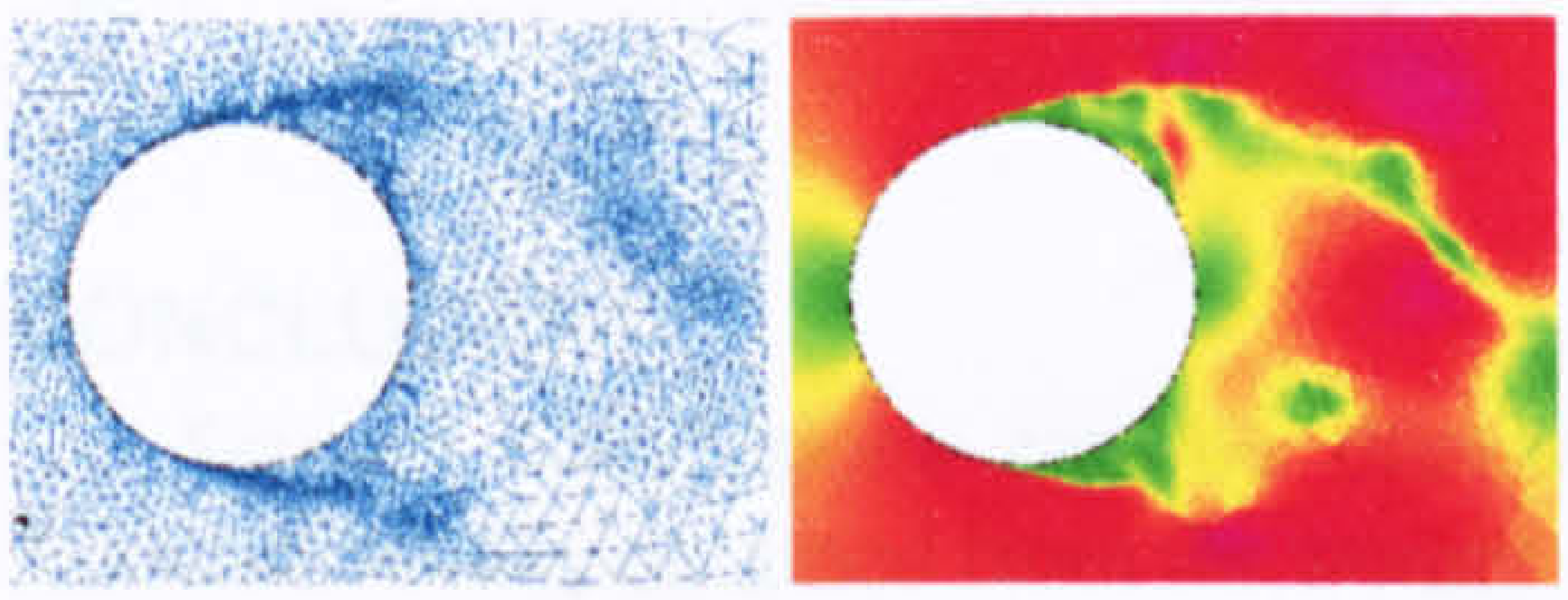

(a) MESH (b) FLOWFIELD

Figure 4. MESH AND FLOWFIELD AROUND CIRCULAR CYLINDER $C_m = 1\text{-}C_{str} = 2$

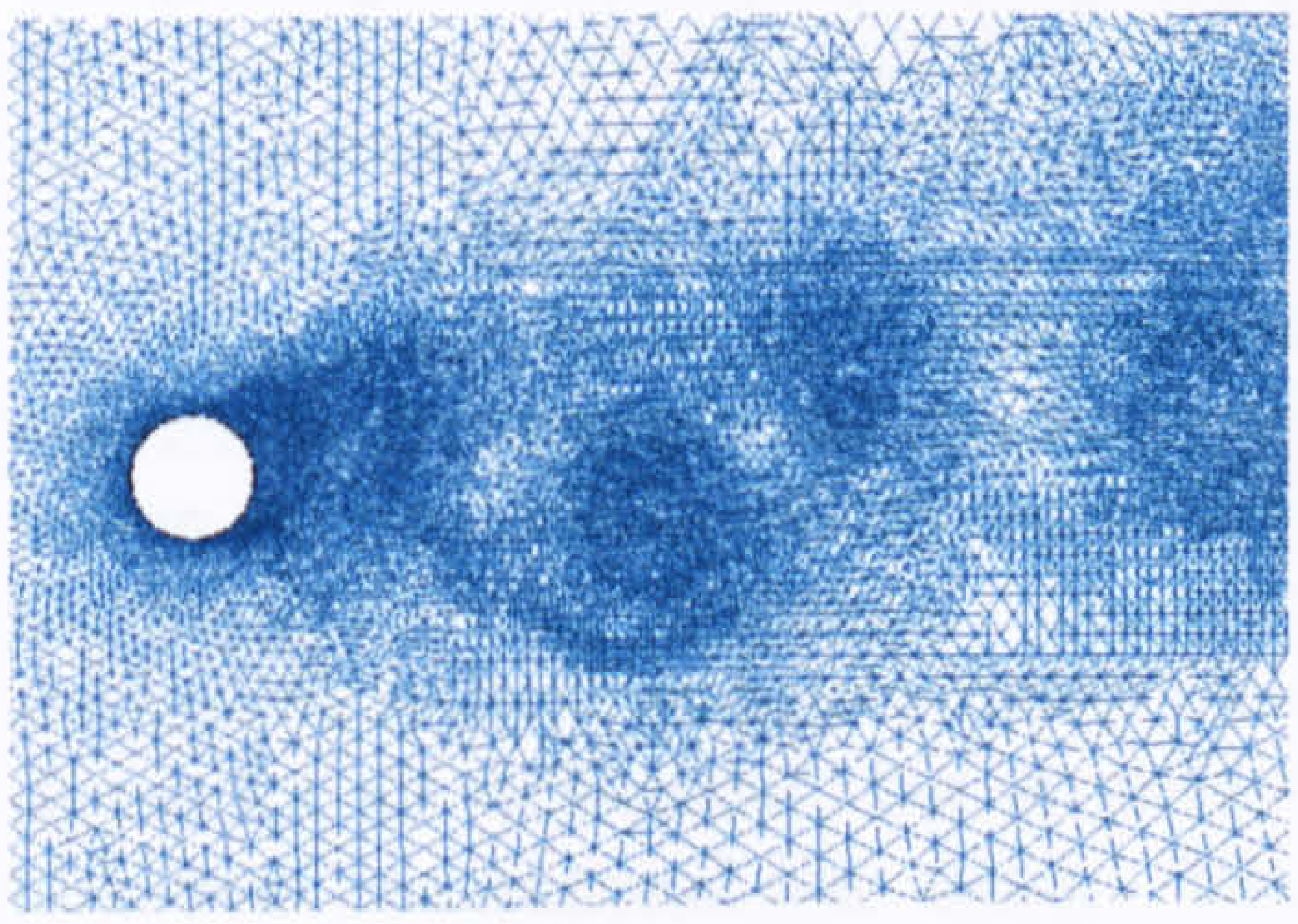

Figure 5. MESH IN THE DOWNSTREAM REGION $C_m = 1\text{-}C_{str} = 1$

$C_{str} = 2$) which fulfills this need, and leads to strong mesh refinement in the boundary layer and shear layers. As a consequence, a whole range of small scale vortices are observed in the vicinity of the wall, these vortices do move along the boundary in both up- and downstream direction. It are the upstream moving vortices that crawl underneath the shear layer, penetrating into the region where separation occurs, leading to an upstream movement of the separation point. It is due to this mechanism that the separation angle in the second simulation ($C_m = 1\text{-}C_{str} = 2$) is over predicted with only 4° .

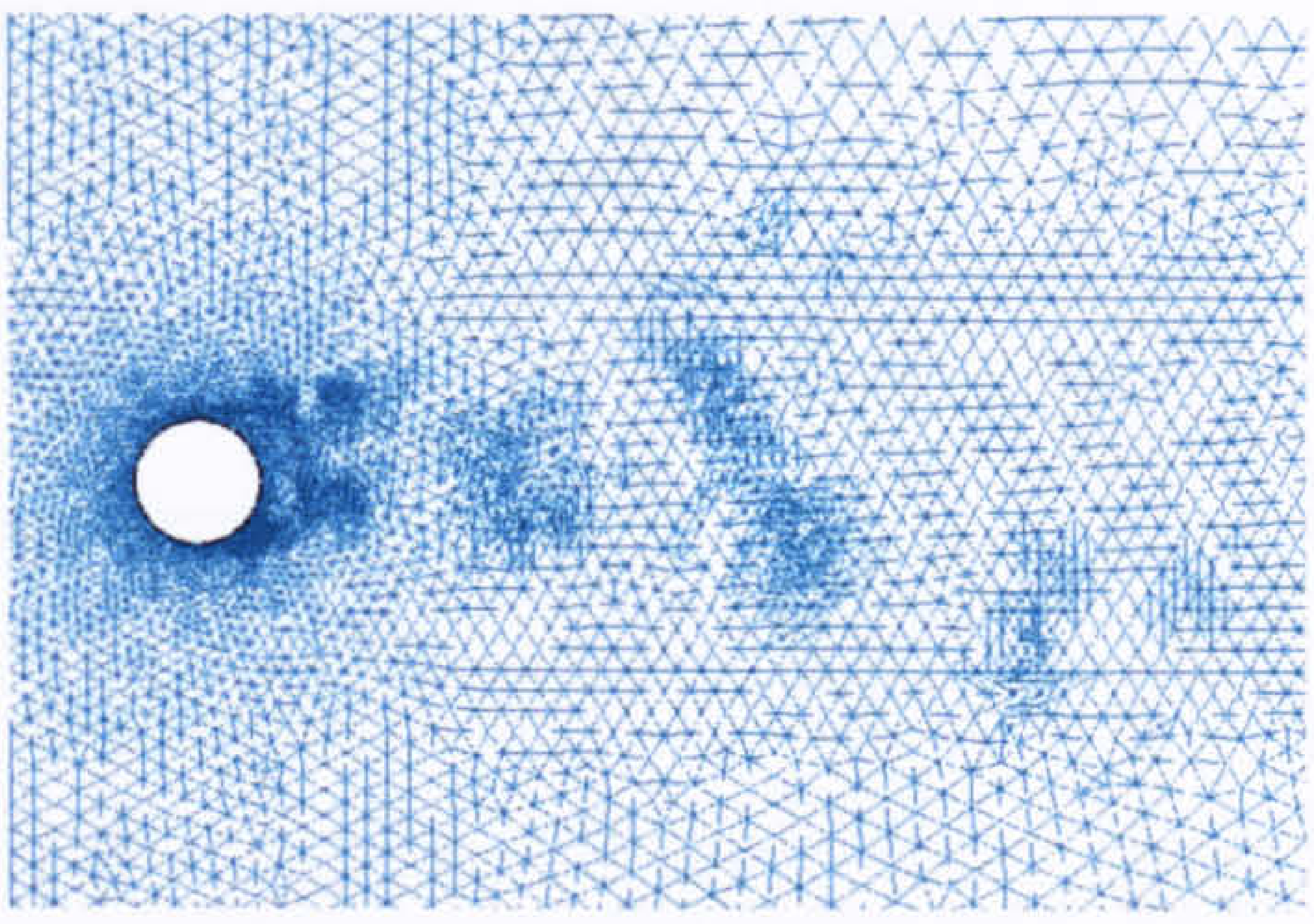

Figure 6. MESH IN THE DOWNSTREAM REGION $C_m = 1\text{-}C_{str} = 2$

The error bounds presented in this work are specific for the utilized DGA algorithm, and do not have a wide applicability, however to ensure a stable grid refinement the lower error bound, used for coarsening the mesh, has been set to 50% of the upper error bound, used for mesh refinement. To ensure further stability of the DGA algorithm and to reduce computational demand, grid refinement only takes place after every tenth time step.

The validation of numerical data has been limited to averaged quantities, although it are these quantities which are of main interest from an applied CFD perspective it under exposes the instantaneous effects due to grid adaptation. Typical are the small scale motions in the regions where the mesh has strongly refinement. In here, it could be argued that either the mesh has refined due to the flow field, or a flow motion has developed due to mesh refinement, i.o.w. to what extend can grid adaptation drive the flow field? In the downstream region, this effect should be considered not to be significant, as the flow is already determined by the upstream flow. However in the region, where separation occurs, the mesh can have significant influence onto the flow field. Fact is that a comparison of an instantaneous flow field, at the same time, of both simulations ($C_m = 1\text{-}C_{str} = 1$) and ($C_m = 1\text{-}C_{str} = 2$) shows a radical difference. To quantify the extend in which the DGA is driving the flow field is hard to determine, as the governing equations and DGA algorithm are coupled. However, that the average quantities do show good

Table 2. ERROR BOUNDS FOR COMPARISON WITH ESTIMATED ERROR

	upper bound	lower bound
$C_m = 1\text{-}C_{str} = 1$	$1.0e^{-3}$	$5.0e^{-4}$
$C_m = 1\text{-}C_{str} = 2$	$1.6e^{-2}$	$8.0e^{-3}$

agreement can only mean that the effect of small scale vortices is not dominating the main flow properties. To what extend, this applies to other kind of flow problems, is far beyond the aims of this work, but of significant interest to the CFD society.

CONCLUSION

Several conclusions can be drawn from the results obtained from the numerical data.

* The refinement variable proposed in this work allows control on the refinement behaviour by means of the two constants C_m and C_{str}. By increasing the value of C_m, the grid adaptation becomes more mesh dependent, while an increase of constant C_{str} leads to a more solution dependent refinement behaviour.

* Good agreement with experimental data has been obtained in the downstream region for centerline velocity, and with the vortex shedding frequency . Towards the centerline shear stresses are over predicted for all simulations, but in particular with conventional fine mesh. The drag coefficient has been over predicted as well separation angle, although it has to be mentioned that the second simulation ($C_m = 1\text{-}C_{str} = 2$) has only over predicted the separation angle by 4o.

* It is concluded that the modeling of boundary and shear layer are crucial for good prediction of the flow field. It is the second simulation ($C_m = 1\text{-}C_{str} = 2$) which fulfills this requirement, and has obtained a good level of agreement with a minimum of nodes (1.4e4).

* It has been argued that either the mesh has refined due to the flow field, or a flow motion has developed due to mesh refinement. Nevertheless, the agreement in averaged quantities throughout the different simulations is an indication that the main flow field is not driven by the grid adaptation.

REFERENCES

Babuska, I., Zienkiewicz, O. C., Gago, J., and de A Oliverira, E. R. (1986). *Accuracy Estimates and Adaptive Refinements in Finite Element Computations.* John Wiley. New York.

Cantwell, B. and Coles, D. (1983). An experimental study of entrainment and transport in the turbulent near wake of a circular cylinder. *Journal of Fluid Mechanics,* 136:321–374.

de With, G. (1999). Simulation of a jet at transitional reynolds numbers. Master's thesis, University of Hertfordshire.

Eiseman, P. R. (1987). Adaptive grid adaptation. *Comp. Meth. Appl. Mech. and Eng.,* 64:321–376.

Ferziger, J. H. (1996). Large eddy simulation. In Gatski, T. B., Hussaini, M. Y., and Lumley, J. L., editors, *Simulation and Modeling of Turbulent Flows,* chapter 3, pages 109–154. Oxford University Press.

Habashi, W. G., Dompierre, J., Bourgault, Y., Yahia, D. A. A., Fortin, M., and Vallet, M. G. (2000). Anisotropic mesh adaptation: towards user-independent, mesh-independent and solver-independent cfd. part 1: general principles. *Int. J. Num. Meth. Fluids,* 32:725–744.

Lohner, R. (1995). Mesh adaptation in fluid mechanics. *Eng. Fracture Mechanics,* 50(5-6):819–847.

Mavriplis, C. (1990). A posteriori error estimators for adaptive spectral element techniques. *Proc. 8th GAMM Conf. Numer. Meth. Fluid. Mech.,* 29:333–342.

Muzaferija, S. and Gosman, D. (1997). Finite-volume cfd procedure and adaptive error control strategy for grids of arbitrary topology. *J. Comput. Physics,* 138:766–787.

Smagorinsky, J. (1963). General circulation experiments with the primitive equations. *Monthly Wheater Review*, 91:99–152.

Tutar, M., Holdø, A. E., and Lewis, A. P. (1998). Comparitive performance of various two equation models and les on simulated flow past a circular cylinder. *Proceedings of A.S.M.E. Fluids Engineering Summer Meeting on Finite Element Applications in Fluid Dynamics.*

Wang, Z. J. (1998). A quadtree-based adaptive cartesian/quad grid flow solver for navier-stokes equations. *Computers and Fluids*, 27(4):529–549.

Zeeuw, D. D. and Powell, K. G. (1992). An adaptively refined cartesian mesh solver for the euler equations. *Journal of Computational Physics*, 104:56–68.

Zienkiewicz, O. C. and Zhu, J. Z. (1987). A simple error estimator and adaptive procedure for practical engineering analysis. *Int. J. Numer. Methods Eng.*, 24:337–357.

Appendix B

Proceedings of -
- -, 2002, -, -, USA

MODELING OF FLOW AROUND A CIRCULAR CYLINDER IN SUB-CRITICAL FLOW REGIME WITH THE USE OF DYNAMIC GRID ADAPTATION ALGORITHMS

Govert de With
Arne E. Holdø*
CFD Research Group
Dep. Aeronautical Civil and Mechanical Eng.
University of Hertfordshire
Hatfield Campus, College Lane
Hatfield, Herts AL10 9AB
Email: G.de-With@herts.ac.uk
Email: A.E.Holdo@herts.ac.uk

Thomas A. Huld
Institute for Systems, Informatics and Safety
Joint Research Centre
Ispra (Va), 21020
Italy
Email: Thomas.Huld@jrc.it

ABSTRACT

In the present study a Dynamic Grid Adaptation (DGA) algorithm is used for predicting flow around a circular cylinder in sub-critical flow regime at a Reynolds number of $1.4 \cdot 10^5$. The reason for adopting a DGA algorithm is to use the flow field as a driving criteria for mesh refinement rather then the geometry of the computational domain or the judgment of the CFD user as common in conventional mesh. It is demonstrated how DGA reduces the mesh size significantly and also makes time consuming mesh testing unnecessary.

The concept being adopted is to concentrate mesh refinement in regions with high gradients and high turbulent viscosity, while in the region further downstream where the flow is fully developed a coarser mesh will develop and turbulence is modeled with the Large Eddy Simulation (LES) turbulence model.

The aim of the study is to present an appropriate variable for mesh refinement, which accomplishes a high rate of mesh refinement in the region with high gradients. The new variable is a product of the local mesh cell size and the rate of strain and includes two additional variables to allow control over the refinement behaviour.

---

*Address all correspondence to this author.

NOMENCLATURE

A_{tr}	Element surface
A^+	Constant
C_d	Drag coeficient
C_m	Adaptation constant for mesh
C_s	Smagorinsky constant
C_{str}	Adaptation constant for strain
D	Cylinder diameter
D_{dam}	Damping variable
e_i	Estimated error
N	Number of neighbor elements
p	Pressure
q	Refinement variable
$\hat{q}_i$	Interpolated refinement variable
Re	Reynolds number
$\lvert\bar{S}\rvert$	Magnitude of strain
S_{ij}	Strain tensor
S_t	Strouhal number
t	Time
$\bar{u}$	Average velocity
$\bar{u}_{cl}$	Average centerline velocity
u_i	u,v,w for i=1,2,3 respectively
u	Streamwise velocity component
u'	Streamwise fluc. velocity component
u_τ	Shear friction velocity
v	Lateral velocity component
v'	Lateral fluc. velocity component
x	Space in streamwise direction
x_i	x,y,z for i=1,2,3 respectively
y	Space in lateral direction
y^+	Distance in wall shear units
Δ	Subgrid length scale
μ_{lam}	Laminar viscosity
μ_t	Turbulent viscosity
ν	Kinematic viscosity
ρ	Density

INTRODUCTION

The present study deals with the simulation of flow around a circular cylinder at a Reynolds number of $1.4 \cdot 10^5$. Several studies have been reported for this type of flow (1) and it is gradually accepted that it is a difficult test case for Computational Fluid Dynamics (CFD) (2). Tutar & Holdø's results suggest that the Large Eddy Simulation (LES) method gives improved results compared to those of other Reynolds Averaging Navier Stokes (RANS) based turbulence models and Breuer (2) demonstrates the considerable mesh requirements of the LES type of simulations. In order to overcome the mesh requirements and still obtain results of good quality the present work investigates the suitability of a Dynamic Grid Adaptation (DGA) algorithm. Frequently meshes are generated where due to mesh construction methods the resolution is high in regions where gradients are not significant. Consequently, such meshes have a large number of redundant cells. Conversely, due to time variations in the computed flow field, there will be regions where the mesh resolution is insufficient. The aim of the present work was to use DGA methods to generate mesh refinement in important regions and conversely to reduce mesh refinement in regions with low gradients.

To achieve this aim it was necessary to define and develop mesh refinement variables. There have been many developments related to adaptive methods and adaptive grid strategies (3) (4) (5) (6). However, there is comparatively little work reported on grid adaptation with turbulent, unsteady flows. The present work is focussed on the determination of a reliable refinement variable.

In this work the CFD code REACFLOW (7) has been been utilized. This code has adopted the projection method in the solution procedure and uses a triangular mesh. Due to the triangular mesh being used in the REACFLOW code the definition of the length scale in the LES turbulence model has to be considered. The LES turbulence model belongs to the eddy viscosity type of turbulence models and calculates the turbulent viscosity element wise from both the rate of strain and the cell size of the element.

BACKGROUND

The work being undertaken focuses both on grid adaptation and LES turbulence modeling. The suitability of a LES turbulence model in combination with DGA lies in the concept being chosen for calculating turbulent viscosity. In this turbulence model, turbulent viscosity is proportional to the cell size of the element, therefore an increase in mesh resolution will lead to a reduction in local turbulent viscosity. In case of a very fine mesh the contribution of the LES turbulence model vanishes and the flow is practically calculated without turbulence model.

Dynamic grid adaptation

One method to reduce the numerical error is by reducing the size of the discretization elements. However, an excessive increase in mesh resolution would lead to insurmountable demand for computational power. As a consequence a mesh sensitivity analyses is required to find consensus in numerical error and computational demand. This requires the user to estimate before hand the regions of interest. Research has shown that the flow prediction is sensitive to the mesh resolution, this numerical behaviour indicates a need for dynamically generated mesh, which adapt the mesh to the flow field to cover interesting flow phenomena in high detail. A well developed and robust DGA algorithm can lead to a reduction in both numerical error and computational requirements. This appealing feature has encouraged the CFD society to develop a whole range of algorithms for DGA of different applicability and complexity.

Refinement Strategies In recent years a whole series of strategies have been developed, a small number of these strategies are preprocessing based and focus on a geometry based mesh refinement. For CFD purposes the majority of the strategies is focusing on a solution based mesh refinement. This work will deal with the solution based mesh refinement. Three approaches can be distinguished;

R-refinement r-refinement, or grid movement (relocation). In this approach a basically fixed number of grid points is used, but the point positions are moved in such a way so that the grid points concentrate in critical spatial areas (8). R-refinement plays an important and growing role in computational fluid dynamics, especially where the fluid interacts with moving walls (as in piston engines or structures yielding to an overpressure).

H-refinement in this approach a variable number of grid points is used. Points are added to, or removed from, the grid according to the local requirements, without changing the positions of the other grid points. As a result the grid is locally refined or coarsened (5).

P-refinement in this approach a principally fixed grid is used, but adaptive solution is obtained by locally varying the order of spatial discretization. Methods which do accomplish the addition of higher order shape functions are either the conventional polynomials (9), spectral element functions (10) or hierarchical shape-functions (11). P-refining methods are increasingly used in finite-element methods, often together with h-refining methods (5).

Indication of error In flow simulations the regions of interest will naturally be regions where there are strong gradients. The issue of grid refinement is to modify the grid and focus on the regions of interest.

The information about the regions where the grid should be refined or coarsened ideally should be provided by an error estimator. Error estimation for fluid flow calculations is not an easy task. The Navier-Stokes equations are a coupled, nonlinear system and errors present in any one of these fields in general will effect the solutions of all others, in a nonlinear manner difficult to describe accurately. The discretization error describes the deviation from the analytical solution of the set of differential equations, but is not directly accessible. However, it is possible to construct approximations to this error.

There are a number of adaptive methods in CFD which are designed to be used in combination with finite element, finite volume and finite difference schemes. The different schemes can be divided in four groups:

Jump in property variable The simplest error indicator is obtained by evaluating the jump of some indicator variable like the turbulent viscosity, pressure or temperature within an element or along an edge.

Interpolation theory In this method an interpolated value of some indicator variable is calculated by means of its surrounding points and compared with the actual value.

Comparison of derivatives Inhere the actual value obtained from the utilized numerical scheme is compared with an indicator variable calculated with a low order numerical scheme. This method allows a good estimate of the error in the higher order derivatives. The method can give an indication as to whether it is more efficient to use h-refinement, or to increase the order of accuracy.

Residue of partial differential equation The essence of this error estimator is to use a recovered more accurate, even higher order solution from the finite element approximation in place of the exact solution in the computation of the error.

LES Turbulence Model

The fluctuations occurring in the flow can be associated with a range of different turbulence scales, also known as eddies. The large scales are associated to low frequency vortices and their behaviour is dominated by the main flow. The small scales are more isotropic and uniform in their behaviour, consequently the effects of small scales are easier to estimate.

The idea behind LES turbulence modeling is to use a mesh fine enough to ensure that the larger scales can be resolved explicitly by the mesh, while the small scales –called subgrid scales–, which cannot be observed in the numerical domain, are estimated via the LES model assumptions. The small scales are taken into account via an extra dissipation term, which accounts for the energy dissipation which occurres in the small scales.

For the turbulent flow computations the space averaged Navier-Stokes equations of an incompressible fluid are written as:

$$\frac{\partial \overline{u_i}}{\partial t}+\overline{u_j}\frac{\partial \overline{u_i}}{\partial x_j}=-\frac{1}{\rho}\frac{\partial p}{\partial x_i}+\frac{(\mu_{lam}+\mu_t)}{\rho}\frac{\partial^2 \overline{u_i}}{\partial x_j \partial x_j} \tag{1}$$

Here the overbar represents the filtered variable. The term μ_t for the space averaged equation is called the subgrid scale viscosity or turbulent viscosity. Smagorinsky (12) proposed a method of calculating the subgrid scale viscosity as shown in equation 2.

$$\mu_t=\rho l_s^2\left|\overline{S}\right| \tag{2}$$

$$l_s=C_s\Delta \tag{3}$$

Here C_s is the Smagorinsky constant, which normally has a value in the range of 0.10 to 0.25, Δ is the subgrid length scale associated to the grid size. The quantity $\overline{S}_{ij}$is the resolvable strain rate given by equation 4.

$$\overline{S}_{ij}=\frac{1}{2}\left(\frac{\partial \overline{u}_i}{\partial x_j}+\frac{\partial \overline{u}_j}{\partial x_i}\right) \tag{4}$$

In the next step the locally calculated turbulent viscosity, which for each element varies in magnitude, is added to the laminar viscosity. In the new time step, the governing equations will be resolved, including the turbulent viscosity to account for the subgrid scales.

Near Wall Treatment For the LES simulation no wall function is used, but wall effects were taken into account by reducing the length scale in the vicinity of the cylinder surface. A damping variable D_{damp} was introduced to reduce the Smagorinsky constant in a region 20% of the cylinder diameter around the cylinder. The damping function has an alternative form to the standard van Driest damping function as shown in equation 5. This was suggested by Tutar & Holdø (1) who indicated that the use of the standard van Driest wall function for separated flows, i.e. a flow passing a circular cylinder, is questionable.

$$D_{\text{damp}} = 1 - e^{-\left(\frac{y^+}{A^+}\right)^2} \qquad (5)$$

Here A^+ is a constant, which in accordance with literature, is assumed to be 25, y^+ is the distance of the element to the wall in terms of wall-shear units, i.e. $y^+ = \frac{yu_\tau}{\nu}$. The shear friction velocity u_τ is calculated from the velocity gradient at the wall, i.e. $u_\tau = \sqrt{\nu\frac{du}{dy}}$. Thus, by taking the wall effects into account, a damped value for the length scale is calculated in the wall region via $l_s = C_s \Delta D_{\text{damp}}$.

SOFTWARE DEVELOPMENT

Dynamic grid adaptation

The refinement strategy being used in the REACFLOW code is the so called h-refinement, where grid points are added and removed based on the error estimation and the error bounds, defined at the start of the simulation. The method for error indication is an estimation of the local interpolation error. For a given variable of interest, q, an interpolated value for a grid point x_i can be defined. This value $\widehat{q}_i$ can be defined in various ways, however in the present work the arithmetical mean is defined over the neighbor grid points and compared with the actual value in that grid point, q_i. If the absolute value of the difference exceeds a predefined value, a new grid point will be inserted in the vicinity. An error estimation of this kind assumes the solution to be smooth and will lead to mesh refinement in the region where there are high gradients. An advantage of the interpolation method, in comparison to other methods, is that all neighbor elements are included in the determination of a new node, leading to a smoother mesh refinement. The refinement of the mesh always takes place across the longest edge of the triangular element, which ensures that triangles with very high aspect ratio are not formed.

Refinement Variable The determination of an appropriate refinement variable to approximate the discretization error depends very much on the physical problem investigated. Widely used refinement variables in this respect are the density, pressure and velocity gradients, as well as the turbulent viscosity. However the discretization error describing the deviation from the analytical solution of the set of differential equations is not directly accessible. Therefore the refinement variable is a compromise between the quality of the error indication and the computational complexity of the refinement variable.

Modification to turbulent viscosity as a refinement variable The variable used in this work is derived from the equation for turbulent viscosity *in the LES* turbulence model. By varying the weight of either the cell size or the strain rate, by means of the DGA variables C_m and C_{str}, a different adaptation behaviour can be established. The DGA variables C_m and C_{str} have to be defined at the start of the simulation, and are constant throughout the domain. An increase of the variable C_m will lead to a more solution independent mesh refinement, while an increase in the variable C_{str} will lead to a mesh refinement in the regions where high velocity gradients exist.

$$\mu_t = \rho\,(C_s\Delta)^2\,|\overline{S}| \qquad (6)$$

$$q_i = \rho C_s^2 \Delta^{2C_m}\,|\overline{S}|^{C_{str}} \qquad (7)$$

Turbulence model

Modeling turbulent flow with the Standard Smagorinsky LES turbulence model requires the implementation of equation 2. This equation calculates the subgrid scale viscosity by means of four parameters:

* Subgrid length scale	Δ
* Density	ρ
* Smagorinsky constant	C_s
* Rate of strain	$\lvert\bar{S}\rvert$

Both density and rate of strain can be obtained from the CFD code, while the Smagorinsky constant can be set to 0.15, as suggested in literature (12) (13). Extra attention was given to the definition of subgrid length scale, because of the triangular shape of the elements.

Subgrid length scale A widely used definition for the subgrid length scale in 2-D rectangular mesh is $\Delta = \sqrt{\Delta_x \Delta_y}$, nevertheless in several studies it was found that $\Delta = \sqrt{2\Delta_x \Delta_y}$ leads to more accurate results than $\Delta = \sqrt{\Delta_x \Delta_y}$ (14) and in some cases even $\frac{\Delta}{\sqrt{\Delta_x \Delta_y}} > 2$ seems necessary (15). In the work of Vreman et. al. (14) the subgrid length scale Δ in LES was set equal to $\Delta = \sqrt{2\Delta_x \Delta_y}$, indicating that a minimum of two elements is taken to represent the smallest eddies resolved in the flow field. In other words, what is the minimum grid being necessary for resolving a turbulent scale in a triangular unstructured mesh. Previous work of de With (16) concluded that a suitable definition for the subgrid length scale in a triangular mesh reads:

$$\Delta = \sqrt{\frac{\Delta_x \Delta_y}{2}} = \sqrt{A_{tr}} \qquad (8)$$

Inhere the subgrid length scale is chosen to be the square root of the element surface and indicates that the smallest possible scale to be modeled employs three grid points.

SIMULATION RESULTS AND DISCUSSIONS

Computational domain and simulations

The computational domain and boundary conditions used for the simulations with DGA are shown in figure 1, picture (b) shows the mesh at the start of the simulation. At the inlet boundary a uniform velocity profile is imposed, while on the outlet boundary pressure is imposed and velocity is set free. No-slip boundary conditions are applied to the cylinder wall and all velocity components are set to zero. On both horizontal boundaries velocity is imposed; the velocity in the y direction is set to $v = 0$ so that no flow can be drained off or entrained via these boundaries. To ensure no mesh refinement will take place along the horizontal boundaries, the x-component of the velocity is set equal to the velocity imposed at the inlet in order not to maintain any velocity gradient along the horizontal boundaries.

In this work a total of six simulations are carried out. The first simulation presented is carried out with conventional mesh using $6.1 \cdot 10^4$ nodes. The other five simulations have utilized the DGA algorithm. The configuration of the DGA algorithm required specification of the DGA variables C_m and C_{str}, threshold values for mesh refinement and coarsening, as well as a minimum mesh size to restrict excessive mesh refinement. Details of the DGA configuration are presented in table 2 and 3.

The flow profiles shown are the time integrated streamwise velocity component both in streamwise and transverse direction, as well as the turbulent shear stress along the transverse axis. In addition drag coefficient C_D[1], Strouhal number S_t[2] and separation angle are calculated from the time integrated flow field and presented in table 1.

Basic flow features

In this work a variety of simulations is presented and compared with the experimental data from Cantwell & Coles (17). The dimensions of the wake region behind the cylinder, as well as the turbulence intensity along the transverse axis are predicted with varying success, as shown in

---

[1] The drag coefficient is the sum of the streamwise pressure forces acting on the cylinder relative to the density and inlet velocity $C_D = \frac{2F_D}{\rho u_\infty^2}$

[2] Strouhal number is the frequency of the periodic wave relative to cylinder diameter and inlet velocity $S_t = \frac{fD}{u_\infty}$

figure 2 to 5.

The velocity decay is predicted well for the simulations using $C_m = 1$ and $C_{str} = 2$, however there is a lack of agreement in the simulation with C_m and C_{str} being 1 and 2 respectively and a mesh containing $2.8 \cdot 10^4$ nodes, in the region 3 to 5 cylinder diameters away from the cylinder. Similarly, the downstream region deviates from experimental data in the simulations with a mesh containing $4.3 \cdot 10^4$ and $4.5 \cdot 10^4$ nodes respectively indicating a short wake region. Both simulations have over predicted the Strouhal number with 5% and 17% respectively, while in all other simulations Strouhal number is predicted in good agreement with experimental data. Drag coefficient C_D is over predicted in all simulations and hold values for drag coefficient C_D which are also shown in previous work of Tutar & Holdø (1) and Breuer (2).

Surprisingly the deviation with experimental data grows with increasing mesh resolution. The prediction of turbulent shear stress in the wake region confirms that an increase in mesh resolution does not automatically lead to an improvement of the flow prediction. Although there is a clear trend that an increasing mesh resolution leads to an increase in shear stress, the simulation using a mesh of approximately $4.5 \cdot 10^4$ nodes does over predict the shear stress by about 25%. A reduction in quality of the prediction with increasing mesh resolution was not expected beforehand. Nevertheless, trends of this kind where also seen in the work of Breuer (2). Distinct arguments for these trends are difficult to present as this problem relates to the resolution of small scale vortecies of the small scale flow phenomena.

Influence of grid adaptation constants C_m and C_{str}

With the introduction of the two variables C_m and C_{str} in the refinement variable there is a user defined control. The use of the adaptation constants for the grid adaptation is clearly shown in figure 6 and 7. In the first picture a smooth mesh refinement has taken place in the shear layers and along the cylinder, while in the latter the refinement is sharp and narrow and more focussed on areas that maintain a high rate of strain. Therefore, despite the limited number of nodes in the simulation with $C_m = 1$, $C_{str} = 2$ and $1.4 \cdot 10^4$ nodes, its smallest element (table 4) is still smaller than the equivalent element (table 4) in the simulation with $C_m = 1$, $C_{str} = 1$, and $2.8 \cdot 10^4$ nodes, as shown in table 4.

The variation in flow prediction is primarily due to mesh refinement and confirms the complexity of the physical processes in which certain flow regions and vortex scales in the flow field are over proportionally important. This means that the determination of a proper refinement variable can not be decoupled from the physics that are under investigation. A good refinement variable for separating flows at high Reynolds numbers is not by definition suitable for flows where other features are of key interest. Nevertheless it would be expected that a high level of mesh refinement is only required in limited areas.

The flow field predicted in the simulation with $C_m = 1$, $C_{str} = 2$ and a mesh containing $1.4 \cdot 10^4$ nodes holds not only good agreement with experimental data, but also with the simulation using conventional mesh. Both simulations do maintain similar mesh resolution in the vicinity of the wall and shear layer, the only significant difference lies in the prediction of turbulent shear stress towards the center line. It could be argued that the lack of agreement in turbulent shear stress occurs due to the coarse mesh away from the cylinder in the region where the shear stress profile is located. In this region mesh resolution is only a fraction in comparison with the simulation using conventional mesh. Therefore the importance of these vortices for the flow field is subject to discussion and the simulations indicate that the important flow mechanisms where the flow will be determined take place further upstream, in the vicinity of the wall, separation point and shear layers. A mesh refinement in the critical regions is accomplished by using $C_m = 1$ and $C_{str} = 2$. Here substantially less nodes are used in comparison with the simulations using $C_m = 1$ and $C_{str} = 1$, however the nodes are mainly allocated in the critical regions and is suspected that for this reason better agreement is obtained with the experimental data.

It is interesting to note that a further mesh refinement in the vicinity of the wall does not improve the flow prediction. A decay in the quality of the prediction could occur due to separation taking place in turbulent mode, however there is no turbulent kinetic energy until the point of separation which suggests that separation takes place in the laminar mode as experimentally expected for a sub-critical Reynolds numbers forming free shear layers. However an increase in mesh resolution leads to a wider spectrum of vortices. It is a plausible conjecture that the small scale vortices of this type, generated in the vicinity of the wall, lead to an increase in turbulent activity in the shear layers. As the vortices in the shear layer are growing in magnitude due to coalescing with surrounding vortices there will be an increase in turbulent intensity as supported by figure 3 and 5. The major question relevant is the physical representation of the small scale vortices. Although the numerics are inextricably bound up with the physics to be modeled, numerical requirements have to be fulfilled to ensure numerical stability of the flow field. To fulfill these criteria imperfections in the numerical scheme have to be accepted. In this respect it is important to mention the flux limiter used to ensure the TVD criteria. The existence of sharp velocity profiles makes the flow field more sensitive to dispersion in the flow field (18) leading to numerical dispersion. Another aspect relevant to the modeling of the flow field is the 2 dimensional simplification in this work, as a consequence flow motions in the spanwise direction, which are expected to occur in real live are not considered. Therefore the effect of 3 dimensional flow motions on the flow prediction is subject to discussion and is an interesting point for further investigation.

The use of DGA together with a modified μ_t for error indication enables a reduction in mesh size up to 75% and allows a significant reduction in computational requirements for flows where turbulence is of key interest. The reduction in mesh size is accomplished by using the flow field as the driving criteria for mesh refinement. Instead, with a conventional mesh the refinement is either based on the geometry of the numerical domain, as typically seen in body curved fitted mesh, or based on the judgment of the CFD user. However, in both cases the mesh does not reflect ideally on the flow structures being modeled and requires time consuming mesh testing. Mesh refinement with conventional methods is subject to the users expertise and judgment and is limited by the capabilities of mesh generators. It is the use of DGA algorithms which enables a solution based mesh refinement, whereby refinement criteria are inextricably bound up with the turbulent flow features.

CONCLUSION

The conventional meshes used in previous investigations have significant drawbacks. Due to the fact that the mesh is fixed throughout the simulation, a high mesh resolution has to be applied in all regions where complex flow behaviour is expected. It is most likely that a significant percentage of the mesh will have only a marginal influence on the flow prediction, leading to an inefficient use of the nodes. Therefore a proper design of the mesh requires a good understanding of the fluid dynamics being investigated, in particular if the flow is of high complexity as in flows for industrial application for example. There are several advantages in using the DGA algorithm in flows for industrial application.

* A solution based grid refinement will minimize the need to estimate the flow field beforehand. Instead a DGA algorithm generates a mesh which reflect on the flow structures being modelled. This aspect of DGA is shown in figure 6.

* There is no need for time consuming mesh testing neither for sophisticated mesh generators, instead the mesh generates under its own flow development.

The present work shows that the success of adaptive grid strategies depends on a reliable error estimation and on the adequate determination of acceptable error bounds. The importance of reliable error estimation and determination of error bounds on the flow prediction is shown in figures 2 to 5 and table 1. The present work demonstrates that the use of a modified μ_t yields reliable results. Good agreement in both experimental data (17) and conventional mesh is obtained in the simulation with $C_m = 1$, $C_{str} = 2$ and a mesh containing $1.4 \cdot 10^4$ nodes. The simulation has shown:

*The reduction in number of nodes is 75% and the mesh resolution in the refined areas which is of equal order to the simulation using conventional mesh.

* The predicted flow parameters and averaged velocity profiles are in good agreement with each other, nevertheless the main differences between both simulations, can be found in the turbulent shear stress profiles along the transverse axis as shown in figure 3 and 5.

* A strong, but narrow mesh refinement has taken place in the vicinity of the wall near the point of separation and in the small scale vortices in the shear layers further downstream, while a coarse mesh is maintained in the wake region behind the cylinder.

REFERENCES

M Tutar and A E Holdø. Computational modelling of flow around a circular cylinder in sub-critical flow regime with various turbulence models. *Int. J. Numer. Meth. Fluids*, 35:763–784, 2001.

M Breuer. A challenging test case for large eddy simulation: high reynolds number circular cylinder flow. *Int. J. Heat and Fluid Flow*, 21(5):648–654, 2000.

P R Eiseman. Adaptive grid adaptation. *Comp. Meth. Appl. Mech. and Eng.*, 64:321–376, 1987.

W G Habashi, J Dompierre, Y Bourgault, D A A Yahia, M Fortin, and M G Vallet. Anisotropic mesh adaptation: towards user-independent, mesh-independent and solver-independent cfd. part 1: general principles. *Int. J. Num. Meth. Fluids*, 32:725–744, 2000.

R Lohner. Mesh adaptation in fluid mechanics. *Eng. Fracture Mechanics*, 50(5-6):819–847, 1995.

S Muzaferija and D Gosman. Finite-volume cfd procedure and adaptive error control strategy for grids of arbitrary topology. *J. Comput. Physics*, 138:766–787, 1997.

A Soria and F Ruel. *Finite Volume Analysis of MultiComponent Incompressible Viscous Flows*. Joint Research Centre, i.94.41 edition, September 1994.

A R Diaz, N Kikuchi, and J E Taylor. A method for grid optimization for the finite element method. *Comput. Meth. Appl.Mech. Engng*, 41:29–45, 1983.

I Babuska, O C Zienkiewicz, J Gago, and E R de A Oliverira. *Accuracy Estimates and Adaptive Refinements in Finite Element Computations*. John Wiley, 1986. New York.

C Mavriplis. A posteriori error estimators for adaptive spectral element techniques. *Proc. 8th GAMM Conf. Numer. Meth. Fluid. Mech.*, 29:333–342, 1990.

O C Zienkiewicz and J Z Zhu. A simple error estimator and adaptive procedure for practical engineering analysis. *Int. J. Numer. Methods Eng.*, 24:337–357, 1987.

J Smagorinsky. General circulation experiments with the primitive equations. *Monthly Wheater Review*, 91:99–152, 1963.

J H Ferziger. Large eddy simulation. In T B Gatski, M Y Hussaini, and J L Lumley, editors, *Simulation and Modeling of Turbulent Flows*, chapter 3, pages 109–154. Oxford University Press, 1996.

B Vreman, B Geurts, and H Kuerten. Comparison of numerical schemes in large eddy simulation of the temporal mixing layer. *Intl J. Numer. Meth. Fluids*, 22:297–311, 1996.

T S Lund, H J Kaltenbach, and K Akselvoll. On the behaviour of centered finite difference schemes for large eddy simulation. *Proc. Sixth Intl Symp. on Computational Fluid Dynamics. Lake Tahoe*, September 1995.

G de With. Simulation of a jet at transi-

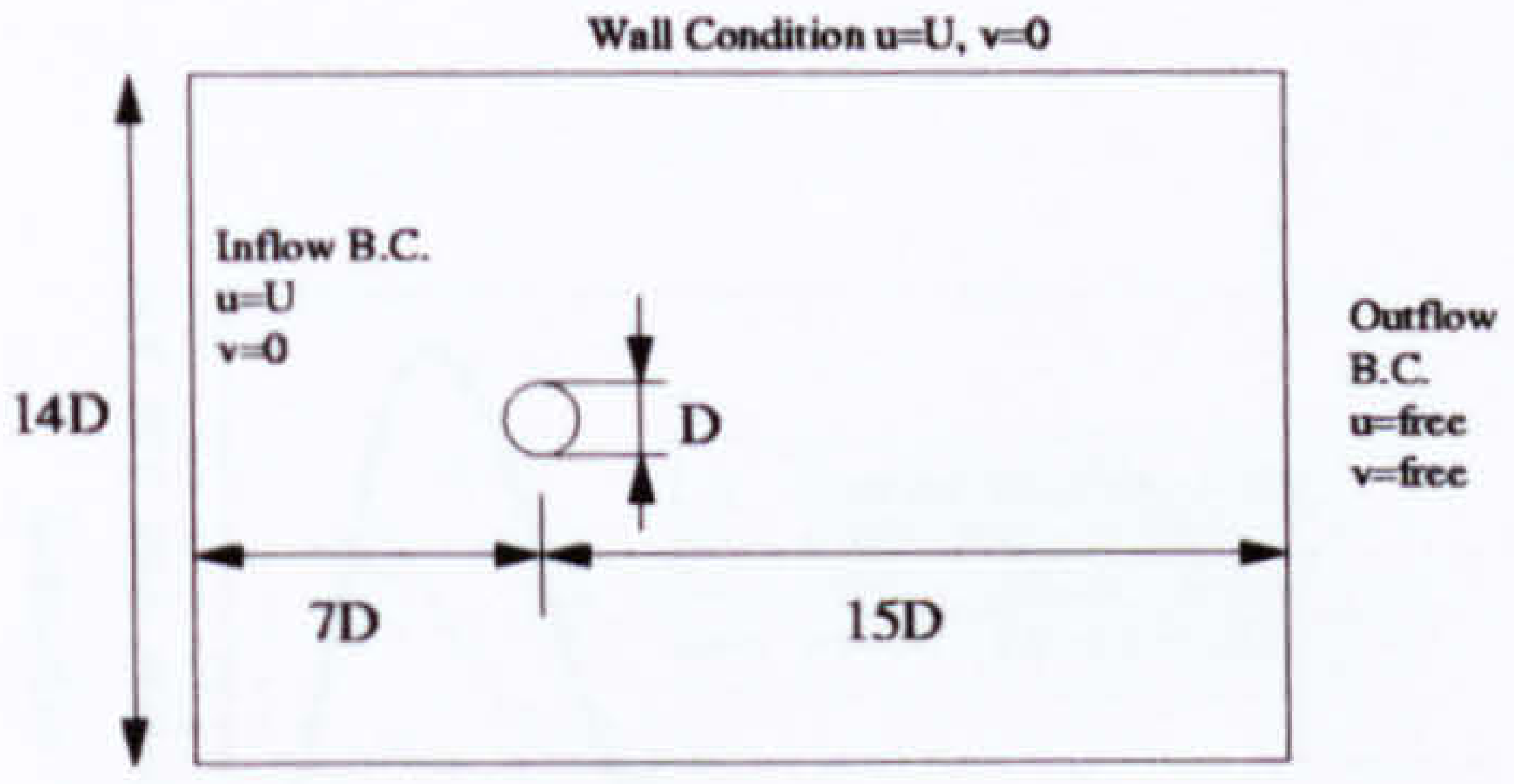

(a) Dimensions in ratio of cylinder diameter

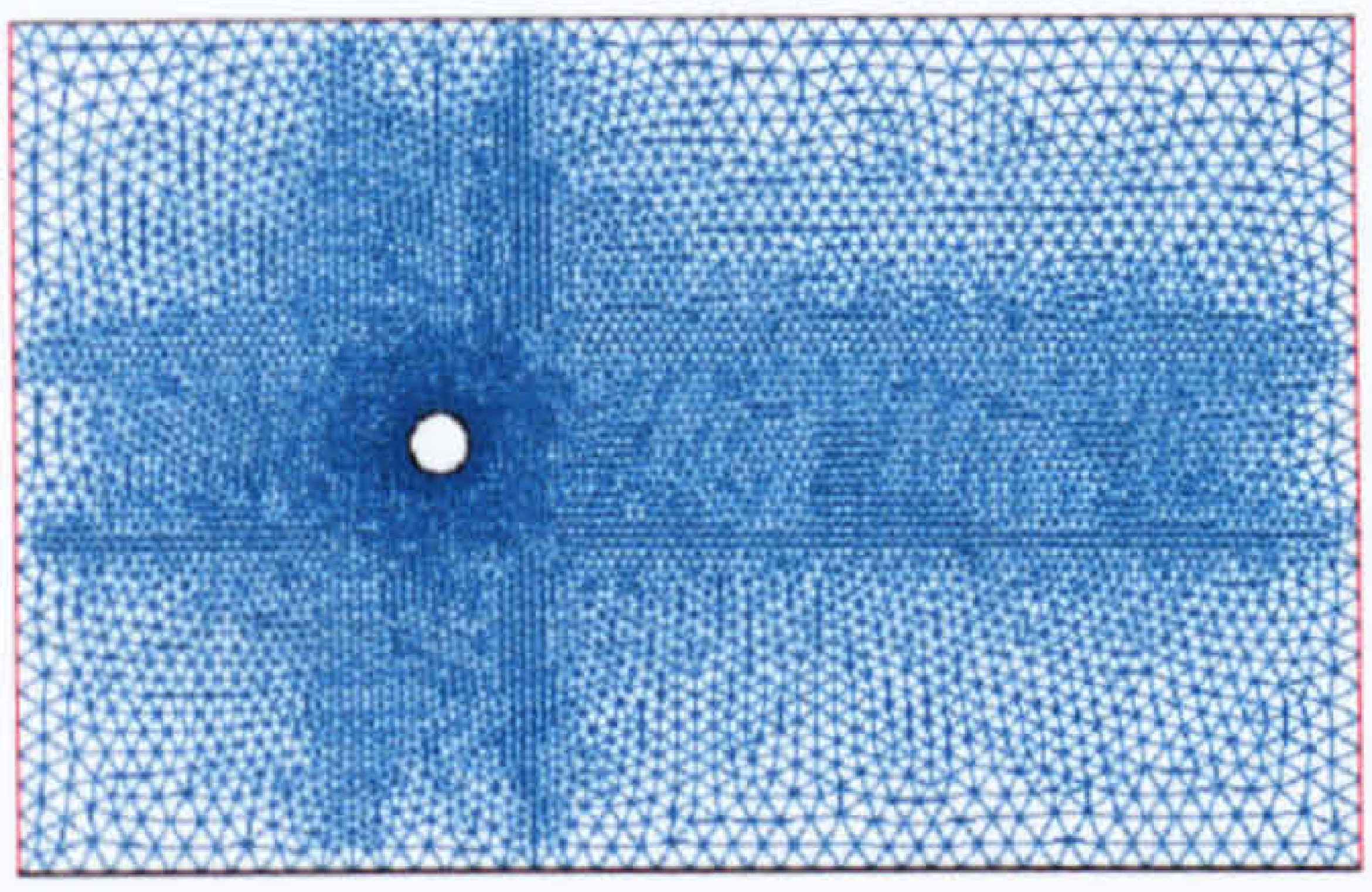

(b) Initial mesh containing 7500 nodes

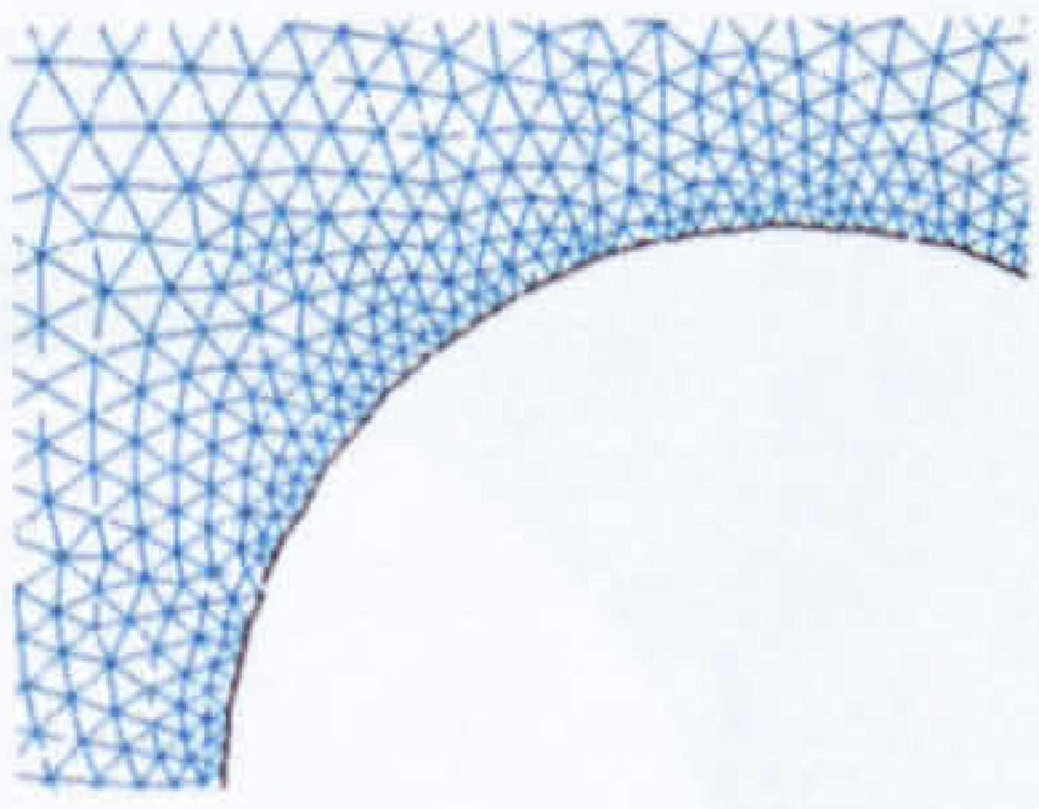

(c) Initial mesh near the wall

Figure 1. DIMENSIONS OF THE COMPUTATIONAL DOMAIN AND THE INITIAL MESH USED FOR DGA SIMULATIONS

tional reynolds numbers. Master's thesis, University of Hertfordshire, 1999.

B Cantwell and D Coles. An experimental study of entrainment and transport in the turbulent near wake of a circular cylinder. *Journal of Fluid Mechanics*, 136:321–374, 1983.

C Hirsch. *Numerical Computation of Internal and External Flows*, volume 1. Wiley, 1988.

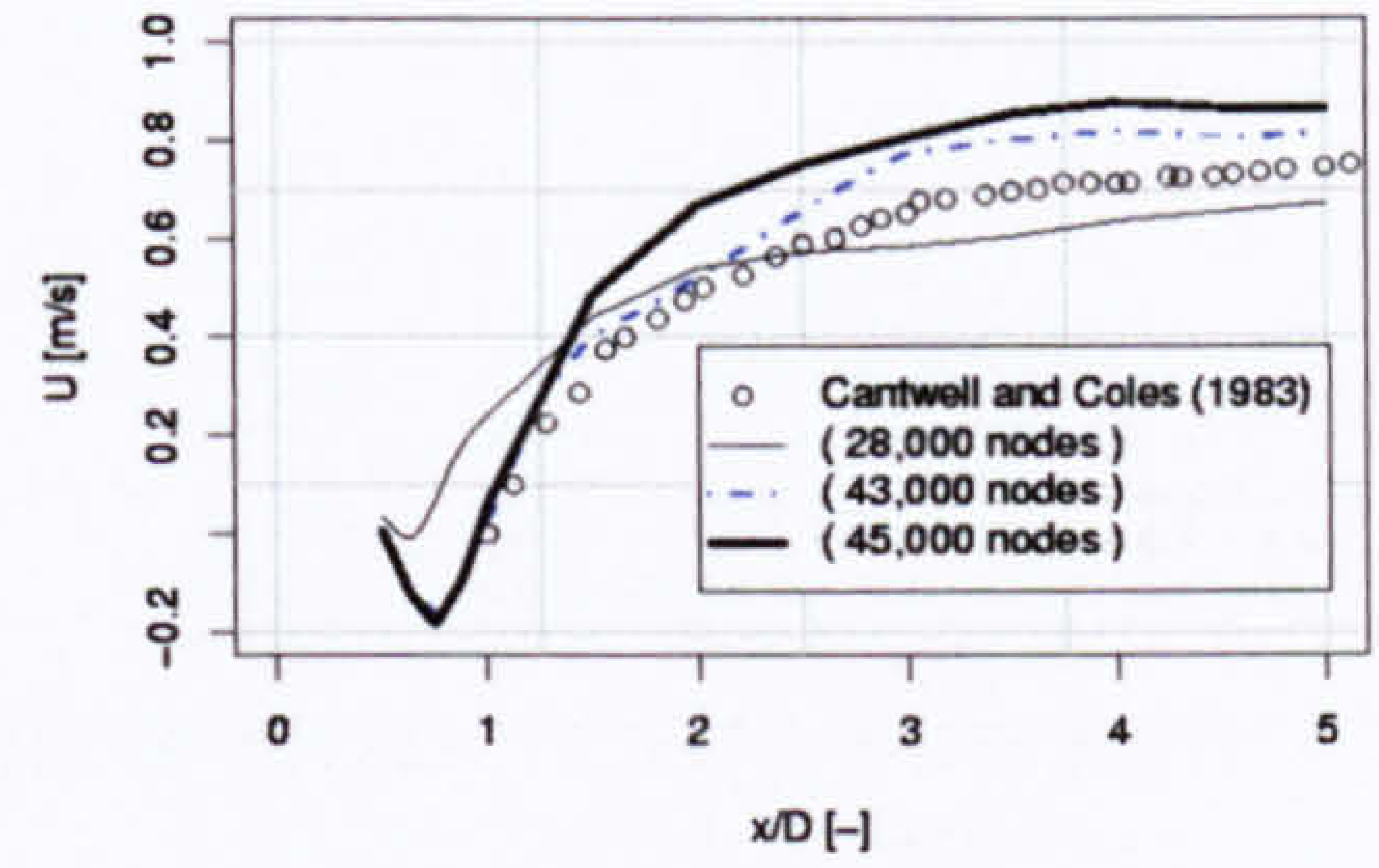

Figure 2. TIME AVERAGED NORMALIZED VELOCITY ALONG STREAMWISE AXIS AT $\frac{y}{D} = 0$, FOR SIMULATIONS USING DGA CONSTANTS $C_m = 1\text{-}C_{str} = 1$

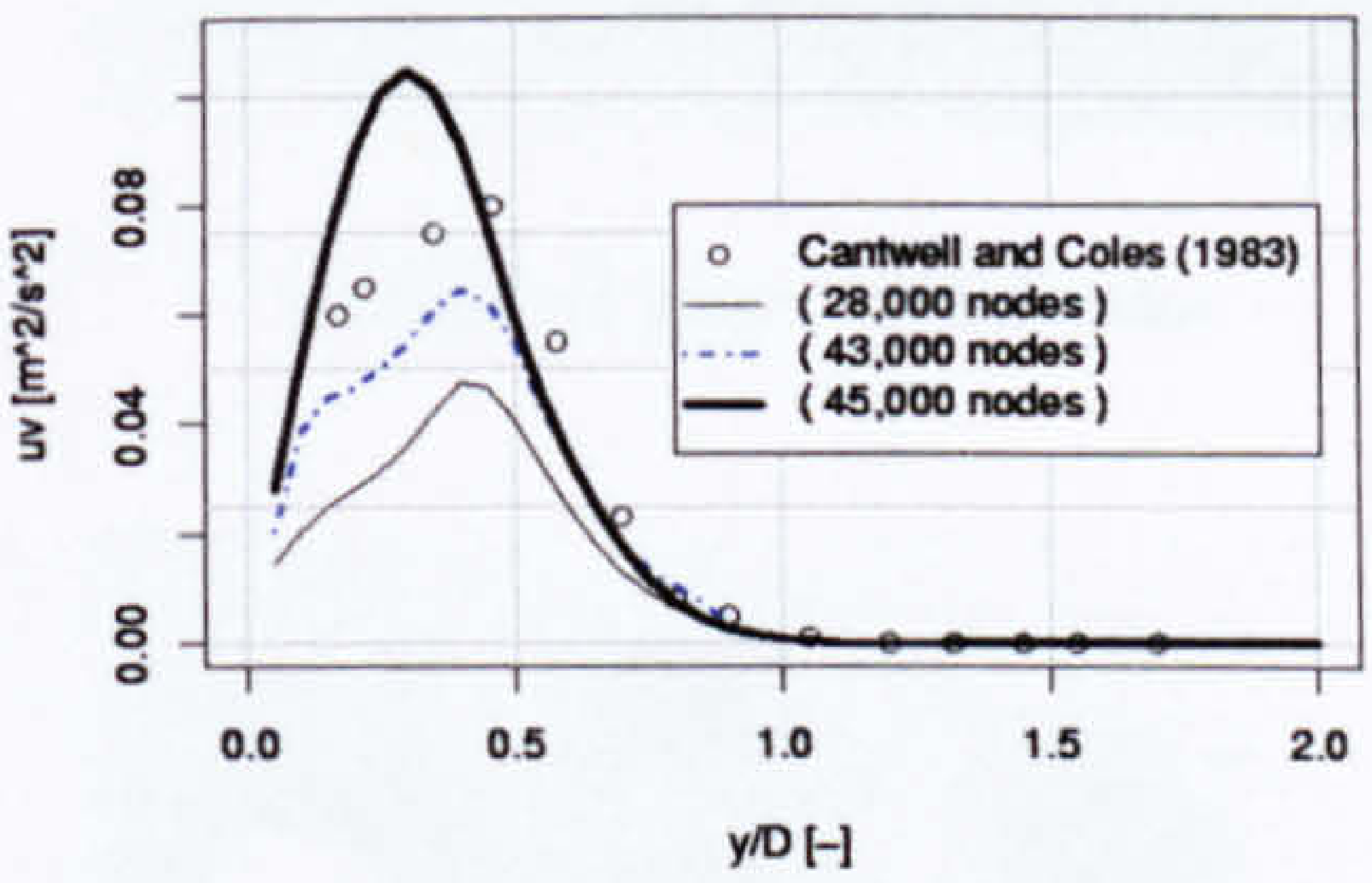

Figure 3. TIME AVERAGED NORMALIZED SHEARS STRESS DUE TO TURBULENCE ALONG THE TRANSVERSE AXIS AT $\frac{x}{D} = 1$, FOR SIMULATIONS USING DGA CONSTANTS $C_m = 1\text{-}C_{str} = 1$

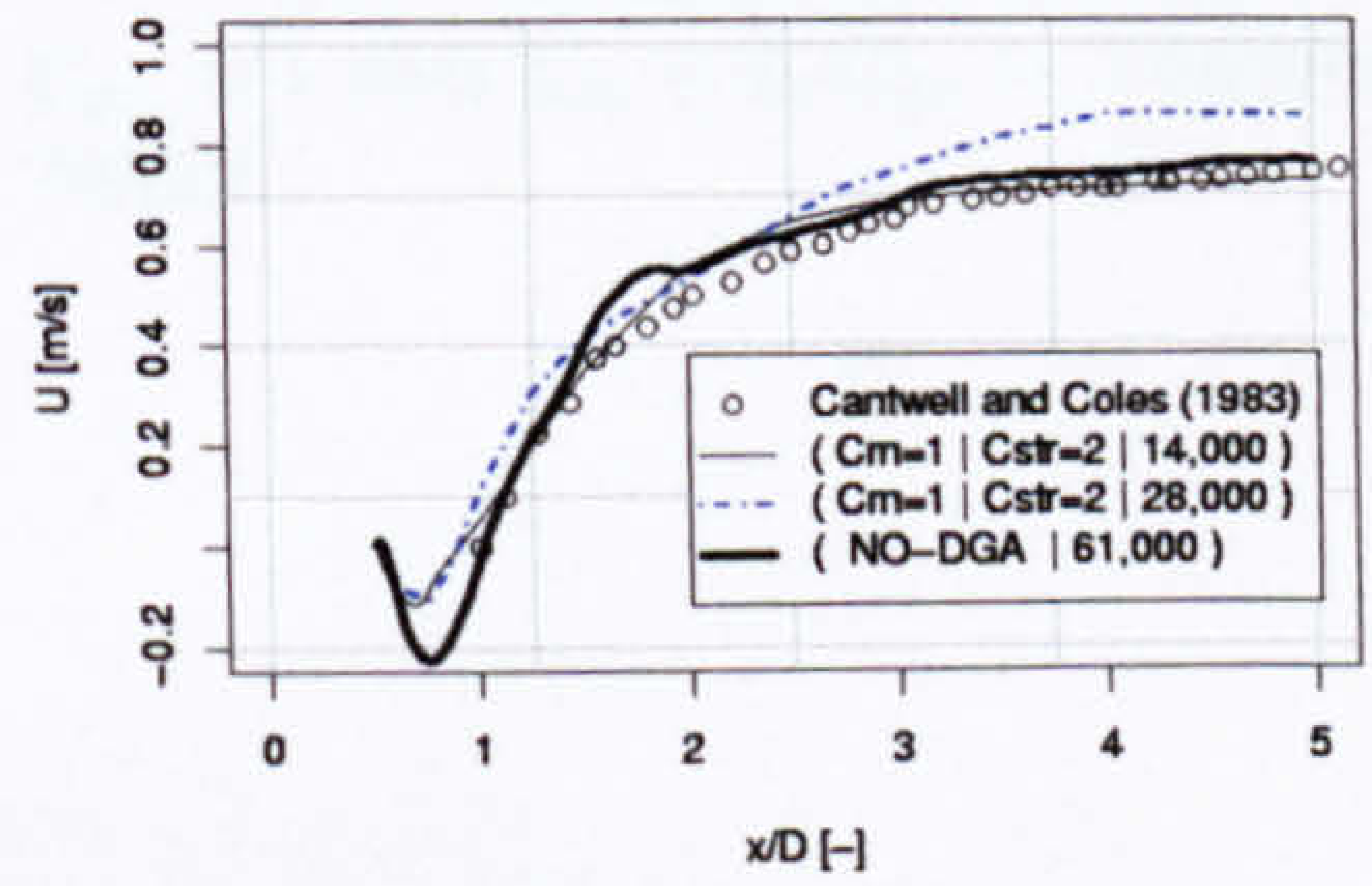

Figure 4. TIME AVERAGED NORMALIZED VELOCITY ALONG STREAMWISE AXIS AT $\frac{y}{D} = 0$, FOR SIMULATIONS USING DGA CONSTANTS $C_m = 1\text{-}C_{str} = 2$ AND CONVENTIONAL MESH

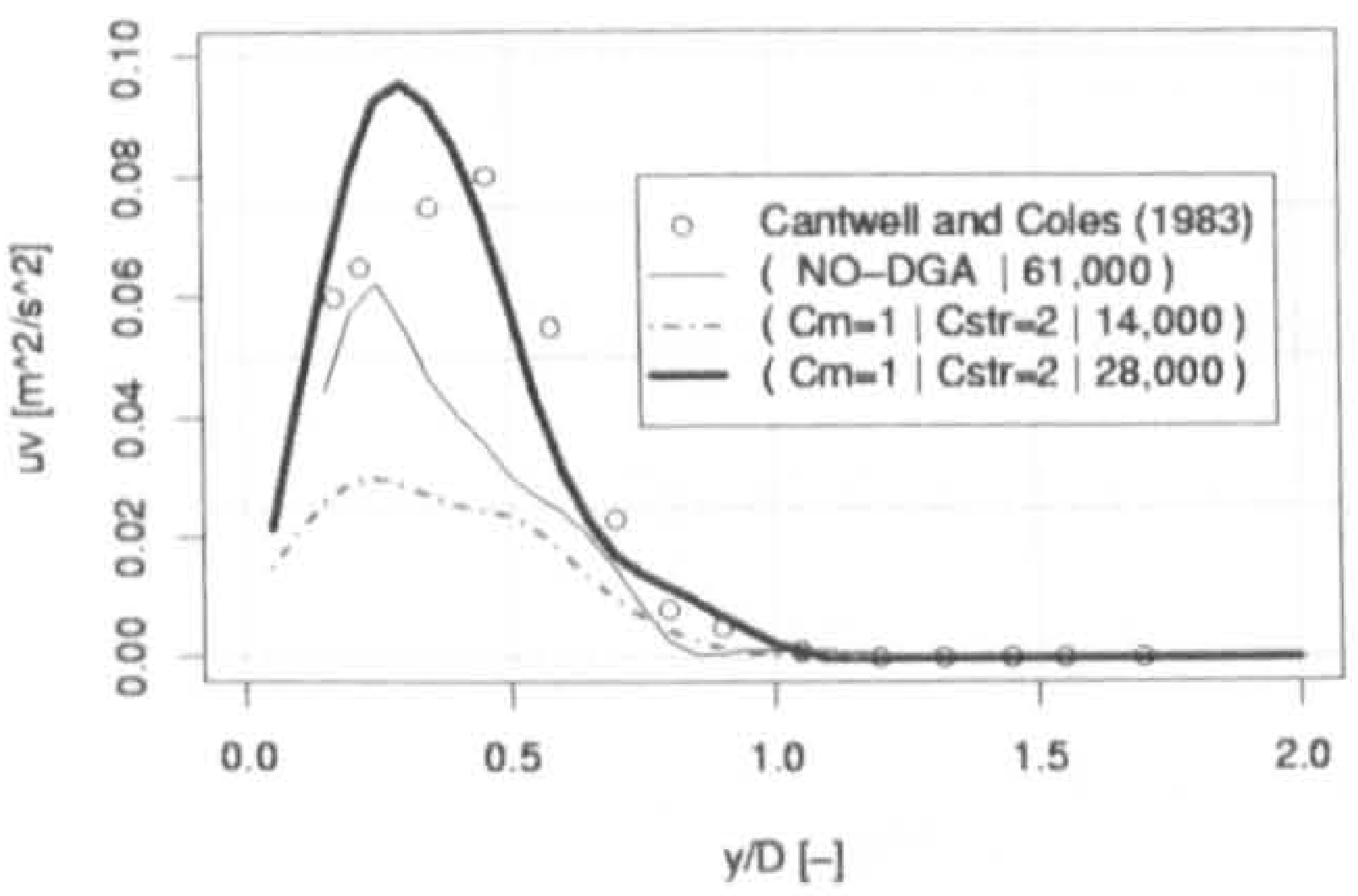

Figure 5. TIME AVERAGED NORMALIZED SHEARS STRESS DUE TO TURBULENCE ALONG THE TRANSVERSE AXIS AT $\frac{x}{D} = 1$, FOR SIMULATIONS USING DGA CONSTANTS $C_m = 1$-$C_{str} = 2$ AND CONVENTIONAL MESH

(a) Cm=1 | Cstr=1 | 45,000 nodes

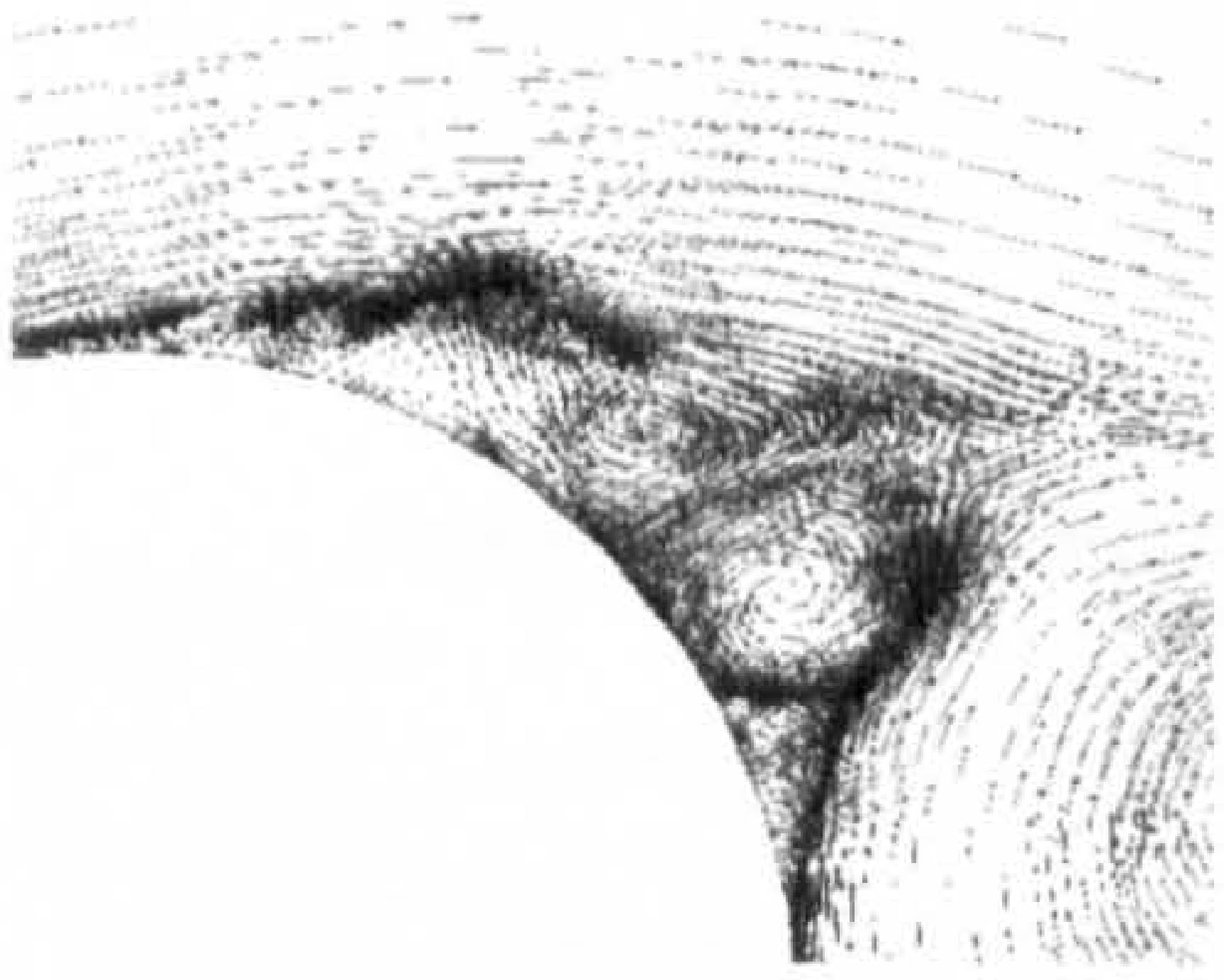

(b) Cm=1 | Cstr=2 | 28,000 nodes

Figure 6. INSTANTANEOUS VECTOR PLOT OF THE FLOW FIELD IN THE VICINITY OF THE WALL FOR SIMULATIONS WITH DGA VARIABLES TO BE $C_m = 1$, $C_{str} = 1$ AND $C_m = 1, C_{str} = 2$ RESPECTIVELY

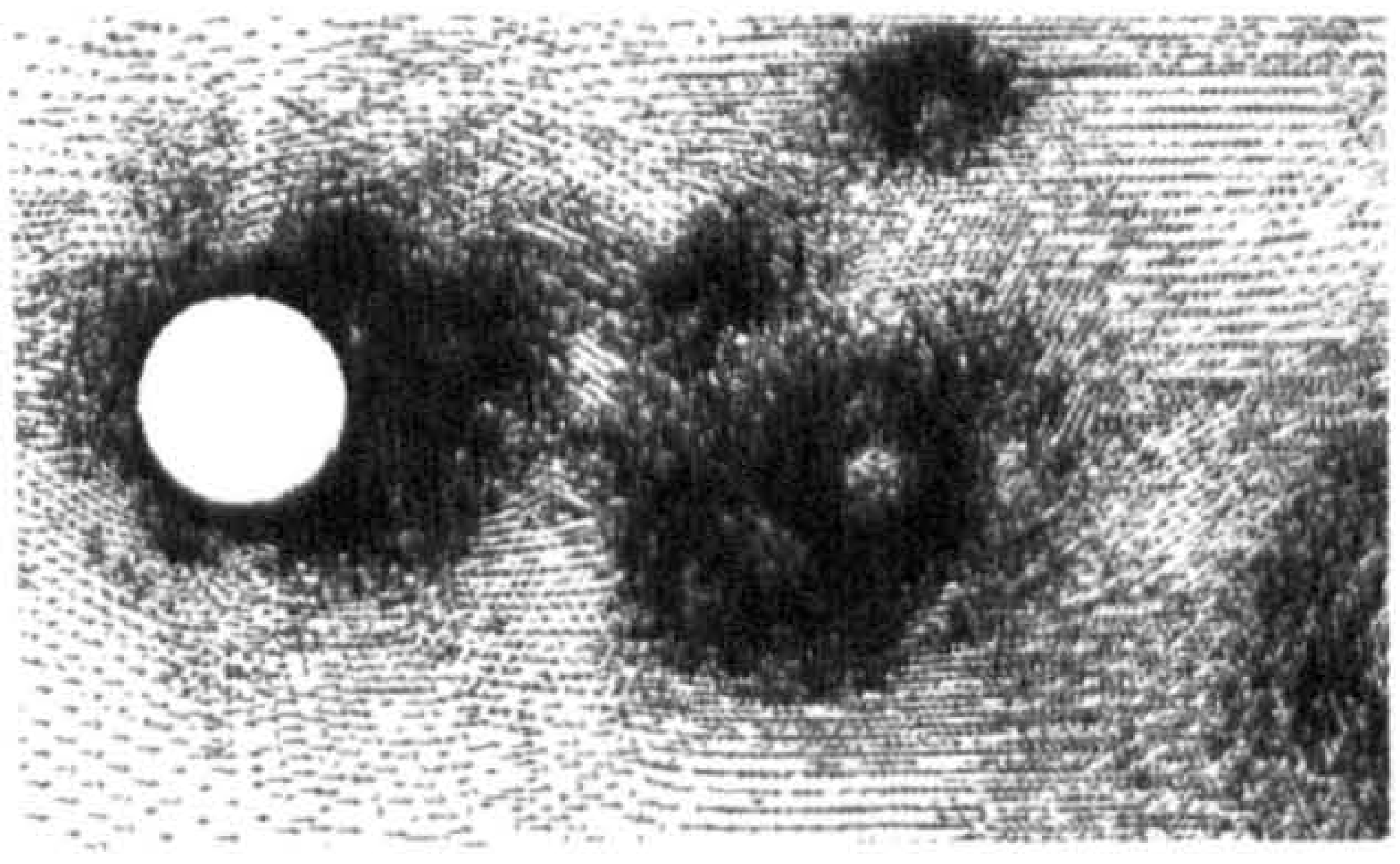

(a) Cm=1 | Cstr=1 | 45,000 nodes

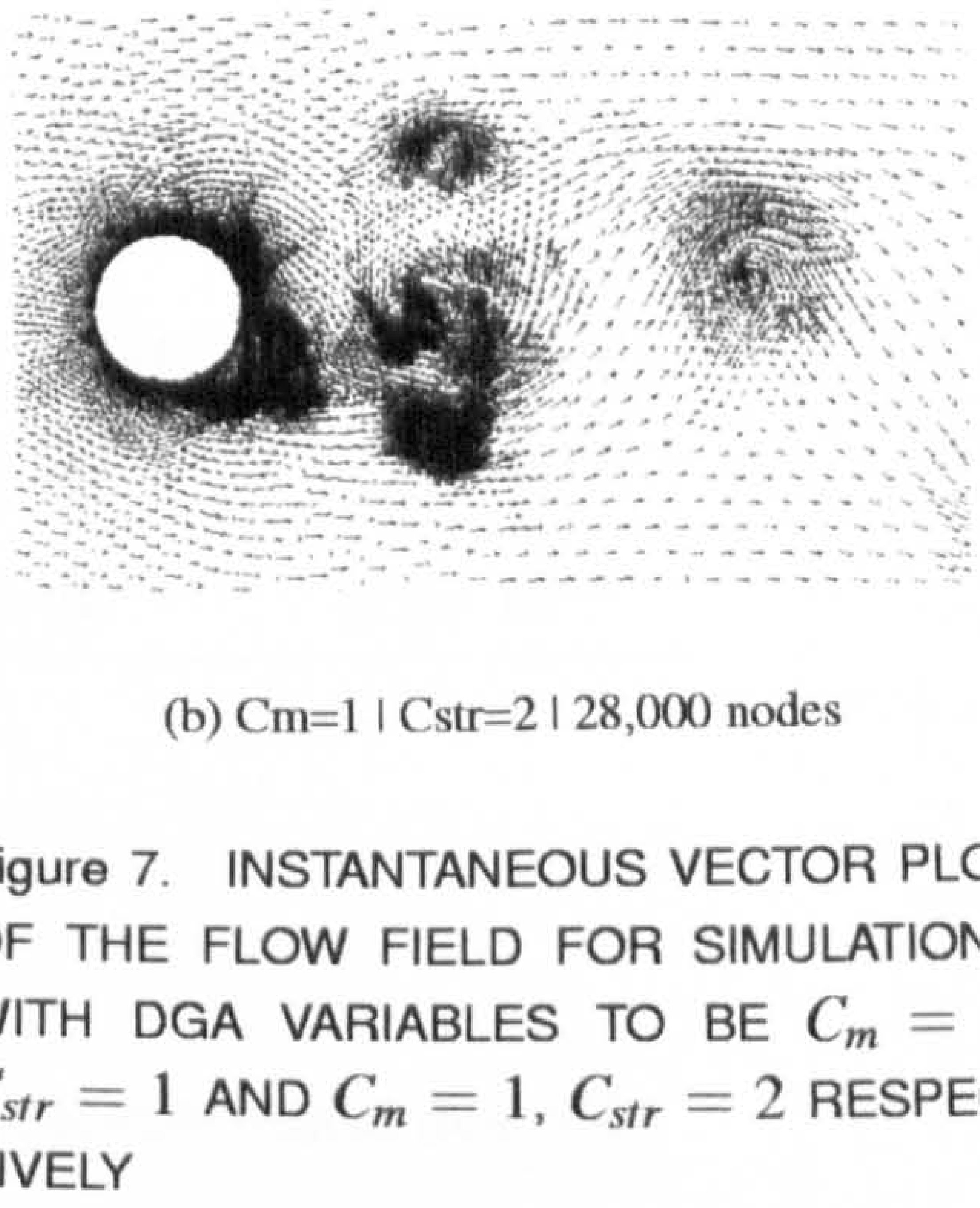

(b) Cm=1 | Cstr=2 | 28,000 nodes

Figure 7. INSTANTANEOUS VECTOR PLOT OF THE FLOW FIELD FOR SIMULATIONS WITH DGA VARIABLES TO BE $C_m = 1$, $C_{str} = 1$ AND $C_m = 1$, $C_{str} = 2$ RESPECTIVELY

Table 1. FLOW PARAMETERS FOR A CIRCULAR CYLINDER AT $Re = 1.4 \cdot 10^5$

	C_D	S_t	*Separation Angle* °
Cantwell and Coles (1983)	1.24	0.179	77
NO-DGA $\mid 6.1 \cdot 10^4$	-	0.174	86
$C_m = 1 \mid C_{str} = 1 \mid 2.8 \cdot 10^4$	1.45	0.180	96
$C_m = 1 \mid C_{str} = 1 \mid 4.3 \cdot 10^4$	1.47	0.188	89
$C_m = 1 \mid C_{str} = 1 \mid 4.5 \cdot 10^4$	1.35	0.210	95
$C_m = 1 \mid C_{str} = 2 \mid 1.4 \cdot 10^4$	1.46	0.173	81
$C_m = 1 \mid C_{str} = 2 \mid 2.8 \cdot 10^4$	1.38	0.176	85

Table 2. CONFIGURATION OF DGA ALGORITHM

	Upper Threshold	*Lower Threshold*
$C_m = 1 \mid C_{str} = 1 \mid 2.8 \cdot 10^4$	$5.0 \cdot 10^{-4}$	$2.50 \cdot 10^{-4}$
$C_m = 1 \mid C_{str} = 1 \mid 4.3 \cdot 10^4$	$2.5 \cdot 10^{-4}$	$1.25 \cdot 10^{-4}$
$C_m = 1 \mid C_{str} = 1 \mid 4.5 \cdot 10^4$	$2.5 \cdot 10^{-4}$	$1.25 \cdot 10^{-4}$
$C_m = 1 \mid C_{str} = 2 \mid 1.4 \cdot 10^4$	$7.0 \cdot 10^{-4}$	$3.50 \cdot 10^{-4}$
$C_m = 1 \mid C_{str} = 2 \mid 2.8 \cdot 10^4$	$3.5 \cdot 10^{-4}$	$1.75 \cdot 10^{-4}$

Table 3. MAXIMUM MESH RESOLUTION FOR DGA ALGORITHM

	Max.mesh resolution $[\frac{1}{A_{tr}}]$
$C_m = 1 \mid C_{str} = 1 \mid 2.8 \cdot 10^4$	$2.44 \cdot 10^5$
$C_m = 1 \mid C_{str} = 1 \mid 4.3 \cdot 10^4$	$2.44 \cdot 10^5$
$C_m = 1 \mid C_{str} = 1 \mid 4.5 \cdot 10^4$	$9.80 \cdot 10^5$
$C_m = 1 \mid C_{str} = 2 \mid 1.4 \cdot 10^4$	$2.44 \cdot 10^5$
$C_m = 1 \mid C_{str} = 2 \mid 2.8 \cdot 10^4$	$2.44 \cdot 10^5$

Table 4. MAXIMUM MESH RESOLUTION FOR A CIRCULAR CYLINDER AT $Re = 1.4 \cdot 10^5$

	Max.mesh resolution $\left[\frac{1}{A_{tr}}\right]$
NO-DGA $\mid 6.1 * 10^4$	$7.20 \cdot 10^4$
$C_m = 1 \mid C_{str} = 1 \mid 2.8 * 10^4$	$1.18 \cdot 10^5$
$C_m = 1 \mid C_{str} = 1 \mid 4.3 * 10^4$	$1.55 \cdot 10^5$
$C_m = 1 \mid C_{str} = 1 \mid 4.5 * 10^4$	$4.72 \cdot 10^5$
$C_m = 1 \mid C_{str} = 2 \mid 1.4 * 10^4$	$1.55 \cdot 10^5$
$C_m = 1 \mid C_{str} = 2 \mid 2.8 * 10^4$	$1.58 \cdot 10^5$